The Pennsylvania State University

The Graduate School

Department of Chemistry

CONTROLLING MOLECULAR ASSEMBLIES

A Thesis in

Chemistry

by

Arrelaine A. Dameron

Submitted in Partial Fulfillment
of the Requirements
for the Degree of

Doctor of Philosophy

May 2006

The thesis of Arrelaine A. Dameron was reviewed and approved* by the following:

Paul S. Weiss
Distinguished Professor of Chemistry and Physics
Thesis Advisor
Chair of Committee

A. Welford Castleman Jr.
Evan Pugh Professor of Chemistry and Physics
Eberly Distinguished Chair in Science

Christine D. Keating
Assistant Professor of Chemistry

Thomas N. Jackson
Robert E. Kirby Chair Professor of Electrical Engineering

Ayusman Sen
Professor of Chemistry
Head of the Department of Chemistry

*Signatures are on file in the Graduate School

Abstract

Using molecules designed to have only specific differences in their functionality, we have explored the influence of molecular conformation on the structural, electronic, and physical properties of self-assembled monolayers using both scanning probe and ensemble techniques. In the former case, we used two structurally similar molecules that differ in the degrees of freedom afforded to each. We found that this influenced the degree of order and conductance of self-assembled monolayers of each molecule, but had little influence of conductance switching of individual molecules inserted in alkanethiolate self-assembled monolayers.

We further demonstrated how molecular structure influences phase separation, displaceability, and molecular mobility of self-assembled monolayers by assembling 1-adamantanethiol on Au{111}. Molecular-resolution imaging of the self-assembled monolayers with the scanning tunneling microscopy confirmed a highly ordered hexagonally close-packed molecular lattice. We found that the 1-adamantanethiolate self-assembled monolayers were susceptible to replacement by the presence of another thiolated species, both from solution and vapor phases. Additionally, we determined that the displacement process is a nucleation and growth mechanism and the structure of the resulting self-assembled monolayers is dependent on the strength of the intermolecular interactions of the displacing molecules

It was hypothesized that 1-adamantanethiolate displacement was driven by a combination of energies gained from the exchange of one self-assembled monolayer for a denser self-assembled monolayer and from the increased stability due to intermolecular interaction forces.

Exploiting the susceptibility of the 1-adamantanethiolate self-assembled monolayers to displacement, we have designed a novel patterning strategy, termed 'microdisplacement printing', by combining these sacrificial self-assembled monolayers with microcontact printing. During microdisplacement printing, a molecular ink is patterned by contact with a patterned stamp directly atop an existing adamantanethiolate self-assembled monolayer, displacing the self-assembled monolayer everywhere the self-assembled monolayer is contacted. In this way, artificial diffusion barriers are created that block lateral mobility of the stamped molecules during patterning, allowing the patterning of molecules that are otherwise not patternable by conventional techniques.

We also studied the influence of deposition time and the substrate species presence on molecular transport during dip-pen nanolithography. The transport rate was dependent on the size of the patterned features, and slowed down as a function of total deposition time. Additionally, the transported molecules interacted with preexisiting substrate molecules, and the transport rate was influenced by the functionality of substrate species.

These studies demonstrate how complex assembles can be controlled by manipulating the properties of the individual components of the molecular device.

Table of Contents

List of Tables

List of Figures

List of Abbreviations

Accronyms and Abbreviations	Definition
Characterization Techniques	
STM	Scanning tunneling microscopy
STS	Scanning tunneling spectroscopy
AFM	Atomic force microscopy
LFM	Lateral force microscopy
KPM	Kelvin probe microscopy (also called electrostatic force microscopy and scanning surface potential microscopy)
FTIR	Fourier transform Infra-red spectroscopy
QCM	Quartz crystal microbalance
XPS	X-ray photoelectron spectroscopy
TPD	Temperature programmed desorption
SPR	Surface plasmon resonance
Patterning Techniques	
DPN	Dip-pen nanolithography
DDPN	Displacement dip-pen nanolithography
μCP	Microcontact printing
μDP	Microdisplacement printing
Molecules	
AD	1-Adamantanethiol(ate)
ADtether	N-Adamantyl-5-mercaptopentanamide
ALK	n-Alkanethiol(ate)
C#	n-Alkanethiol(ate) with # of alkane units (*eg.* C10, 1-decanethiol)
D#	Perdeuterated n-alkanethiol(ate) with # of alkane units
MUDA	11-Mercaptoundecanoic acid
MHDA	16-Mercaptohexadecanioc acid
AUDT	11-Amino-1-undecanethiol(ate)
ODT	n-Octadecanethiol(ate)
Other	
SAM	Self-Assembled Monolayer
V_{sample}	Applied sample bias
I_{tunnel}	Tunneling current setpoint
VDW	Van der Waals
IV	Current versus voltage
ON	High conductance state
OFF	Low conductance state

Acronyms and Abbreviations	Definition
Δh	Difference in apparent height
h_{on}	Apparent height above the surrounding SAM of a molecule in a high conductance state
h_{off}	Apparent height above the surrounding SAM of a molecule in a low conductance state
CV	Cyclic voltammogram
E_p	Cathodic peak potential
I_p	Cathodic peak current
FWHM	Full width at half maximum
CW	Clockwise
CCW	Counter-clockwise
GL	Gaussian-Lorentzian
Θ_{STM}	Fractional coverage calculated by STM
Θ_{FTIR}	Fractional coverage calculated by FTIR
Θ_{Echem}	Fractional coverage calculated by electrochemical desorption
X_{Echem}	Molecular fraction calculated by electrochemical desorption
Ink	Molecules on or deposited from the AFM tip during DPN
I (M, O)	An ink (MHDA, ODT) feature patterned in the first experimental step by DPN
I^* (M*, O*)	An ink (MHDA, ODT) feature patterned by DPN in the second experimental step
$A_{I^*|\mathrm{Au}}$	Area of I^* patterned on a bare Au{111}surface
$A_{I^*|I}$	Area of I^* that was patterned on a surface of I
$R_{I^*|I}$	Relative transport rate for I^* patterned on a surface of I compared to I^* on a bare surface

Acknowledgments

Firstly, I would like to acknowledge my thesis advisor Prof. Paul Weiss, who provided me with the opportunity and the resources to be as creative as I like, inspiring me to do my best, surrounding me with intelligent and helpful coworkers, and making sure I am progressing along a forward path. It is these things that have given me the most confidence in my scientific abilities.

I acknowledge all the Weiss group members I have encountered for their individual contributions to my graduate work. Without them I would never have made it through. I would like to acknowledge several people for their support and guidance during my graduate career. Many postdocs, current and former, have served as my mini-advisors, and have endured countless questions. To Prof. Kevin Kelly, Prof. Jennifer Hampton, Prof. Tom Pearl, Prof. Charlie Sykes, and Prof. Luis Fernandez-Torrez̀ I owe many thanks. I thank Dr. Brent Mantooth, Dr. Rachel Smith, and Dr. Penelope Lewis for their guidance inside and outside the lab, and for being excellent mentors and great friends. I thank Dr. Dan Fuchs, Amanda Moore, Steve Bumbarger, Dr. Terry Donofrio, TJ Mullen, Hector Saavedra, and Otis Butkattan for bringing sunshine and laughter, and for being just as moody and temperamental as I. Also, I send smiles to my classmates, Sanjini Nanayakkara, Beth Anderson, and Julia Heetderks, for (in no particular order) being the nice ones, the krazy ones, the picky ones, the mean ones, the competitive ones, and for being my partners in all of this.

Many of the projects included in this thesis are with the help of our collaborators. Prof. James Tour, and his student Dr. Jacob Ciszak were responsible for the synthesis of the molecules in Chapter 2. Prof Ayusman Sen, and his student Timothy Kline synthesized the adamantane tether molecule in Chapter 3. Sungku Park helped with the ellipsometry measurements. Dr. Bob Hengstebeck did the XPS analysis in Chapter 5. Valeriy Gorbonov and Xiomei Li let us use the beta version of Veeco's Nanolithography software for the work in Chapter 7, and worked with us to tweak it just so. Additionally, the physics machine shop personnel and chemistry electronic shop personnel were a huge help for all instrument development projects both big and small. I thank all of my collaborators for their effort.

I also acknowledge my thesis committee members, Dr. Will Castleman, Dr. Chris Keating and Dr. Tom Jackson, for their questions and guidance during my thesis work.

In addition to all the help I received in graduate school, I also acknowledge my undergraduate research advisors, Prof. Jacob Isrealachvili and Prof. Wolfgang Knoll, and the then graduate students and postdoc, Dr. Yufang Hu, Dr. Tobias Baumgarten and Dr. Delphine Gordon, who helped and motivated me to continue my research path. Additionally, I (finally) thank all the teachers that have encouraged me all these years, particularly Louise Perry, Matt Ellinger, Cynthia Way, and Jaime Marantz.

I owe an extra special thank you to Dr. Stephan Kraemer for being extremely supportive, enduring many hours of my complaining, and convincing me so often that I really did not want to quit and to keep going. Also, thanks for the many helpful suggestions (usually they were good ones, even if I did not want to hear them). Ich danke dir für deine Unterstützung und dafür, dass du mir die Perspektive gegeben hast, Wichtiges zu erkennen. Deine Freundschaft und deine Hilfestellung haben mir über diesen Zeitraum sehr viel bedeutet.

Finally, I thank my parents and family for being there to catch me should I fall (even when you could not watch) and showing me that I can do anything if I try hard enough. Without their love and support I would not be the person that I am.

Chapter 1

Controlling Molecular Assemblies

1.1 Introduction

We have designed, synthesized, assembled, and measured molecules with varied structures, interaction strengths, and electronic conductance to determine what qualities molecules must have to form ordered self-assembled monolayers (SAMs) with extraordinary properties such as phase-separated domains, displaceable regions, and controlled molecular mobility. These fundamental studies extend our control and understanding of complex nanoscale assemblies that are constructed from individual molecules upward (bottom-up assembly). These studies create a foundation for finding alternative strategies to traditional (light-wavelength-limited to the ten- and hundred-nanometer scale) lithographic techniques and silicon technology.

Here, using scanning probe techniques and analytical ensemble measurements, we associate molecular and supramolecular structures with function. Additionally, we have demonstrated how these tailored structures can be applied to molecular electronics and nanoscale patterning.

1.2 Background

All of the research described within this thesis pertains to SAMs, scanning probe characterization or molecular patterning. Most of the data are a combination of more than one of these. The following is a brief introduction to these three topics.

1.2.1 Self-assembled monolayers

Self-assembly, the spontaneous assembly of molecular structures without external guidance, uses the inherent chemical and physical properties of molecules to form controlled local geometries on a variety of substrates [1]. Since their inception, much progress has been made in the fabrication of SAMs and they are now accepted as a major component in many types of molecular assemblies because of their ease of preparation, stability and high structural order [2–6]. They have been used as insulating layers and as matrices in which other molecules can be studied [7–12]. Self-assembled

monolayers are more dynamic than thin films prepared from molecular beam epitaxy [13, 14] or chemical vapor deposition, [4, 15, 16] and can be formed from a variety of molecules ranging in size and functionality [3, 17–23].

Although the majority of this thesis does not focus on n-alkanethiolate (ALK) SAMs, it is useful to have a model to which to refer. The most rigorously characterized SAMs to date are ALK SAMs on Au{111} (see Figures 1.1 and 1.2) [24–30]. n-Alkanethiolate SAMs are fabricated easily from thiols or disulfides via a variety of methods, forming spontaneously on Au{111} by chemisorption of the sulfur head group to the gold surface. The formation of SAMs occurs by a quick adsorption process occuring in the first few seconds of exposure of the Au{111} to the thiol or disulfide solution, followed by a much slower adsorption-desportion exchange process with the molecules in solution, during which the molecules interact and order [29, 31]. Similar SAMs can also be created by vapor deposition [29, 32, 33] or by contact [34, 35].

During the solution or vapor deposition processes, the Au{111} surface is reconstructed by the ejection of Au atoms during molecular exchange, causing one-atom-deep substrate vacancy islands. The resulting SAMs are well ordered and highly stable because of two properties: the strong sulfur-gold bond (44 kcal/mol), and the attractive van der Waals (VDW) forces between adjacent alkyl chains ($\sim$4-8 kcal/mol) [29, 31, 36–38].

As illustrated in Figure 1.2, the ALK SAMs pack into a $(\sqrt{3} \times \sqrt{3})R30^\circ$ geometry with respect to the underlying Au{111} lattice, with a nearest neighbor distance of 5.0 Å. The molecules pack in domains that are oriented with a 30° tilt with respect to the surface normal to maximize VDW interactions between neighboring molecules (see Figure 1.2A). The domains are defined by the substrate vacancy islands, substrate step edges, and by domain boundaries (denoted by the arrows in Figure 1.1A). A domain differs from its neighbors by differences in translation, rotation or tilt, each causing a different variety of domain boundary [32, 39]. In addition to the $(\sqrt{3} \times \sqrt{3})R30^\circ$ unit cell, a primitive c(4 × 2) superlattice has been observed and is shown in Figure 1.2B. This has been explained by an alternating azimuthal orientation of one molecule with respect to its neighbor.

1.2.2 Molecular-scale characterization using scanning probe microscopy

There are many quantitative ensemble measurements of the physical and electronic properties of SAMs, such as optical spectroscopy [4, 23, 40] and electrochemistry [41–43]. However, ensemble measurements of physical properties are not capable of resolving the local environment of
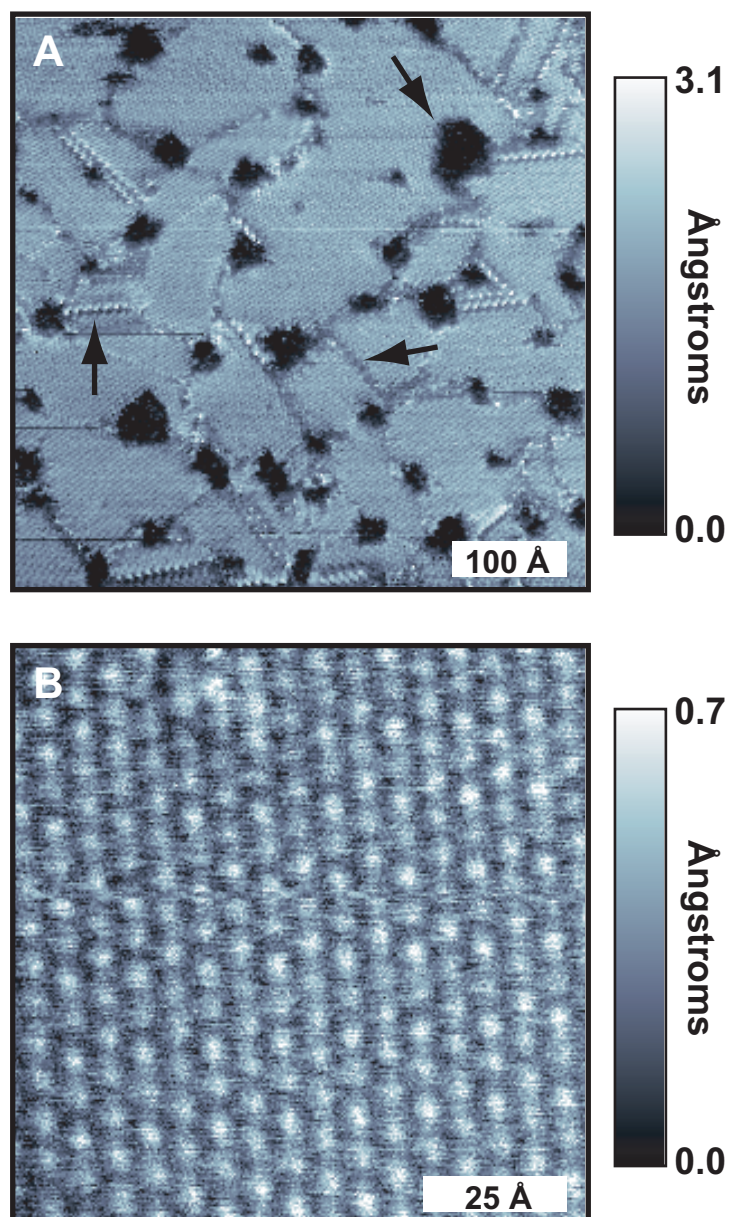
Figure 1.1.   A) A STM image of a 1-octanethiolate SAM on Au{111}. The arrows show the different varieties of domain boundaries. Imaging parameters: V_{sample}: 1 V; I_{tunnel}: 2 pA; 500 Å× 500 Å. B) A higher resolution STM image of a 1-octanethiolate SAM V_{sample}: 1 V; I_{tunnel}: 2 pA; 100 Å× 100 Å.
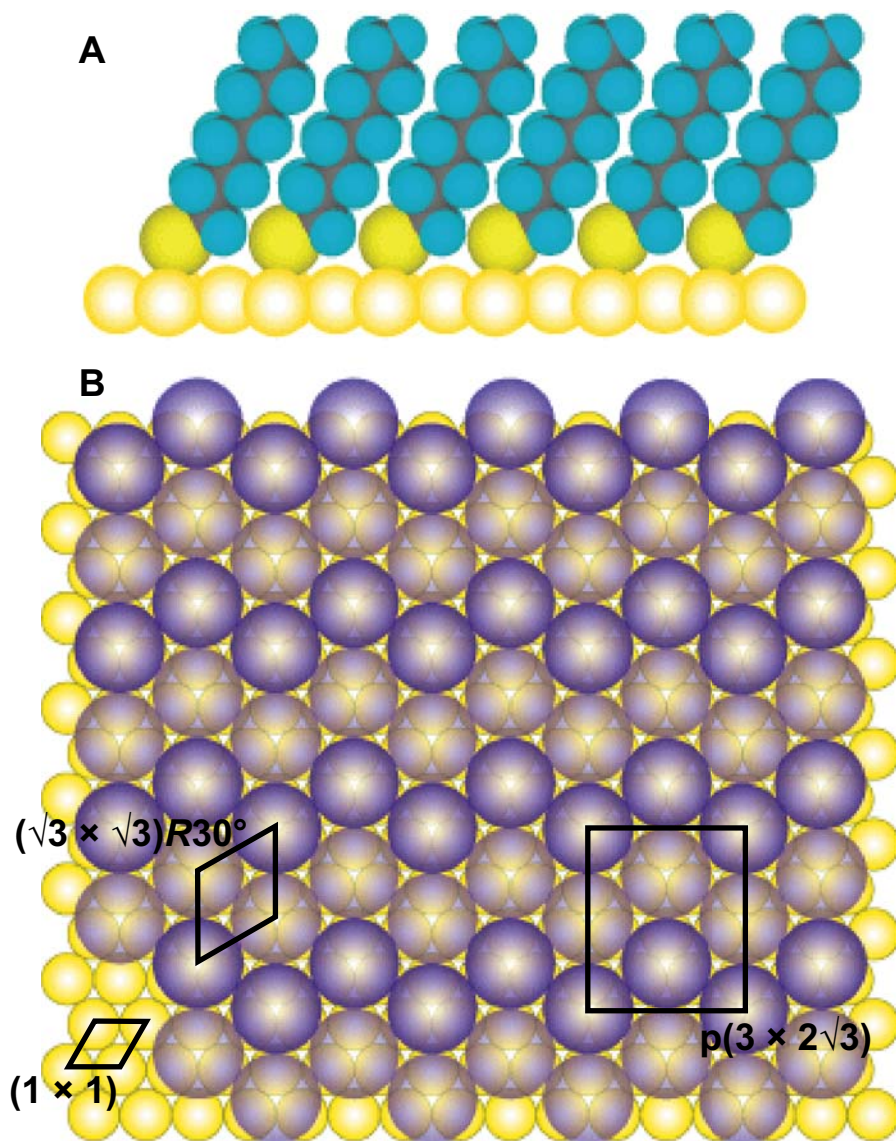
Figure 1.2. Schematics showing n-alkanethiolate SAM structure on Au{111}. A) A side view along the nearest neighbor direction showing the 30° tilt to maximize van der Waals interactions. B) A top down view showing the unit cells of the underlying Au{111} substrate as well as the ($\sqrt{3} \times \sqrt{3}$)$R30°$ unit cell and the p($3 \times 2\sqrt{3}$) (equivalent to c(4×2)) superlattice of the n-alkanethiolate SAM. The darker and lighter molecules highlight the c(4×2) superstructure.

single molecules, and conductance measurements of one molecule (or a very few) are possible, but difficult, relying on techniques such as lithographically fabricated pores or contacts [44–46], break junctions [45, 47], and mercury drop experiments [48–50]. Additionally, determining whether the measured electronic properties of an assembly are a result of one molecule or a few molecules is often difficult. For determination of the physical properties of nanoscale features and real-space images of surfaces, scanning probes, such as scanning tunneling microscopy (STM) and atomic force microscopy (AFM), are unsurpassed. Because most of the data in this thesis were obtained by either STM or AFM techniques, a brief introduction follows. A more thorough explanation of specific techniques is given in each chapter.

Scanning probes are all based on the same components: a tip, a scanning assembly, a detection mechanism and a feedback control system. Except for the scanning mechanism, AFM and STM differ from each other in all these categories. Both are rastering techniques that measure the sample properties via the detection mechanisms at a single point on the surface and then move to the next point and repeat the measurement. An image is generated by assembling the points into a two-dimensional map of the surface.

Rastering is achieved by the use of piezoelectric material, which stretches or contracts upon application of an electric potential. The majority of scanners (inclusive of those used for these works) are based on the tube configuration. In this configuration, the outside of the tube is separated into four sections that are electrically isolated from each other. An electrode is applied to each section and the inside. The tube stretches or contracts vertically by applying a voltage between the inside and outside, and by applying a voltage across the tube it stretches laterally.

1.2.2.1 Scanning tunneling microscopy

Figure 1.3 shows the basic instrumental set up for STM. An atomically sharp metallic tip is brought within Ångstroms of an atomically flat conductive surface. At this distance, electrons can tunnel across the vacuum barrier from the sample to the tip and vice versa. When a bias (V) is applied between the tip and sample, causing a shift in equilibrium, resulting in a tunneling junction similar to the one shown schematically in Figure 1.4. In this simplified case, due to the offset of the Fermi levels of the tip and the sample (designated by the lower dashed line in Figure 1.4), electrons flow from the tip to the sample by tunneling across the vacuum barrier, and inducing a net tunneling current. The tunneling current (I) decays exponentially with barrier width (z) and
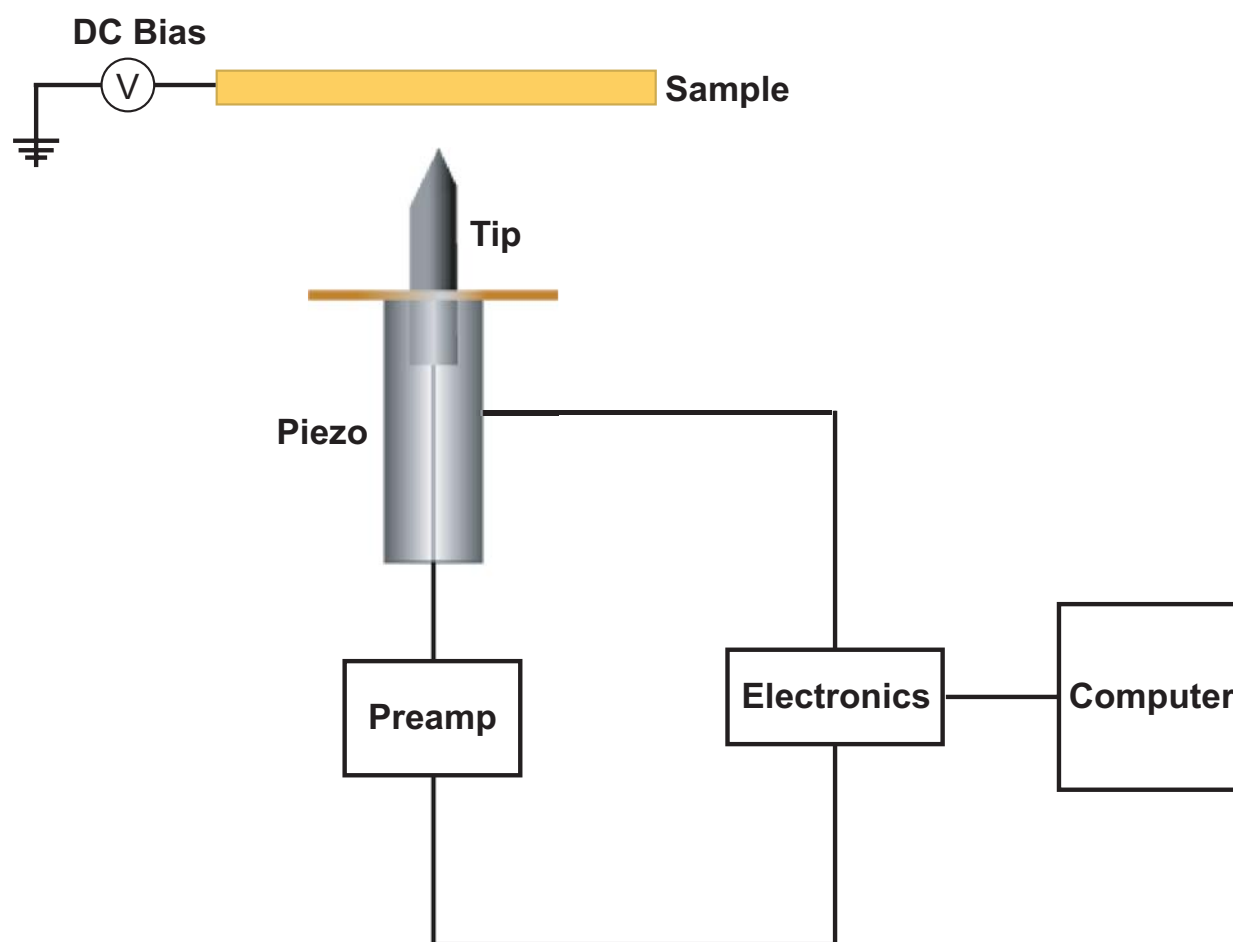
Figure 1.3.   A schematic of the scanning tunneling microscope. A bias is applied between the sample and tip, and the resulting current is recorded and is simultaneously adjusted by changing the tip-sample separation via the feedback loop.
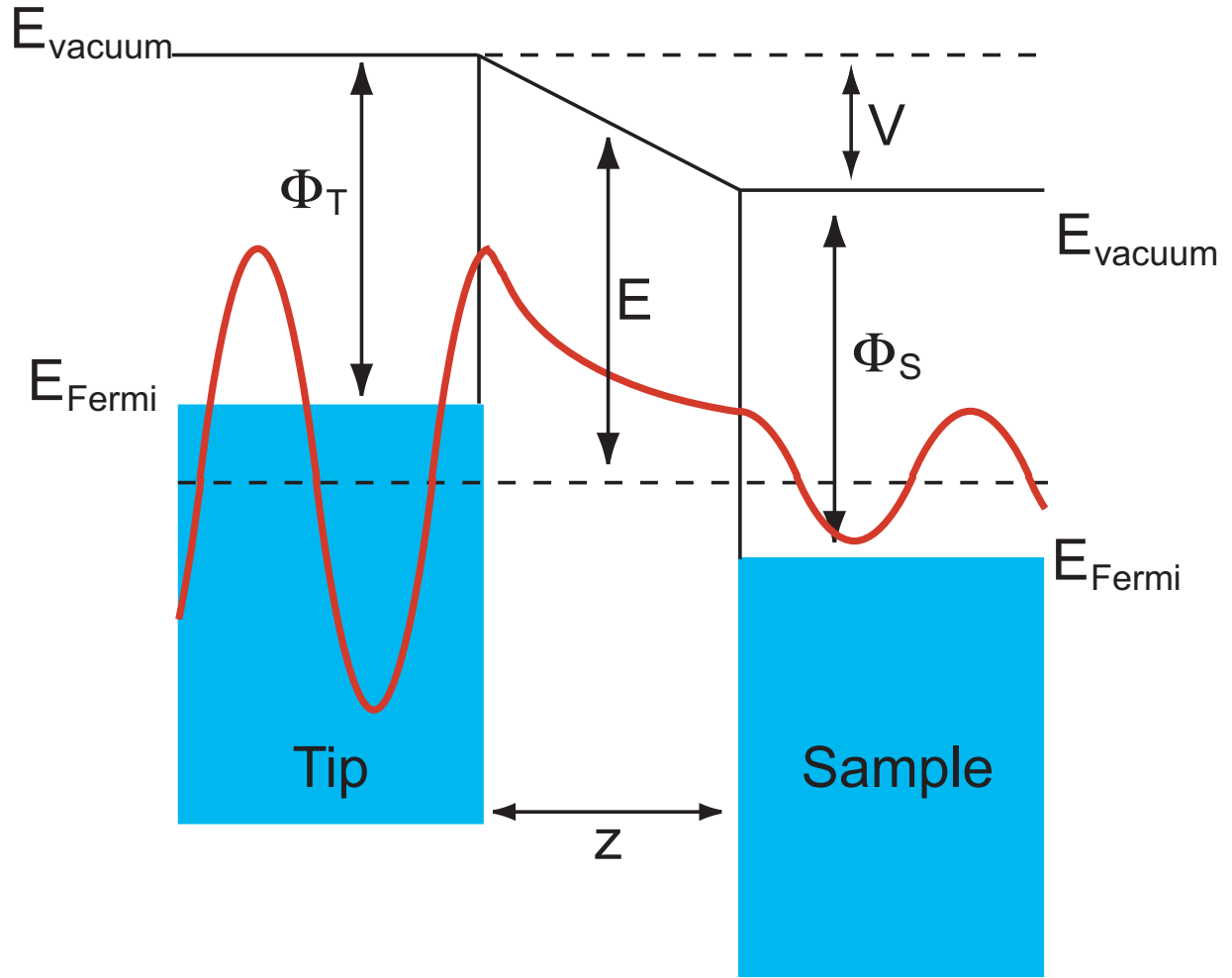
Figure 1.4. A one-dimensional metal-vacuum-metal tunneling junction. By applying a bias (V), the electrons (the wavefunction is shown schematically in red) tunnel across the vacuum barrier to balance the Fermi levels (designated by dashed line) of the tip and sample (shown in blue). The resultant current is exponentially proportional to the distance between the sample and the tip (z) and the height of the barrier (E), influenced by the work functions of the sample (Φ_S) and the tip (Φ_T).

is defined as

$$I \propto e^{-2\kappa z}, \tag{1.1}$$

where

$$\kappa = \frac{\sqrt{2m(V-E)}}{\hbar}, \tag{1.2}$$

m is the electron mass, and $\hbar$ is Plank's constant. E is the energy of the state (the energy of the electron) and for electrons at the Fermi level $V - E = -\Phi$, the height of the barrier, influenced by the workfunctions of the tip and the sample [51]. Note that the introduction of molecules or a surface film into the tunneling junction influences the workfunction of the sample, and thus the potential barrier.

Because the tunneling current decays exponentially with increased tip-sample separation, only the atoms at the apex of the tip contribute to the tunneling current. As a result, the tunneling current is extremely localized and the STM is highly sensitive (within tenths of Ångstroms) to both lateral and vertical changes in topography.

Although it is possible to use the STM in constant height or constant current mode, the data herein was collected using constant current mode. In this mode, a feedback mechanism monitors the preamplified tunneling current and changes the tip-sample separation to maintain a constant current. Simultaneously, the tip is rastered in the x and y directions across the sample and by measuring the voltage applied to the piezoelectric transducer that controls the tip-sample separation to maintain a constant current, an image of the surface is generated.

A significant limitation of STM is that the sample must be conductive because the feedback is based on the tunneling current. This limits the thickness of insulating material (i.e., SAM height) that may be imaged. If the potential barrier is too high (from a locally non-conductive surface), or too wide (z is large), then tunneling cannot occur. Additionally, the measured signal is always a convolution of topography and conductance since the measured current, and therefore tip-sample separation, are affected by both of these properties, and must be interpreted as such.

1.2.2.2 Atomic force microscopy

For measurements of pure topography or of nonconductive samples on the nanoscale, AFM is a better choice. The ability to measure topography from the nanometer to the micrometer scale in vacuum, ambient and biologically relevant environments, makes AFM a versatile instrument,

capable of techniques ranging from surface friction and potential to magnetism. However, AFM is not typically capable of the resolution of STM, because it does not have the same exponential sensitivity to tip-sample separation as STM.

Atomic force microscopy relies on the detection of the forces occurring between the tip and the sample, many of which are short-range interactions, namely VDW interactions. Depending on the measurement, long-range forces, such as electronic and magnetic forces may also be measured [52].

Van der Waals interactions arise from three components: polarization, the contribution from permanent dipoles in the material; induction, the contribution from induced dipoles; and dispersion, the contribution from temporary fluctuations in induced dipoles from moving electrons in neighboring molecules [52]. The VDW potential ($W(z)$) for two identical atoms is given by the equation

$$W(z) = -(\frac{1}{4\pi\epsilon_0})^2(\frac{\mu^4}{3kT} + 2\mu^2\alpha + \frac{3}{4}\alpha^2\hbar\omega)(\frac{1}{z^6}),$$ (1.3)

where ϵ_0 is the permittivity of free space, μ is the dipole moment, k is Boltzman's constant, T is temperature, α is the polarizability, and $\hbar\omega$ is the ground state energy of the electrons [53]. This equation can be simplified to

$$W(z) = -\frac{C}{z^6},$$ (1.4)

where C is the London dispersion constant. Assuming the interaction is non-retarded (*i.e.* there is no delay between an action and when it is felt) and additive it is possible to sum the energies of all atoms in a body with all the atoms in another body to calculate the VDW interaction between macroscopic objects. For a sphere and a plane where the radius is much larger than the separation (tip and sample) Equation 1.3 becomes

$$W(z) = -\frac{Ar}{6z},$$ (1.5)

where r, is the radius of the sphere. The simplified Hamaker constant, A, is

$$A = \pi^2 C \rho_1 \rho_2,$$ (1.6)

where ρ_1 and ρ_2 are the number densities (particles per cm^3) of each material [53].

A

Laser

Detector

Electronics

Computer

Tip

Sample

Piezo

B

Laser

Detector

Electronics

Computer

Tip

Sample

Piezo
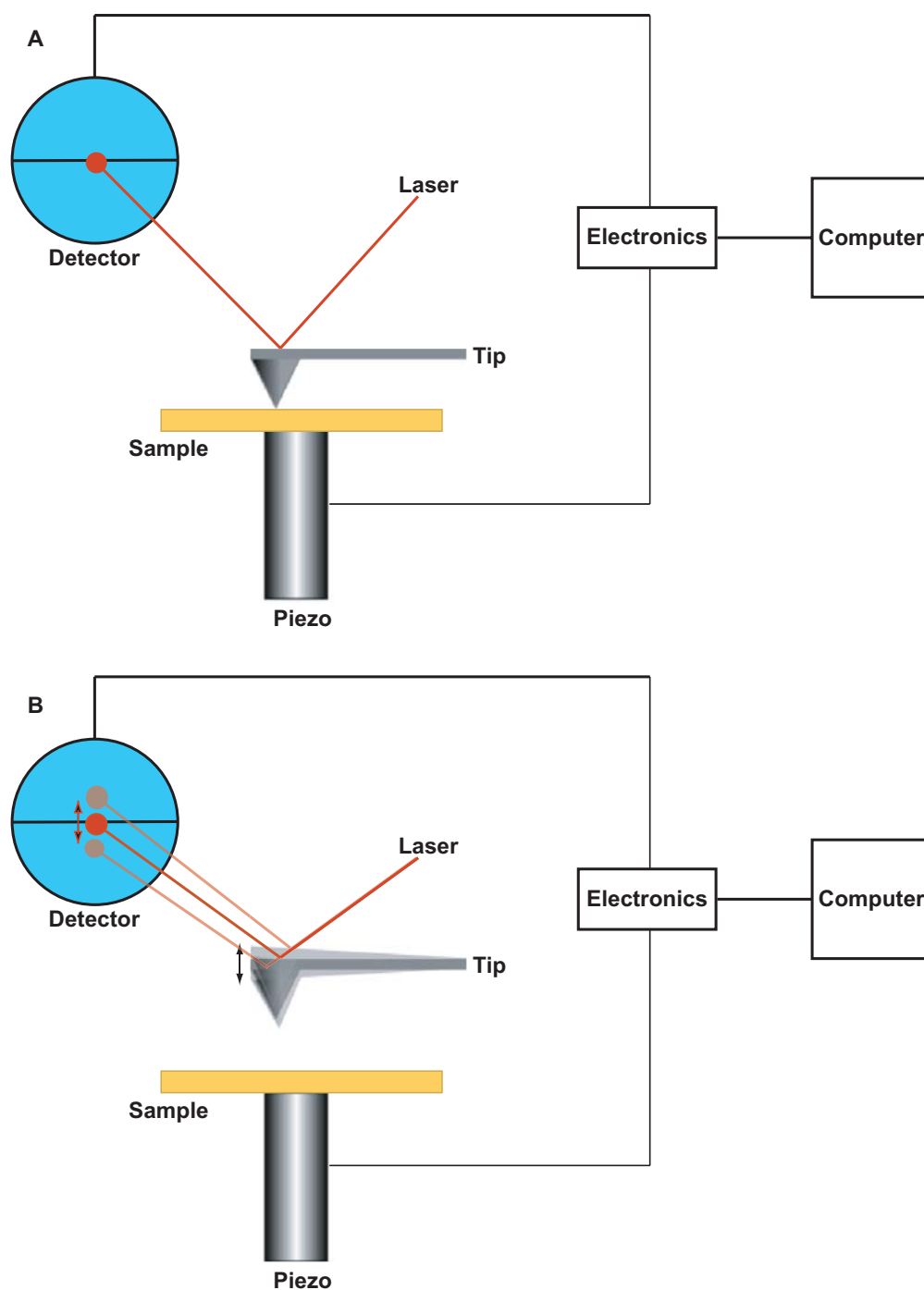
Figure 1.5.   Schematics of (A) contact and (B) non-contact mode atomic force microscopy. A laser reflected off the back of the cantilever, focused on a photodetector is used for feedback. In contact mode, the position of the laser spot on the photodetector is recorded and simultaneously used in the feedback mechanism. In non-contact mode, the amplitude of the laser modulation on the photodetector is recorded and simultaneously used in the feedback mechanism.

From the above equations, we can approximate the force $(-\frac{dW}{dz})$ on the tip from the sample. The force between any identical materials is attractive at separations greater than chemical bond distances, the force between two different materials can be repulsive (when the permittivity of the surrounding medium is between those of the two interacting materials, causing the induced dipoles to act destructively and resulting in a negative Hamaker constant [53–57]), and the force is highly sensitive to the tip-sample separation [52].

Figure 1.5 shows the two major modes of AFM. In contact mode (Figure 1.5A), an AFM cantilever with a sharp tip is brought into contact with the surface to maintain a constant force. A laser is reflected off the back of the cantilever onto a detector. A deflection in the cantilever from a change in surface topography (and change in force on the tip) causes a deflection of the laser on the detector. The feedback mechanism then adjusts the sample position to maintain a constant force on the tip from the sample. Similar to STM, an image is created by rastering the tip (generally the sample is moved) across the surface while measuring the voltage applied to the piezoelectric transducer to maintain a constant force.

Non-contact mode (Figure 1.5B) is a more sensitive technique that uses the vibrational resonance of the cantilever. The resonant frequency is material and geometry dependent and is related to the spring constant by

$$\omega_0 = \sqrt{\frac{k}{m_{\text{eff}}}}, \tag{1.7}$$

where k is the spring constant and m_{eff} is the effective mass, when approximated as a classical fixed-free beam. In non-contact mode, an AC modulation is applied to the cantilever at a fixed frequency (near its resonance frequency) and fixed driving force. The force gradient $(-\frac{d^2W}{dz^2})$ that is created by surface proximity causes a shift in the cantilever resonance by decreasing the spring constant, and the shift is given by

$$\Delta\omega_0 = c\sqrt{k} - c\sqrt{k - \frac{d^2W}{dz^2}}, \tag{1.8}$$

where c is a constant. The frequency shift causes a decrease in vibration amplitude proportional to the force gradient [52]. Therefore, as the tip is brought near the sample, the modulation is dampened. As in contact mode, a laser is reflected off the cantilever and the modulation amplitude and frequency are amplified by the light beam, focused onto the photodetector. The feedback mechanism adjusts the sample position to maintain a constant modulation amplitude, and an

image is created by rastering the sample and measuring the voltage applied to the piezoelectric transducer to keep the modulation amplitude constant.

1.2.3 Molecular patterning

Currently, irradiative lithographies such as photolithography, and electron-beam, extreme UV and soft x-ray lithographies, are the primary tools for microfabrication. However, traditional light-based lithographic methods are ultimately limited by the optical diffraction of the light used (or by the availability of sources and optics to focus the light in the case of extreme UV or x-ray techniques), can only be used on relatively flat surfaces with specific photoresist materials, and in some cases can be slow and costly [35]. A variety of molecular patterning techniques have been developed to overcome these shortcomings and to incorporate specific chemical functionalities into patterned, nanoscale systems. These techniques vary significantly in their strategies to fabricate molecular patterns, but all involve molecule manipulation by selective removal, placement, reaction, or destruction. These techniques also vary greatly in their ease and speed of fabrication, and the achievable resolution of the fabricated patterns. For example, electrochemical "whittling" is a fast [6, 35], parallel technique with a resolution in the range of hundreds of nanometers, while scanning probe placement or removal of molecules is a slow, serial technique with resolution in the range of 1 nm [77].

However, all of these techniques are impacted by the properties of the molecules that are being used for patterning. Incorporating functionalities and using more than one type of molecule allows for structures that have specifically engineered properties (such as wettability, permeability, or reactivity). Furthermore, understanding and manipulating the intermolecular interaction strengths allows for the rational design of complex molecular structures.

This thesis focuses on two techniques developed for the specific placement of molecules to form patterned SAMs, microcontact printing (μCP) and dip-pen nanolithography (DPN). Microcontact printing is the direct transfer of molecules to a substrate by contact of a molecularly-coated, elastomeric stamp to the substrate (similar to a rubber stamp on paper) and belongs to a subclass of non-photolithographic techniques called soft lithography [58] established by Whitesides and coworkers [35]. This is a parallel technique for patterning the entire substrate simultaneously with the minimum resolution demonstrated being $\sim$30 nm for a single pattern applied [59]. However, although the technique is fast, it is difficult to use μCP in multiple steps to place two patterns in exact

registration with each other. Many molecule-substrate systems have been used with μCP such as lipophilic molecules and biomolecules on metallic and glass substrates for cell, vesicle and protein attachment [60–63], organic molecules on metallic substrates for etch resists [64–68], and colloid and polymers on metallic and semiconductor surfaces for microfabrication applications [69–76]. Dip-pen nanolithography is a technique developed by Mirkin and coworkers [77, 78], which rasters a molecularly coated AFM tip, transferring molecules to a substrate (similar to an ink pen on paper). This is a much slower serial technique, but is capable of greater resolution on the order of 10 nm [77, 78]. This too has been used for a variety of molecule and substrate systems including polymers [79] and inorganic solid state materials [80–82] for microfabrication, although a great deal of effort has gone towards deposition of bioassays for protein and virus detection, [83–85]. In the works discussed here, we further develop existing patterning techniques by the manipulation of intermolecular interaction strengths of SAMs and study the patterned films created by these techniques using several scanning probe measurements.

1.3 Thesis Overview

The research described in the following chapters pertains to the effects of molecular structure on the chemical, physical, and electronic properties of SAMs, and in turn, how the properties of SAMs affect molecular patterning.

In Chapter 2, we investigate the influence of molecular structure on SAM formation and conductance using STM and scanning tunneling spectroscopy (STS). Using 4-thiobiphenyl and 2-thiophenanthrene, we show that the additional degrees of freedom afforded to the 4-thiobiphenyl dramatically influence SAM packing. We also explore the influence of hindered internal rotation on the molecules' ability to change from high to low conductance states, when inserted in ALK matrices.

In Chapter 3, we discuss the preparation of 1-adamantanethiolate (AD) and N-adamantyl-5-mercaptopentanamide (ADtether) SAMs and characterize them using STM, Fourier transform infrared spectroscopy (FTIR), electrochemical desorption, contact angle measurements and ellipsometry.

The structure of the n-alkanethiolate-inserted AD (displaced) SAMs are discussed in Chapter 4. In this chapter, we characterize the displaced regions and the remaining AD molecular regions. Additionally, we discuss the origins of AD SAM displacement.

Chapter 5 describes the kinetics of AD SAM displacement in solution measured by STM, FTIR, x-ray photoelectron spectroscopy, and electrochemical desorption techniques. Based on our observations, we suggest a displacement mechanism.

In addition to observing and quantifying AD displacement, we have also exploited the labile nature of the AD SAMs for patterning (Chapters 6 and 7). In Chapter 6, we increase the sophistication of μCP by first assembling a labile AD SAM on the substrate and then displacing it by contact with a molecularly coated elastomeric stamp – a process we call microdisplacement printing. Additionally we show complex patterning using this method.

In order to extend the displacement patterning method to DPN, we studied the influence of the surface on molecular transport from the AFM tip to the substrate (Chapter 7). Transport experiments onto bare surfaces as well as onto surfaces that have been previously patterned are discussed. Additionally, the impacts of these transport phenomena and the prospects for displacing an existing SAM with DPN are discussed.

Finally, the results from each project are summarized and future directions are discussed in Chapter 8.

Chapter 2

Structure and Conductance of 4-Thiobiphenyl and 2-Thiophenanthrene Self-Assembled Monolayers

2.1 Introduction

The current objective of the field of molecular electronics is to derive ways to fabricate and to control individual molecular components so that one may couple them into nanoscale devices. While control of local placement and molecular stability are essential for the fabrication of molecular devices, understanding conductance through nanoscale molecular assemblies aids in our ability to manipulate and to interface the assemblies with one another as well as with existing devices [86]. In this chapter, we use synthetic chemistry and self-assembly to place conductive molecules in well-defined environments for study with STM.

Many groups [87–93] have engineered molecules for molecular electronics (such as those containing a high degree of conjugation from the electron delocalization through π-bonds, leading to enhanced electron transfer [94]) and have experimented with functional group placement. By measuring the electronic properties of these molecules it should be possible to find general trends in conductivity with changes in structure. We have used the completely rigid, planar structure of 2-thiophenanthrene to take advantage of the conductivity of the π-band overlap, increased girth and rotational inflexibility afforded by such a configuration. It is expected that these considerations will have effects on the molecule's ability to form well ordered SAMs, its orientation in SAMs, and its conductance.

There are many quantitative ensemble measurements of conductance such as optical spectroscopy [4, 23, 40] and electrochemistry [41–43], but measurements of one molecule (or a very few) are more difficult, and rely on techniques such as lithographically fabricated pores or contacts [45, 95], break junctions [45, 47], and mercury drop [48–50] experiments. However, determining whether the measured electronic properties of an assembly are a result of one molecule or a few molecules is often difficult. Scanning probe techniques such as STM and AFM have the advantage of localized imaging on the molecular scale [23, 40, 86, 96]. Furthermore, few techniques allow for

the simultaneous electronic and topographic characterization on the nanoscale that is possible with the STM. In this chapter, we use ambient STM to characterize the topography of two molecules, 4-thiobiphenyl and 2-thiophenanthrene (Figure 2.1), self-assembled on a Au{111} substrate. Using STM, a circuit is created with the molecule chemically attached to one electrode (the Au{111} substrate) and the STM tip as the second electrode (although detached because of the tunneling gap). With this circuit, the electronic properties, in addition to the topographic features of each molecule are measured individually. These molecules switch conductance states when inserted into ALK matricies, as has been shown previously for similar molecules [10, 97]. The structures and conductivities of both 4-thiobiphenyl and 2-thiophenanthrene SAMs as well as their behavior after insertion into ALK SAMs are discussed below.

2.2   Experimental Procedure

2.2.1   4-Thioacetobiphenyl and 2-thioacetophenanthrene synthesis

Both the 4-thioacetobiphenyl and 2-thioacetophenanthrene molecules were synthesized by Jacob W. Ciszek in Dr. James Tour's research group at Rice University and are described elsewhere [9, 98].

2.2.2   Sample preparation

All the SAMs were assembled on Au{111} via solution deposition in argon- or nitrogen-sparged ethanol. All glassware was cleaned in a base bath of saturated potassium hydroxide in ethanol, rinsed extensively with ultrapure water (18 MΩ) and thoroughly dried prior to use. Commercially available Au{111} on mica substrates (Molecular Imaging, Tempe, AZ) were annealed using a hydrogen flame immediately prior to deposition. n-Alkanethiolate SAMs were prepared by immersing the annealed substrates in a 1 mM ethanolic solution for 24 h. The 4-thiobiphenyl and 2-thiophenanthrene SAMs were made using 1 mM solutions in tetrahydrofuran (THF) with 0.4 mM ammonium hydroxide to remove the acetyl protecting groups. 4-Thiobiphenyl SAMs were made using protected or unprotected thiols and there was no observable difference in SAM quality. Post-deposition, each sample was rinsed in neat ethanol and blown dry twice with nitrogen.

Insertion was performed in an oxygen-free environment by exposing the assembled ALK SAMs to nanomolar concentrations of the guest molecules in THF (and ammonium hydroxide, if
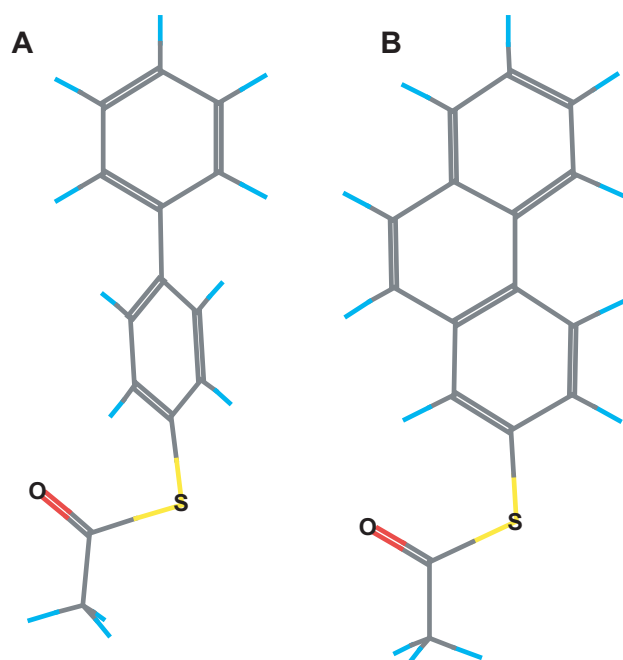
Figure 2.1. Biphenyl derivatized molecules that were studied. A) 4-Thioacetobiphenyl. B) 2-Thioacetophenanthrene. The gray, light blue, yellow, and red atoms are carbon, hydrogen, sulfur, and oxygen, respectively.

deprotection was necessary) for a short period ranging from seconds to minutes. These samples were then rinsed with neat THF and dried with nitrogen before being exposed to air, then rinsed with neat ethanol and dried again with nitrogen before scanning with the STM. The samples were stored in nitrogen-purged plastic vials in a benchtop dessicator at room temperature when they were not being imaged with the STM. Although the SAMs remain stable for weeks, all experiments were performed within 48 hours of fabrication of the samples.

2.2.3 Scanning tunneling microscopy analysis

The STMs used for collection of the STM data herein are all Besocke-beetle style with custom built hardware and software [7, 99]. The STMs use a National Instruments DAC/ADC acquisition cards (National Instruments, Austin, TX) to provide computer control in conjunction with WinSTM, an acquisition program designed by Brent Mantooth [99]. The tips are mechanically sheared from 20/80 Pt/Ir (Goodfellow, Devon, PA) composite wire and RHK IVP300 preamplifiers (RHK Technology, Troy, MI) are used for detection of current. As discussed in the pervious chapter, rastering is achieved with the use of piezoelectric ceramic tubes (Stavley NDT Technologies, East Hartford, CT). All STM and scanning tunneling spectroscopy (STS) measurements were performed under ambient conditions.

To measure the conductances of SAMs of both 4-thiobiphenyl and 2-thiophenanthrene, current versus voltage (IV) curves were measured using STS. For these measurements, at chosen points during imaging, the probe tip was stopped, the feedback loop controlling the STM tip-sample separation was blanked and the voltage was ramped while recording the current. The voltage was ramped in forward and reverse directions for several sweeps (usually three). Between each sweep, the feedback loop was reset to compensate for any drift in the tip-sample separation during the previous sweep and the imaging tunneling conditions were reestablished. After recording the spectra at one point, imaging resumed until the next selected point. The conductance plots were then generated mathematically from the IV curves. Unfortunately, it was not possible to do spectroscopy at room temperature slowly enough to measure the second harmonic of the IV curves without substantial thermal drift.

For the insertion studies, similar to the methods reported previously [10,97], large areas (1200 – 1700 Å on a side) were imaged repeatedly for $\geq$10 h. The data for each molecule (along with the height of the SAM near that inserted molecule) were extracted from those images and the statistics

for many individual molecules were extracted simultaneously. Using tracking software [100,101], the data extracted from each image are correlated to the next image to piece together the conductance history (observed as changes in apparent height) over the duration of the movie (a collection of sequential images). It should be noted that this sampling method favors molecules that start in or switch to a high conductance state, as molecules in a high conductance state are more easily discernable from the surrounding matrix and are therefore more likely to be included. The data are thus biased against switches that remain in a low conductance state.

2.3   Results and Discussion

From theory, in solution the lowest energy conformation of a biphenyl molecule (it is presumed that the 4-thiobiphenyl will behave similarly) has a $\sim 40°$ offset between the two phenyl rings [102–105]. This is due to competition between the energetically favorable π-bond overlap and the energetically unfavorable hydrogen steric repulsion that occurs in a planar formation. The maximum of the barrier to rotation from the lowest energy conformation to either a planar or an orthogonal conformation is calculated to be ~ 87 meV [103–105]. In addition, there is a slight deformation of the middle carbon-carbon bond (less than 0.2 Å) between the two conformations [104]. The 4-thiobiphenyl molecule is therefore estimated as 4.3 Å across (from one H to the opposite H across the vertical axis) and 12.4 Å long [106] (from the Au surface to the farthest H).

The planar 2-thiophenanthrene has a dissociation energy for the aromatic carbon-carbon bond of ~ 3 eV, estimated from studies of benzene on copper substrates [107,108]. From calculations performed on ethylene complexes [109,110], the rotational barrier around the central bond is assumed to be greater than 1.7 eV. Together, these estimations demonstrate that the movement of any of the phenyl rings of 2-thiophenanthrene out of a planar conformation is unlikely at room temperature (kT ≈ 26 meV). All the carbon-carbon bonds are assumed aromatic and therefore, the 2-thiophenanthrene molecule is estimated to be 5.6 Å across (from a H on the middle ring to the nearest H across the vertical axis) and 12.3 Å long (from the Au surface to the farthest H).

2.3.1   Self-assembled monolayer structures

Scanning tunneling microscopy images of the 4-thiobiphenyl and 2-thiophenanthrene SAMs are shown in Figures 2.2 and 2.4. As has been observed for similar self-assembled thiolate systems
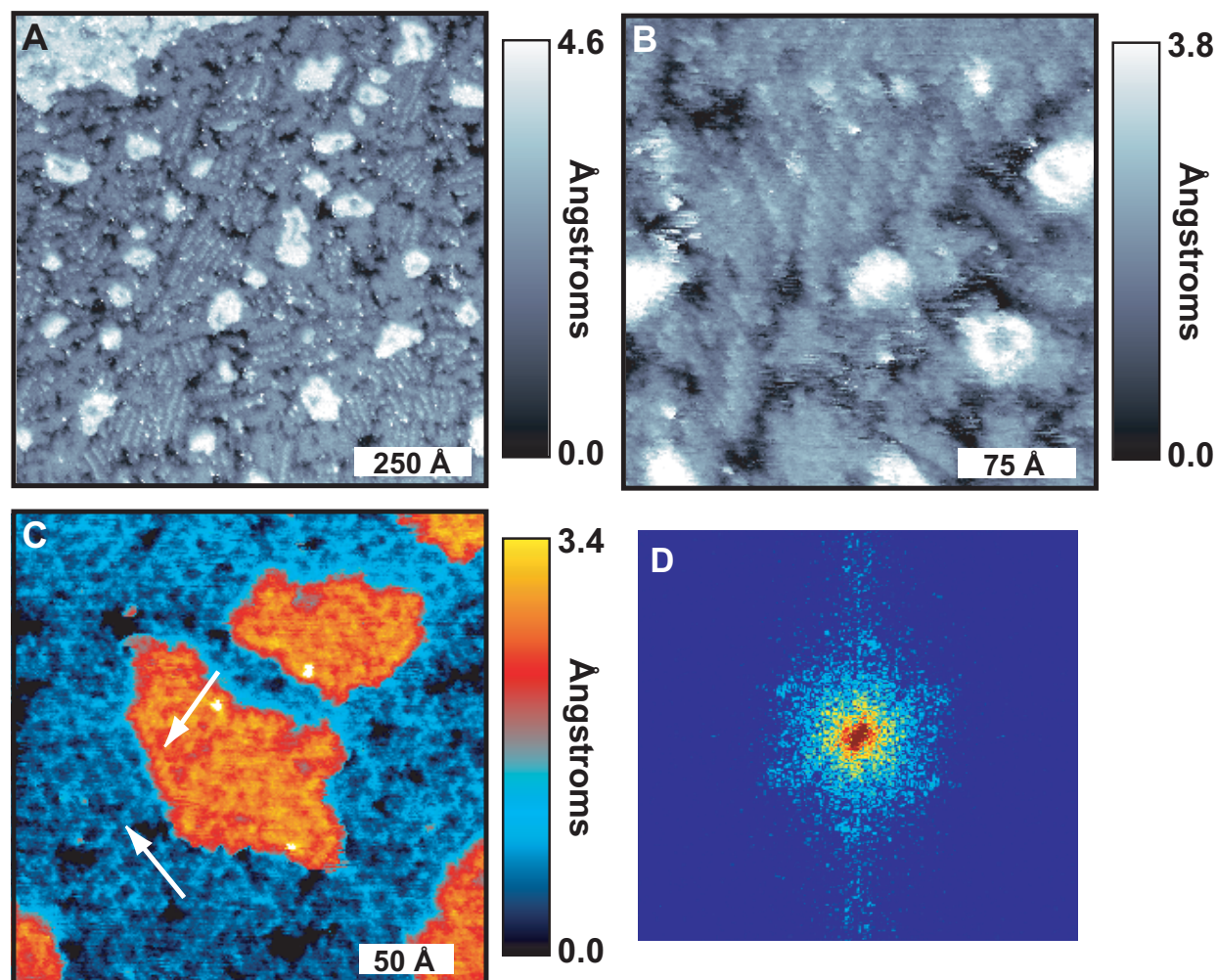
Figure 2.2. A 4-thiobiphenyl SAM on Au{111}. A) An STM image showing the substrate islands caused by the thiolated molecules rearranging the substrate. Imaging parameters: V_{sample}: 1 V; I_{tunnel}: 2 pA; 1000 Å × 1000 Å. B) An STM image showing the stripe phase observed for shorter deposition times. Imaging parameters: V_{sample}: 750 mV; I_{tunnel}: 2 pA; 300 Å × 300 Å. C) An STM image showing the close-packed molecular order observed for longer deposition times. The molecules zigzag in the lattice and line up along the substrate step edges. Imaging parameters: V_{sample}: 750 V; I_{tunnel}: 2 pA; 200 Å × 200 Å. D) Fast fourier transform of the image shown in C).
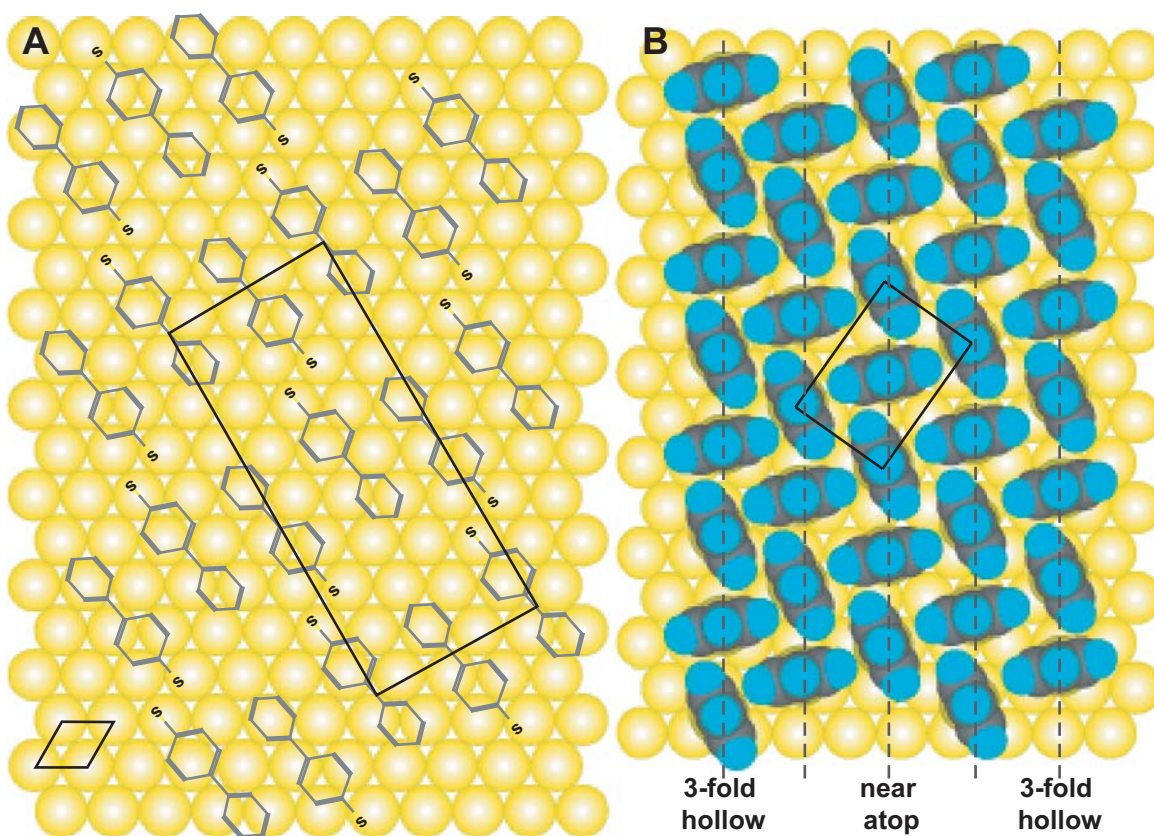
Figure 2.3. A schematic showing the proposed structures of a 4-thiobiphenyl SAM on Au{111}. A) In the striped phase the molecules lie down head to toe across the substrate in ordered rows. The black box shows the commensurate $(8 \times 2\sqrt{3})$ unit cell. B) In the close-packed phase, the molecules zigzag to maximize π stacking between adjacent molecules. The black box shows the incommensurate $(\sqrt{3} \times 2\sqrt{3})R30°$ unit cell. The molecules are incommensurate because they do not all fall on the same lattice position, as shown by the gray dashed lines.
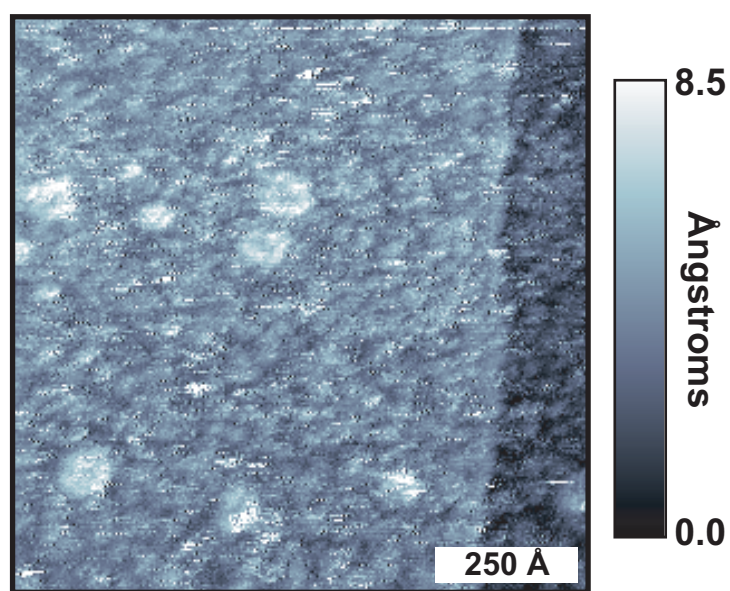
Figure 2.4.   A STM image of a 2-thiophenanthrene SAM on Au{111} showing the substrate rearrangement observed in 4-thiobiphenyl SAMs, but lacking order. Imaging parameters: V_{sample}: 1 V; I_{tunnel}: 1 pA; 1000 Å× 1000 Å.

[17, 19], both molecules greatly affect the gold substrate, creating jaggedness at the step edges as well as islands and vacancies comparable in height to one atomic layer of gold.

Shown in Figure 2.2 are two observed structures for the 4-thiobiphenyl SAM. A primarily striped phase was observed for insertion times up to 12 h (Figure 2.2B), a hexagonal close-packed formation was observed for insertion times longer than 30 h (Figure 2.2C), and a mix of both phases was seen for insertion times between 12 h and 30 h. In the striped phase, the molecules assembled in rows in one of three possible orientations that were rotated $60°$ from one another. In this conformation, the molecules lie along the surface with a measured height difference from head to tail of 1.8 ± 0.3 Å. This apparent height difference is a convolution of geometric and electronic structure and is not easily interpreted in terms of molecular tilt. The difference is most likely due to the relative position of the aromatic units rotated around the molecular axis, which is nearly parallel to the surface [1, 20]. The measured distance between rows is ∼21 Å and the distance along the rows of ∼11 Å corresponding to a square packing structure similar to that seen for methyl-4'-mercaptobiphenyl [1, 4, 20].

In the hexagonal close-packed formation, the molecules demonstrate a zigzag orientation with respect to each other with a nearest neighbor distance of 4.7 ± 0.5 Å (measured from the two dimensional Fourier transform of the STM images shown in Figure 2.2D), which corresponds to the preferred sulfur positions on Au{111} of $(\sqrt{3} \times \sqrt{3})R30°$ [4, 17, 111]. The formation of this zigzag structure can be seen in Figure 2.2C as the mottled slight protrusions and depressions (shown as lighter and darker blue) throughout the image. In addition, there is alignment of the molecules perpendicular to the step edges that is most visible on the Au islands in Figure 2.2C, middle island).

These parameters closely correspond to the two packing structures shown in Figure 2.3 that have been proposed for substituted biphenyl SAMs as well as other highly conjugated aromatic structures [1, 4, 17, 31, 112, 113]. Figure 2.3A shows the striped phase in which the molecules lie flat on the surface oriented head to tail in alternating rows. The close-packed SAM structure in modeled in Figure 2.3B. Here the molecules zigzag in alternating rows to maximize π-overlap between neighboring molecules. Additionally, the rows that zigzag in the $45°$ direction vary in their position on the Au lattice; every third row alternates from near-top to threefold hollow, making every fifth row the same position. This change from near-top to three-fold-hollow has been observed as a slight change in apparent height in some STM studies of conjugated aromatic molecules, but is not observed here [17, 112, 113].

No instance of a well-ordered 2-thiophenanthrene SAM has been observed (Figure 2.4) for either long or short deposition times. At longer deposition times (greater than 24 h), the surface becomes increasingly difficult to image with the STM. The width of the 2-thiophenanthrene molecule prevents it from packing in either of the two biphenyl orientations. It has been shown that the phenyl rings of the biphenyl molecule are oriented askew in the striped phase and it is presumed that internal rotation helps to achieve a minimum packing energy [20], something that is not possible for the fused rings of the 2-thiophenanthrene molecule.

2.3.2 Molecular conductance

From Figure 2.5, it can be seen that reproducible current versus voltage curves are generated regardless of the area of the SAM that is chosen for spectroscopy, indicating, together with the measured apparent height, that the observed islands are due to substrate mesas and are not multilayers of the SAM.

Figure 2.6 shows the IV and conductance spectra over the two types of SAMs taken at the same setpoint. In the positive sample bias regime, the current in the 4-thiobiphenyl SAM spectrum increases steadily up to 0.5 V, when the conductance suddenly increases. Between -0.4 V and +0.4 V the SAM shows a nearly constant conductance of 1.5 pA/V. This trend continues for negative sample biases with only a very small increase in conductance for sample biases below -0.4 V. This results in an asymmetric curve with a 1.5 pA/V difference in conductance between -1 V and +1 V. The 2-thiophenanthrene SAM behaves nearly identically in the positive sample bias regimes. It also shows linear trends between ±0.4 V, almost overlapping the 4-thiobiphenyl spectrum. At voltages below -0.4 V, however, the SAM greatly increases conductance down to -1 V, when it exceeds the conductance at +1 V by 1 pA/V.

Seen most clearly in Figure 2.6B, both SAMs display asymmetric conductance curves, although the 2-thiophenanthrene spectrum is more symmetric. The 2-thiobiphenyl SAM is more conductive at positive sample bias, while the 4-thiophenanthrene SAM is more conductive at the opposite polarity.

We attribute the asymmetry observed for both molecules to the sulfur-gold contacts in the circuit [114]. At the metal-molecule interface, there is a thiolate bond to the gold through which electrons can flow, but on the tip side of the molecule there is only a terminal aromatic ring and small gap through which the electrons must tunnel. This difference in bonding may cause a
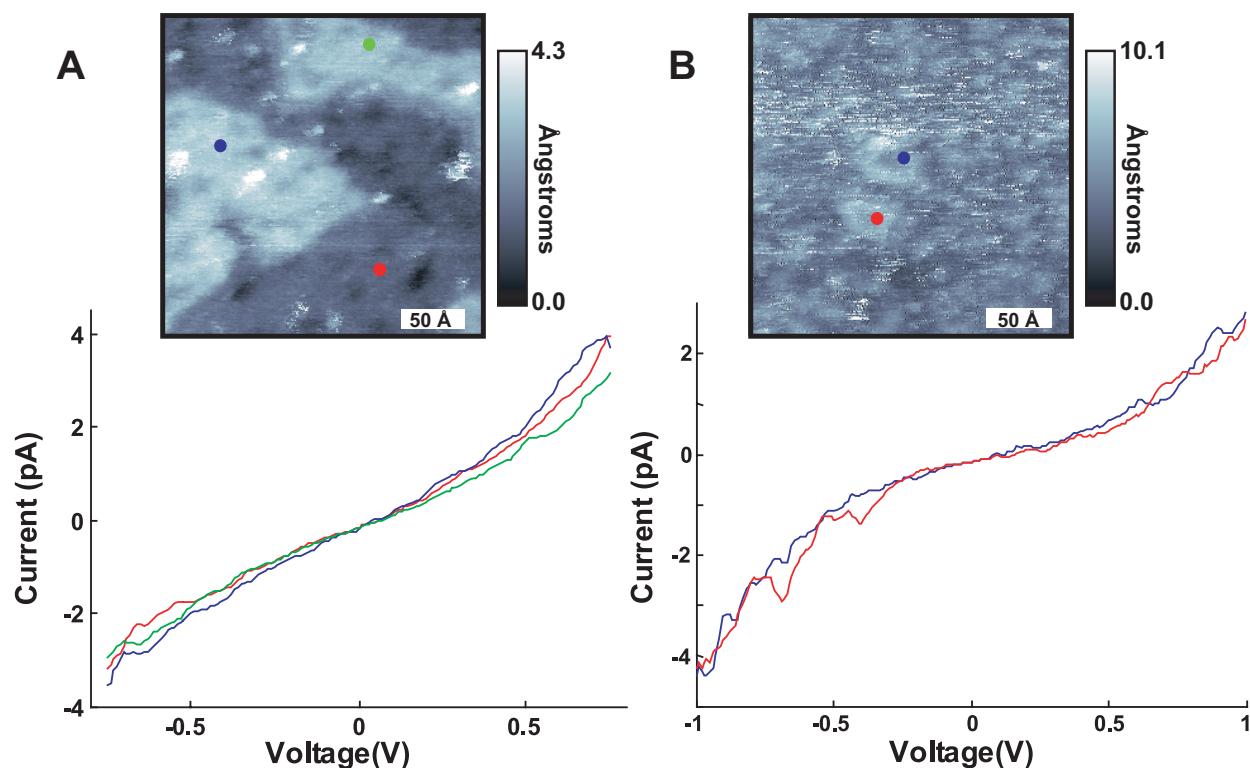
Figure 2.5. Reproducible current versus voltage plots generated at a variety of areas across each type of SAM. A) Current versus voltage curves generated at the three points on the 4-thiobihenyl SAM on Au{111} shown in the inset. Imaging parameters: V_{sample}: 750 mV; I_{tunnel}: 3 pA; 250 Å× 250 Å. B) Current versus voltage curves generated at the two points on the 2-thiophenanthrene SAM on Au{111} shown in the inset. Imaging parameters: V_{sample}: 1 V; I_{tunnel}: 3 pA; 500 Å× 500 Å. Note: At each point (shown by the corresponding colored dot in the image), the feedback was blanked and three sweeps were made in the forward and reverse direction. The spectra shown are each averages of the three sweeps.
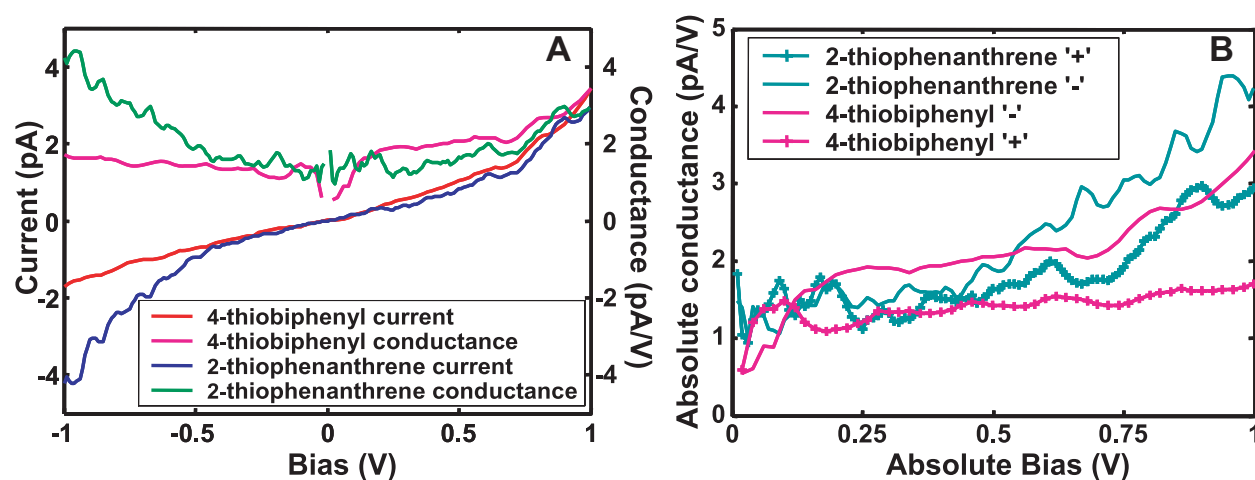
Figure 2.6. A) A comparison of representative current versus voltage and conductance versus voltage plots for both 4-thiobiphenyl and 2-thiophenanthrene SAMs taken with the same setpoint of V_{sample}: 1 V and I_{tunnel}: 2 pA. Note: At each point, the feedback was blanked and three sweeps were made in the forward and reverse direction. The spectra shown are each averages of the three sweeps. B) The same conductance curves from (A) plotted as absolute conductance versus absolute bias to highlight the differences in asymmetry in the spectra.

Schottky barrier responsible for the observed rectification [114]. We discount that the anomaly is a result of drift of the tip-sample separation during data acquisition, because this trend remains at many points within the SAM and occurs for many tunneling conditions.

The difference in conductance between the 4-thiobiphenyl and the 2-thiophenanthrene we attribute to increased π-orbital overlap in the 2-thiophenanthrene molecule because of the fused aromatic rings that constrain the molecule to being coplanar, thus maximizing the π-orbital overlap. However, it is expected that the enhanced conductance because of π-orbital overlap would be observed at both positive and negative biases. It may be that for the small bias range measured, the observed asymmetry of the contacts has a larger influence on the overall conductance than the comparative conductances of the molecules. We do not believe that *this* conductance difference arises from molecular motion due to forces applied by the electric field due to the tip via the molecular dipole [12]. The molecules here have similar dipoles and would be expected to behave similarly to a tip-induced electric field.

2.3.3   Insertion into n-alkanethiolate self-assembled monolayers

To understand what effect the geometry of molecules has on their conductance states, both the 2-thiophenanthrene and the 4-thiobiphenyl molecules were inserted into 1-octanethiolate (C8) SAMs and were studied on individual bases. Insertion of the molecules into SAMs reproducibly isolates each molecule (or small bundle of molecules) from one another and restricts them to the SAM defects and gold step edges, thus controlling the placement of the molecule within the SAM [7, 8, 11]. As depicted in the top portion of Figures 2.7 and 2.9, at these sites, the guest molecules insert nearly normal to the surface with the head groups adhering to the exposed gold and the conjugated region of the molecule sticking up out of the SAM [7, 8, 11].

The same area of each sample type was imaged repeatedly for many hours to generate a series of images, each containing tens of inserted molecules (example images from a series of images for each molecule are given in Figures 2.7 and 2.9). Using the analysis routines discussed above, each molecule appearing in the series of images was individually tracked and its apparent height was recorded in every frame. An example apparent height versus time plot for the duration of the movies and a series of frames tracking the individual molecules in the boxes in Figures 2.7 and 2.9 is given for each type of molecule in Figures 2.8 and 2.10. As discussed elsewhere, the two-state apparent height changes of the molecules throughout the duration of the data aquisition
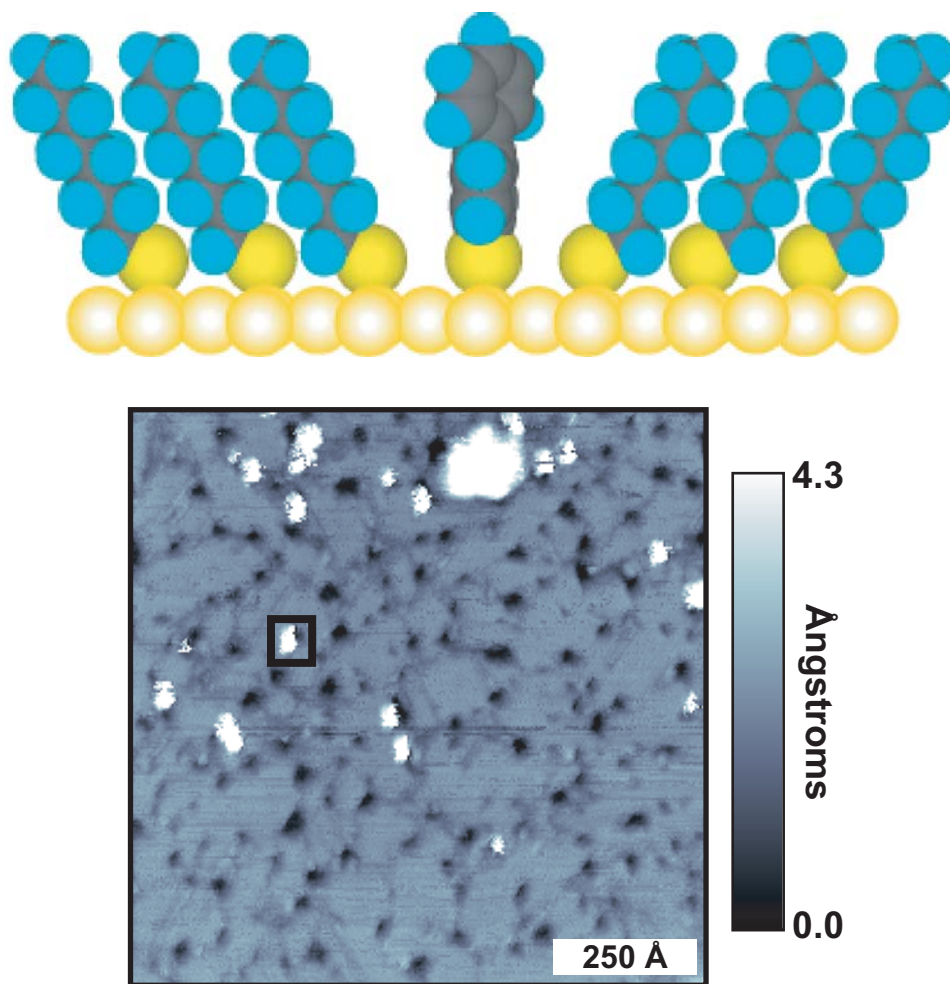
Figure 2.7. A schematic depicting and an example frame from a series of images showing insertion of 4-thiobiphenyl molecules into defects in a 1-octanethiolate SAM. Imaging parameters: V_{sample}: 1 V; I_{tunnel}: 3 pA; 1200 Å × 1200 Å.
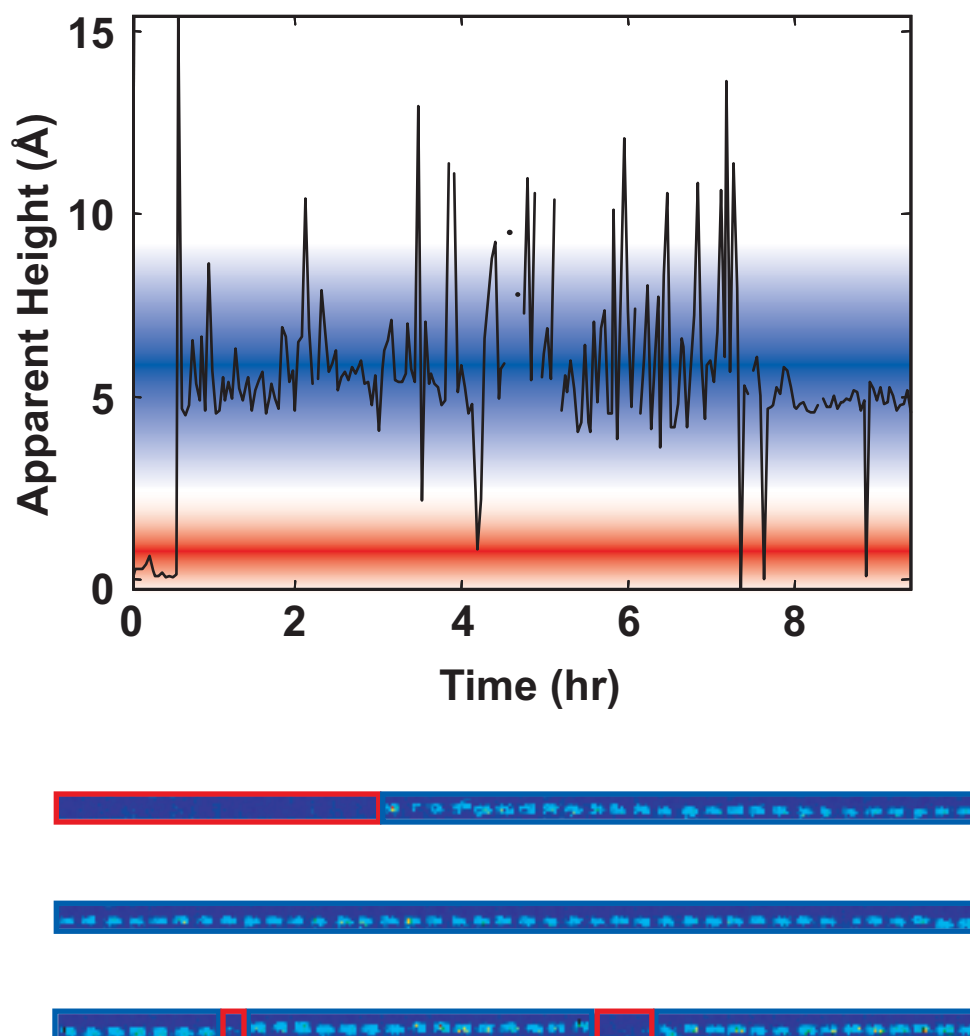
Figure 2.8. An example height versus time plot and extracted frames after tracking analysis for the inserted 4-thiobiphenyl molecule shown in the black square in Figure 2.7. The molecule shows both ON and OFF (denoted by blue and red bands in the plot and squares around the frames) states over the series of images.

were not correlated to any changes in tip geometry, changes of the gold substrate, or movement across substrate step edges [10, 100, 101]. It was also possible to distinguish single molecules from bundles of molecules and to interpret separately each molecule's conductance state [101].

As shown by the histogram (extracted from a 250-frame sequence of images that was taken over a $\sim$12-h period) in Figure 2.11A, the 4-thiobiphenyl demonstrates two conductance states: a high conductance state, termed ON (shown in blue) and a low conductance state, termed OFF (shown in red). From Gaussian fits to the distributions, the difference in apparent height (Δh) between the ON and OFF states is 4.5 ± 0.9 Å. The apparent height of the molecule (h_{on} and h_{off} for the ON and OFF states, respectively) was measured from the height of the SAM and changed with the type (and therefore height from the substrate) of the SAM. Although an OFF state was usually still visible protruding from the SAM, any molecule that falls below the level of the SAM will have an apparent height of zero resulting in narrower apparent height distributions for the OFF states.

The 2-thiophenanthrene also exhibits two conductance states (Figure 2.11B), with a Δh of 5.1 ± 1.2 Å. The topographic height of these two molecules normal to the surface is comparable, so the deviations in apparent height are associated with differences in conductance. It is expected that the 2-thiophenanthrene molecule is more conductive because of the increased conjugation of the middle ring extending the overlap of the π-orbitals [115–117]. The existence of switching in the 2-thiophenanthrene molecule eliminates internal ring rotation as the sole mechanism responsible for the change in conductance states. In addition, internal rotation of biphenyl at room temperature would give states that are too short lived to be observed by these methods [92, 116, 117].

Qualitatively, the 2-thiophenanthrene molecules switch states less frequently and favor the OFF state. This is quantitatively verified by the calculated ON/OFF ratios (calculated from the areas under the Gaussian fits) of 2.45 for the 2-thiophenanthrene and 4.61 for the 4-thiobiphenyl molecules. Considering that both molecules are in similar environments, this difference can be explained by the degrees of freedom available to each molecule. In both cases the ALK SAM is surrounding the molecule (see Figures 2.7 and 2.9). Due to size and rotation constraints, the 2-thiophenanthrene molecule needs larger defect sites to be able to insert and to have the same degrees of freedom afforded to the 4-thiobiphenyl. For the same defect site, one would expect that the biphenyl is more likely to switch (provided that the switching is due to conformational changes), but we do not know if the distributions of sites at which the two molecules insert are

equivalent. Theory has predicted that a tilted thiolate bond is the energetically favorable and a more conductive (ON) molecular conformation, although it is not possible to measure experimentally only the thiolate-substrate bond angle with the STM [94, 118, 119]. However, recent data on electric-field-mediated conductive switching [12] indicate that the more conductive state is when the dipole of the molecule is oriented such that the tailgroup has a polarity opposite of the tip bias, and thus is oriented more normal to the surface. It is expected, and has been observed, that a molecule that is increasingly constrained by the host SAM is less likely to undergo motion that will result in a dramatic change of conductivity [97].

2.4 Conclusions

In order for the mechanism of molecular switching to be more fully understood, 2-thiophen-anthrene has been used to maximize the conductance and to minimize the mechanical freedom present in 4-thiobiphenyl. The mechanical hindrances are apparent in the structural order of the SAMs made from each molecule. The 2-thiophenanthrene SAMs exhibited no observable ordered structures, regardless of insertion time. The 4-thiobiphenyl SAMs displayed two packing structures with a primarily striped phase for insertion times less than 12 h and a hexagonal phase for insertion times greater than 30 h. The current-voltage characteristics of the 2-thiophenanthrene SAMs are slightly more symmetric around zero sample bias than the 4-thiobiphenyl SAMs, although further investigation of the system is needed. Upon insertion into ALK SAMs, both molecules exhibit similar bistable conductance switching. While internal rotation is therefore not the sole mechanism for conductance switching, it does allow the molecules to relax conformationally within the matrix, making switching more likely.
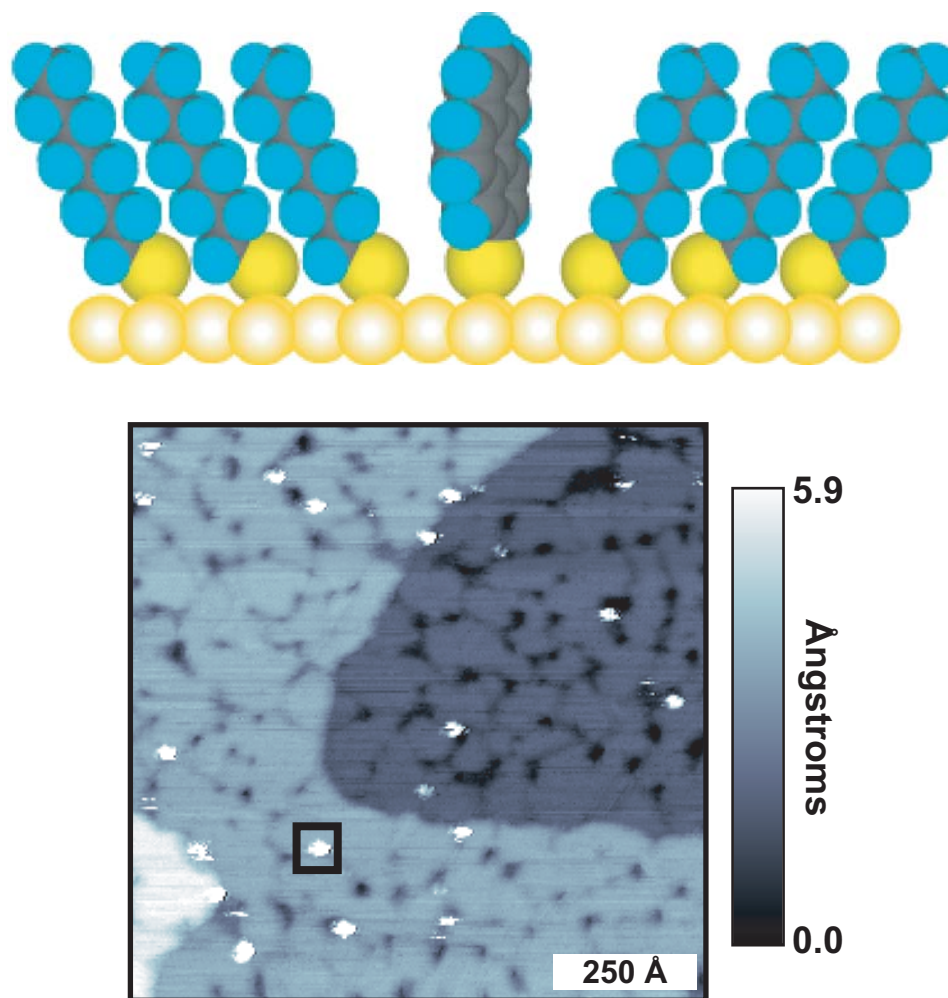
Figure 2.9. A schematic depicting and an example frame from a series of images showing insertion of 2-thiophenanthrene molecules into defects in a 1-octanethiolate SAM. Imaging parameters: V_{sample}: 1 V; I_{tunnel}: 3 pA; 1200 Å × 1200 Å.
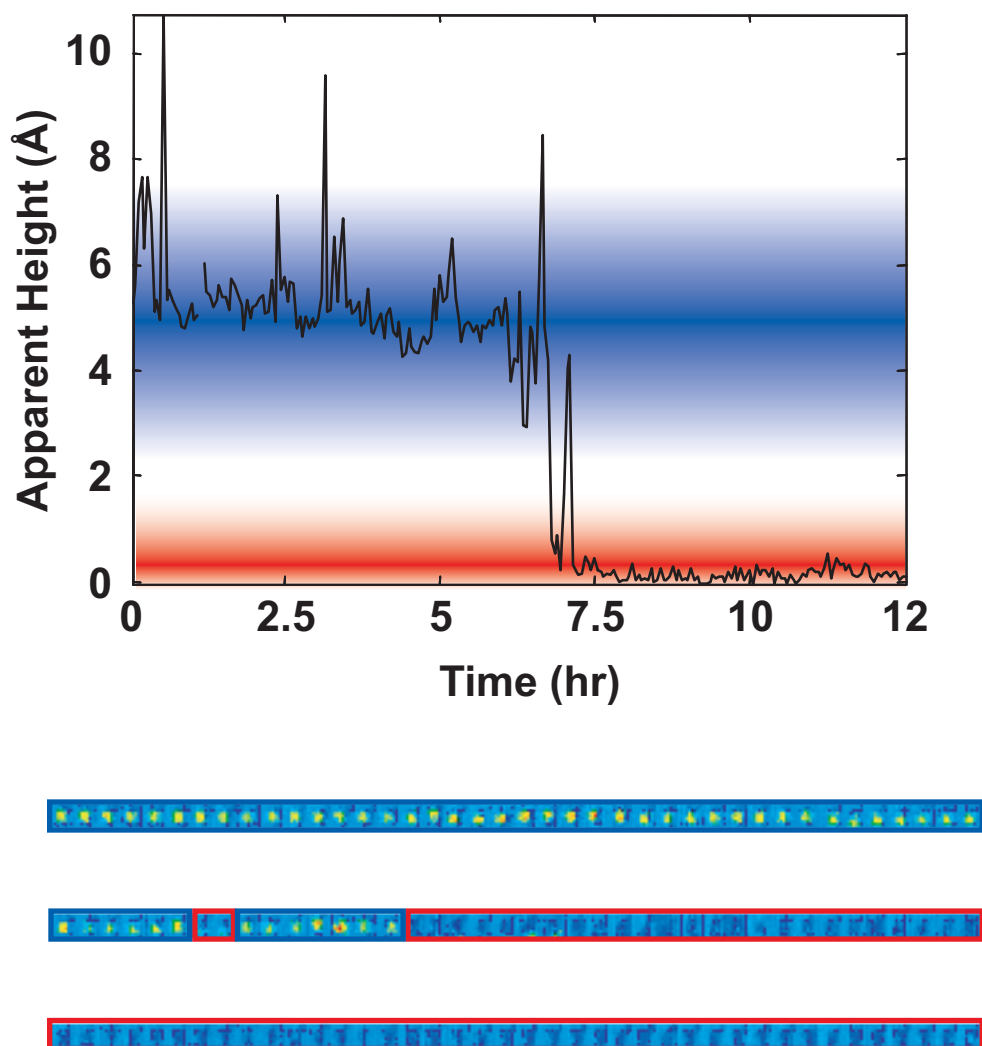
Figure 2.10. An example height versus time plot and extracted frames after tracking analysis for the inserted 2-thiophenanthrene molecule shown in the black square in Figure 2.9. The molecule shows both ON and OFF (denoted by blue and red bands in the plot and squares around the frames) states over the series of images.
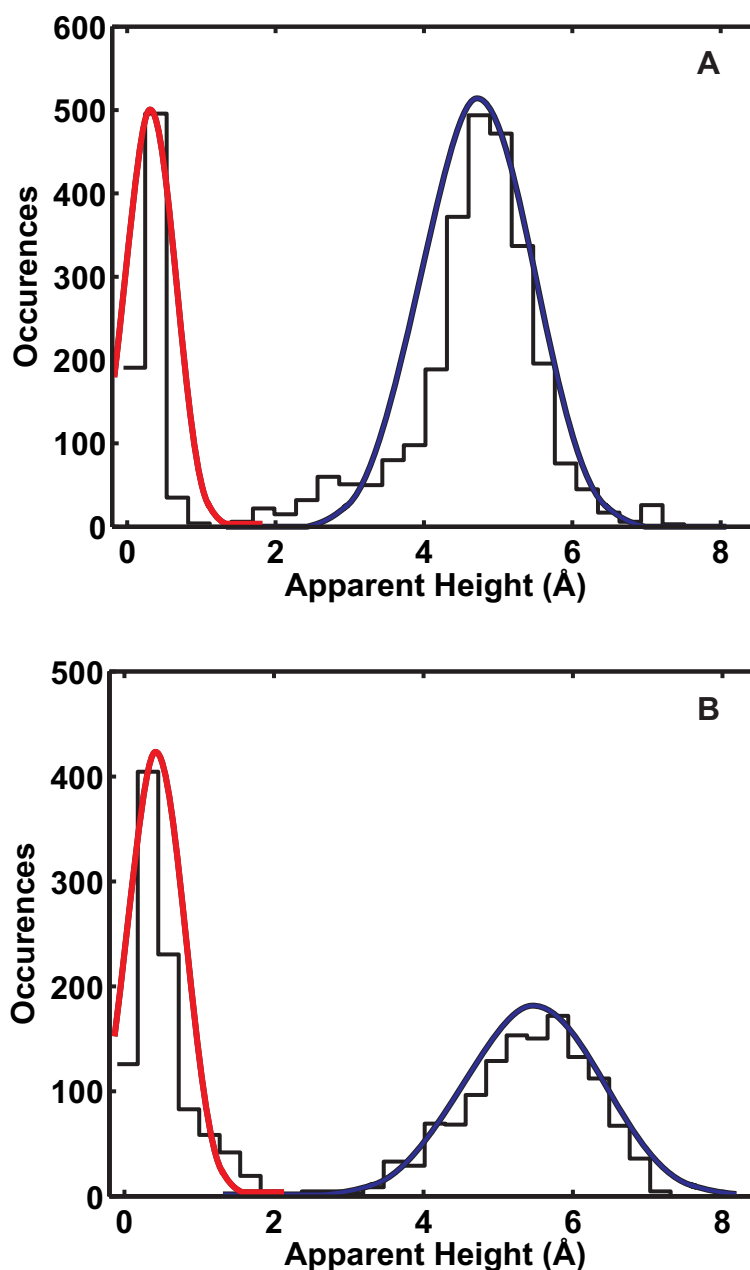
Figure 2.11.   Apparent height distributions for the 4-thiobiphenyl and 2-thiophenanthrene molecules inserted in 1-octanethiolate matrixes, shown in Figures 2.7 and 2.9. The distribution data are digitally extracted from sequential images taken over more than 10 h. A) Apparent height distribution of 4-thiobiphenyl molecules that were inserted into a 1-octanethiol SAM. Apparent heights: $h_{\mathrm{on}} = 4.7 \pm 0.9$ Å and $h_{\mathrm{off}} = 0.3 \pm 0.2$ Å. B) Apparent height distribution of 2-thiopehnanthrene molecules that were inserted into a 1-octanethiol SAM. Apparent heights: $h_{\mathrm{on}} = 5.4 \pm 1.1$ Å and $h_{\mathrm{off}} = 0.4 \pm 0.2$ Å. Imaging Parameters: V$_{sample}$: 1 V, I$_{tunnel}$: 3 pA 1200 Å $\times$1200 Å.

Chapter 3

Characterization of 1-Adamantanethiolate and *N*-adamantyl-5-mercaptopentanamide Self-Assembled Monolayers

3.1   Introduction

The supramolecular structure and interaction strengths of the molecules within self-assembled systems mediate the local placement, molecular stability and function of the molecular assemblies. Control of these attributes is sought for molecular device fabrication and more generally for ultrahigh resolution patterning [120–122]. For this purpose, it would be useful to have a library of molecules that form SAMs with distinctive properties so that in the future, it will be possible to create monolayers that are uniquely designed for their specific application. This can be achieved by tuning both the molecular topology and the intermolecular interactions within the SAMs.

The individual molecules within ALK SAMs tilt to maximize their VDW interactions, making the SAMs well ordered, stabile and tenacious systems. However, because of the prominent defects of ALK SAMs such as tilt boundaries, rotational boundaries, and stacking faults [32, 123], they are never completely reproducible matrices for device fabrication or patterned interfaces. Although some defects are inherent to the formation of thiolated SAMs on gold, with the correct choice of molecule, it should be possible to create SAMs with few domains and indistinct domain boundaries lacking significant defects [124–126].

In this chapter, we explore the influence of a bulky adamantyl tailgroup on the packing structure of SAMs. As a member of the diamondoid family, with the space group F$\bar{4}$3m, adamantane forms highly crystalline three-dimensional structures and is the subject of several crystallography and theory papers [127–129]. The molecule is comprised of a ten-carbon cage made of four fused cyclohexane rings in chair conformations [130]. Thus, each carbon is tetrahedral and sp^3-hybridized, and there is limited strain because each carbon-carbon bond is staggered [127, 131, 132]. The addition of a sulfhydryl group, creating 1-adamantanethiol (see Figures 3.1 and 3.2, hereafter referred to as AD), allows the carbon cage to be tethered to a gold surface while maintaining its
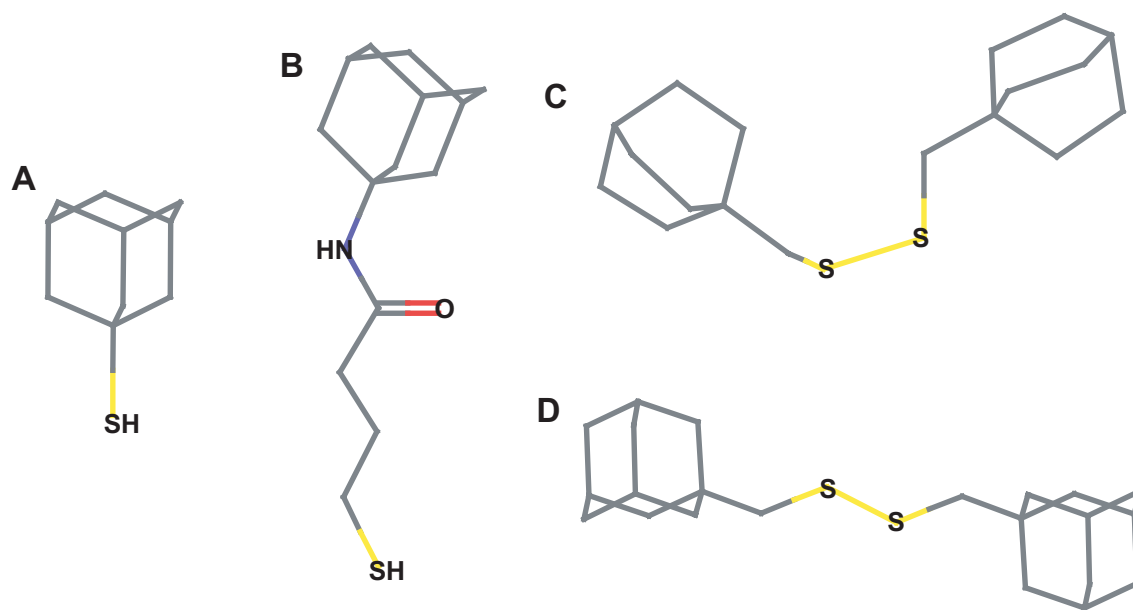
Figure 3.1.   Molecules studied here and from the literature with adamantane tailgroups. A) 1-Adamantanethiol; B) *N*-adamantyl-5-mercaptopentanamide; C) Bis(bicyclo[2,2,2]octylmethyl)-disulfide); D) Bis(tricyclo[3,3,1,1]decylmethyl)disulfide. The gray, yellow, blue and red atoms are carbon, sulfur, nitrogen and oxygen, respectively. For clarity, the hydrogens on the hydrocarbon cage and chains are not shown.

round topology [124, 133, 134]. Structures similar to AD such as bis(bicyclo[2,2,2]octylmethyl)-disulfide) and bis(tricyclo[3,3,1,1]decylmethyl)disulfide have been assembled on Au{111} and studied by STM [135, 136]. The two possible unit cells assigned to the SAMs of the latter, which differs from AD by an additional methylene unit between the adamantane cage and the sulfur atom, are $(4\sqrt{3} \times 4\sqrt{3})R30°$ and (7×7). Below, we demonstrate that AD also forms flat, highly ordered hexagonal close-packed, one-molecule-thick films on Au{111}.

Further addition of a short hydrocarbon tail, via an amide linkage, between the adamantane tailgroup and the sulfur headgroup, resulting in N-adamantyl-5-mercaptopentanamide (hereafter referred to as ADtether), moves the bulky adamantane tailgroup farther from the gold surface. This allows us to study the influence of the bulky adamantane tailgroup on a molecule similar to a short ALK. We demonstrate that ADtether forms films on Au{111}, but no significant order was observed.

3.2 Background

The techniques described briefly below were used to characterize the AD and ADtether SAMs. These descriptions are introductions to the techniques. The reader is directed to references [53, 137–143] for a more thorough explanation of each technique.

3.2.1 Ellipsometry

Ellipsometry is used to determine physical properties such as film thickness, refractive index, surface roughness, film composition, film uniformity, crystallinity, and anisotropy of thin films on reflective surfaces. The measurement is based on the property that linearly polarized light becomes elliptically polarized when it is reflected off a surface. By measuring the polarization of light off a reflective surface and using the equation,

$$\frac{r_p}{r_s} = \tan \Psi * \exp^{i\Delta},\tag{3.1}$$

where Ψ and Δ, the amplitude ratio and phase shifts, respectively, of the parallel (p) and perpendicular (s) components of the electric field can be determined [142]. In equation 3.1, the reflectance coefficients r_p and r_s are related to the optical constants of the surface and are given by the Frensel
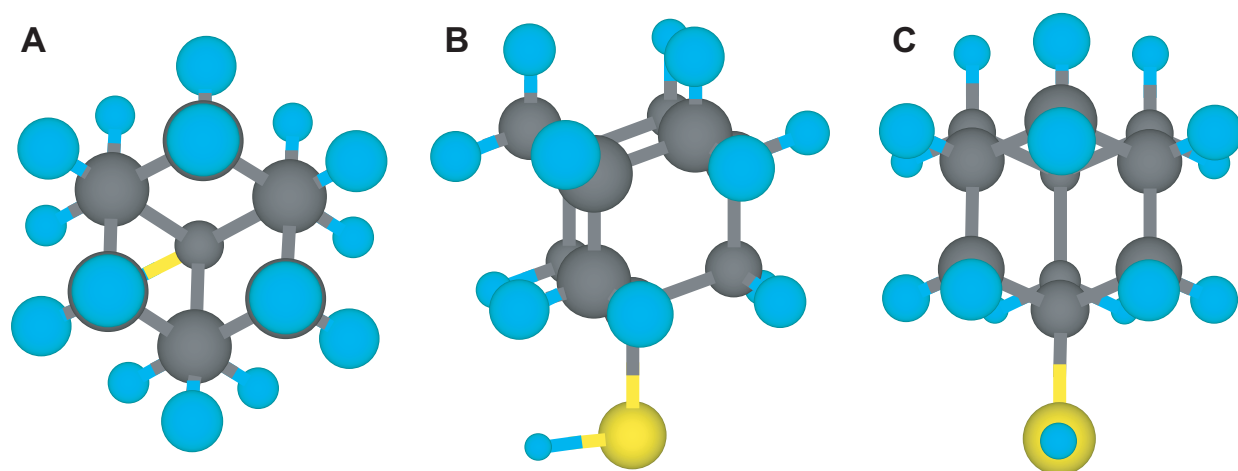
Figure 3.2. A schematic of 1-adamantanethiol, shown from three perspectives. The gray, light blue and yellow atoms are the carbon, hydrogen and sulfur atoms, respectively.

equations

$$r_p = \left(\frac{n_0 \cos \varphi_i - n \cos \varphi_t}{n_0 \cos \varphi_i + n \cos \varphi_t}\right)2 \tag{3.2}$$

and

$$r_p = \left(\frac{n \cos \varphi_i - n_0 \cos \varphi_t}{n \cos \varphi_i + n_0 \cos \varphi_t}\right)2, \tag{3.3}$$

where φ_i is the light angle of incidence, φ_t is the light angle of refraction (and can be derived from the angle of incidence), and n_0 is the refractive index of the ambient medium (for the case of air, $n_0 = 1$). n is the complex refractive index of the film, $n = N + ik$, where N is the real part of the refractive index and k is the extinction coefficient. Using these optical constants and mathematical models it is possible to determine the aforementioned physical properties of the thin films.

3.2.2 Fourier Transform Infrared Spectroscopy

Infrared (IR) spectroscopy is the measurement of absorption of IR light, which excites vibrational modes within molecules, creating a specific spectrum [138–140]. Fourier Transform IR spectroscopy (FTIR) refers to the use of an interferometer, rather than a spectral grating to separate the IR wavelengths, thus giving greater throughput. Grazing angle FTIR, where the sample is oriented in the path of the IR beam so that the light crosses the sample at shallow angle with respect to the surface maximizing the light-sample interaction, has been used extensively to study the properties of SAMs [144, 145]. Combined wtih molecular modeling, FTIR can not only identify the species present on the surface, but can be used to deduce the orientation of the molecules relative to the surface because the intensity of the signal depends on the orientation of the vibrating bond with respect to the light [146–148].

3.2.3 Contact angle

Wettability is the affinity a liquid droplet has for a solid surface. A liquid with a weak affinity for the solid surface will collect into beads to minimize solid-liquid contact area, while a liquid with high affinity for the surface will spread out to maximize the solid-liquid contact area. Measuring the angle at the point where the liquid solid and vapor phases all meet (at the edge of the drop) is a direct measurement of wettability. The contact angle (CA) measured when the liquid drop is stationary and the surrounding conditions are at a steady state, called the static CA, depends strongly on the surface properties of the solid-liquid-vapor system under those environmental conditions. From

the classical perspective, at equilibrium, the CA and interfacial tensions are related by the Young equation,

$$\gamma_{LV} \cos \theta_e = \gamma_{SV} - \gamma_{SL}, \tag{3.4}$$

where θ_e is the equilibrium contact angle, γ_{LV} is the liquid surface tension, γ_{SV} is the solid surface tension, and γ_{SL} is the solid-liquid interfacial tension. Furthermore, the work of adhesion is given by

$$W_A = \gamma_{SV} + \gamma_{LV} - \gamma_{SL}. \tag{3.5}$$

3.2.4   Electrochemical deposition

Electrochemistry investigates the electron transfer processes between a molecule and an electrode (see references [137, 143] for an introduction to electrochemical techniques). For a gold electrode modified with a thiolated SAM, applying a cathodic potential will cause a one-electron reductive desorption of the thiol,

$$RS - Au + 1e^- \rightarrow RS^- + Au_0. \tag{3.6}$$

This electrochemical measurement reflects properties of the SAM such as surface coverage, intermolecular interaction strengths, domain size, and molecular order. For cyclic voltammetry of a SAM-modified electrode, the cathodic peak current (I_p) and the peak area consist of a faradaic component due to the reduction of the thiol molecules and a nonfaradaic component from double layer charging due to the presence of a SAM on the electrode surface and are directly proportional to surface coverage of the SAM. The strength of the lateral interactions between the molecules within a SAM is inversely related to the full-width-at-half-maximum (FWHM) of the cathodic peak (i.e., the smaller the FWHM, the larger the interactions) [149, 150]. The cathodic peak potential (E_p) at which ion flux occurs reflects intermolecular interaction between the adsorbed molecules and can give information about the ordering of the molecules adsorbed to the surface. Porter and coworkers showed a linear relationship between the cathodic peak potential and ALK chain length that they attributed to the potential gradient required to establish an ion flux through the monolayer to the electrode surface, inducing reductive desorption [151–153]. Additionally, Imabayashi and coworkers manipulated the peak potential by modifying the tail groups of the thiolated molecules used to create the SAM [154–156]. They found that as the ALK SAM was allowed to assemble, the potential

at which reductive desorption of the ALK occurred shifted towards more negative potentials. They attributed this shift to increased intermolecular interactions due to increased order of the SAM.

3.3 Experimental Procedure

3.3.1 1-Adamantanethiol synthesis

1-Adamantanethiol was synthesized based on previously reported methods [124,133,134,157] and the reaction scheme is shown in Figure 3.3. In a three-neck flask, 10.7 g 1-bromoadamantane (Sigma-Aldrich, St. Louis, MO), 50 mL glacial acetic acid (Acros Organics, Geel, Belgium), 7.6 g thiourea (Acros Organics, Geel, Belgium) and 25 mL 48% hydrobromic acid (Acros Organics, Geel, Belgium) were refluxed for more than 3 h at approximately 120 °C under argon. All solutions were sparged with argon for 20 min prior to addition to the reaction vessel. As the reaction continued, the mixture turned from a transparent solution to a bright orange solution with a white precipitate, and the reaction was monitored with thin layer chromatography using a 25% chloroform (Sigma-Aldrich, St. Louis, MO) and 75% hexanes (Sigma-Aldrich, St. Louis, MO) mobile phase. After refluxing, the mixture was allowed to cool to room temperature overnight and the solution turned from orange to pale yellow. The salt was filtered from the acidic solution, rinsed with cold dichloromethane (Sigma-Aldrich, St. Louis, MO) and dried in a vacuum desiccator for 6 h, yielding 9.85 g (69% yield) shiny white 1-adamantyl isothiuronium salt crystals.

In an argon-purged flask, 9.8 g 1-adamantyl isothiuronium salt was hydrolyzed by stirring for 15 h under argon in a solution of 10 g sodium hydroxide (EMD Chemicals, Gibbstown, NJ) in 200 mL water and 75 mL ethanol. The resulting solution was slowly acidified (approximately 300 mL) with 1 mM hydrochloric acid (EMD Chemicals, Gibbstown, NJ) while stirring, causing the suspended crystals to clump and quickly float on the solution. The AD crystals were filtered and rinsed with weakly acidic, cold water. The resulting extracts were separated via liquid-liquid extraction using hexanes and water. The organic extracts were dried over anhydrous sodium sulfate (Sigma-Aldrich, St. Louis, MO), filtered, rinsing with hexanes, and rotovaped to a pale yellow oil, before the remaining solvent was removed by evaporation under argon. The resulting yield of the filtered and extracted crystals together was 4.1 g (93% yield). In small portions, before use, all the crystals were further purified by recrystalization using methanol (Sigma-Aldrich, St. Louis, MO)
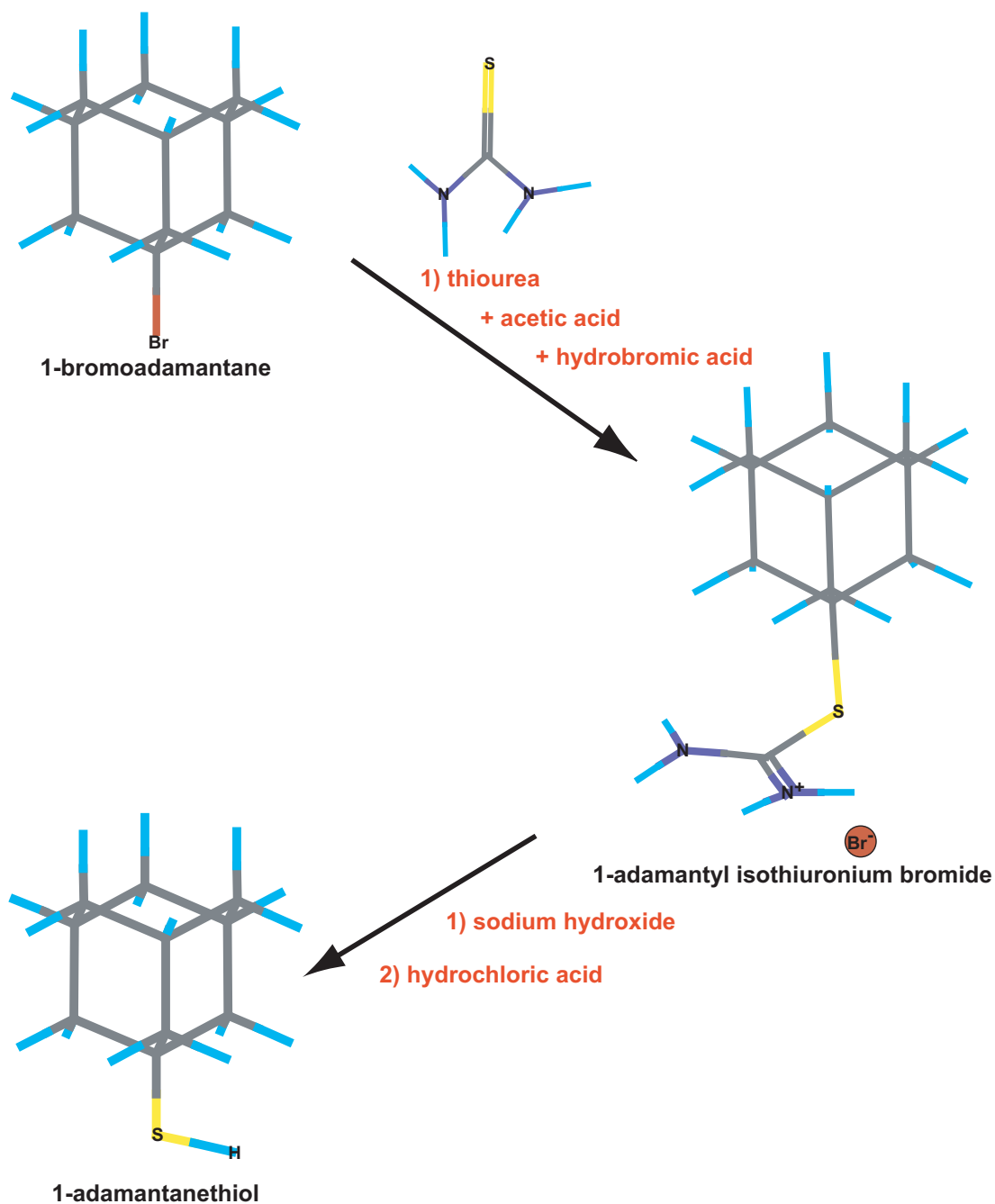
Figure 3.3. Synthesis scheme for the formation of 1-adamantanethiol from 1-bromoadamantane via the 1-adamantyl isothiuronium salt intermediate. The light blue, gray, yellow, red and dark blue atoms are hydrogen, carbon, sulfur, bromine, and nitrogen, respectively.

and toluene (Sigma-Aldrich, St. Louis, MO) or by sublimation onto a cold finger condenser filled with ice at a pressure of 8 Torr and a bath temperature of 85 °C.

Using a Mel-temp (Barnsead International, Dubuque, Iowa), the melting point of the solid was determined to be 102–104 °C. Proton and carbon NMRs were taken in CDCl$_3$ using a Bruker AMX-360 NMR (Bruker BioSpin, Billerica, MA) and solid IR spectra were taken using a Nicolet 6700 FTIR spectrometer (Thermo Electron Corporation). The characteristic peaks are summarized in Figure 3.4. Gas chromatography analysis indicates that the material is ∼98% and ≥99.5% pure before and after sublimation, respectively [158].

3.3.2 *N*-adamantyl-5-mercaptopentanamide synthesis

The synthesis of ADtether was performed by Timothy R. Kline in Dr. Ayusman Sen's research group at the Pennsylvania State University. The basis of the synthesis (shown in Equation 3.7) was the formation of an adamantyl amide and subsequent reaction with thioacetate, by methods similar to those for fabrication of amide-containing alkanethiols, described in the literature [159].

$$C_{10}H_{15}NH_2 \ + \ Br(CH_2)_4COCl \ \rightarrow \ C_{10}H_{15}NHCO(CH_2)_4Br$$

$$\xrightarrow{CH_3COSH} C_{10}H_{15}NHCO(CH_2)_4SCOCH_3$$

$$\xrightarrow{HCl} C_{10}H_{15}NHCO(CH_2)_4SH \quad (3.7)$$
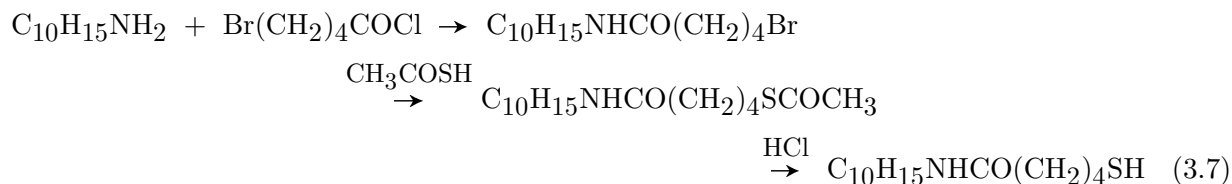
1-Adamantylamine hydrochloride was purchased from Lancaster (Pelham, NH). The 1-adamantylamine hydrochloride was protonated, creating 1-adamantylamine, with sodium hydroxide and subsequently extracted by liquid-liquid extraction into toluene. The 5-bromopentanoyl chloride was purchased from Alfa Aesar (Ward Hill, MA) and was used as received. In an ice bath, the adamantylamine and 5-bromopentanoyl chloride were reacted in 2:1 stoichiometric excess in methylene chlroide, using triethylamine as a catalyst. The catalyst was added slowly over a 3 h time period and then the reaction was stirred for an additional hour at room temperature. The methylene chloride was removed *in vacuo* generating a white precipitate (*N*-adamantyl-5-bromopentanamide). The completion of the reaction and purity were confirmed by NMR and thin layer chromatography.

The addition of the thiol was achieved by two methods, each producing equivalent products. In the first method, the *N*-adamantyl-5-bromopentanamide was reacted with 2 equivalents of
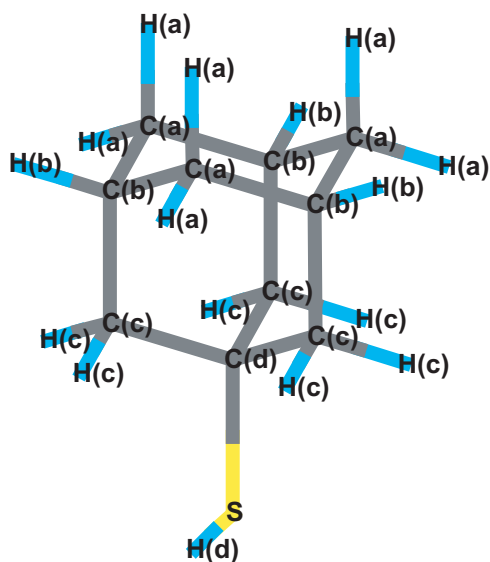
^{1}**H NMR**	
Assigned Hydrogens	**Peak Position (ppm)**
H(a)	1.67
H(b)	1.82
H(c)	1.94
H(d)	2.03
^{13}**C NMR**	
Assigned Carbons	**Peak Position (ppm)**
C(a)	30.1
C(b)	35.8
C(d)	43.1
C(c)	47.5
IR Spectroscopy	
IR Modes	**Peak Position (cm^{-1})**
C-H$_2$ stretch	2900
C-H stretch	2845
S-H stretch	2565
C-H scissoring	1450
C-C bend	1040
Mass Spectrometry	
Assigned Fragments	**Mass/Charge**
C$_{10}$H$_{15}$SH$^+$	168
C$_{10}$H$_{15}^+$	135
C$_8$H$_{11}^+$	107
C$_7$H$_9^+$	93
C$_6$H$_7^+$	79
C$_5$H$_7^+$, C$_{10}$H$_{15}^{2+}$	67
C$_4$H$_7^+$, C$_8$H$_{11}^{2+}$	55

Figure 3.4. Characteristic peaks for 1-adamantanethiol analyzed by ^{1}H NMR, ^{13}C NMR, IR spectroscopy and mass spectrometry. The NMR peaks reference the figure at the left of the table.

thioacetic acid (Sigma-Aldrich, St. Louis, MO) and 1.5 equivalents of triethylamine (used as a cata-lyst) in methlylene chloride [159]. First, the triethylamine and thioacetic acid were stirred together and cooled to 0 °C in a nitrogen atomosphere. Then, the adamantane amide was slowly added. The organics were dried with magnesium sulfate and removal of the solvent *in vacuo* yields a pale yel-low compound (*N*-adamantyl-5-(thioacetate)pentanamide). The product was purified on a column using a 20% ethyl acetate and 75% hexanes mobile phase. The thioacetate product was confirmed using NMR and mass spectrometry. Under nitrogen, the thioacetate was converted to a thiol by hydrolysis with hydrochloric acid (38%) for 12 h [159]. The *N*-adamantyl-5-mercaptopentanamide product was recovered *in vacuo*, and confirmed by NMR and mass spectrometry.

For the second method, potassium thioacetate (Sigma-Aldrich, St. Louis, MO) was dissolved in tetrahydrofuran and methanol and then the *N*-adamantyl-5-bromopentanamide was added. The reaction proceeded until the thioester peak, as observed by NMR, remained unchanged. The products were dried *in vacuo* and then purified and hydrolyzed as described for the previous method.

3.3.3 Sample preparation

1-Adamantanethiolate SAMs were prepared similarly to the ALK SAMs in Chapter 2. SAMs were fabricated on commercially available Au{111} on mica (Molecular Imaging, Tempe, AZ) and polycrystaline gold on silicon samples in base-bath-cleaned glass v-vials. Annealed substrates were immersed in a 10 mM solution of AD in sparged ethanol. It should be noted that it is also possible to make 1-admantanethiolate SAMs from 1 mM solutions. However, it was found at the beginning of this study that more reproducible SAMs were obtained from 10 mM solutions. Subsequent electrochemical desorption studies, discussed at the end of this chapter, have shown that there is no observable difference in the packing structure of the SAMs both with increased thiol concentration of the deposition solution as well as increased deposition time. Therefore, the 24-h deposition time and 10 mM solution concentration for the fabrication of the SAMs were chosen for consistency.

Gold on silicon samples were prepared by e-beam evaporation (Kurt J. Lesker Co., Pitts-burgh, PA) onto 6 inch silicon wafers (Silicon Quest, Santa Clara, CA). 1500 Å of gold (Kurt J. Lesker Co., Pittsburgh, PA) were evaportated onto a 150 Å chromium (Kurt J. Lesker Co., Pitts-burgh, PA) adhesion layer. Both the gold and the chromium were evaporated at a rate of 1 Å/s at room temperature and a base pressure of 1×10^{-7} Torr.

Self-assembled monolayers of ADtether were also fabricated by similar methods using annealed Au{111} on mica substrates. Ethanolic solutions ranging in concentration from 0.1 mM to 50 mM, and solution annealing at temperatures of 68 °C to 78 °C were attempted, all with similar results. However, the higher concentrations and temperatures resulted in samples with a cloudy visual appearance, while the lower concentrations resulted in samples that did not differ in appearance from that of bare Au{111}.

3.3.4 Scanning tunneling microscopy imaging

All the following STM measurements were performed under ambient conditions using a custom beetle-style STM (see chapter 2 and references [99, 160]). To determine the lattice spacing of the AD SAMs, the same tip was used to scan a SAM of known spacing (i.e. an ALK SAM) before and/or after scanning an AD SAM. Alternatively, the lattice spacing was determined from a multicomponent SAM in which there were distinct ordered areas of AD and ALK. In this way, the same tip was used to determine the lattice spacing of both simultaneously. In both cases, the measured spacing of the ALK SAM was used to calibrate the gain of the piezoelectric scanners and thus the measured lattice parameters. The AD lattice spacing was measured from Fourier transforms of the images of the AD lattice, and was calibrated using the Fourier transform of the ALK lattice from the same or subsequent images. SAM corrugation was calibrated using the known height of the step edges of the Au{111} substrate in the same or subsequent images.

3.3.5 Ellipsometry

Ellipsometry measurements were performed with both a single wavelength fixed angle ellipsometer (Stokes Ellipsometer LSE, Gaertner Scientific Corp., Skokie, IL) and a spectral ellipsometer. The Stokes Ellipsometer uses a 6328 Å laser measuring beam at a 70° incidence angle. The spectral ellipsometer used was an M-2000 (J.A. Woollam Co., Inc., Lincoln, NE) with WVASE32 acquisition and analysis software. These measurements were performed with the help of Sungkyu Park in Dr. Thomas N. Jackson's research group at the Pennsylvania State University.

3.3.6 Contact angle

Contact angle measurements were made using a custom-built CA apparatus with a CCD camera (Hitachi Denshin America, LTd., Woodbury, NY) outfitted with an InfiniStix 0.50× magnification lens with a 94 mm focal length (Infinity, Boulder, CO), and coupled to a National Instruments IMAQ-PCI card (National Instruments, Austin, TX). Images were captured using National Instruments Measurements and Automation software. Reproducible droplets of 60 μL were formed from a 2 mL Gilmont micrometer syringe using a blunt tip 18 gauge needle (VWR Inc., West Chester, PA). All CA measurements shown here were made using 18 MΩ water. The CA was measured from the images using Scion Image (Scion Corp., Frederick, MD) and each measurement was an average of three measurements on each side of the static drop.

3.3.7 Grazing angle Fourier transform infrared spectroscopy

Fourier transform infrared spectra were acquired using a Nicolet 6700 FTIR spectrometer (Thermo Electron Corporation) operating with a liquid-nitrogen-cooled mercury cadmium telluride detector. Monolayer spectra were obtained in grazing incidence reflection with p-polarized light at an angle of 86°, relative to the surface normal, using a "Seagull" unit (Harrick Scientific Inc., Ossining, NY). The spectrometer setup was purged with dry and CO_2-free air delivered from a purge gas generator (Parker-Balston, Cleveland, OH). All IR data were collected with a mirror speed of 1.8988 cm/s, a resolution of 2 cm^{-1}, averaged over 1024 scans, and transformed using N-B Medium apodization.

All SAM FTIR spectra were normalized with data recorded from perdeuterated 1-decanethiolate monolayers on Au{111} [161], which protect the gold substrate against environmental contamination. This was found crucial in preventing anomalies with data normalization, since even small amounts of hydrocarbons give rise to strong signals in the region of interest.

3.3.8 Electrochemical desorption

Electrochemical measurements were performed employing a custom-built electrochemical cell and a BAS Epsilon potentiostat (Bioanalytical Systems Inc, West Lafayette, IN). The working electrode was defined by a perfluoroelastomer o-ring (McMaster Carr, Cleveland, OH) mounted inside the electrochemical cell. The working electrode area was electrochemically determined to be

$\sim$0.5 cm^2 using the Randell Sevic equation [137, 143]. A Ag/AgCl saturated KCl reference electrode (Bioanalytical Systems Inc, West Lafayette, IN) and Pt wire counterelectrode (Bioanalytical Systems Inc, West Lafayette, IN) were employed to control the potential of the cell. The supporting electrolyte was 0.5 M potassium hydroxide (99.99%, semiconductor grade, Sigma-Aldrich, St. Louis, MO), sparged using ultra-high purity argon for 20 min. Cyclic voltammograms were acquired from -200 mV to -1500 mV and back at a rate of 20 mV/s. The voltammograms were baseline corrected using a straight line subtraction in the first 100 mV of the sweep where no faradaic processes occur.

3.4 Results and Discussion

3.4.1 Self-assembled monolayer structure of 1-adamantanethiol

Figure 3.5A shows two Au{111} terraces covered with an AD SAM. A typical SAM of this type consists of very flat topography with depressions on the order of Au{111} substrate vacancy islands. With this resolution, it can be seen that AD SAMs lack the protruding domain boundaries that are typical in ALK SAMs [31, 32, 94, 162–164].

Closer inspection at higher resolution (Figures 3.5B and C) shows individual molecules arranged in a hexagonal close-packed formation, and in addition to the substrate vacancy islands, there are apparent depressions of the molecular lattice of less than 0.5 Å. A Fourier transform of Figure 3.5C (shown in Figure 3.5D) shows a hexagonal lattice with the first- and second-order reciprocal lattice spots visible. However, these spots are not single points, but rather a collection of points the same distance from the center but slightly rotated. This distance in reciprocal space corresponds to a measured nearest neighbor distance of 6.9 ± 0.4 Å and a next nearest neighbor distance of 11.8 ± 0.4 Å. Measuring the angle spanned by the first-order spots (the angle formed by drawing a line from one end of the spot to center and back to the other end of the spot) in the Fourier transforms also shows that there exist rotational domains of the hexagonal lattice.

With careful inspection, one should also observe that the rows of molecules shift direction slightly throughout the molecularly resolved images. It can be seen in Figure 3.6 that the apparent depressions mentioned above are domain boundaries separating different rotational domains. Five distinct domains (color coded in the right image of Figure 3.6) are observed, and their rotations with respect to one another are given in Table 3.1. The difference in orientation angles between domains
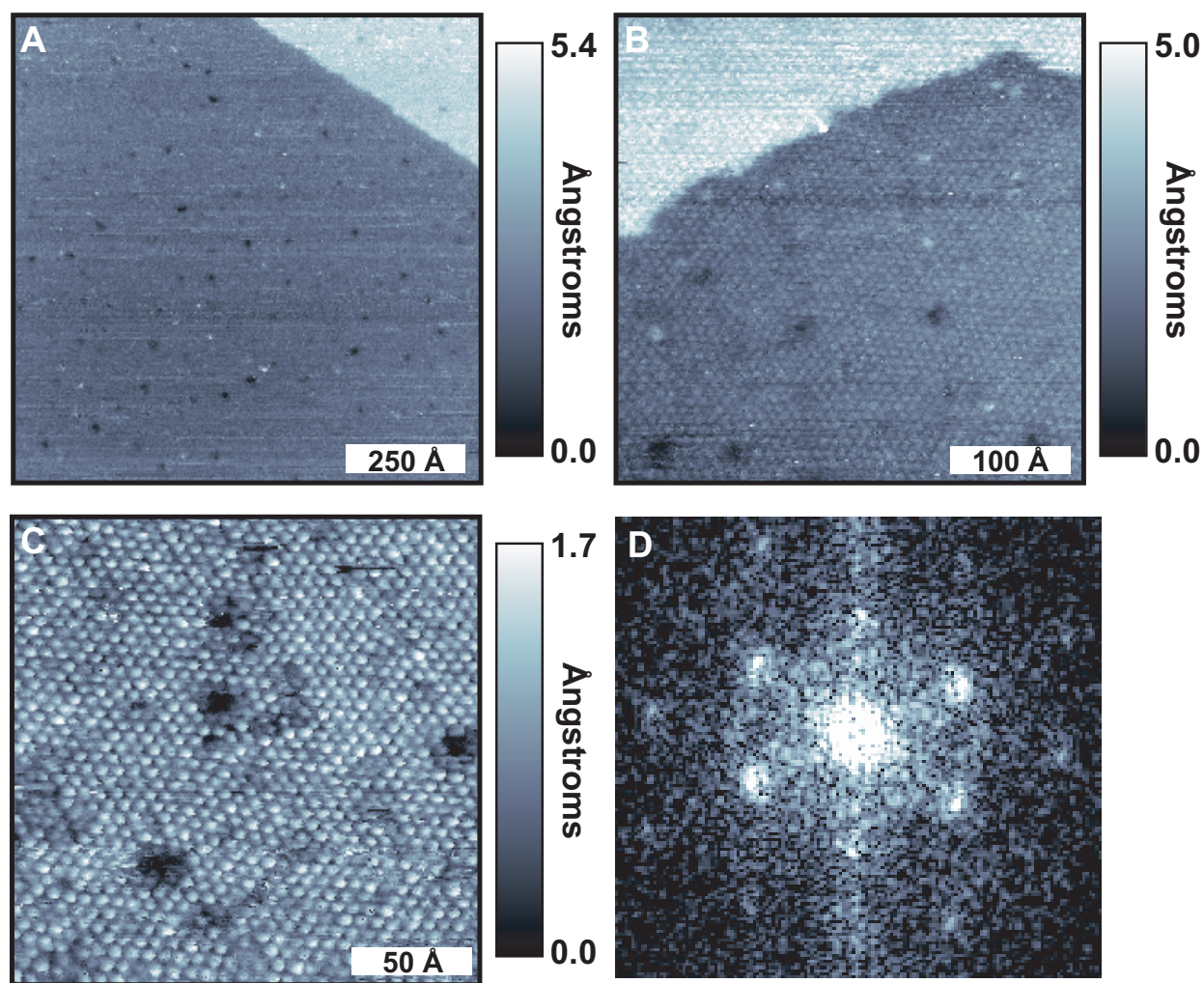
Figure 3.5. Scanning tunneling microscopy images showing the well ordered hexagonal close-packed lattice of 1-adamantanethiolate SAMs on Au{111}. A) 1500 Å × 1500 Å, V_{sample}: 0.75 V, I_{tunnel}: 6.0 pA B) 400 Å × 400 Å, V_{sample}: 1.0 V, I_{tunnel}: 2.0 pA C) 200 Å × 200 Å, V_{sample}: 1.0 V, I_{tunnel}: 5.0 pA D) Fourier transform of the 1-admantanethiolate SAM showing first-order and a few second-order reciprocal lattice points.
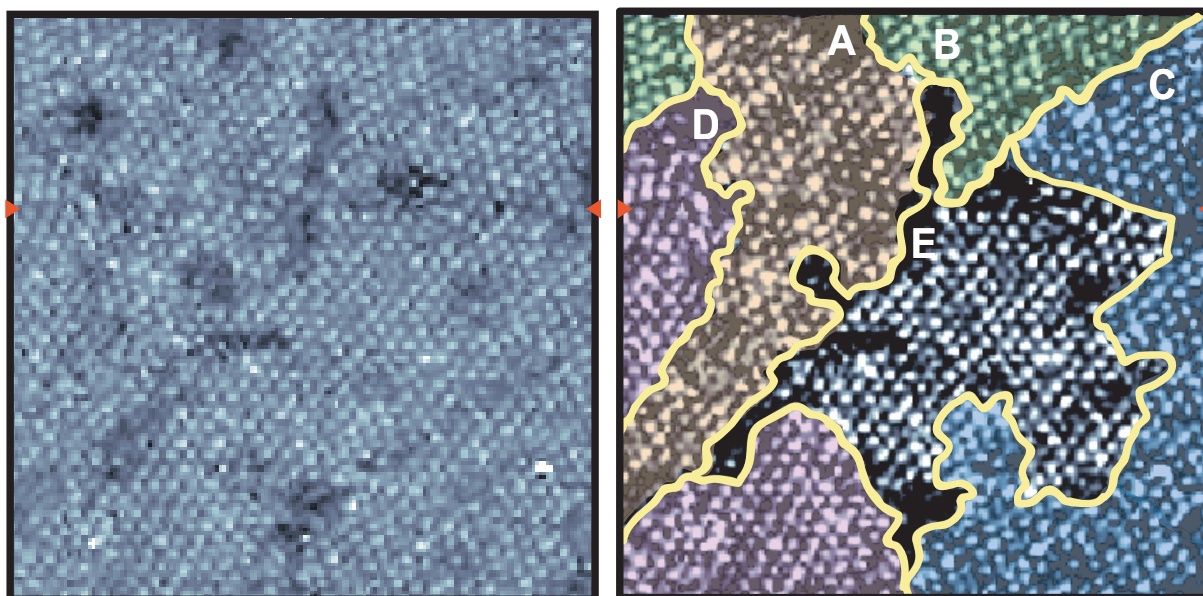
Figure 3.6. A scanning tunneling microscopy image of the domains of a 1-adamantanethiolate SAM on Au{111}. The same image is shown to the right with the domains highlighted and the contrast increased for clarity. The measured angles between the unit cells of the domains are given in Table 3.1 using the alphanumeric labels, indicated on the figure. A slight tip jump, marked by the red arrowheads, approximately two-thirds of the way up the image, gives the appearance of a change in rotation of the lattice, but instead the molecules are all uniformly shifted to the left across the image. The imaged area is 200 Å × 200 Å V_{sample}: 1.0 V, I_{tunnel}: 5.0 pA.

A and E is small and it is possible that these molecules belong to the same rotational domain. It should be noted that the exact rotation with respect to the substrate cannot be determined by imaging only the adlayer, although it is possible to estimate this rotation from straight step edges of the Au{111} substrate, which follow close-packed substrate directions.

Given the above observations, the most likely unit cells assignments are (7×7) with two rotationally equivalent unit cells of $(7 \times 7)R21.8°$ with respect to the Au{111} substrate, or the four rotationally equivalent unit cells $(\sqrt{91} \times \sqrt{91})R27°$ and $(\sqrt{91} \times \sqrt{91})R5.2°$ with respect to the Au{111} substrate, as shown schematically in Figure 3.7. It is also possible that the preferred orientation is some combination of each unit cell; additional possibilities with nearest neighbor distances near 6.9 Å are not ruled out. Using a gold lattice spacing of 2.89 Å, a (7×7) unit cell has a lattice constant of 20.23 Å and has 9 molecules per unit cell (corresponding to 38.9 Å^2/molecule). Therefore, a (7×7) unit cell gives a nearest neighbor distance of 6.74 Å and a next nearest distance of 11.68 Å. A $(\sqrt{91} \times \sqrt{91})$ unit cell has a lattice constant of 27.57 Å with 16 molecules per unit cell (cooresponding to 40.7 Å^2/molecule), resulting in a nearest neighbor distance of 6.89 Å and a next nearest neighbor distance of 11.94 Å. All the calculated distances and angles for these unit cells are within the error of those measured. Note that these lattice spacings are significantly larger than those found in ALK SAMs. From the combination of assignments given to similar monolayers in the literature and the modeling of displaced AD SAMs, discussed in the next chapter, the (7×7) unit cell seems the more likely AD SAM unit cell.

Based on literature bond distances, AD is estimated to stand 7.9 Å off the surface, including the 2.36 Å sulfur-gold bond [106]. Due to steric hindrance between the beta hydrogens and the Au surface, there is expected to be little tilt of the AD molecules with respect to the gold surface (see Figure 3.8) and therefore, it is likely that the different observed domains are due to changes in rotation of the unit cell.

3.4.2   Self-assembled monolayer structure of *N*-adamantyl-5-mercaptopentanamide

Figure 3.9 shows the best STM images collected of the ADtether molecules assembled on Au{111}. It should be noted that these images are atypical. In most cases, the images of the surface lacked any features identifiable of a SAM, and in many cases, the surface was difficult to tunnel into (and therefore remain in feedback) with STM. Images of samples made from lower solution concentrations and/or with shorter deposition times were similar, and also show no regions of

	A	B	C	D	E
A	–	15°CW	7°CW	10°CCW	2°CCW
B	15°CCW	–	9°CCW	24°CCW	15°CCW
C	7°CCW	9°CW	–	15°CCW	8°CCW
D	9°CW	24°CW	15°CW	–	8°CW
E	2°CW	15°CW	8°CW	8°CCW	–

Table 3.1. The measured angles between each of the observed rotational domains, shown in Figure 3.6, of a 1-adamantanethiolate SAM. The direction of each angle is specified as clockwise (CW) or counter-clockwise (CCW). All the measured angles have an associated error of $\pm 4°$.
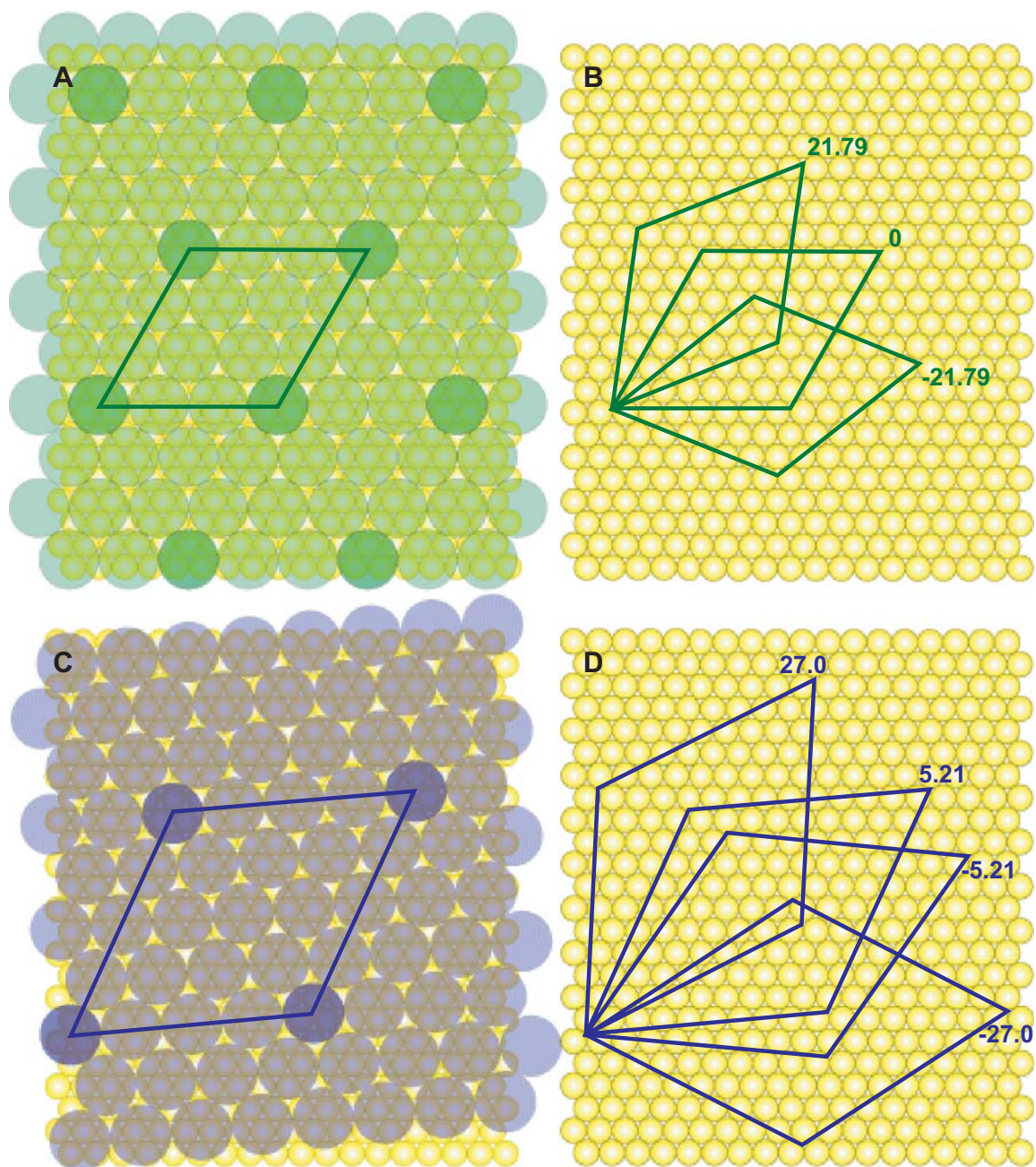
Figure 3.7. Schematics of the possible unit cells for 1-adamantanethiolate SAMs on Au{111}. A) The (7×7) unite cell with respect to the underlying Au{111} lattice. The green circles represent the lateral area each molecule consumes. B) Equivalent (7×7) rotational unit cells. C) The $(\sqrt{91} \times \sqrt{91})R5.21°$ unit cell with respect to the underlying Au{111} lattice. The blue circles represent the lateral area each molecule consumes. D) Equivalent $(\sqrt{91} \times \sqrt{91})$ rotational unit cells.
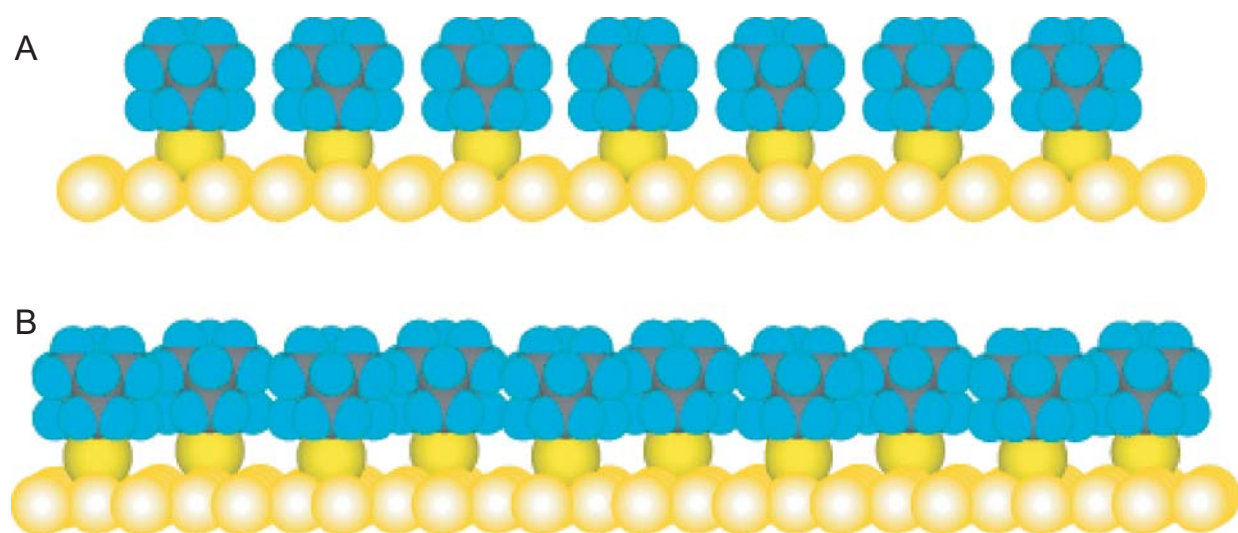
Figure 3.8. Side-view schematics of a 1-adamantanethiolate SAM on Au{111} along the nearest neighbor (A) and next nearest neighbor (B) directions, using a (7 × 7) unit cell. The gray, light blue, yellow and gold atoms are the carbon, hydrogen, sulfur and gold atoms, respectively and are scaled with respect to each atom's van der Waals radius.
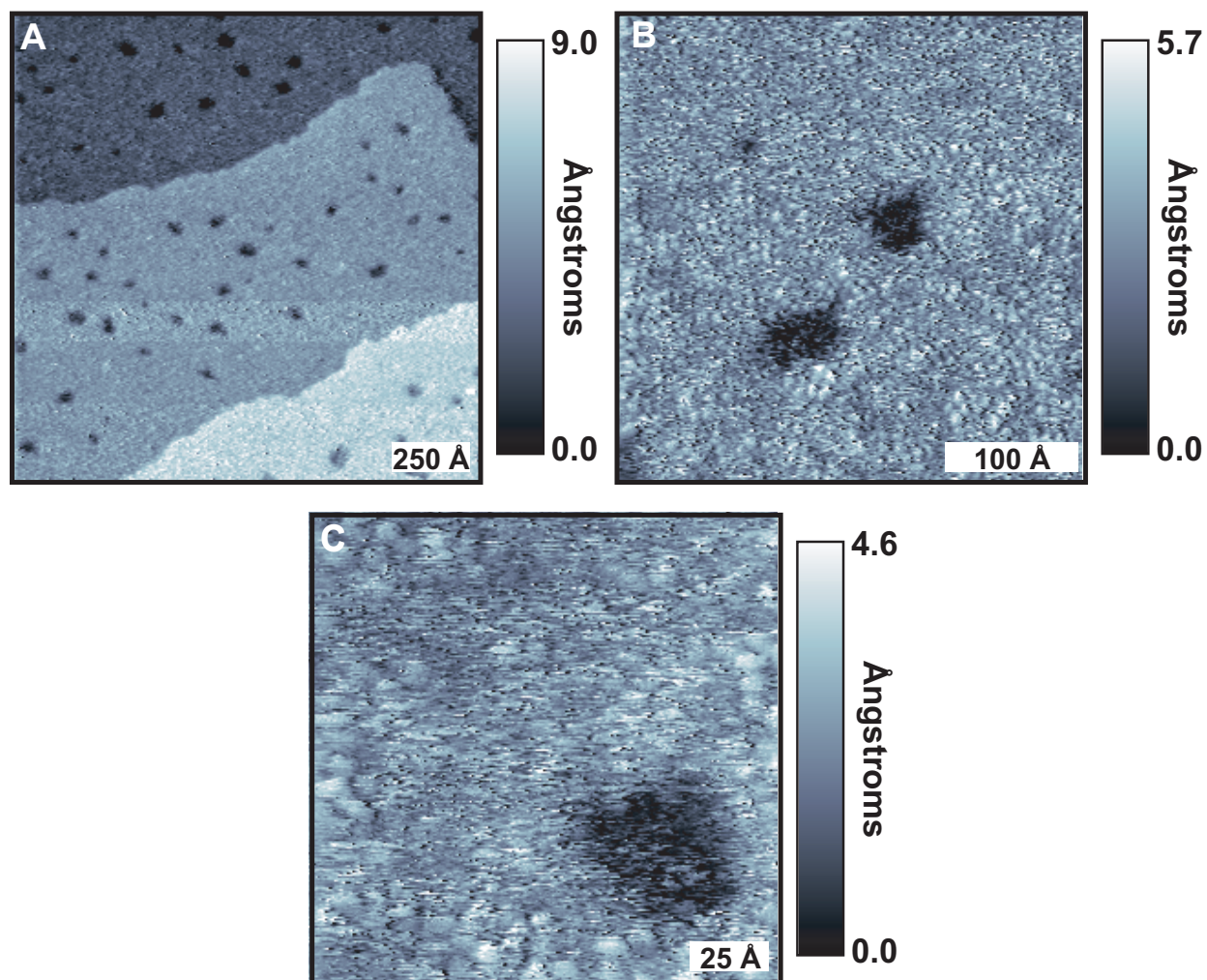
Figure 3.9.   Scanning tunneling microscopy images of *N*-adamantyl-5-mercaptopentanamide SAMs on Au{111} A) 1500 Å × 1500 Å, V$_{sample}$: 1.0 V, I$_{tunnel}$: 2.0 pA B) 350 Å × 350 Å, V$_{sample}$: 1.1 V, I$_{tunnel}$: 1.0 pA. C) 150 Å × 150 Å, V$_{sample}$: 1.1 V, I$_{tunnel}$: 1.0 pA.

ordered lattice. In this figure, one-atom-deep substrate vacancy islands, caused by the adsorption of the sulfhydryl headgroup to the surface were observed (see Figure 3.9A). Additionally, gold terraces were uniformly covered by the molecular film, and step edges were observed. However, SAM rotational, translational or tilt domain boundaries are not perceived. Higher resolution images (Figure 3.9C) show uniform protrusions approximately 8 Å in size that are attributed to individual ADtether molecules. The molecules seem to be randomly distributed across the surface, with the molecules arranged in small clusters of 3-5 molecules at most. No long range ordered lattice is observed.

3.4.3   Further self-assembled monolayer characterization

In addition to STM, each SAM was further characterized by ellipsometry, CA measurements, FTIR, and electrochemical desorption by the experimental methods described above.

3.4.3.1   Ellipsometry

No reproducible results by single wavelength were obtained for AD SAMs on either surface using a refractive index of 1.5, typically used for ALK SAMs, as well as indices ranging from 1.1 to 1.6 obtained for measurements of bulk adamantane and adamantane derivatives [165,166]). Values of 8 ± 2 Å were obtained on a few occasions by spectral ellipsometery, but values also ranged from as low as 2 Å to as high as 20 Å. This result was puzzling because reproducible results were obtained for C8 SAMs, which theoretically are approximately the same topographic distance from the surface within a few Ångstroms.

Ellisometery measurements of the ADtether molecules give reproducible thicknesses of 23 ± 2 Å on polycrystalline gold. In both cases, each thickness is too large for a single monolayer, and are instead indicative of multiple layers of the molecules on the surface.

3.4.3.2   Contact angle measurements

Table 3.2 gives the CA measurements of 18 MΩ water droplets on AD and ADtether SAMs on both polycrystalline gold and Au{111}, and gives the measured values of a C8 SAM and each kind of bare gold surface for comparison. It should be noted that all the SAMs are more hydrophobic than the bare gold surfaces but the AD and ADtether SAMs are both more hydrophilic than the C8 SAMs. This is likely the result of the difference in hydrophobicity of the exposed CH_3, and CH_2

and CH groups for the ALK SAMs and the adamantane-containing SAMs, respectively. The small difference in wettability between the AD and the ADtether SAMs on Au{111} perhaps indicates that the adamantane tailgroup is oriented similarly for both of these SAMs on this surface.

Additionally, both the AD and the ADtether SAMs show different CA on polycrystalline gold compared to Au{111}. This phenomenon has been observed for ALKs previously, and was observed for the C8 films also. It is likely due to the increased grain boundaries in the polycrystalline gold, leading to more defects and regions of disorder in the films. However, for the ADtether this difference is in excess of $10°$, indicating that these SAMs may cover the polycrystalline gold in a different way than Au{111}, i.e. instead forming multilayers (see below).

3.4.3.3   Grazing angle fourier transform infrared spectroscopy

Figure 3.10 shows the FTIR spectra of AD SAMs on an Au{111} and on polycrystalline gold. Both spectra show all the same peaks as observed for the solid FTIR spectra (see Figure 3.4). However, there are differences between the two spectra, indicating a difference in molecular orientation on the two substrates, as observed with the CA measurements (the differences are outlined in Table 3.3). The most prominent difference is the position of the shoulder on the main peak around 2900 cm^{-1}. For the SAM on Au{111}, this shoulder is on the higher energy side of the peak and is almost a separate peak, but for the polycrystalline gold the distinct shoulder is on the low energy side. Fourier transform infrared spectra of AD SAMs with solution or environmental contaminants (observed by STM) are similar to the one shown in Figure 3.10B, suggesting that the SAMs adsorbed on polycrystalline gold are less well ordered.

Figure 3.11 shows several spectra of AD SAMs assembled from a 10 μM solution for adsorption times ranging from 5 min to 6 h. It can be seen that the peaks both shifted in energy as well as increased in intensity with time, indicating different orientations of the AD molecules during the adsorption process. The peak at 2850 cm^{-1}, attributed to a CH_2 symmetric stretching mode [146,148], changed very little with adsorption time. However, the smaller peak at 2934 cm^{-1}, attributed to the CH_2 asymmetric stretching mode [146,148], was a well resolved narrow peak for short deposition times, that then shifted to lower energy and was enveloped by the much larger peak at 2911 cm^{-1}. The largest peak, attributed to a C-H stretching mode [170], was much narrower and had a clear shoulder on the lower energy side for smaller adsorption times. It then became less well resolved and shifted to lower energies with increased adsorption times, indicating a more ordered

Monolayer type	Au{111}	Polycrystalline gold	Literature values
None	$35 \pm 4°$	$37 \pm 2°$	$30\text{-}70°$
1-Adamantanethiolate	$80 \pm 2°$	$85 \pm 3°$	–
N-adamantyl-5-mercaptopentanamide	$83 \pm 2°$	$95 \pm 4°$	–
1-Octanethiolate	$108 \pm 4°$	$110 \pm 3°$	$112 \pm 3°$

Table 3.2.   Measured contact angles of water on bare gold, and on 1-adamantanethiolate, N-adamantyl-5-mercaptopentanamide, and 1-octanethiolate SAMs assembled on Au{111} and on polycrystalline gold. Literature values are from references [167–169].

SAM. Differences in SAM structure for different adsorption times or concentrations have not been observed by STM. For all the conditions tried, images similar to the ones shown above (Figures 3.5 and 3.6) were obtained. It is therefore assumed that the differences in molecular orientation are small, and do not severely impact the SAM packing structure.

Figure 3.12 shows the FTIR spectra of ADtether SAMs on both Au{111} and on polycrystalline gold. The peaks and their physical assignments are given in Table 3.3 [170,171]. As observed for the AD SAM spectra, but much more prominent here, the ADtether spectra were different depending on the substrate. It should be noted that the overall absorption intensities of spectra of the SAMs on polycrystalline gold were more than 10 times higher than for any of the other spectra. Intensities of this magnitude have been observed for thick films and multilayers, suggesting that the ADtether molecules here were not in the form of single monolayers, in agreement with the other techniques. ADtether films assembled from both less concentrated solutions and for shorter adsorption times showed slightly decreased intensity in the FTIR spectra, but had the same spectral shape. Another notable difference between the spectra from each substrate was the relative intensity of the COOH absorption peak around $1500 \, \text{cm}^{-1}$. The spectra for ADthether on Au{111} had strong peaks at this frequency, while the other spectra clearly did not. Dipoles parallel to the surface do not absorb (a mirror dipole is created in the metallic surface and the dipoles cancel), while dipoles perpendicular to the surface strongly absorb. From these observations, it would seem that the molecules on the polycrystalline surface were arranged such that the carbonyl groups were parallel to the surface.

The ADtether SAM on Au{111} spectrum (Figure 3.12A) has some strong similarities with the AD SAM on Au {111} (Figure 3.10A). The peaks in the CH_2 stretch region at $\sim 2855 \, \text{cm}^{-1}$ and at $\sim 2916 \, \text{cm}^{-1}$ almost exactly overlap the AD SAM spectrum in that same region. The inset in Figure 3.12A shows the $2855 \, \text{cm}^{-1}$ peak in detail. Here, it can be seen that this peak is the overlap of two CH_2 stretch peaks – one for the methlyene on the adamantyl tailgroup (at around $2911 \, \text{cm}^{-1}$) and one for the tether portion (at around $2920 \, \text{cm}^{-1}$) of the molecule. The additional peak in this region, at $\sim 2970 \, \text{cm}^{-1}$, is attributed to the C-H stretch on the adamantyl tailgroup [170], as observed in the solid IR spectra (see Figure 3.4).
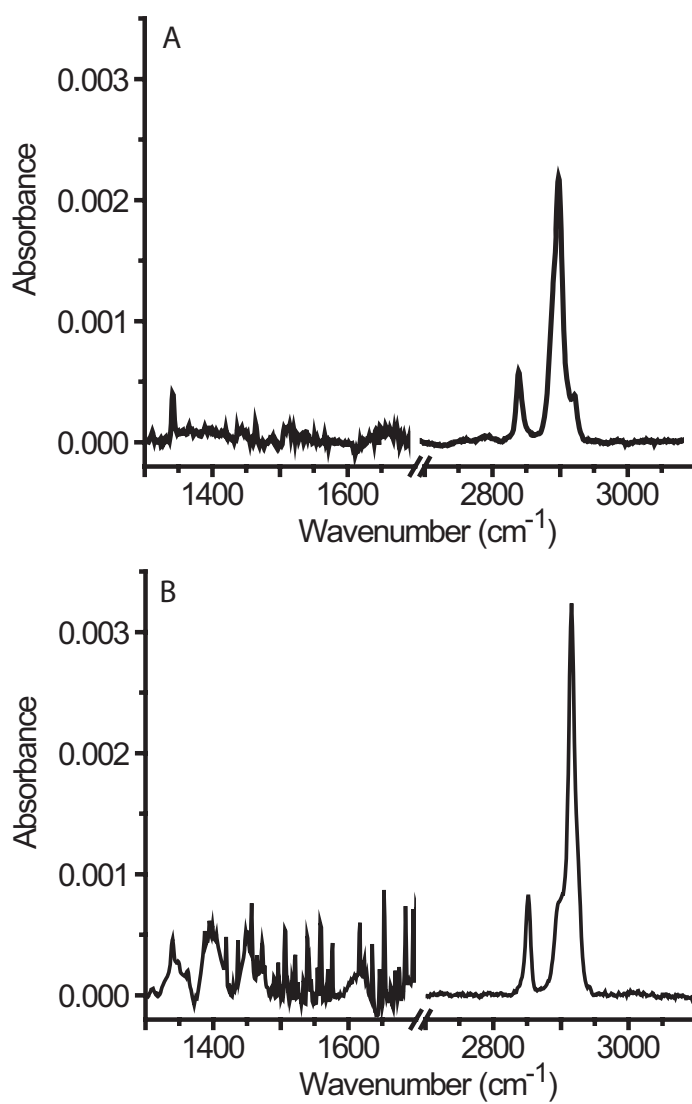
Figure 3.10. Fourier transform infrared spectra of 1-adamantanethiolate SAMs on Au{111} (A) and on polycrystalline gold (B).
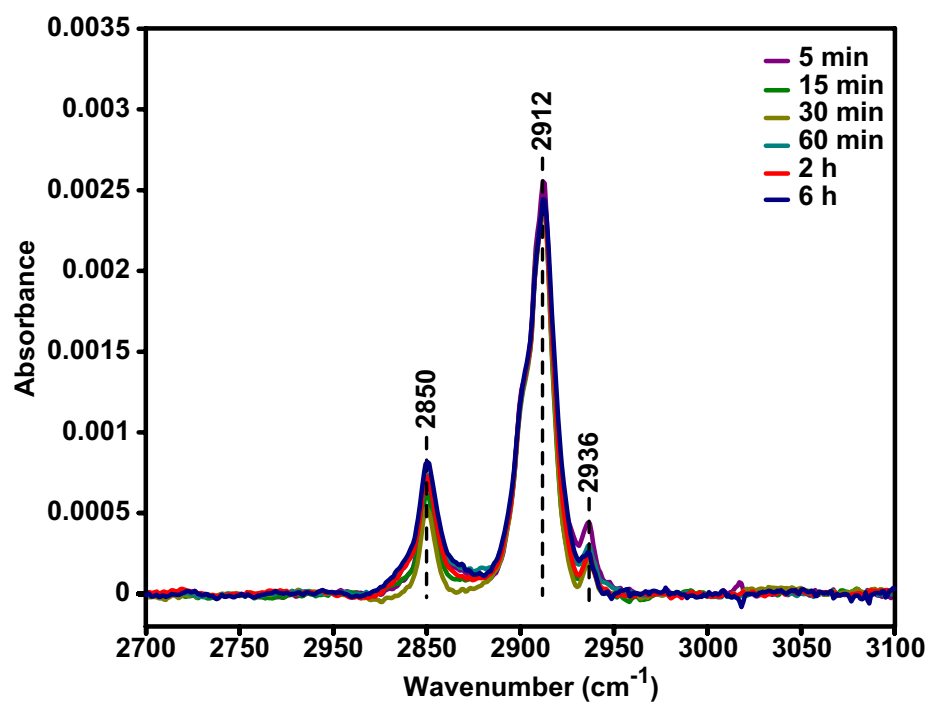
Figure 3.11. Fourier transform infrared spectra with increasing adsorption time of 1-adamantanethiolate SAMs on Au{111} assembled from 10 μM solution.
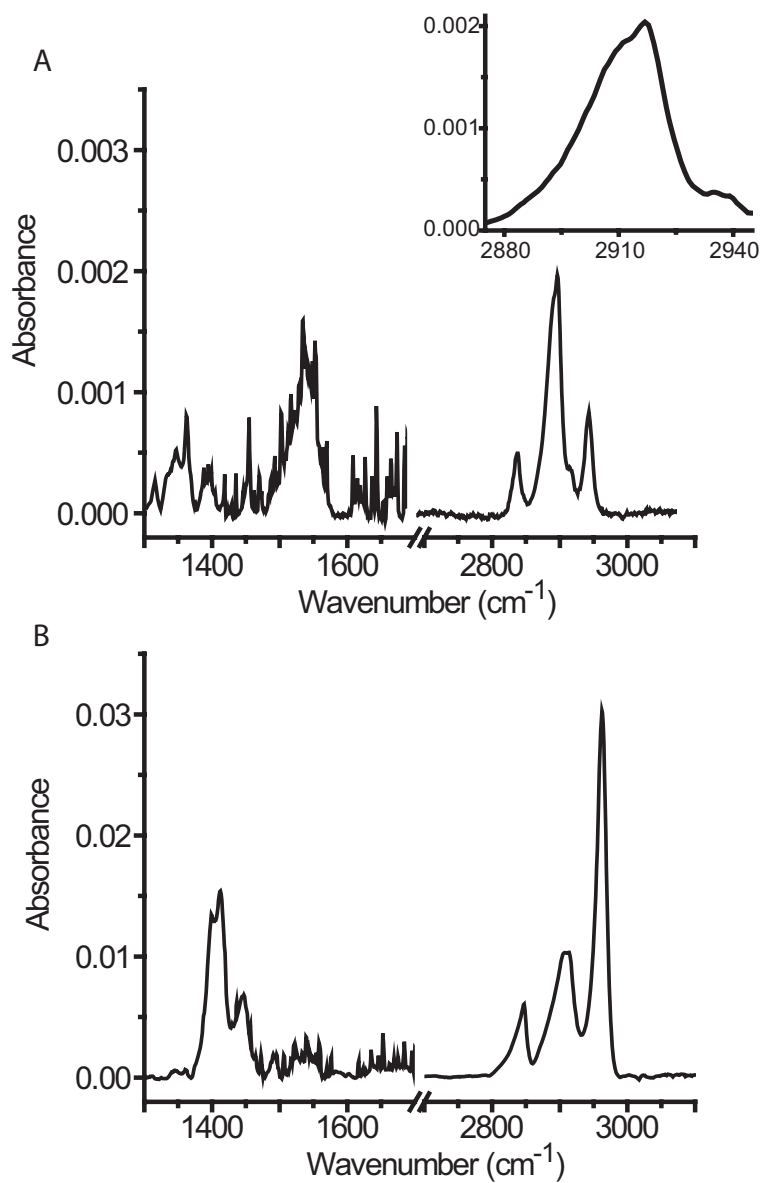
Figure 3.12. Fourier transform infrared spectra of *N*-adamantyl-5-mercaptopentanamide SAMs on Au{111} (A) and on polycrystalline gold (B).

AD on Au{111}

Peak Assignment	Peak Position (cm^{-1})
CH_2 asymmetric stretch	2934
CH stretch	2911
	2904 (shoulder)
CH_2 symmetric stretch	2850
CH_2 scissor	1442
CH_2 wag	1339

AD on polycrystalline gold

Peak Assignment	Peak Position (cm^{-1})
CH stretch	2916
	2898 (shoulder)
CH_2 symmetric stretch	2851
CH_2 scissor	1456
CH_2 wag	1339

***N*-adamantyl-5-mercaptopentanamide on Au{111}**

Peak Assignment	Peak Position (cm^{-1})
CH_2 asymmetric stretch	2963-65
CH stretch	2916-18
CH_2 symmetric stretch	2855
NH_2 stretch	1660
C=O	1550-52
CH_2 scissor	1442
CH_2 wag	1339
CH_2 bend	1310

***N*-adamantyl-5-mercaptopentanamide on polycrystalline gold**

Peak Assignment	Peak Position (cm^{-1})
CH_2 asymmetric stretch	2961-62
CH stretch	2906-13
CH_2 symmetric stretch	2846
NH_2 stretch	1660
C=O	1550-52
CH_2 scissor	1455
CH_2 wag	1361
CH_2 bend	1310

Table 3.3.   Observed Fourier transform infrared spectroscopy peaks and their assignments for 1-adamantanethiolate and *N*-adamantyl-5-mercaptopentanamide SAMs on Au{111} and on polycrystalline gold.

3.4.3.4   Electrochemical desorption

Figure 3.13A shows a representative CV of an AD SAM adsorbed on the Au{111} working electrode. The CV shows a cathodic peak at ∼-990 mV and, in some cases, a smaller anodic peak at -710 mV (not shown) was observed [172]. As discussed above, the cathodic peak represents the reductive desorption of the AD molecules from the surface of the electrode, while the anodic peak represents the oxidative adsorption of the AD molecules to the electrode surface. The anodic peak was always smaller due to diffusion of some the AD away from the electrode. The peaks associated with the bare surface (black voltammogram in Figure 3.13) were not observed in the AD voltammogram except after the AD had been reductively desorbed from the gold surface; therefore, the AD SAM was sufficiently ordered to block the electrolyte from reacting with the gold surface. The cathodic E_p was significantly more positive then those observed for the long chain ALK SAMs (see gray voltammogram in Figure 3.13 and Table 3.4), indicating that it takes less energy to remove the SAM from the surface (i.e. it is easier for the electrolyte to reach the electrode surface). This is due to a combination of the increased lateral distance between the SAM molecules, the decreased intermolecular interactions in the AD SAMs (also indicated by the larger FWHM of the peaks), and the shorter physical size of the molecules separating the electrolyte from the Au{111} electrode. The smaller I_p and peak area of AD SAMs compared to those generally seen for ALK SAMs indicate a lower surface coverage than for the ALK s (see Table 3.4), as observed by STM. Using a (7×7) unit cell for the AD SAM and a $(\sqrt{3} \times \sqrt{3})R30°$ unit cell for the C12 SAM, 1.8 times more C12 molecules compared to AD molecules are present in the same area of Au{111}. For example, in a $(7\sqrt{3} \times 7\sqrt{3})R30°$ unit area of Au{111} (the unit area where the AD and C12 unit cells overlap) there are 49 C12 molecules (21.4 Å^2/molecule) and 27 AD molecules (38.9 Å^2/molecule). Because of the one electron loss per molecule during electrochemical desorption, this difference was reflected in the C12:AD ratios for both the I_p and the peak areas.

As discussed above, increased order in ALK SAMs induces a shift in the cathodic E_p towards a more negative potential. Figure 3.13B shows the cathodic E_p of AD SAMs as a function of both adsorption time (top axis, black points) and adsorption solution concentration (bottom axis, red points). There was no observed shift in the cathodic E_p; both sets of points were horizontally linear within error. There are two possibilities to explain this phenomenon: 1) the molecules do not reorder once they bind to the surface (after the first 2 min) or 2) there are insufficient interactions between the AD molecules, so that reordering has no impact on the measured E_p.

Given the conformational changes observed in the FTIR spectra (see Figure 3.11), the latter seems more likely.

Figure 3.14 shows a representative set of consecutive voltammograms with the ADtether SAM assembled on the Au{111} working electrode. The cathodic peak from the reduction of the thiol of the ADtether molecules was observed at $\sim$-870 mV, which is a less negative potential than the cathodic potentials measured with both the ADSAMs and the ALK SAMs. The top (blue) voltammogram in Figure 3.14 was the first sweep of the potential. The large peak here represents the desorption of the ADTether molecules from the surface. This peak was much larger in current than for the SAMs in Figure 3.13 (see Table 3.4), indicating more molecules per unit area were desorbed. The peaks surrounding the large peak resulted from the gold surface (the black voltammogram in Figure 3.13A), indicating that the molecules were not blocking the surface from the electrolyte, despite the large population. The three remaining (teal, magenta and olive) voltammograms were the second, third and fourth sweep, respectively. The peaks at $\sim$-850 mV are from the desorption of the ADT molecules that remained after or readsorbed during the previous sweep. Even after the fourth sweep, a quantifiable amount of molecules remained on the surface.

3.5   Conclusions

Upon exposure to Au{111}, AD was observed to form well ordered monolayers by STM. The lattice had measured nearest neighbor distances of 6.9 Å$\pm$ 0.5 Å and next nearest neighbor distances of 11.8 $\pm$ 0.4 Å. Additionally, several rotational domains were observed. After modeling, the most likely orientations with respect to the underlying gold lattice were either (7×7), $(7 \times 7)R21.8°$, $(\sqrt{91} \times \sqrt{91})R27°$ or $(\sqrt{91} \times \sqrt{91})R5.2°$ unit cells. Further characterization by CA, FTIR and electrochemical desorpotion measurements showed reproducibly ordered monolayers, although the exact monolayer orientation is unknown (requiring further experiments and modeling). All techniques indicated that these films have much different properties than the model ALK SAMs. Furthermore, electrochemical desorption experiments indicated that the AD SAMs have a weaker affinity for the surface than their ALK counterparts. The AD molecules also formed reproducible SAMs on polycrystalline films, possibly with a different lattice structure than for Au{111}, but the exact SAM structure remains unknown.

The addition of a short alkyl tether to the AD molecules, forming ADtether, greatly impacted the molecular lattice. The ADtether also formed SAMs, but no instance of a completely ordered film

Monolayer type	Average potential (mV)	Average current (μA)	Average area (μC)	Average FWHM (mV)
1-Adamantanethiolate	-996 $\pm$ 4	3.2 $\pm$ 0.4	9 $\pm$ 2	58 $\pm$ 11
N-adamantyl-5-mercaptopentanamide	-895 $\pm$ 20	6 $\pm$ 3	12 $\pm$ 2	48 $\pm$ 15
1-Dodecanethiolate	-1113 $\pm$ 9	6 $\pm$ 1	14.2 $\pm$ 0.8	45 $\pm$ 9

Table 3.4. The average cathodic peak potential, current, area and FWHM from voltammograms (first sweep) of 1-adamantanethiolate, N-adamantyl-5-mercaptopentanamide and 1-dodecanethiolate SAMs.
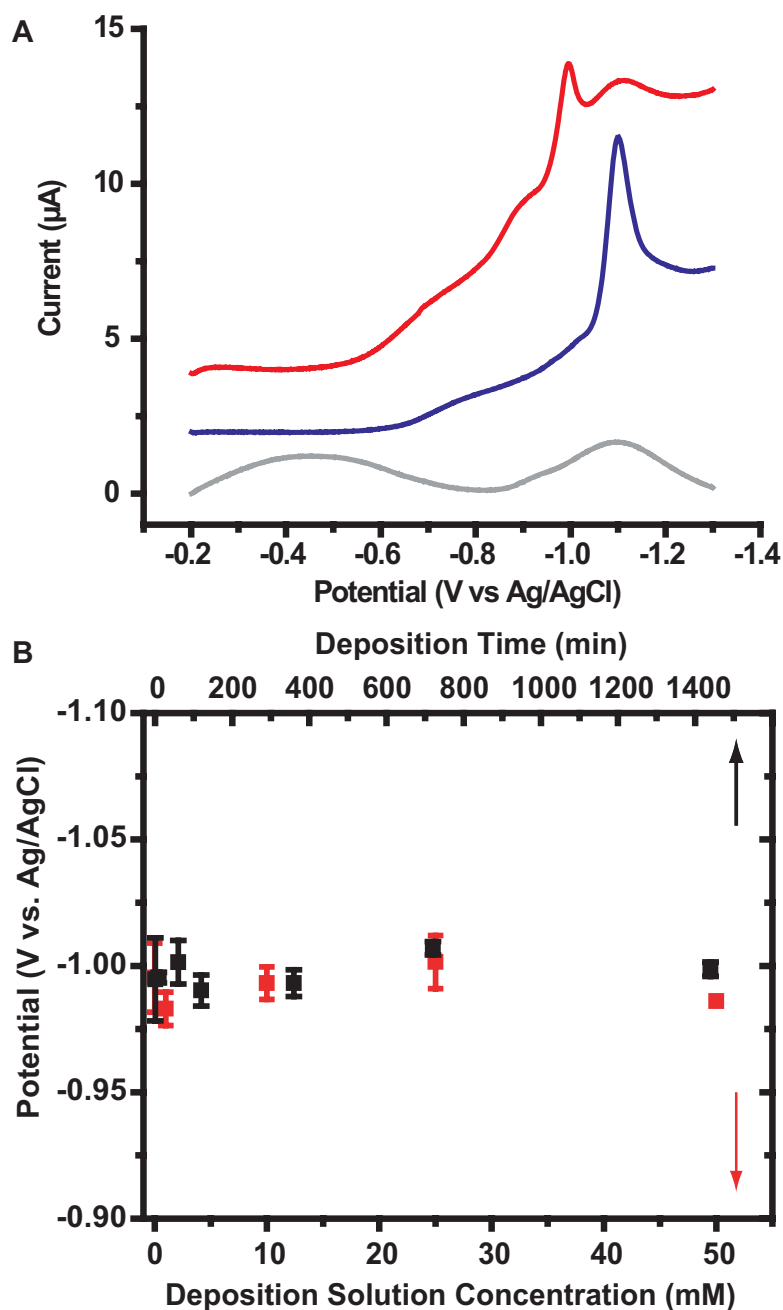
Figure 3.13. A) A representative cyclic voltammogram of a 24 h 1-adamantanethiolate SAM (red) with a 24 h dodecanethiolate SAM (blue) and bare Au{111} (gray) shown for reference. Sweep parameters: forward and backward from -200 mV to -1500 mV at 20 mV/s. Note: only the forward sweep (the cathodic peak) is shown and the voltammograms are offset for clarity. B) Plots of cathodic peak potential versus adsorption time for which all SAMs were made from 10 mM ethanolic solution (black points, top axis), and adsorption solution concentration (red points, bottom axis) for which all SAMs were assembled for 2 h.
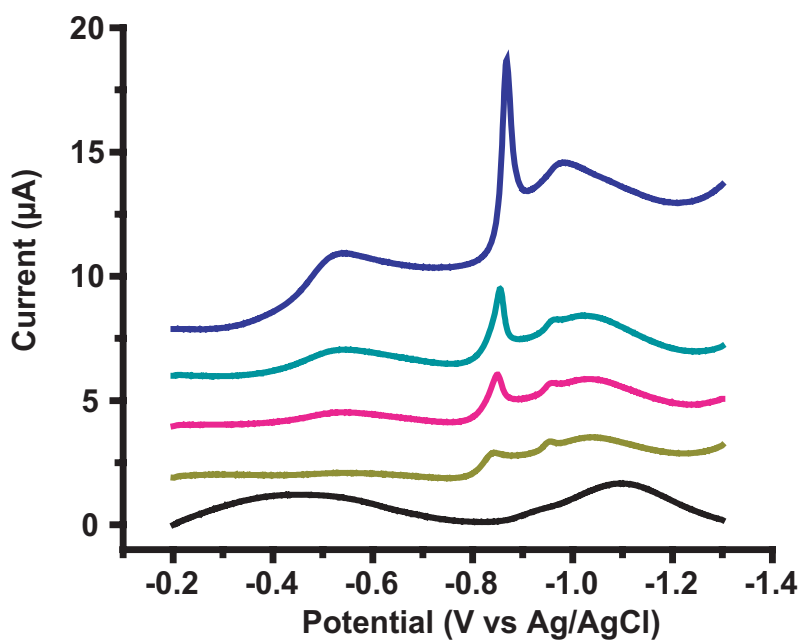
Figure 3.14. A representative set of consecutive voltammograms (the colored plots, in order from top to bottom) of a *N*-adamantyl-5-mercaptopentanamide SAM. Sweep parameters: forward and backward from -200 mV to -1500 mV at 20 mV/s. Note: only the forward sweep (the cathodic peak) is shown and the voltammograms are offset for clarity.

was observed by STM. Additional characterization suggested that the ADtether formed multilayers rather than monolayers.

Chapter 4

Displacement of 1-Adamantanethiolate
Self-Assembled Monolayers

4.1 Introduction

Transient monolayers are useful as temporary protective layers in pattern and in fabrication of nanoscale assemblies [6, 68, 173–176]. Furthermore, films that can be tuned so that they are easily removable upon exposure to one specific type of molecule, but are otherwise impermeable, are valuable because they can be used to eliminate process contamination.

The regularity and lack of large defect sites as well as the minimal internal conformational relaxation makes AD SAMs appealing matrices for molecular electronics and pattern fabrication. However, described here, insertion of molecules with electronic function into an existing AD SAM by previously described methods [7] was attempted for several molecules, but resulted in coverages of the inserted species that were too high to allow single inserted molecules to be probed when conditions that had previously been used for inserting molecules in ALK matrices were mimicked [7–10]. This chapter investigates this phenomenon using STM imaging of preformed AD SAMs that were inserted with ALK molecules of varying lengths (from 6 to 12 methylene units) for a variety of timescales from the solution and vapor phases. Additionally, X-ray photoelectron spectroscopy (XPS) and electrochemical desorption experiments were used to investigate the origins of AD SAM displacement.

4.2 Background

See chapters 1 and 3 for introductions to STM and electrochemical desorption, respectively.

4.2.1 X-ray photoelectron spectroscopy

X-ray photoelectron spectroscopy is an electron spectroscopy that uses monochromatic x-rays to ionize and to eject electrons from the inner-shell orbitals of the atoms in the material being studied [177, 178]. Every element has a characteristic binding energy associated with

each inner shell orbital that is dependent on the exact chemical environment of the element. If the energy of the incoming x-rays, $h\nu$, is larger than the binding energy of the electron (E_b), the excess energy is converted to kinetic energy of the emitted photoelectron (E_k). The kinetic energy is measured (with respect to the Fermi level of a standard metal, rather than the vacuum level) and thus the binding energy of the material can be determined by,

$$E_b = h\nu + E_k + \Phi, \tag{4.1}$$

where Φ is the work function of the metal standard. Measuring a kinetic energy distribution of the emitted photoelectrons gives a spectroscopic fingerprint of the material. For each material there is a distance that an electron can travel before being inelastically scattered (inelastic mean free path, λ), and therefore, the probability (P) that a photoelectron will be scattered while travelling through a surface film of thickness t is

$$P = exp^{(-t/\lambda)}. \tag{4.2}$$

The thicker the film is, the more the signal will be attenuated. However, the surface sensitivity can be increased by changing the angle of the incoming x-rays with respect to the sample. Because of the attenuation of the signal, the larger the incoming angle of the x-rays with respect to the surface normal, the more the analyzed region is localized to the surface. Additionally, this same technique can be used to determine at what depth specific elements are located within the film.

The basic instrumentation for XPS measurements includes a monochromatic x-ray source, and an electron energy analyzer and detector to disperse and to count the photoelectrons according to their kinetic energy. Additionally, a high vacuum environment is required to eliminate interference of collisions of the photoelectrons with ambient gasses.

4.3   Experimental Procedure

4.3.1   Sample Preparation

Single component AD and ALK SAMs were prepared by the methods described in Chapters 2 and 3. Unless otherwise specified, the samples were fabricated using ethanolic solutions. Inserted

SAMs were prepared by first fabricating a single component SAM and then immersing it in another thiolated solution of the specified concentration and for the specified time.

Bi-component codeposited SAMs were fabricated using deposition solutions with mixed molar ratios of two components to make solutions that were 1 mM in overall thiol conentration. These samples were prepared in the same manner as for the single-component SAMs. Separate samples were made for each molar ratio.

Solution-displaced AD SAMs were made by first fabricating a single-component AD SAM, confirming the presence of a well ordered lattice for each sample set using STM, and then immersing the sample into a 1 mM solution of ALK for the specified time period. Vapor-displaced AD SAMs were fabricated by sealing preformed AD SAMs in v-vials that contained 60 μL neat ALK in the bottom for the specified time period. For elevated temperature vapor displacement, the v-vial containing the neat ALK was heated at 78 $^\circ$C for 30 min prior to exposing the ADSAM, and then was returned to the oven for the specified time period. In each case, separate samples were made for each insertion time.

For the XPS studies, to minimize water presence in the SAMs, samples were also made from solutions using aynhydrous hexanes purified via freeze-pumped-thaw cycles. For these samples, the substrates were hydrogen flame annealed and then transferred to an oxygen-free, inert environment glovebox. Both the AD and C12 solutions were prepared from the dry hexanes and both the self-assembly and the insertion steps were performed in the glovebox. The samples were then sealed in plastic vials and were not exposed to ambient conditions until they were mounted in the XPS system ($<$5 min exposure).

4.3.2   Scanning tunneling microscopy

The samples were imaged using STM within 24 h of fabrication. The STM measurements and the instrumentation used are discussed in Chapters 1 and 2. Lattice spacings were determined by sequential imaging of SAMs with unknown spacing and know spacing, or by imaging of samples containing regions of both molecules (see Chapter 3).

4.3.3   X-ray photoemission spectroscopy

X-ray photoemission spectroscopy (XPS) spectra were collected using similar Au{111} on mica samples that were prepared in the same manner as for the STM and electrochemical deposition

experiments. Spectra were collected from single-component AD and C12 samples, in addition to AD inserted (displaced) with C12 samples using various solution displacement times.

Spectra were acquired using a Kratos Axis Ultra photoelectron spectrometer using a mono-chromatic Al-K-α source (20 mA, 14 kV), and a base pressure of 1×10^{-9} Torr, spot size of 300 μm $\times$ 700 μm. Survey spectra were acquired at a pass energy of 80 eV and high-resolution spectra of the O 1s, C 1s, S 2p and Au 4f regions were collected at a pass energy of 20 eV. The binding energies were referenced to Au 4f$_{7/2}$ peak at 83.98 eV. All the peaks from the spectra were fit using Gaussian-Lorentzian (GL) line shapes (CasaXPS analysis software [179]) using a Tougard background when necessary. The Au 4f peaks were fit with a fixed area ratio of 3:4, and the S 2p peaks were fit with a fixed area ratio of 2:1 and with a fixed energy separation of 1.18 eV.

4.3.4 Electrochemical desorption

Electrochemical desorption measurements were performed with the same instrumentation and in the same manner as discussed in Chapter 3.

4.4 Results and Discussion

4.4.1 Structure of 1-admantanethiolate and 1-decanethiolate codeposited self-assembled monolayers

Figure 4.1 shows STM images of samples made from two-component solutions in which the relative molar ratio of C10 to AD was varied. Figure 4.1A shows a 1:1 solution molar ratio, and is representative of samples made from solution containing less than 90% AD. The image shows an ordered SAM that strongly resembles a single-component C10 SAM. The lattice spacing and domain boundaries in these samples were typical of ALK SAMs. However, these SAMs had smaller and greater numbers of domains than typically observed for single-component C10 SAMs. No AD molecules, neither in the form of ordered regions or as single molecules inserted at the SAM defects, were observed. For molar fractions of ~10% C10, a disordered SAM of both C10 and AD resulted (see Figure 4.1 B). Shown in Figure 4.1, molar fractions of less than 5% C10 resulted in ordered SAMs of AD with small clusters of C10 molecules randomly dispersed throughout the SAM. The clusters of molecules were similar to those observed in insertion studies (see Chapter 2), but were often observed in the middle of domains, rather than around defect sites of the SAMs.
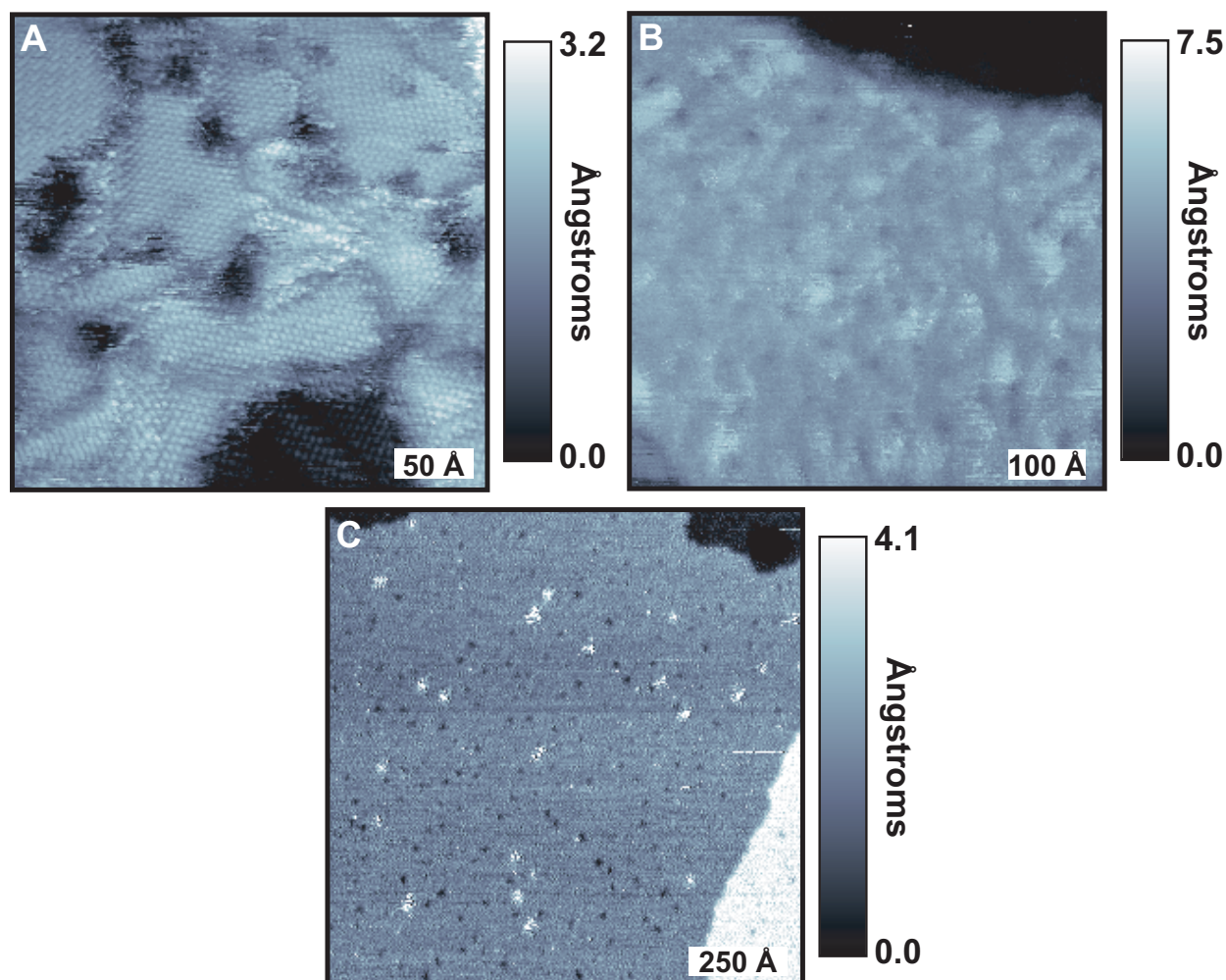
Figure 4.1. Scanning tunneling microscopy images of SAMs fabricated from solutions of varying molar ratios of 1-adamantanethiol and 1-decanethiol. A) A SAM fabricated from a 1:1 1-adamantanethiol:1-decanethiol solution molar ratio. Imaging parameters: V_{sample}: 1.0 V; I_{tunnel}: 5 pA; 300 Å × 300 Å. B) A SAM fabricated from a 9:1 1-adamantanethiol:1-decanethiol solution molar ratio. Imaging parameters: V_{sample}: 1.0 V; I_{tunnel}: 2 pA; 700 Å × 700 Å. C) A SAM fabricated from a 99:1 1-adamantanethiol:1-decanethiol solution molar ratio. Imaging parameters: V_{sample}: 1.0 V; I_{tunnel}: 7 pA; 1200 Å × 1200 Å.

These experiments demonstrated that the molar ratio of the solution is not necessarily reflected in the molar ratio on the surface. Additionally, they highlighted the differences in affinity for the surface between C10 and AD. At room temperature, below a molar percentage threshold of ~90% AD, the C10 molecules were more competitive than the AD molecules for the Au{111} surface. The following experiments further demonstrated the relative stabilities of AD SAMs compared to ALK SAMs.

4.4.2 Structure of 1-decanethiolate self-assembled monolayers inserted with 1-adamantanethiol

Figure 4.2 shows a preformed C10 SAM that was subsequently exposed to a 1 mM solution of AD for 5 min, 15 min, 30 min, and 18 h. In all cases, the AD molecules inserted sparsely around the defects of the C10 SAM, and often were not observed at all. No instances of AD molecules inserted in the middle of domains or AD molecular clusters were observed. Additionally, insertion times to 24 h still resulted in nearly pure ALK SAMs.

4.4.3 Structure of 1-admantanethiolate self-assembled monolayers displaced by n-alkanethiolates

4.4.3.1 Solution displacement

Figure 4.3 shows preformed AD SAMs that were subsequently exposed to 1 mM solutions of C10 for 10 min (Figure 4.3A and B) and C8 for 30 min (Figure 4.3C and D). Emersion of AD SAMs in a 1 mM solution of C10 for less than 1 min resulted in SAMs composed of mostly AD lattices with sporadic clusters of a few C10 molecules observed at the SAM defects. After 5 min, some of the clusters grew to patches of C10 and more clusters were observed. With longer insertion times, the C10 coverage increased radially outward from the patches (protruding regions in the images, denoted by the black arrow) until the entire AD SAM was replaced by C10 (see Chapter 5 for a discussion of the kinetics of displacement). As shown in Figure 4.3A and B, the patches were ordered domains of C10, and it was possible to resolve the lattice of both the AD and C10 portions simultaneously. From the images, both the AD and C10 lattice had the same lattice spacings as in their respective single-component SAMs. No instance of lattice compression of either lattice type was observed.
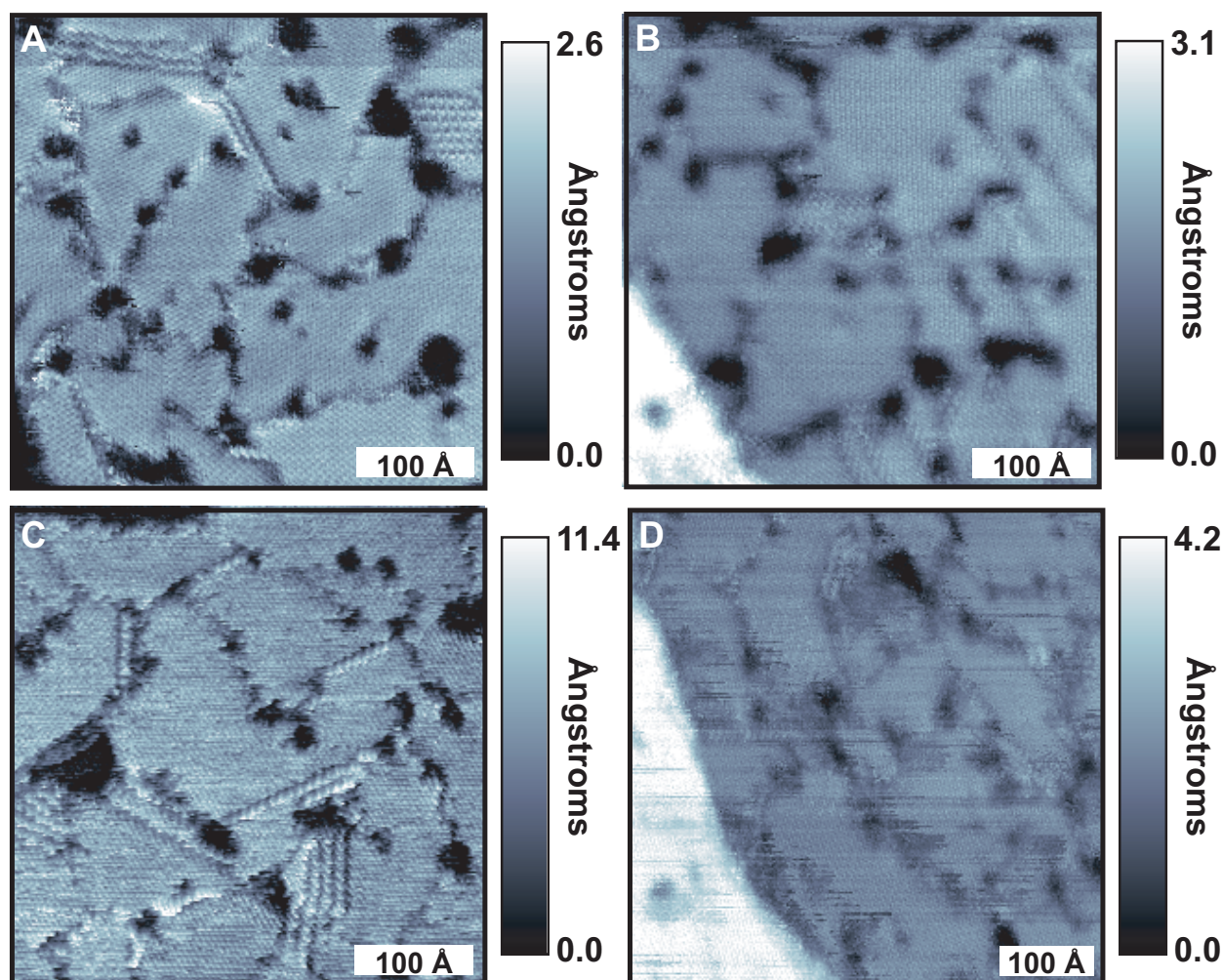
Figure 4.2. Scanning tunneling microscopy images of samples of prefabricated 1-decanethiolate SAMs inserted with 1-adamantanethiol. A) Before 1-adamantanethiol insertion. Imaging parameters: V_{sample}: 1.0 V; I_{tunnel}: 2 pA; 400 Å × 400 Å. B) Insertion for 5 min. Imaging parameters: V_{sample}: 1.0 V; I_{tunnel}: 2 pA; 400 Å × 400 Å. C) Insertion for 30 min. Imaging parameters: V_{sample}: 1.0 V; I_{tunnel}: 2 pA; 400 Å × 400 Å. D) Insertion for 18 h. Imaging parameters: V_{sample}: 1.0 V; I_{tunnel}: 2 pA; 500 Å × 500 Å.

When C8 was inserted into AD SAMs from 1 mM solutions, the same process occurred. Spotty coverage primarily around the defects was observed for low insertion times, with increased coverage extending out from the insertion points for longer time scales. However, slightly lower fractional coverages (although not dramatically different) were observed on the same time scales as for C10 insertions. Although more studies are necessary, this may correlate to the difference in hydrocarbon tail lengths and to the difference in the speed of ordering due to larger intermolecular VDW forces between the C10 relative to C8 molecules [36, 161, 163, 164].

Insertion of 1-hexanethiol (C6) into AD SAMs from 1 mM solutions also resulted in mixed SAMs with both lattices apparent. However, instead of the SAM being composed of mostly AD lattice with patches of C6 (as seen for the other ALK insertions), in addition to small C6 patches, there were also striped regions and regions of disorder (see Figure 4.4A). The regions of disorder were likely areas of mixed, disordered AD and C6 molecules. The stripes were observed in three orientations, rotated $120°$ from one another. As shown in Figures 4.4C and 4.5, each stripe set consists of a row of smaller molecules spaced 5.1 ± 0.5 Å apart (row A on Figures 4.4C), then two rows of larger molecules spaced 11 ± 1.0 Å apart (rows B and C), followed by another row of molecules that appear less protruding in the STM images (row D). The molecular spacings of row A (shown in red in Figure 4.5), and rows B and C (shown in blue in Figure 4.5) correlated well to the nearest-neighbor distance of an ALK lattice and the measured next-nearest-neighbor distance of an AD lattice (discussed in Chapter 3), respectively. Based on these spacings and the relative sizes of the two molecules, the molecules of rows A and D were assigned as C6, and the molecules in the middle rows B and C as AD. Seen most clearly in Figure 4.4B and C, the ALK molecules in row A were positioned directly across from those in row D, while the AD molecules in row B were staggered with the molecules in row C (i.e., the molecules in row B were nearest neighbors of the molecules in row C). Furthermore, the AD rows in a stripe set were staggered with respect to the equivalent rows in neighboring stripe sets. Upon closer inspection of the C6 rows, additional C6 molecules were observed. The arrow in Figure 4.4C shows the apparent pairing of two C6 molecules in row D with a third molecule in the nearest-neighbor position between rows C and D. Other C6 molecules were observed along row D as well as above row A. The extra molecules did not occur all the way along the row and did not appear uniformly spaced, nor were they uniformly the same apparent height, possibly indicating strained or varied conformations.
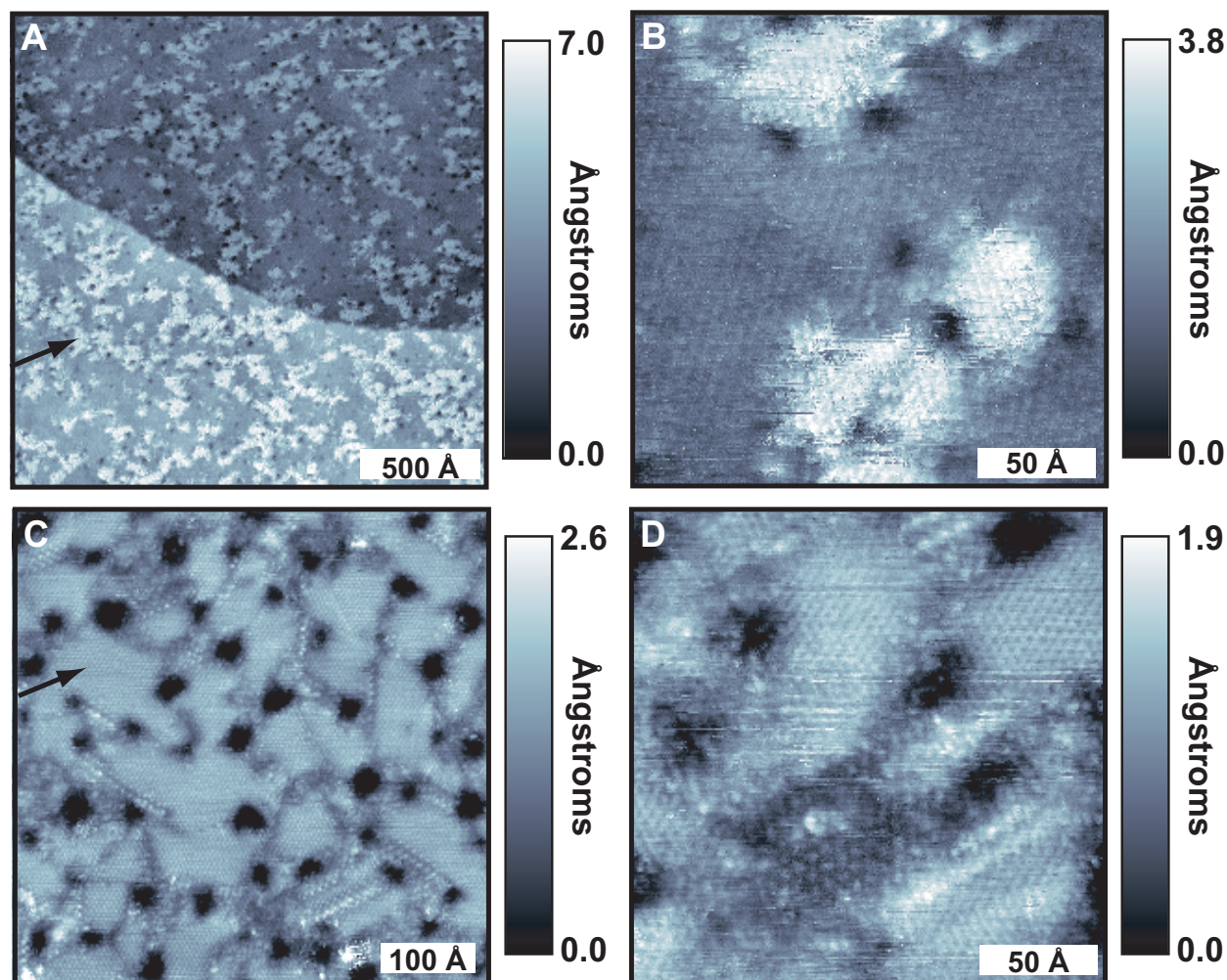
Figure 4.3. Scanning tunneling microscopy images of 1-adamantanethiolate SAMs inserted with 1-decanethiol and 1-octanethiol using two different insertion times, respectively. The arrows (A and C) indicate the protruding regions of ALK molecules. The higher resolution images (B and D) show that both the inserted ALK and the remaining 1-adamantanethiolate molecules are ordered. A) 1-Decanethiol insertion for 10 min. Imaging parameters: V_{sample}: 1.0 V; I_{tunnel}: 2 pA; 2000 Å × 2000 Å. B) 1-Decanethiol insertion for 10 min. Imaging parameters: V_{sample}: 1.0 V; I_{tunnel}: 2 pA; 200 Å × 200 Å. C) 1-Octanethiol insertion for 30 min. Imaging parameters: V_{sample}: 1.0 V; I_{tunnel}: 4 pA; 500 Å × 500 Å. D) 1-Octanethiol insertion for 30 min. Imaging parameters: V_{sample}: 1.0 V; I_{tunnel}: 2 pA; 200 Å × 200 Å.
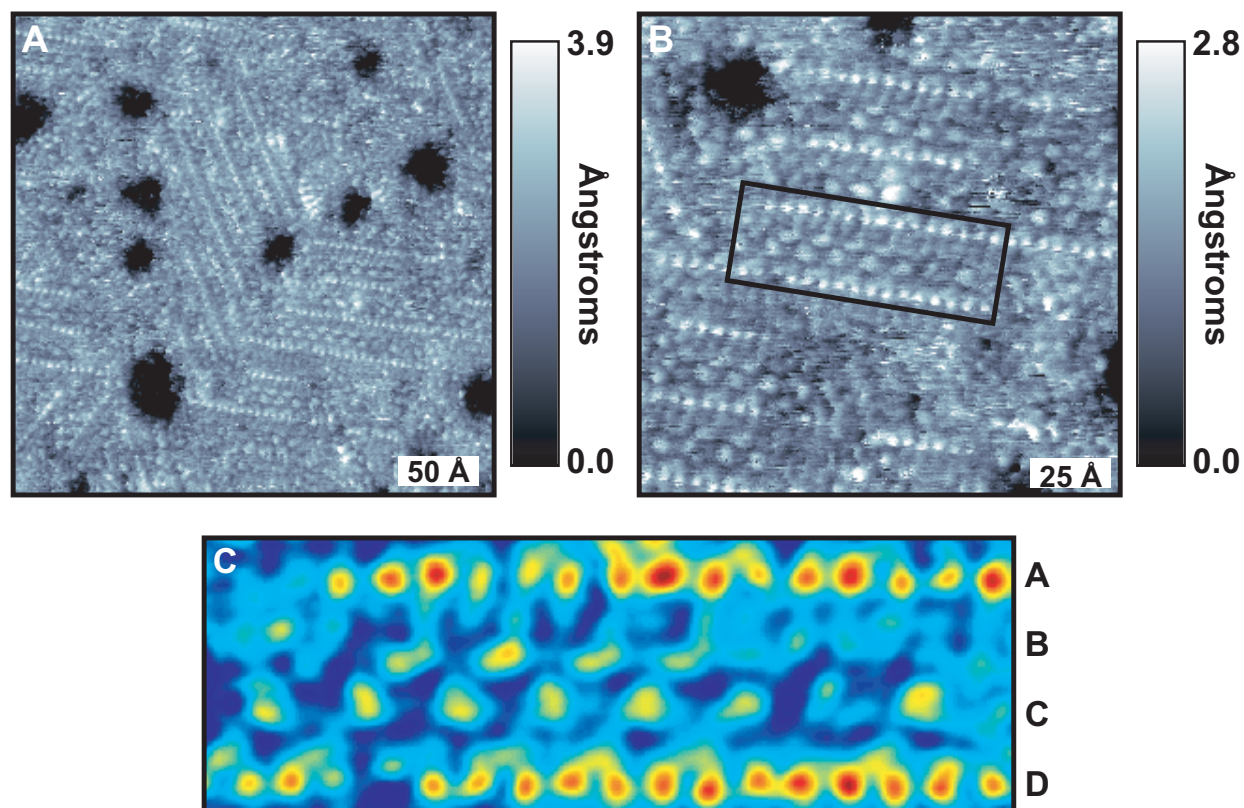
Figure 4.4. Scanning tunneling microscopy images of a 1-adamantanethiolate SAM that was inserted with 1-hexanethiol for 30 min. A) The red, blue, and yellow arrows indicate patches of ordered 1-hexanethiolate, regions of ordered 1-adamantanethiolate, and regions of disorder, respectively. Imaging parameters: V_{sample}: 1.0 V; I_{tunnel}: 4 pA; 300 Å × 300 Å. B) A higher resolution image showing several alternating stripes. Imaging parameters: V_{sample}: 1.0 V; I_{tunnel}: 4 pA; 150 Å × 150 Å. C) A detailed single stripe set with the 1-adamantanethiolate molecules zig-zagging on the interior, displayed in yellow (rows B and C), and the 1-hexanethiolate molecules lined up on the exterior, displayed in red (rows A and D). The black arrow indicates an example additional 1-hexanethiolate molecule close to the nearest-neighbor position of the 1-hexanethiolate molecules in row D. Extracted from the image in B). Imaging parameters: V_{sample}: 1.0 V; I_{tunnel}: 4 pA; 150 Å × 150 Å.

The measured distances between the C6 rows (A to D) were 22 ± 2 Å. The measured distances between C6 and the nearest AD (A to B) rows were 8 ± 2 Å and between C6 and the farthest AD rows (A to C) of the unit cell were 12 ± 2 Å. Therefore, the measured distances between two AD rows (B to C) were approximately 4 Å; this was possible because of the staggered arrangement of the molecules.

As shown in Figure 4.6, it was possible to model the striped regions using a $(\sqrt{3} \times \sqrt{3})R30°$ unit cell for C6 and a (7×7) unit cell for AD with respect to the Au{111} surface. Using the orientation of the C6 lattice with respect to a substrate step edge (not shown), it was possible to determine the orientation of the Au{111} lattice and therefore, the associated orientation of the AD lattice. Given the above observation that the rows of C6 molecules were aligned with one another and the AD molecules were not, it was determined that two C6 rows must be an even integer apart (i.e. every second, fourth, sixth etc. row), while the AD rows must be an odd integer apart (i.e. first (nearest neighbor), third etc. row). From the measured row spacings, the most likely orientation was the one shown in the model, with the C6 rows repeating every four rows and the AD rows paired and repeating every three rows. In this orientation, the C6 molecules were arranged in a $(6 \times \sqrt{3})$ unit subcell and the AD molecules formed a $(4 \times 4\sqrt{\frac{7}{3}})R30°$ unit subcell with respect to the Au{111} lattice. Both molecules together formed a $(13 \times 2\sqrt{3})$ unit cell (shown in black in Figure 4.6). The model also demonstrated that there was enough room for an extra C6 molecule near the C6 nearest neighbor positions, although not always at the preferred nearest-neighbor ALK spacing, explaining the strained appearance.

The reason for the striping of inserted C6 molecules rather than the patches observed for C8 and C10 is most likely the result of lowered van der Waals forces between C6 molecules because of the shorter alkyl tails. With decreased tail length, the direction of tilt of the ALK molecules shifts towards the nearest neighbor direction because of a balance between the amount of molecular strain and the degree of molecular packing order, both of which are influenced by the hydrocarbon tail length [180]. n-Alkanethiolate molecules with alkyl tail lengths below eight carbons demonstrate an affinity for the striped phase in single-component SAMs, especially for shorter deposition times [26, 39, 123, 181–184]. Under low surface coverage conditions, it has been demonstrated that ALK molecules form a $(p \times \sqrt{3})$ rectangular unit mesh with thee equivalent orientations [185]. Furthermore, Noh *et al.* have shown that recrystalization of a disordered C6 SAM results in a $(6 \times \sqrt{3})$ structure with alternating missing rows in the nearest-neighbor direction [26, 181].
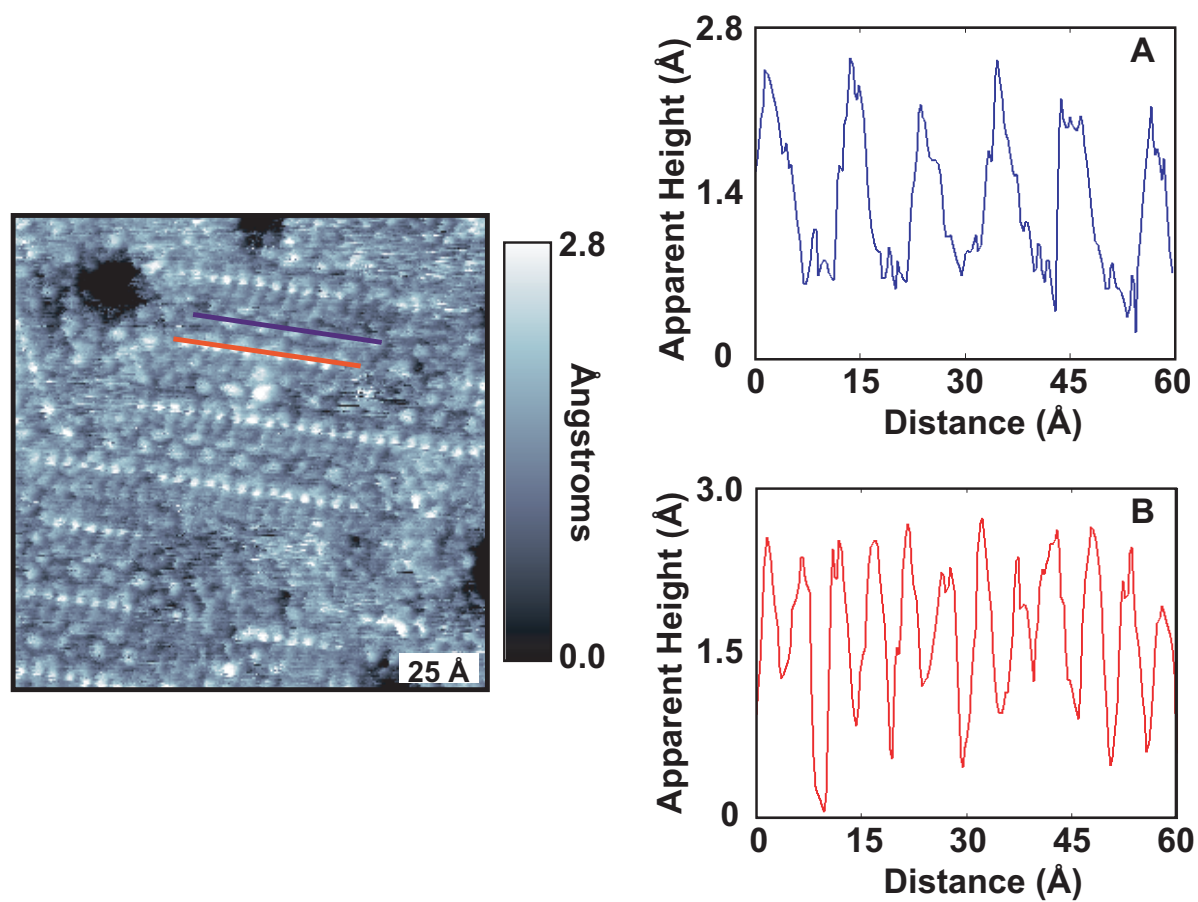
Figure 4.5. Apparent height profiles of the assigned 1-adamantanethiolate (A) and 1-hexane-thiolate (B) rows in a 1-adamantanethiolate SAM displaced with hexanethiol, shown in blue and red on the STM image, respectively.
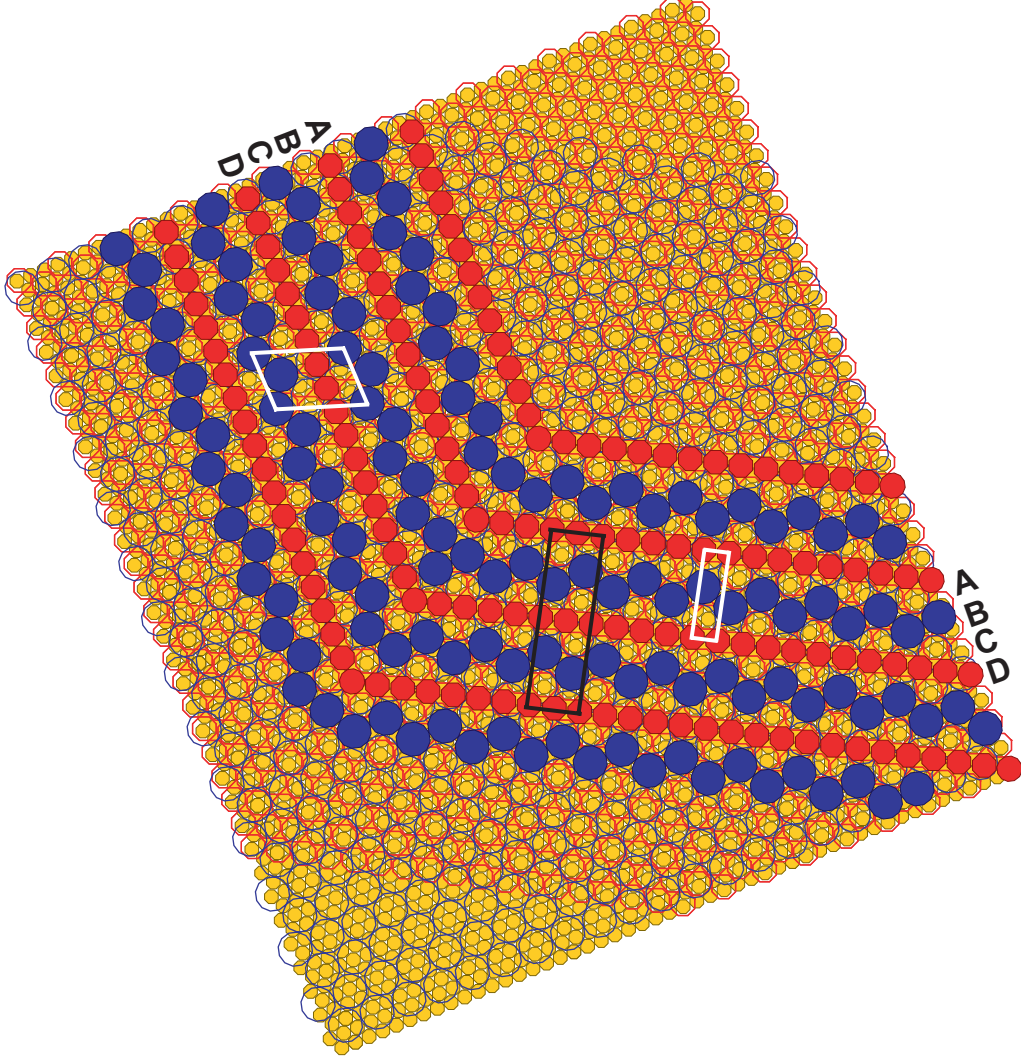
Figure 4.6. A schematic modeling the 1-adamantanethiolate and 1-hexanethiolate stripes of a 1-adamantanethiolate displaced with hexanethiol SAM on Au{111}, using a (7×7) unit cell for 1-adamantanethiolate SAM and a $(\sqrt{3} \times \sqrt{3})R30°$ unit cell for 1-hexanethiolate SAM. The white boxes indicate the $(4 \times 4\sqrt{\frac{7}{3}})R30°$(left) and $(6 \times \sqrt{3})$ (right) subunit cells of the striped 1-adamantanethiolate lattice and 1-hexanethiolate lattice, respectively. The black box indicates the $(13 \times 2\sqrt{3})$ unit cell of the 1-hexanethiolate and 1-adamantanethiolate stripes together.

It is postulated that the inserted C6 molecules assemble in linear stripes rather than growing radially in patches because of the combination of lowered van der Waals molecular interactions (related to the decreased alkyl tail length) and anisotropy created by the insertion of a tilted molecule. Because of the lowered van der Waals interactions there is no driving force for the C6 molecules to insert near existing C6 molecules, however should one insert near an existing C6 molecule the alkyl tails could tilt so as to maximize interactions creating linear anisotropy. This anisotropy would cause strain of the AD molecules in that direction, thereby enabling the next C6 molecules to displace the neighboring strained AD molecules.

4.4.3.2   Vapor displacement

Figure 4.7 shows STM images of AD SAMs that were exposed to neat C10 vapor at 78 °C for 5 min, 15 min, and 30 min. The images all show AD SAMs that were displaced completely (or nearly completely) by C10 lattice, demonstrating that the displacement process occurs without the presence of solvent. As with the samples made in solution, the longer the exposure, the more ordered the C10 SAMs became and the domains grew somewhat, but still there remained more and smaller domains than were typical for a C10 SAM assembled on bare gold.

Figure 4.8 shows AD SAMs that were exposed to neat C10 vapor at room temperature. The images also show displacement of the AD lattice for C10 lattice, but with lower coverages.

All the vapor displacement samples fabricated had higher C10 surface coverage than was observed for similar deposition times using solution deposition. Due to the mode of fabrication, it was not possible to reproducibly expose the AD SAMs to C10 vapor for less than 1 min. This indicates that the degree of displacement is sensitive to the vapor pressure (or concentration) of the displacing molecules. Further experiments are needed to verify this result, but similar results have been observed for insertion of molecules into preformed SAMs [112, 186].

4.4.4   Displacement origins

Assuming a (7×7) AD unit cell, 1.8 times more ALK molecules than AD molecules can exist in the same (defect free) area (see Chapter 3). It is expected that the enthalpic contribution from replacing the AD lattice with almost twice as many ALK molecules is a substantial driving force for displacement. A weaker S-Au bond tethering the AD molecules to the surface, from steric strain from the adamantyl headgroup, or a different chemical environment (such as oxides or disulfides,
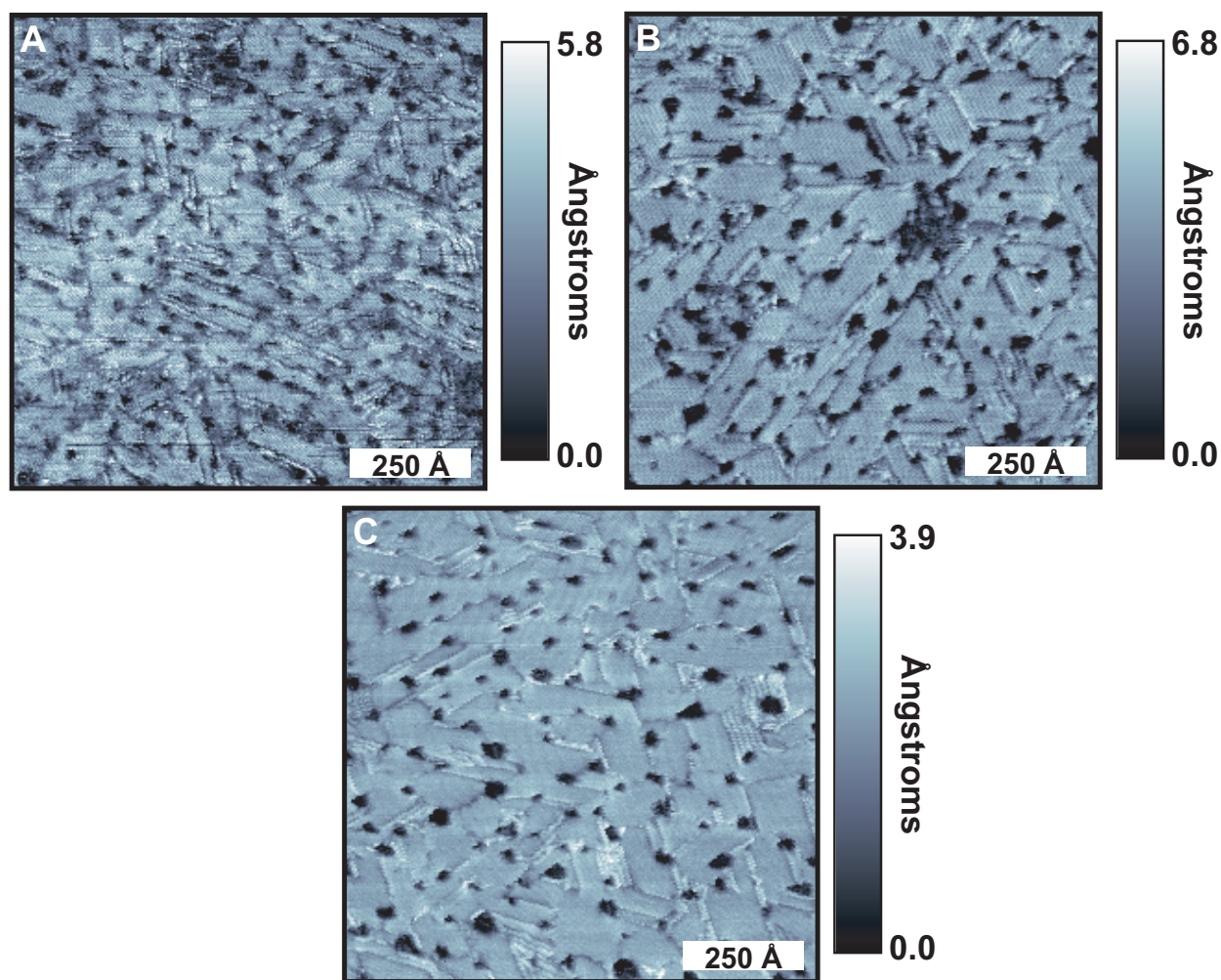
Figure 4.7. Scanning tunneling microscopy images of 1-adamantanethiolate SAMs that were vapor displaced with 1-decanethiol at 78 °C. A) Displacement for 5 min. Imaging parameters: V_{sample}: 1.0 V; I_{tunnel}: 2 pA; 1000 Å × 1000 Å. B) Displacement for 15 min. Imaging parameters: V_{sample}: 1.0 V; I_{tunnel}: 2 pA; 1000 Å × 1000 Å. C) Displacement for 30 min. Imaging parameters: V_{sample}: 1.0 V; I_{tunnel}: 2 pA; 1000 Å × 1000 Å.
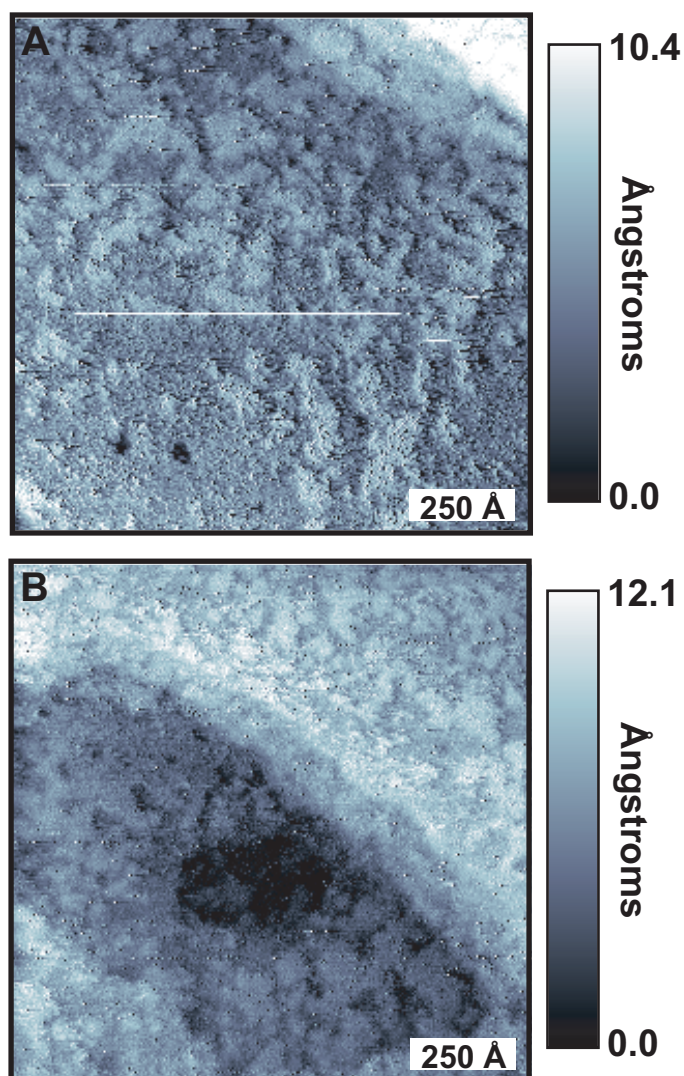
Figure 4.8. Scanning tunneling microscopy images of 1-adamantanethiolate SAMs that were vapor displaced with 1-decanethiol at room temperature. A) Displacement for 5 min. Imaging parameters: V_{sample}: 1.0 V; I_{tunnel}: 2 pA; 1500 Å × 1500 Å. B) Displacement for 15 min. Imaging parameters: V_{sample}: 1.0 V; I_{tunnel}: 2 pA; 1500 Å × 1500 Å.

either present in the starting materials or formed during deposition, and overlooked in the analysis in Chapter 3) would increase the energy gained and the likelihood of displacement.

However, other possible contributions include the additional enthalpic contribution from the increased VDW interactions in the ALK SAM. As discussed in Chapter 1, SAMs of ALK are stabilized considerably by the presence of intermolecular VDW forces and tilt so as to maximize these chain-chain attractive interactions. It is expected that the AD SAMs have substantially lower VDW forces than those that strengthen and order ALK SAMs because of the larger distance between the molecules, the limited intermolecular contact, and the insignificant conformational relaxation. Also, due to the length of the thiolate tether to the gold and the bulky shape of the molecule, it is unlikely that the AD molecules could be significantly tilted from normal to the gold surface without straining the thiolate-gold bond.

Further, there may be solvation contributions. The ALK molecules are more hydrophobic than the AD molecules, and for every AD molecule added to the solution, almost two ALK molecules are removed. However, considering that displacement occurs without solvent presence, this is not believed to be a major factor.

To test the viability of the instability of the AD SAMs resulting from the above contributions, XPS and electrochemical deposition were used to probe the chemical environment of the AD bond to the Au{111} surface, and to investigate the relative intermolecular interaction strengths of the AD lattice with respect to the ALK lattices, respectively.

4.4.4.1   X-ray photoelectron spectroscopy of displaced self-assembled monolayers

Figure 4.9A shows XPS survey spectra of a single-component AD SAM (the C12 and inserted SAMs have similar survey spectra) showing the relative intensities of each atomic component present in the SAM. The majority of the peaks are from the Au{111} substrate, but O 1s, C 1s and S 2p peaks are also observed. Table 4.1 gives the atomic concentrations of the O 1s, C 1s, S 2p and Au 4f peaks for single-component AD and C12 SAMs and C12 inserted AD SAMs for three different insertion times, and several atomic concentration ratios.

X-ray photoelectron spectroscopy analysis showed oxygen presence in all the SAMs (see Table 4.1 for the oxygen concentration in each SAM). The measured energy of the O 1s peak, with a binding energy of 532.8 eV, suggests the presence of water ($\sim$533.0 eV [187, 188]). The O 1s was greatly reduced in all the samples made with dry hexanes in an oxygen-free environment.
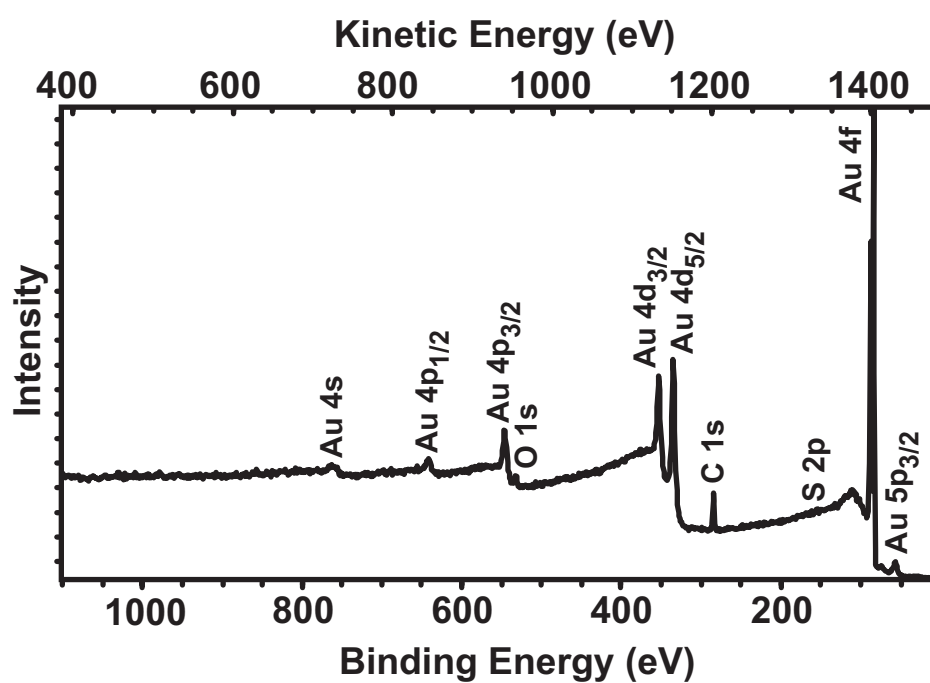
Figure 4.9.   An XPS survey spectra of a 1-admantanethiolate SAM.

Therefore, this peak is attributed to water from solvent trapped in the monolayer or from exposure to ambient humidity.

The existence of gold oxide would both shift the O 1s peak to a lower energy of 530 $\pm$ 0.2 eV, and simultaneously shift the Au 4f peaks to a higher energy with the Au $4f_{7/2}$ positioned at $\sim$86 eV [189–192]. These shifts would also be accompanied by the asymmetric broadening of the Au 4f peaks [190,192]. None of these shifts nor broadening of either the Au 4f or O 1s peaks were observed here; therefore, surface oxide contamination was not considered to be a contributing factor to displacement.

The C 1s peaks (shown in Figure 4.10) show a shift in energy and a difference in peak FWHM between each type of SAM. For the C12 SAM (Figure 4.10 E), the C 1s peak can be fit by two GL line shapes; a small peak centered around 286.5 eV and a much larger intensity peak at 284.9 $\pm$ 0.1 eV. The position of the smaller, higher energy peak suggests the presence of a C-O functionality. When the SAMs were prepared using hexanes instead of ethanol the smaller peak was not observed, and was therefore assumed to have been a result of trace ethanol molecules trapped in the monolayer. However, the necessary carbon contribution to the C 1s peak to account for all the observed oxygen to be considered a C-O species greatly exceeds that observed at 286.5 eV, further suggesting the presence of water.

The larger, lower energy peak is attributed to the hydrocarbon tail of the C12 molecules and is in agreement with values found in the literature [146,193,194].

Shown in Figure 4.10A and Table 4.2, the C 1s spectrum for the AD SAM was observed shifted to lower energy with respect to the C12 SAM. The peak was also asymmetric, with a wider tail on the higher binding energy side. The C 1s peak was therefore fit with three GL line shapes. The highest energy peak at 286.5 eV was attributed to trapped solvent, as above. The other two peaks, a larger peak with a binding energy of 284.4 $\pm$ 0.1 eV and a smaller peak with a binding energy of 285.1 $\pm$ 0.1 eV, had an area ratio of approximately 9:1. The difference in energy between the two peaks is likely a result of the electron distribution through the carbon cage of the AD molecules. The presence of the S atom changes the electron configuration of the alpha C, causing the observed shift in binding energy. The overall shift to lower energy of both of the AD C 1s peaks in comparison to the ALK C 1s peak is likely because of the increase in C-C bonding in the adamantane compared to the mehtylene units of the alkyl chain in the ALK molecules. However, this shift is substantial compared to that usually seen (0.1-0.3 eV [188]), and is shifted closer to the

	Atomic Concentration (%)				Atomic Ratios		
	C 1s	S 2p	O 1s	Au 4f	$\frac{\text{C 1s}}{\text{S 2p}}$	$\frac{\text{C 1s}}{\text{Au 4f}}$	$\frac{\text{S 2p}}{\text{Au 4f}}$
AD	27.7	1.8	2.2	68.3	15.6	0.4	0.026
AD/C12 20 min	26.9	1.9	0.4	70.7	14.0	0.4	0.027
AD/C12 40 min	31.5	1.9	5.4	61.2	16.7	0.5	0.031
AD/C12 120 min	37.1	2.7	4.2	56.0	13.9	0.7	0.048
C12	40.0	2.7	0.8	56.5	14.7	0.7	0.048

Table 4.1. Atomic concentrations measured from single-component 1-adamantanethiolate and 1-dodecanethiolate SAMs, and 1-admantanethiolate SAMs displaced with 1-dodecanethiol for 20 min, 40 min and 120 min.

C 1s binding energies found for highly ordered pyrolytic graphite at 284.4 eV [188], and diamond at 284.0 eV [188].

The C 1s spectra for the C12 inserted AD SAMs (Figure 4.10B though D) were all shifted towards higher binding energy with respect to the AD SAMs. The longer the insertion time, the closer in energy these C 1s peaks were to the energy observed for the C12 SAMs. The C 1s FWHM for the inserted SAMs are larger than the single-component SAMs (see Table 4.2), indicating the presence of both lattice types. Each inserted SAM spectrum was fit with four GL line shapes to account for a combination of C 1s contributions from both molecular lattice types. From the fits, the percentage of each type of molecule was estimated and is given in Table 4.2. As expected, for longer insertion times more AD displacement was observed (also observed by the C 1s:Au 4f and S 2p:Au 4f concentration ratios in Table 4.1).

Figure 4.11 shows the S 2p region of the XPS spectra for each SAM. The increased concentration of sulfur (see the S 2p atomic concentration and the S 2p:Au 4f concentration ratios in Table 4.1) for the C12 and inserted SAMs compared to the AD SAMs is expected due to the differences in molecule packing densities for the AD and C12 molecular lattice. In spectra for both the AD SAMs and the displaced SAMs, there was no observable shift in binding energy with respect to the C12 spectra, for either of the S 2p peaks caused by a change in the chemical environment of the sulfur-gold bond from the presence of SAM contaminants. For all the SAMs, the binding energies of the S $2p_{3/2}$ peaks were too low to account for the presence of sulfinates (>166 eV [195, 196]), sulfonates (>168 eV [195–198]), or disulfides (163.2 ± 0.2 eV [196, 199–201]). Additionally, these binding energies do not suggest the presence of unbound thiols (165 eV [202]) nor unbound disulfides (164 eV [202]).

From the STM images, the possibility that the AD displacement was caused by scission of the adamantyl from the sulfur tether seems unlikely. Besides the AD lattice, the only other species observed by STM protrudes from the existing monolayer with the same packing structure as that of an ALK SAM. Although the STM measurements are a convolution of both topography and conductance, the measured apparent height difference of 2.6 ± 0.5 Å seems more likely to be due to the difference between AD and C12 than the difference in conductance between AD and reorganized, cleaved sulfur atoms. Futhermore, the XPS data do not reflect the presence of atomic sulfur (the S $2p_{3/2}$ peak at a binding energy of 161 eV [200, 203–205]).

	C 1s Binding Energy (eV)	C 1s FWHM (eV)	Molecular Species (%)	
			AD	**C12**
AD	284.2	1.22	100	0
AD/C12 20 min	284.5	1.15	68	32
AD/C12 40 min	284.4	1.45	44	56
AD/C12 120 min	284.9	1.19	1	99
C12	284.9	1.11	0	100

Table 4.2. On the left are the binding energies and the FWHM of the C 1s peaks in XPS spectra of single-component 1-adamantanethiolate and 1-dodecanethiolate SAMs, and 1-adamantanethiolate SAMs inserted with 1-dodecanethiol for 20 min, 40 min and 120 min. On the right are percentages of each lattice type calculated from the Gaussian-Lorentzian fits discussed in the text.
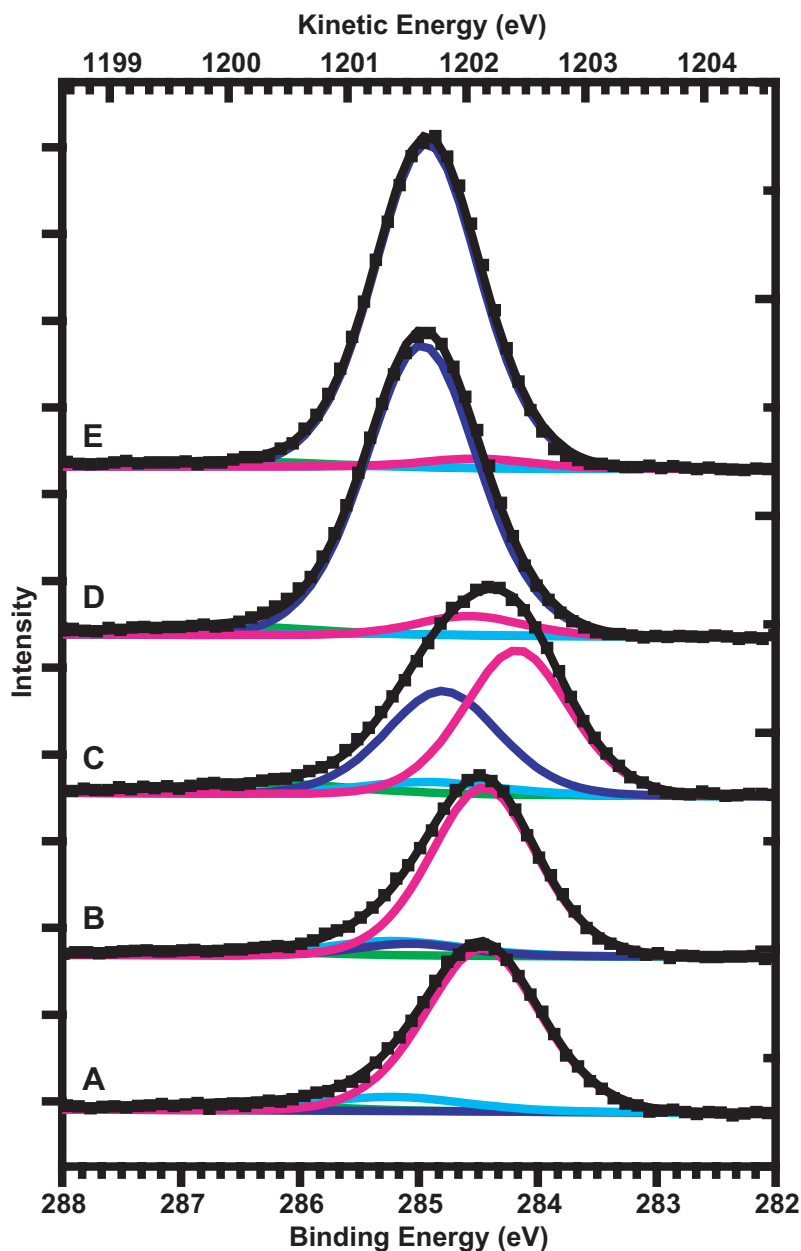
Figure 4.10.   The C 1s region of XPS spectra of A) a 1-adamantanethiolate SAM B) a 1-adaman-tanethiolate SAM displaced with C12 for 20 min, C) a 1-adamantanethiolate SAM displaced with 1-dodecanethiol for 40 min, D) a 1-adamantanethiolate SAM displaced with 1-dodecanethiol for 120 min, and E) a 1-dodecanethiolate SAM. Each spectrum was fitted with Gaussian-Lorentzian line shapes for contributions from binding energies centered around 284.3 eV (pink), 284.9 eV (cyan), 285.2 eV (green) and 286.5 eV (blue), discussed in the text. Note: the spectra and the fits are offset for clarity.
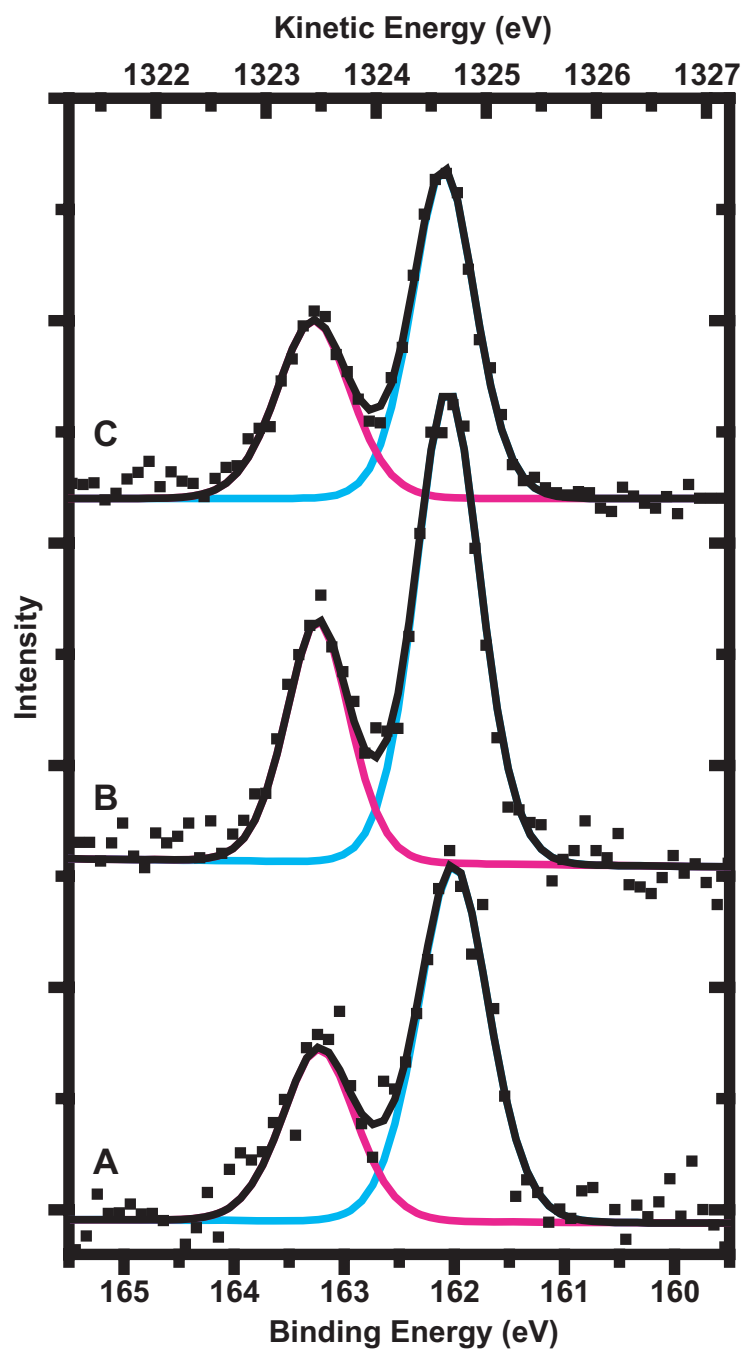
Figure 4.11. The S 2p region of XPS spectra of A) a 1-adamantanethiolate SAM, B) a 1-adaman-tanethiolate SAM displaced with 1-dodecanethiol for 40 min, and C) a 1-dodecanethiolate SAM. Each spectrum was fitted with Gaussian-Lorentzian line shapes for contributions from binding energies centered around 162.0 eV (pink), 163.2 eV (cyan), for S $2p_{1/2}$ and S $2p_{3/2}$ respectively, with a fixed area ratio of 2:1 and a fixed energy of 1.18 eV between them. Note: the spectra and the fits are offset for clarity.

Together, the XPS studies indicated that the S-Au chemical environment was equivalent in all types of SAMs studied, including the displaced SAMs. No oxides nor disulfides were present to weaken this bond. Further there was no indication that the S-Au bond was strained in the AD SAMs.

4.4.4.2 Electrochemical desorption of displaced self-assembled monolayers

From the displacement studies using C6, we deduced that VDW interactions are involved in the displacement process. The electrochemical desorption experiments of single-component AD SAMs, discussed in the last chapter (Chapter 3), demonstrated that there were likely decreased VDW interactions between AD molecules in AD SAMs, compared to C12 in C12 SAMs. Figure 4.12 shows a representative voltammogram of a two-component SAM fabricated by the displacement of a AD SAM with C12. The two distinct cathodic peaks in the voltammogram indicate that there are separated domains of two lattice types, in agreement with the STM images of displacement using C10 and C8. [155, 206, 207]. The more positive cathodic peak, -903 $\pm$ 21 mV, is attributed to the AD lattice, and the less positive cathodic peak, -1054 $\pm$ 18 mV, is attributed to the C12 lattice type. Compared to the values given in Chapter 3, both cathodic peaks are shifted to more positive potentials. The C12 cathodic peak is shifted from -1113 $\pm$ 9 mV for a single component SAM compared to -1054 $\pm$ 18 mV for the displaced SAM, and the AD cathodic peak is shifted from -996 $\pm$ 4 mV for a single component SAM compared to -903 $\pm$ 21 mV for the displaced SAM. The positive shift in E_p for both lattice types indicates that ion flux to the Au{111} electrode surface through the different lattice regions is easier in the displaced SAMs than in the single component SAMs. This difference in ion flux implies that the displacement of AD molecules by C12 molecules disrupts both lattice types of the monolayer. It further suggests that there is very little intermolecular interaction between the AD and C12 regions [151]. These results are in contrast to previous work that studied separated SAMs of 3-mercaptopropionic acid and 1-hexadecanethiolate, and observed a shift in the E_p of the two distinct cathodic peaks towards each other, indicating that there were some intermolecular interactions between the domains of these two more similar molecules [155, 207, 208].

These results further demonstrate that VDW interactions are important factors in displacement. It is proposed that the enthalpic contribution from the exchange of the AD for ALK molecules, together with the enthalpic energy gleaned from the difference in VDW interactions
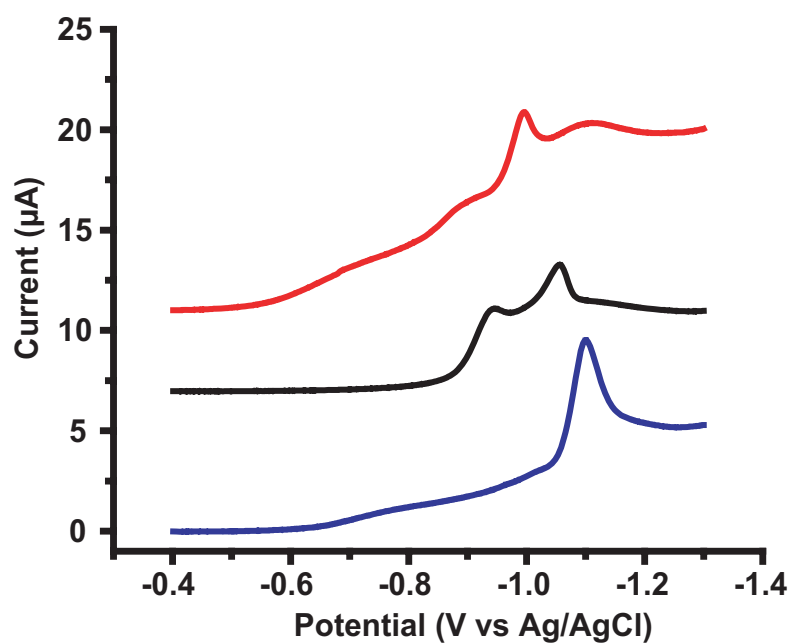
Figure 4.12. A representative voltammogram (black) of a 1-admantanethiolate SAM that was displaced with 1-dodecanethiol for 30 min showing that both peaks are shifted to more positive potential. Voltammograms of 1-admantanethiolate (red) and 1-dodecanethiolate (blue) SAMs are shown for reference. Sweep parameters: forward and backward from -200 mV to -1500 mV at 20 mV/s. Note: only the forward sweep (the cathodic peak) is shown and the voltammograms are offset for clarity.

between the AD and ALK molecules, mediate the displacement process. Which enthalpic energy contribution is more dominant depends on the difference in enthalpies between removing one AD molecule from and adsorbing one ALK molecule to the Au {111} surface, which could be determined using molecular modeling or temperature-programmed desorption experiments. Whether the displacement process occurs is then determined by the free energy (ΔG_{disp}):

$$\Delta G_{disp} = ((\Delta H_{\text{AD}_{desorp}} + \Delta H_{\text{ALK}_{adsorp}}) + (\Delta H_{\text{AD}_{VDW}} + \Delta H_{\text{ALK}_{VDW}}))$$
$$- \text{T}(\Delta \text{S}_{\text{AD}_{\text{desorp}}} + \Delta \text{S}_{\text{ALK}_{\text{adsorp}}}), \quad (4.3)$$

where $\Delta H_{\text{AD}_{desorp}}$ and $\Delta H_{\text{ALK}_{adsorp}}$ are the enthalpy terms for AD desorption and ALK adsorption, respectively, and are influenced by the surface-headgroup bond, the orientation of the molecule, the presence of other surface species, and the surface-tailgroup interactions. $\Delta H_{\text{AD}_{VDW}}$ and $\Delta H_{\text{ALK}_{VDW}}$ are the enthalpy terms for the difference in VDW interactions between the AD and ALK SAM, and are influenced by the functional group present on the molecule, the distance between the molecules, the molecule conformation, and the presence of other like molecules. $\Delta S_{\text{AD}_{desorp}}$ and $\Delta S_{\text{ALK}_{adsorp}}$ are the entropy terms for AD desorption and ALK desorption, respectively. Regardless of the sign of the entropy terms, it is assumed that they are small, because the number of molecules in the system far exceeds the number that is exchanging on the surface. Using this equation, as long as the combined enthalpic contributions are favorable, the displacement process is spontaneous. This explains why ALK displaces AD, but the opposite does not occur. Furthermore, a molecule displaced by its own kind would have a ΔG value of zero, and would therefore be in equilibrium.

4.5   Conclusions

We observed that AD SAMs were displaced by exposure to ALK molecules from both the solution and vapor phases. This displacement resulted in ordered regions of both the inserted ALK lattice and the remaining AD lattice. Using XPS, we have shown that the displacement is not a result of a weakened S-Au surface bond in the AD SAMs, and that there is no chemical difference in the environment around these bonds. Alternatively, verified by electrochemical desporption experiments, we account for the displacement as a combination of energetically favorable contributions

from the increase in S-Au bond density and increase in VDW interactions in the displaced SAMs. These conclusions suggest that displaceability is not unique to AD SAMs. Other SAMs could be created with either relatively less dense molecular lattices, or lowered VDW strengths, that would be labile also.

Chapter 5

Dynamics of Solution Displacement of 1-Adamantanethiolate Self-Assembled Monolayers

5.1 Introduction

Applications of the displacement of AD or similar molecules will require precise control of the displacement process. The dynamics of the AD displacement process must be understood at the molecular level in order to control the degree of displacement accurately. The previous chapter explored *why* displacement occurs; this chapter discusses *how* displacement occurs. Here, we use three techniques – STM, FTIR and electrochemical desorption – in parallel, to study AD displacement by C12 on both molecular and ensemble scales, to determine the displacement mechanism, to estimate the rate of displacement and to establish what experimental parameters influence the displacement kinetics.

5.2 Background

Most kinetic studies of SAM growth have been limited to the model systems of ALK SAMs on Au{111} grown from ethanolic or hexane solutions in the μM to mM range. Despite the control of environmental parameters afforded by studies of growth from the gas phase, solution-phase studies are more common because of the simple and inexpensive nature of the experimental setup. Varying results, such as different rate constants or delays in the onset of growth, have been reported and are attributed to the cleanliness and defect density of the substrates (due to differing cleaning procedures) or purity of the solutions [209].

Most studies observe some variation of logarithmic growth with deposition time and a number of approaches have been used to fit the uptake curves. The simplest, Langmuir growth, relates the growth rate to the number of available sites [137, 209–211],

$$Bc = \frac{\Theta}{1 - \Theta} \tag{5.1}$$

where Θ is the surface coverage (the number of filled sites divided by the number of total sites), c is the adsorbate concentration, and B is a constant. The surface coverage as a function of time, t, is then,

$$\Theta = 1 - e^{-Bct}. \tag{5.2}$$

This isotherm has been used extensively because of its simplicity. However, it makes a few notable assumptions [211, 212]: 1) all surface sites are equivalent; 2) a surface site is filled by reaction with one molecule; molecules cannot adsorb in the regions around a site, nor can multilayers form; 3) there is no surface reconstruction; the total number of sites remains unchanged during the reaction; 4) the molecules do not interact laterally or vertically; there are no lateral intermolecular interactions nor are there any changes in sticking coefficients across the surface; 5) the degrees of freedom of the molecules are not modified by adsorption to the substrate; and 6) the gas phase is ideal, governing the dependence on temperature, pressure and concentration; there are no solvation effects.

Remarkably, despite all the above assumptions, which do not apply to any real system, Langmuir isotherms fit the uptake curves fairly well. However, several modifications have been made to account for the assumptions, and to fit kinetic data more accurately [209–211].

To account for a delay in nucleation time, t_c, which is often observed, Equation 5.2 becomes

$$\Theta = 1 - e^{-Bc(t-t_c)}. \tag{5.3}$$

A diffusion-limited Langmuir adsorption model was proposed to account for some solvent effects [213, 214], and is given by

$$\Theta = 1 - e^{-B'ct^{\frac{1}{2}}}, \tag{5.4}$$

where B' is proportional to the diffusion constant. Furthermore, to account for intermolecular interactions other deviations have been proposed. Because sensitivity to different processes is dependent on the measurement technique, it is difficult to assess which model is best. To account for different sticking coefficients on occupied and unoccupied areas (i.e. islanding), a sticking coefficient term, k, was added [213]. Assuming that the desorption rate from a precursor state is higher than

the chemisorption rate [209–211], the equation becomes,

$$\Theta = \frac{1e^{(-B'c(1+k)t)}}{1 + ke^{(-B'c(1+k)t)}}. \tag{5.5}$$

A decrease of the adsorption rate with increasing ALK hydrocarbon chain length has been observed [213, 214], indicating a dependence of the growth kinetics on lateral intermolecular interactions. To account for lateral intermolecular interactions during the adsorption process, the Tempkin isotherm,

$$Bc = e^{\Theta g'} \tag{5.6}$$

when the interactions are repulsive, and Frumkin-Frowler-Guggenheim isotherm,

$$Bc = \frac{\Theta}{1 - \Theta} e^{-\Theta g'} \tag{5.7}$$

when the interactions are attractive, were created [137, 210–212]. In each case,

$$g' = \frac{2g\Gamma}{RT}, \tag{5.8}$$

where g is the interaction parameter, and is positive for attractive interactions and negative for repulsive interactions. The terms Γ, R and T are the number of adsorbed molecules at the point of substrate saturation, the gas constant and temperature, respectively. The relation of the Frumkin-Frowler-Guggenheim isotherm with time is not algebraically solvable, and must be treated numerically. However, as g approaches zero, the Frumkin-Frowler-Guggenheim isotherm becomes the Langmuir isotherm.

As the sophistication of the surface model increases, the complexity of the kinetic equations quickly rises. The above equations all assess the environment of an adsorbed molecule first, and then consider the kinetics on the basis of the average environment. This only approximates the local environment of a given adsorbate. Thus, these equations are all limited by their assumptions of the surface environment. Monte Carlo simulations have been used to treat each adsorbate site independently and model more complex adsorption systems [210, 215–217].

Despite the differences in the uptake curves or in the modeling of them, it is generally agreed that ALK adsorption during SAM formation occurs in three major steps. Even for very low (μM) concentrations, the first step results in between 80 and 90% coverage, and occurs within the first

few min (40% coverage has been observed in as little as 500 ms [218]). This step is associated with chemisorption of the S to Au substrate along with the release of H_2. The second step proceeds more slowly (on the order of 3 to 4 times slower than the first step [209]) and is associated with straightening and ordering of the internal methylene groups on the hydrocarbon chains. This step allows for the adsorption of ALK molecules to most of the remaining sites. The final step is the slowest, has been reported to be more than 50 times slower than the first step [209], and is associated with the reorganization of the terminal groups.

5.3 Experimental Procedure

5.3.1 Sample preparation

All the samples described below were AD SAMs that were displaced by exposure to 1 mM C12 solutions. The synthesis of AD and the fabrication of AD SAMs are described in Chapter 3. All the samples were fabricated using quartered, small (1.0 cm by 1.1 cm) commercially available Au{111} on mica substrates, except for the IR studies, which used whole large (2.0 cm by 1.6 cm) substrates (Molecular Imaging, Tempe, AZ). The samples were made by first fabricating single-component AD SAMs on bare Au{111} by deposition from 10 mM solutions for 24 h, then immersing the samples in 1 mM solutions of C12 for the specified displacement time period. Then, the samples were removed from solution, rinsed and dried with nitrogen twice, and analyzed. A new sample was made for each measurement of displacement time.

5.3.2 Experimental analysis

The STM analysis was described in Chapters 2 and 3. The electrochemical desportion and FTIR analyses are described in Chapter 3.

The fractional coverage of each sample was determined by each technique independently. For STM, the fractional coverage (Θ_{STM}) was calculated from representative images of each sample using Matlab (MathWorks, Natick, MA). Binary images were generated from the STM images using a user-defined threshold based on the apparent height of the molecular features. The pixel fraction of the image covered by each apparent height type (A_{C12}, A_{AD}) was calculated and then

divided by the pixel total of the image, minus the defects (A_{image}),

$$\Theta_{STM/C12} = \frac{A_{C12}}{A_{Image}} \tag{5.9}$$

and

$$\Theta_{STM/AD} = \frac{A_{AD}}{A_{Image}}. \tag{5.10}$$

Defects in the substrates were not included because determination of the lattice types inside the defects was inconclusive from the images. All the coverages were calculated from images 1000 Å × 1000 Å in size that included only one substrate terrace. Single terraces were chosen because it simplified the thresholding, however, we note that the analysis is biased against areas with step edges and major substrate defects.

For FTIR, the fractional coverage (Θ_{FTIR}) of C12 was determined from FTIR spectra by taking the ratio of the area under the 2878 cm^{-1} (CH$_3$ stretch) peak for the displaced sample (A_{C12}) to the same sample after it had undergone full displacement ($A_{totalC12}$),

$$\Theta_{FTIR/C12} = \frac{A_{C12}}{A_{totalC12}}. \tag{5.11}$$

The fully displaced SAM was immersed in C12 solution for at least 24 h and was used instead of a single-component C12 SAM to account for the increase in SAM defects in displaced SAMs. Using D12 for displacement, the AD fraction was determined from the ratio of the area under the 2911 cm^{-1} (CH stretch) peak of the displaced sample (A_{AD}) to the initial AD SAM ($A_{totalAD}$),

$$\Theta_{FTIR/AD} = \frac{A_{AD}}{A_{totalAD}}. \tag{5.12}$$

Due to the difference in experimental procedures because of spectral overlap in the C-H stretch region, the fractional coverages of AD and C12 could not be determined simultaneously, and together may not precisely total 1.

For electrochemical desorption studies, the molecular fraction (X_{Echem}, which, as discussed below, is *not* the same as the fractional coverage) of C12 was calculated by dividing the average I$_p$ of the C12 lattice (I_{C12}) by the sum of the average I$_p$ of the C12 lattice and the average I$_p$ of the

AD lattice (I_{AD}). The AD fraction was calculated similarly, giving

$$X_{Echem/C12} = \frac{I_{C12}}{I_{C12} + I_{AD}} \qquad (5.13)$$

and

$$X_{Echem/AD} = \frac{I_{AD}}{I_{C12} + I_{AD}}. \qquad (5.14)$$

It is important to note that, using these calculations, STM measured the fraction of the area taken up by one type of molecule compared to the total available area. Fourier transform infrared spectrocopy measured the number of molecules of one type compared to the total possible number of molecules in a SAM of that same type. These calculations are equivalent and should yield similar results. On the other hand, electrochemical desorption measures the number of molecules of one type compared to the total number of molecules present. Because of the difference in lattice spacing between AD and C12 SAMs, the fraction of molecules of one type does not necessarily equal the fraction of the surface that is occupied by that molecule type. Therefore, the equations must be revised to account for this difference. To convert between the fractional coverage from STM and FTIR measurements, and molecular fraction from electrochemical desorption measurements a conversion factor was used, giving the fractional coverage for electrochemical desorption (Θ_{Echem}). As discussed in Chapter 4, in a defect-free area, for the same unit area, there are 1.81 more C12 molecules than AD molecules. Therefore, equations 5.13 and 5.14 become

$$\Theta_{Echem/C12} = \frac{(I_{C12} * 1)}{(I_{C12} * 1) + (I_{AD} * 1.81)} \qquad (5.15)$$

and

$$\Theta_{Echem/AD} = \frac{(I_{AD} * 1.81)}{(I_{C12} * 1) + (I_{AD} * 1.81)}. \qquad (5.16)$$

5.4 Results and Discussion

5.4.1 Displacement process

As discussed in the previous chapter, given sufficient differences in VDW forces and molecular lattice density, ALK molecules displace AD molecules on the surface. Insertion of ALK with 7 or more methylene units (although displacement with C7 has not been performed) results in small clusters of ALK molecules around the defect sites that upon further exposure grow into islands and
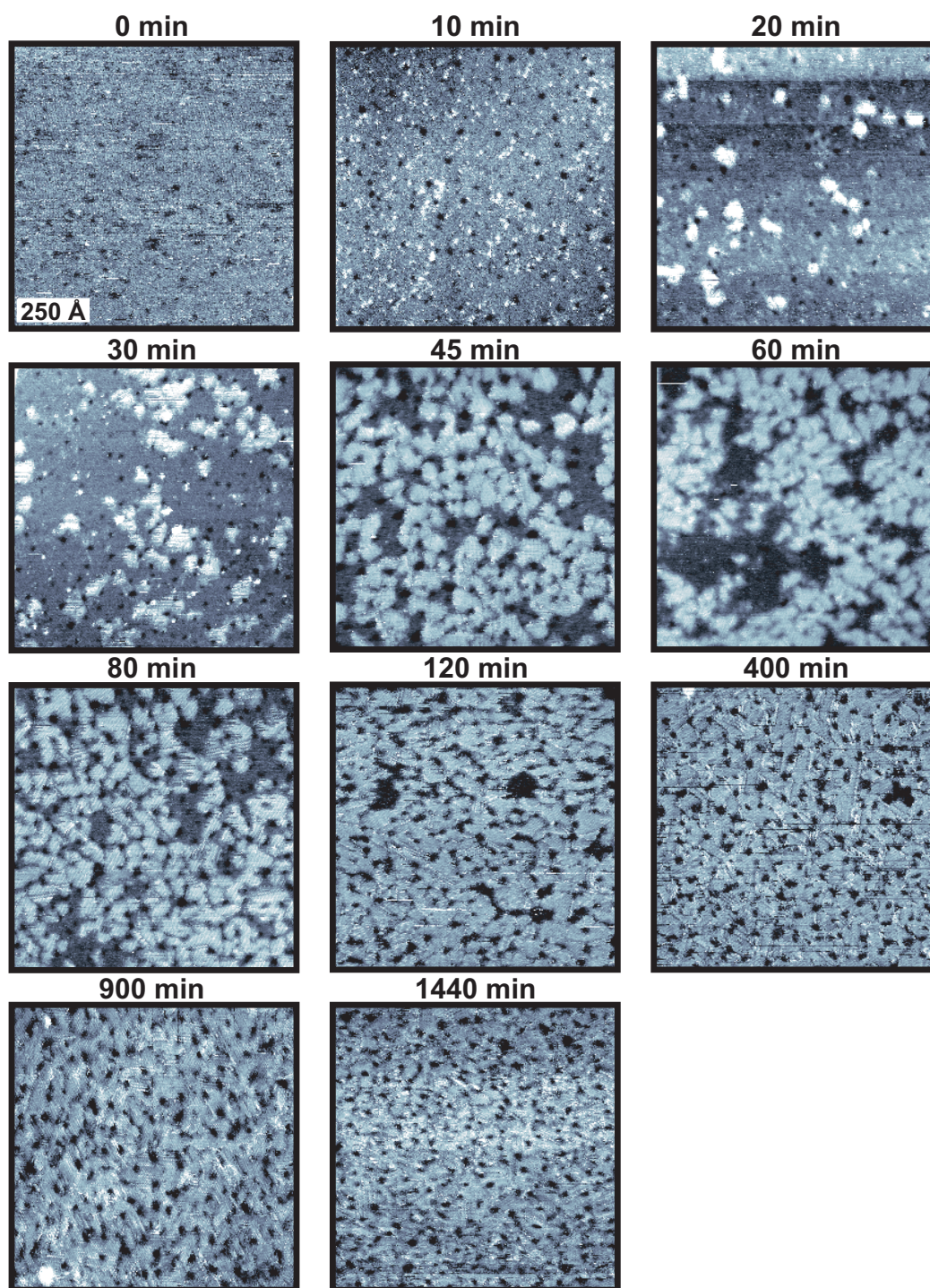
Figure 5.1. Scanning tunneling microscopy images of 1-adamantanethiolate SAMs displaced in 1-dodecanethiol solution for displacement times ranging from 0 min to 24 h. Imaging parameters (all images): V$_{sample}$: 1.0 V; I$_{tunnel}$: 2 pA; 1000 Å× 1000 Å.

merge into domains, finally replacing the entire AD SAM. This process is shown in detail in Figure 5.1 with STM images of AD SAMs exposed to 1 mM C12 solution for times ranging from 10 min to 24 h. An initial AD SAM (displacement time of 0 min) is also shown for reference. In the figure, after 10 min, single C12 molecules and small C12 clusters were observed throughout the film at the defects in the AD SAM. These inserted molecules served as nucleation sites where islands of C12 molecules grew. After 20 min, a few of the molecular clusters became islands of ordered C12, and more C12 molecules inserted at the defects of the AD SAM. Between 30 and 60 min, the number of C12 islands and their size dramatically increased. At this point, it was observed that there were fewer new islands nucleated, and the existing islands grew in size. Between 80 min and 120 min, the remaining AD molecules that were present were displaced. After 400 min, the sizes and shapes of the C12 domains changed. There were fewer domains observed, and they were larger in size. No difference in surface coverage was observed. After 24 h, the SAM was composed entirely of C12, however, there were more defects present than for a typical C12 SAM that was fabricated on a bare Au{111} surface in 24 h from a 1 mM solution. Even after annealing the substrate in a C12 solution at 78 °C overnight, the resulting SAM was not as ordered as observed in a typical C12 SAM. However, the domains were larger in size and fewer in number than the AD SAM that was displaced for 24 h in 1 mM C12 solution. A similar phenomenon has been observed for monolayer growth on bare substrates. The domains in solution-grown monolayers were typically smaller than for gas-phase deposition. Only for growth from very low concentration (in the μM range) solutions were the resulting domains similar in size [209]. The difference in domain size is likely because the displaced SAMs are in a kinetically trapped state. The activation energy required to change the orientation of an entire domain of molecules, to match the orientation of the neighboring domain is larger than the available energy. The parameters required to anneal the SAM fully are unknown and are currently under investigation.

Figure 5.2 shows the same AD displacement process as observed by FTIR. The overlapping spectra of the C-H stretch region of single-component C12 (blue) and AD (red) SAMs are shown at the top (Figure 5.2A). All the peaks from both spectra overlap in this region except the peak for the CH$_3$ stretch of the C12 molecules, at 2877 cm^{-1}. Therefore, this peak was used to monitor the presence of C12 in the displaced SAMs. Additionally, this peak is not as sensitive to the orientation of the molecule because of the tetrahedral nature of the terminal methyl group. Figure 5.2B shows sequential FTIR spectra of the AD displacement process using C12. The top and bottom spectra
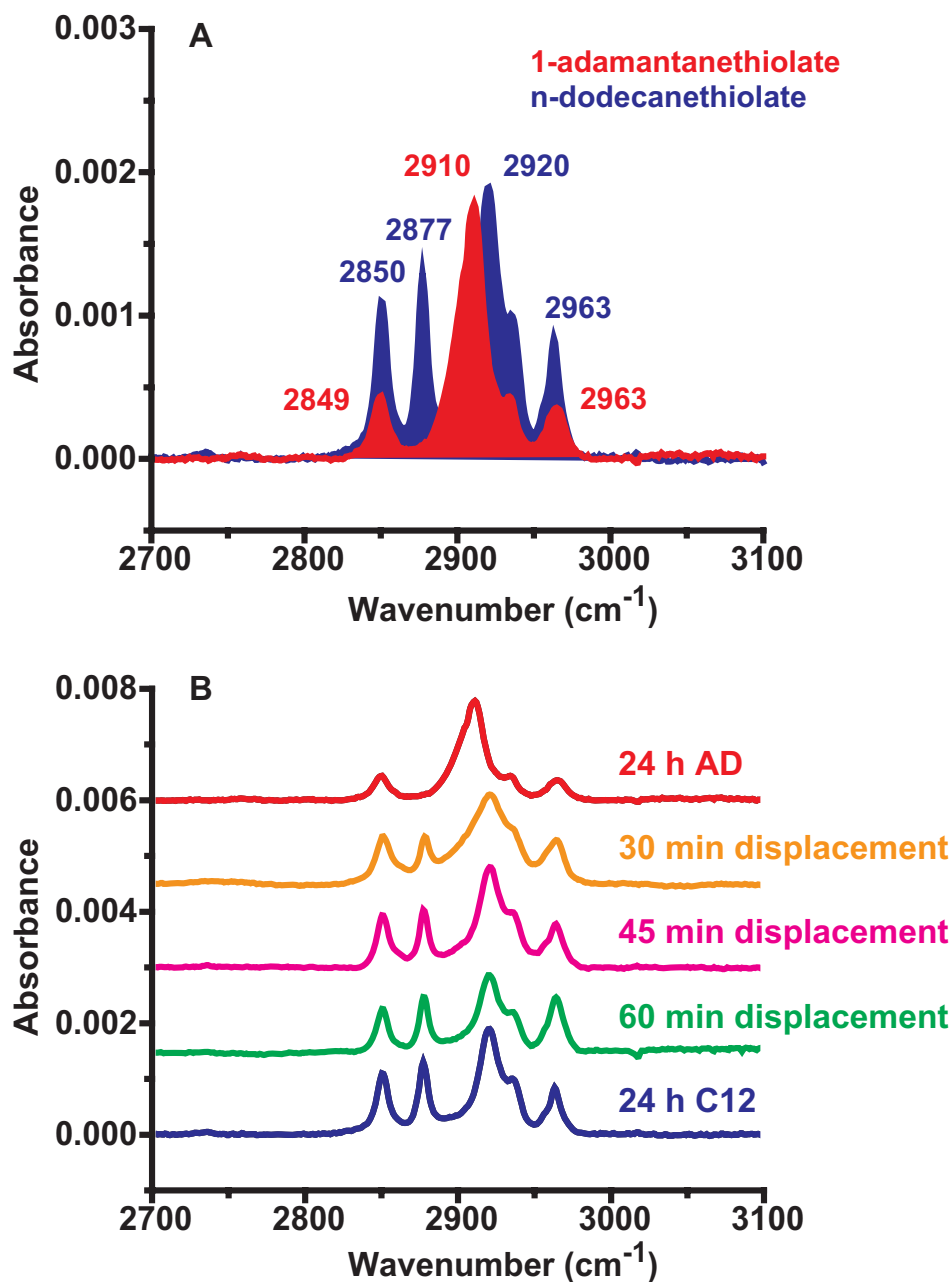
Figure 5.2.   A) Fourier transform infrared spectra of a 1-adamantanethiolate SAM and a 1-dodecanethiolate SAM, showing the spectral overlap in the C-H stretch region. B) Fourier transform infrared spectra of a 1-adamantanethiolate SAM, 1-adamantanethiolate SAMs displaced in 1-dodecanethiolate solution for 20 min, 40 min and 60 min, and a 1-dodecanethiolate SAM for reference, showing that the 1-adamantanethiolate molecules were replaced by 1-dodecanethiolate. Note: the spectra are offset for clarity.

show the single-component AD and C12 SAMs, respectively. After 30 min, the spectrum reflects peaks that are a combination of the spectra of the single-component SAMs. The spectrum of the AD SAM that was exposed to 1 mM C12 solution for 45 min also has contributions from both molecular species, but more strongly resembles the single-component C12 SAM. After 60 min, the spectrum is almost identical to the spectrum from a single-component C12 SAM, indicating that the AD presence has been greatly diminished. After 24 h exposure to C12, the observed spectra (data not shown) were nearly identical to those from a C12 SAM that was fabricated on a bare Au{111} surface in 24 h from a 1 mM solution. These spectra reflect a process similar to that observed with the STM images.

Using D12 as the displacing molecule, it was possible to monitor the fraction of AD displaced, because the D12 and AD spectra do not overlap. Figure 5.3 shows the disappearance of the AD C-H stretch peaks with increased exposure to D12. After 20 min, the main peak in the spectrum was observed at half the intensity of the spectrum for the initial AD SAM. After 40 min, the AD spectrum was just barely evident, and after 60 min, the AD spectrum was no longer visible. It was observed that D12 displacement occurs faster than C12 displacement, and further experiments are needed to explore this phenomenon. However, the experiment verifies that the AD is completely displaced by the D12 (similar results are assumed for C12). In contrast, Schlenoff *et al.* found that after a sufficiently long time that no further changes were observed, insertion of 1 mM radiolabeled (^{35}S) C18 into C18 SAMs resulted in up to 60% displacement of the initial SAM [219]. Additionally, up to 70% exchange was observed for D12 SAMs that were immersed in 2.8 mM C12 solutions [220]. To the best of the author's knowledge, 100% displacement has not been observed previously for two thiolated molecules using such low solution concentrations at room temperature.

Electrochemical desorption of AD SAMs that were displaced in 1 mM C12 solutions also gave analogous results. Figure 5.4 shows voltammograms of samples displaced with C12 for 30 min, 45 min and 60 min, the initial AD SAM and a C12 SAM that was fabricated on a bare Au{111} surface in 24 h from a 1 mM solution. The differences between the voltammograms for the AD and C12 SAMs are discussed in detail in Chapters 3 and 4. The voltammograms of the displaced SAMs (the middle voltammograms in Figure 5.4) all show two peaks from the presence of both molecular species. The smaller, higher-potential peak at ∼-900 mV is attributed to the AD regions, and the larger, lower potential peak at ∼-1050 mV is attributed to the C12 regions. It should be observed that the longer the SAM was exposed to C12, the larger the C12 peak became, and simultaneously,
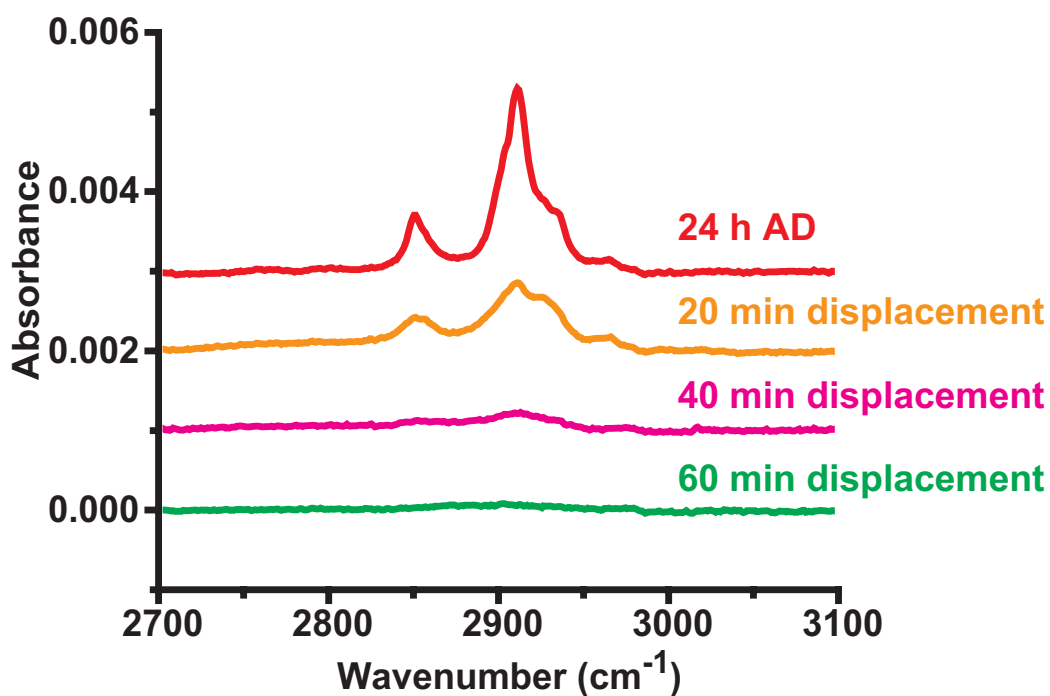
Figure 5.3. Fourier transform infrared spectra of a 1-adamantanethiolate SAMs, and 1-adamantanethiolate SAMs displaced in perdeuterated 1-dodecanethiolate solution for 20 min, 40 min and 60 min, showing that the 1-adamantanethiolate molecules were completely removed from the surface during the displacement process. Note: the spectra are offset for clarity.

the AD peaks diminished. Additionally, as observed and discussed in Chapter 4, the peaks shifted towards more positive potentials because of the interrupted intermolecular interactions within each lattice region, caused by the presence of the other lattice type.

A notable feature in all the two-component voltammograms was that as the displacement time increased, the C12 E_p shifted towards a more negative peak potential with respect to its position for SAMs created using short displacement times. For example, the C12 E_p in the voltammogram from the 20 min displacement SAM was -1014 $\pm$ 25 mV, and the C12 E_p in the voltammogram from the 900 min displacement SAM was -1091 $\pm$ 21 mV. The C12 E_p shifted $\sim$-77 mV. This shift is assumed to have been due to the increase in VDW interactions between ALK molecules as the ALK islands grew [150]. However, the E_p of a AD SAM that was displaced for 24 h in 1 mM C12 solution was never observed at the peak potential of the C12 SAM that was fabricated on a bare Au{111} surface in 24 h from a 1 mM solution, indicating that the displaced SAMs were never as ordered as the single-component SAMs, in agreement with the STM results. Additionally, it has been demonstrated that voltammograms of single-component ALK SAMs may have two cathodic peaks – one peak resulting from large domains of well-ordered ALK molecules, and one peak at a more positive E_p (-1079 mV, near the E_p for a single-component AD SAM) from ALK molecules trapped at step edges or defect sites in the underlying substrate [152, 153, 221]. This influences the interpretation of the voltammograms for long displacement times. The peak that is attributed to AD, instead may be from C12.

Figure 5.5 shows the calculated fractional coverages of C12 as a function of displacement time. Figure 5.5A shows the calculated fractional coverage using STM from two different sample sets. The associated error between sample sets is due to sample variations and differences in uncontrollable environmental parameters. Further statistics are needed to determine the parameters that influence these differences. However, although the rate of displacement is slower for the red sample set, the shape of the curves is similar.

Figure 5.5B shows the calculated fractional coverage for one sample set using all three analytical techniques. For the most part, the fractional coverages calculated from each technique are in agreement; however, there are a few deviations. Electrochemical desorption (green circles in Figure 5.5B) and FTIR (black squares) are ensemble techniques that average over the entire sample, while STM (red triangles) is a localized technique and only monitors small areas of the sample. Efforts were made to sample randomly from different areas of each sample with the STM.
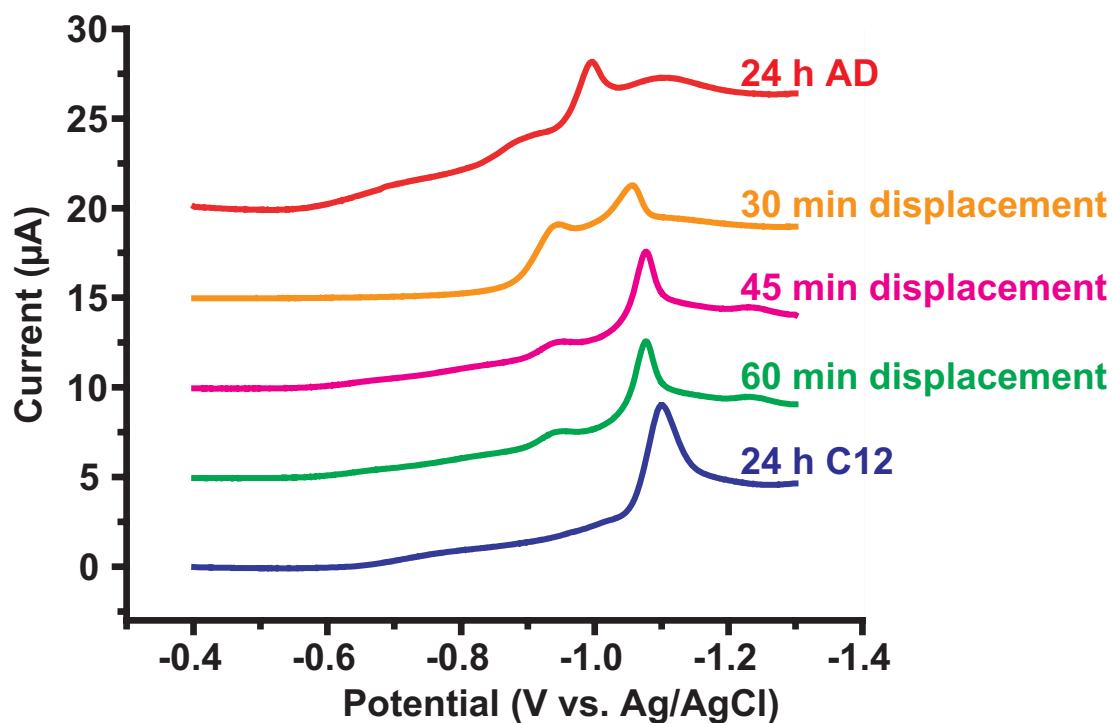
Figure 5.4. From top to bottom, voltammograms of a 1-adamantanethiolate SAM, 1-adamantanethiolate SAMs displaced in 1-dodecanethiolate solution for 20 min, 40 min and 60 min, and a 1-dodecanethiolate SAM for reference, showing that the 1-adamantanethiolate molecules are replaced by 1-dodecanethiolate. Scan parameters: forward and backward from -0.4 V to -1.3 V to - 0.4 V at 0.020 V/s. Note: only the forward sweep (the cathodic peak) is shown and the voltammograms are offset for clarity.
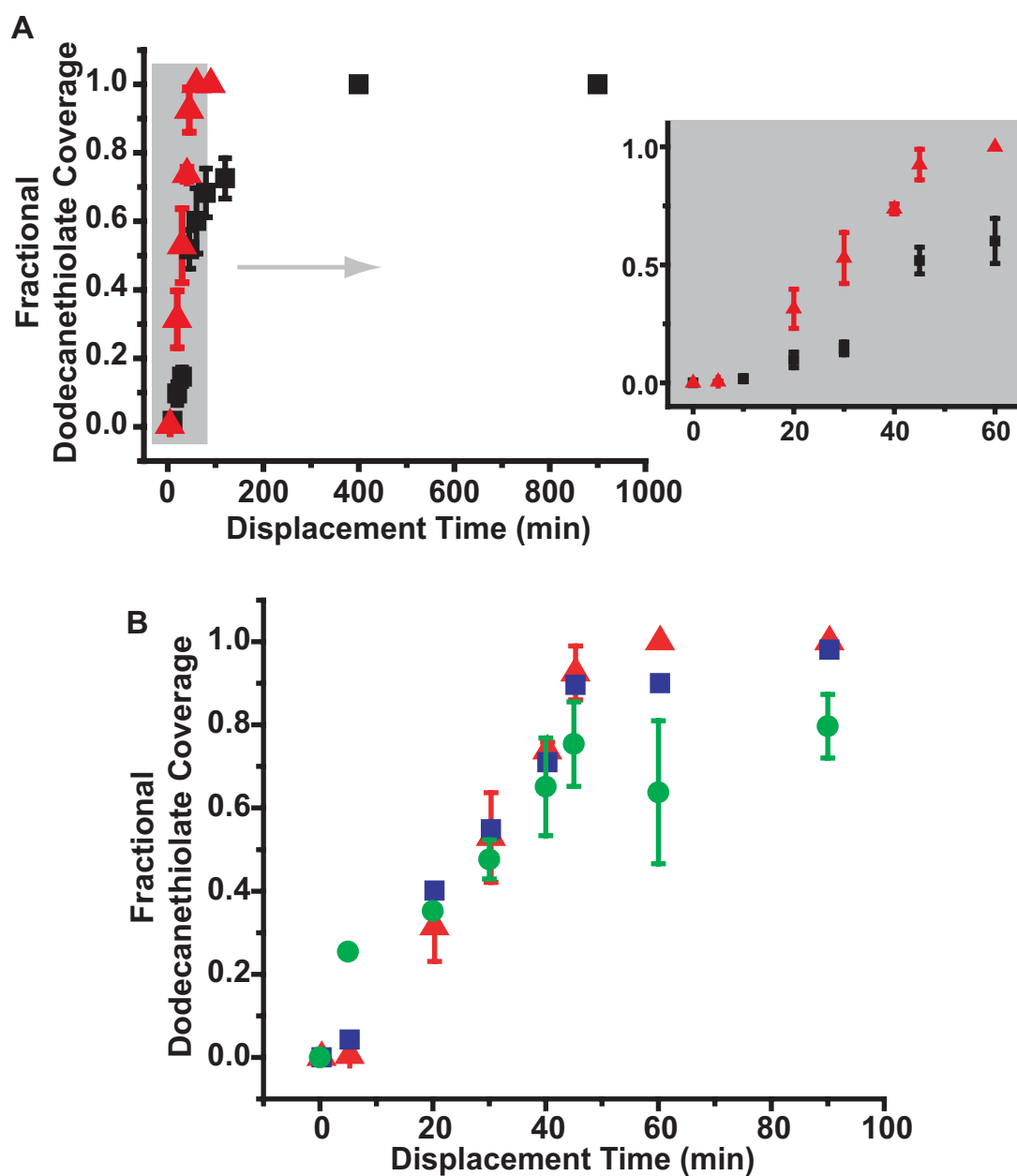
Figure 5.5. A) Fractional 1-dodecanethiolate coverage as a function of displacement time measured from 1-adamantanethiolate displaced SAMs as observed by STM for two different sample sets. The inset shows the smaller displacement time region. B) Fractional 1-dodecanethiolate coverage as a function of displacement time of the same sample set (red triangles shown in A) observed by FTIR (black squares), electrochemical desorption (green circles) and STM (red triangles) techniques, showing the correlation of the three techniques.

Additionally, FTIR and electrochemical desorption are not sensitive to molecules below a certain fractional coverage. Fourier transform infrared spectroscopy has high sensitivity in the 0.05 to 0.95 fractional coverage range, but outside that range cannot determine the presence of and distinguish between both types of molecules. Electrochemical desorption is not sensitive to molecular domains of less than 15 nm^2 (approximately 50 ALK molecules). Additionally, an incorrect assignment of the AD cathodic peak (discussed above) may account for the low fractional surface coverage for the large displacement times calculated from the electrochemical desorption voltammograms. Each of these experimental considerations account for the differences in the fractional coverage measured by the different techniques.

The plots of fractional C12 coverage that were calculated from the analysis by each method all have the same distinctive shape. For small C12 exposure times (between 0 and 10 min), little displacement was observed. This was followed by a region of near-linear growth (20 to 50 min) that eventually leveled off at the limit of 100% displacement (60 to 100 min). After 2 h, the curve was saturated and no further changes were observed. Each region reflects the observations from the STM images. At small displacement times, during nucleation, the C12 surface coverage was low, and the rate of displacement was slow. At some later point, as nucleation dropped off, the surface coverage dramatically increased as the islands grew radially. The growth slowed as the available number of sites decreased, and the fractional coverage approached 1. Although, ordering was observed in the STM images, it was not reflected in the curves; however, a larger statistical dataset may uncover some less noticeable changes in the uptake curves for the longer displacement times.

Overall, the uptake curves can be described as logarithmic growth that saturates at 100% displacement, similar to previous adsorption studies on bare Au{111}. However, much slower growth is observed at low displacement times than is observed on the bare surfaces (shown more clearly in the inset of Figure 5.5A). This difference is attributed to the insertion and nucleation events observed by STM. On the bare surface, nucleation events are too fast to observe except at low temperatures and with low vapor pressures (molecular concentrations). However, it is believed that the AD SAM slows down these events during displacement so that it *is* observed, and that the observed uptake curve is the combination of nucleation and growth events. The inflection point at the lower displacement time may be the time point at which the growth events overtake the nucleation events.

5.4.2 Rate of displacement

To compare the rates of displacement to those rates observed for ALK adsorption on bare Au{111}, Figure 5.6A shows one STM dataset that has been fit with a Langmuir curve. Rate constants for C12 adsorption on bare gold surfaces range from 2700 to 2200 $M^{-1}s^{-1}$, depending on the measurement technique and the solution concentration used [213, 218, 222, 223]. From the Langmuir fits to the calculated fractional coverages by all the techniques of the displacement datasets, the rate of displacement from a 1 mM solution is estimated to be on the order of 0.3 $M^{-1}s^{-1}$. Therefore, the rate of displacement is approximately 10,000 times slower than those reported for ALK adsorption on bare Au{111}. The AD monolayer inhibits the direct adsorption of the ALK molecules to the surface, thus slowing down the process. However, the Langmuir fit is insufficient to model the behavior at short displacement times, as shown in Figure 5.6B. No model in the literature sufficiently fits this region.

5.4.3 Displacement parameters

Due to insufficient statistics, modeling of the displacement process is beyond the scope of this work. However, based on the above observations, a few experimental parameters are expected to influence the kinetics and should be considered for an adequate model. Similar to the studies of SAM formation kinetics on bare surfaces, solution concentration and temperature are expected to impact the rate of displacement, because they influence the number of molecules impinging on the surface. Preliminary concentration studies see a difference in the rate of displacement, and the influence of temperature on displacement is demonstrated for vapor displacement in Chapter 4.

The number of insertion sites, which is expected to correlate to the number of nucleation sites, is predominately determined by the defect density of the AD SAM because the other sites are not immediately available for adsorption. In turn, the SAM defect density is somewhat influenced by the defect density of the underlying substrate. However, neither the defect density of the SAM nor the underlying substrate is easily controllable or quantifiable.

Based on the STM observations of nucleating islands that grow radially, the probability of ALK absorption is not uniform across the surface. There is a higher probability of an incoming ALK molecule binding at the edges of preexisting ALK islands. Assuming a physisorbed precursor to chemisorption, this suggests that there are different sticking coefficients for the AD, C12 and defect regions of the substrate. Additionally, in this case, the number of reactive sites increases with
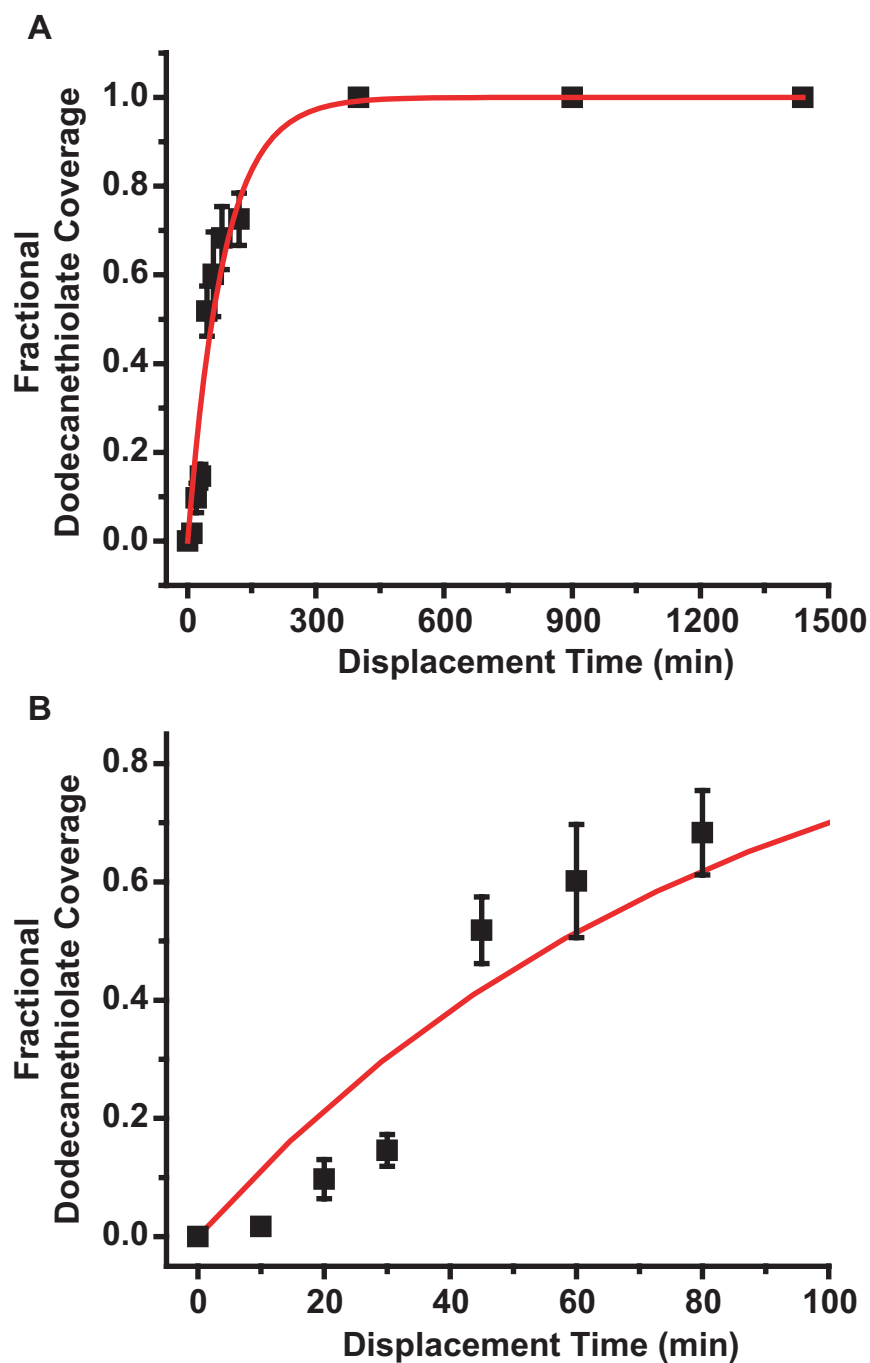
Figure 5.6. Fractional 1-dodecanethiolate coverage as a function of displacement time, calculated from STM images (black squares in Figure 5.5A) and fit using first order Langmuir kinetics. A) Over the entire curve, the Langmuir kinetics show the same sharp increase to substrate saturation as the data. From the fit, for 1 mM concentrations, the rate of displacement was $0.20 \text{ M}^{-1}\text{s}^{-1}$. B) At low displacement times, the Langmuir fit is poor, and does not account for the region attributed to nucleation.

the square root of the ALK surface coverage. Thus, the probability of ALK molecules adsorbing increases with surface coverage (rather than linearly decreasing, as Langmuir kinetics suggest), which has been observed previously for similar systems [222, 224].

Furthermore, it has been demonstrated that VDW interactions greatly influence the displacement process, and preliminary data show that the ALK displacement kinetics may be influenced by the length of the alkyl chain. Since VDW forces are the primary contributor to ALK intermolecular interactions, it is expected that the VDW forces influence the reactivity of the island edge sites compared to the rest of the surface. This influence has been observed for the insertion of C6 discussed in Chapter 3. Additionally, previous adsorption studies have shown a dependence of adsorption rates on alkyl chain length [213, 218, 222].

5.5   Conclusions

We propose a nucleation and growth mechanism for AD displacement. Displacement as a function of time was observed as an approximately logarithmic uptake curve that saturates at 100% displacement. However, at low displacement times, we observed significant deviation from logarithmic Langmuir growth that we attribute to the nucleation process. The uptake curve cannot be modeled by existing kinetic models, but we estimate the displacement of AD by C12 to be 10,000 times slower than adsorption of similar molecules on a bare Au surface. These estimates allow for the optimization of one parameter for a specific system, but further studies are needed to control the displacement process sufficiently over a range of conditions.

Chapter 6

Nanoscale Patterning I: Microcontact Printing and Microdisplacement Printing

6.1 Introduction

As discussed in Chapter 1, non-photolithographic techniques offer inexpensive, quick, and reusable fabrication techniques (such as microcontact printing, dip-pen nanolithography, nanoimprint lithography, and micromolding) for patterning on the nanometer scale [6, 35, 225]. One of the most common soft lithographies [58] is microcontact printing, the patterning of a substrate by contact ('stamping') with a 'molecularly inked' elastomeric stamp. Although many other systems have been studied, ranging from polymers on silicon surfaces [226–228] to nanoparticles on metallic substrates [74, 75, 229, 230], a great deal of attention has been placed on μCP of ALK molecules on gold substrates, because this system is regarded as the model system for many other molecule-substrate pairs [66, 231–233]. However, some molecules are susceptible to lateral mobility across the substrate surface during and after patterning steps, which leads to pattern dissolution. It has been demonstrated that lateral surface diffusion rates increase with decreasing alkyl chain length [123, 234, 235]; thus, short chain ALK and other low-molecular-weight molecules are particularly susceptible to such diffusion during the patterning process. This lateral mobility increases if no molecule is used to fill in the empty spaces where no pattern is present on the substrate (a process called 'backfilling'). In addition, although some solvent presence may be necessary for ordering the patterned molecules, prolonged exposure to solvent during backfilling steps mobilizes the patterned molecules at the pattern interfaces and furthermore promotes molecular exchange of the patterned molecules for backfilling molecules.

These problems can be avoided by an alternate patterning technique, microdisplacement printing (μDP), which uses a pre-assembled monolayer that is sufficiently ordered to protect the surface, but is sufficiently labile such that other molecules can displace it through competitive adsorption (the competition of binding to the surface by two molecules due to differences in their relative adsorption probabilities [236, 237]). Stamping on such a surface directs the molecules to

adsorb where their local concentration is highest and holds the ink molecules in place once adsorbed during the stamping procedure. This procedure also limits the need for solution processing because the unpatterned regions are prefilled.

In this chapter, we demonstrate the μDP process using AD SAMs (discussed in Chapters 3–5 and in references [238, 239]) and a variety of molecules, including those that are unpatternable by traditional μCP methods, such as short-chain ALK. Trends in the degree of AD displacement were explored by stamping with unpatterned polydimethylsiloxane (PDMS) stamps for a variety of displacement times and ink concentrations. This information was used to choose appropriate times and concentrations for patterned samples. Additionally, the remaining AD in μDP patterned samples was replaced by further displacement steps, both solution immersion and contact stamping. Immersion of a patterned sample in a different thiol solution for several h does not degrade the pattern. Finally, three-component patterned SAMs were fabricated by the inclusion of a second displacement patterning step both on μCP patterned samples containing AD and on μDP samples. The samples were characterized by AFM and STM methods.

6.2 Background

6.2.1 Lateral force microscopy imaging

The instrumental setup for later force microscopy (LFM) is shown in Figure 6.1. LFM works similarly to constant force contact-mode AFM, discussed in Chapter 1. A tip with a low force constant that can also twist left and right is used. The laser bounces off the cantilever and the feedback loop uses the signal from the upper and lower portions of a segmented photodetector to adjust the sample height to maintain a constant normal force. Additionally, the signal from the left and right portions of the photodetector, caused by deflection of the laser from lateral twist of the tip as it encounters regions of higher and lower attractive forces is recorded as a lateral force. Unfortunately, there is no reproducible way to get quantitative lateral force differences from the images, it is only possible to compare patterned regions qualitatively as producing either higher or lower lateral friction.
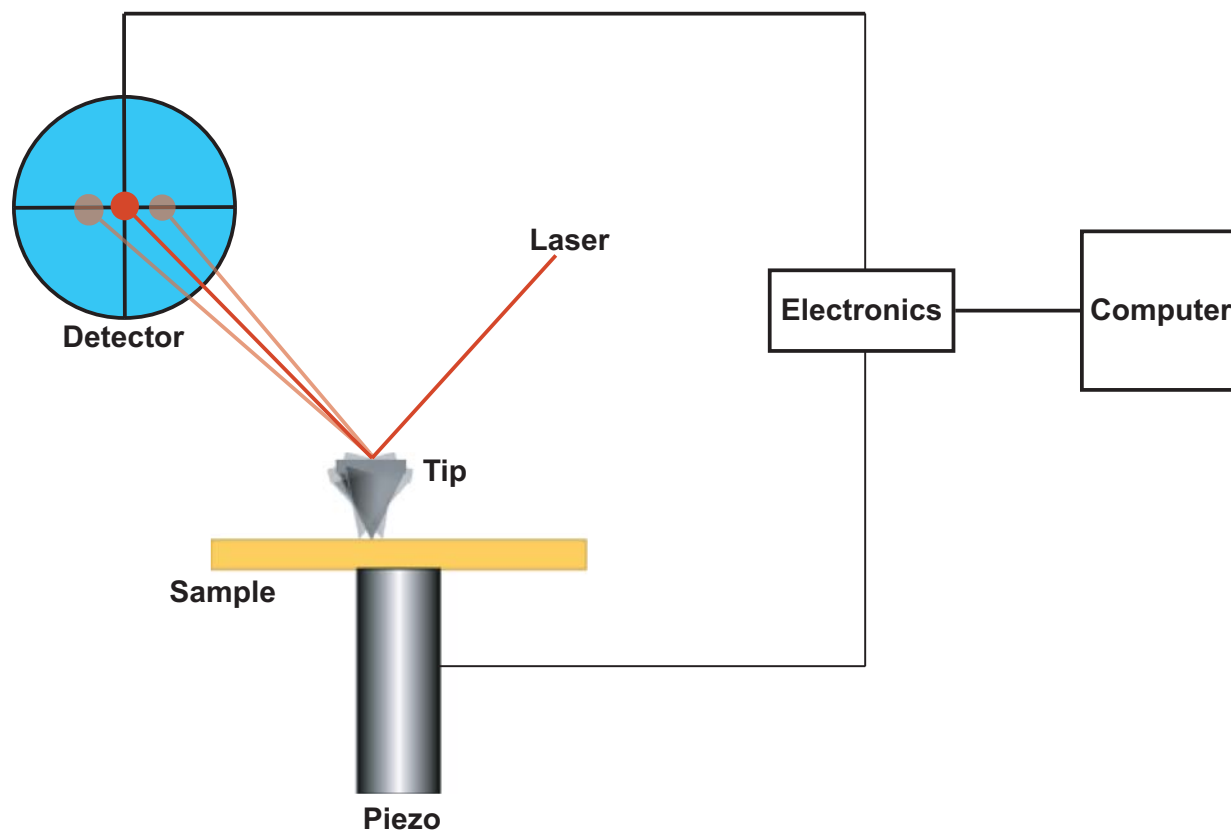
Figure 6.1.   A schematic of lateral force microscopy with the tip oriented out of the plane of the paper to show the torsional movement of the tip that is detected in the left and right quadrants of the segmented photodector, in addition to the normal up and down movements of the tip, which are detected on the upper and lower quadrants.

6.2.2 Phase imaging

As discussed earlier (see Chapter 1), in non-contact mode AFM, the proximity of the sample to the tip causes a shift in the resonant frequency of the cantilever. In addition to changing the amplitude, this shift also changes the phase of the cantilever resonance with respect to the driving frequency. By measuring the change in phase as a function of position, a map of the surface forces can be created. Although some groups have reported reproducible contrast for certain free-oscillation-amplitude to setpoint-amplitude ratios, we have not found this to be the case [240–245]. For our purposes we have used phase imaging solely for verification of the existence of a pattern because of its increased sensitivity and speed of acquisition in comparison to other AFM techniques.

6.2.3 Kelvin probe microscopy imaging

Another non-contact mode measurement, Kelvin probe microscopy (KPM), also known as electrostatic force microscopy (EFM) and scanning surface potential microscopy (SSPM), measures the electrostatic force on the tip caused by the surface charge of a surface. When two metallic surfaces are in contact, the electrons flow between them until equilibrium is reached by aligning the Fermi levels of the two solids. However, the flow of charge creates a potential gradient and the two surfaces become equally but oppositely charged. This potential difference is the local contact potential difference (CPD) and is sensitive to the surface material, the molecules on the surface, and the molecular orientation.

Figure 6.2 shows the basic instrumental layout for KPM. Both AC and DC bias voltages $((V_{AC})$ and (V_{DC}) , respectively) are applied between the sample and the tip. Assuming parallel plate geometry, the total bias (V_{Total}) can be expressed as:

$$V_{Total} = V_{DC} - V_{Sample} + V_{AC}\sin(\omega t), \qquad (6.1)$$

where ω is the frequency of the AC bias. The electrostatic force (F_{Total}) between the tip and the sample then becomes:

$$F_{Total} = (\frac{C}{z})((V_{DC}-V_{Sample})^2+\frac{1}{2}V_{AC}^2)+2(\frac{C}{z})(V_{DC}-V_{Sample})V_{AC}\sin(\omega t)-\frac{1}{2}(\frac{C}{z})V_{AC}^2\cos(2\omega t),$$
$$(6.2)$$
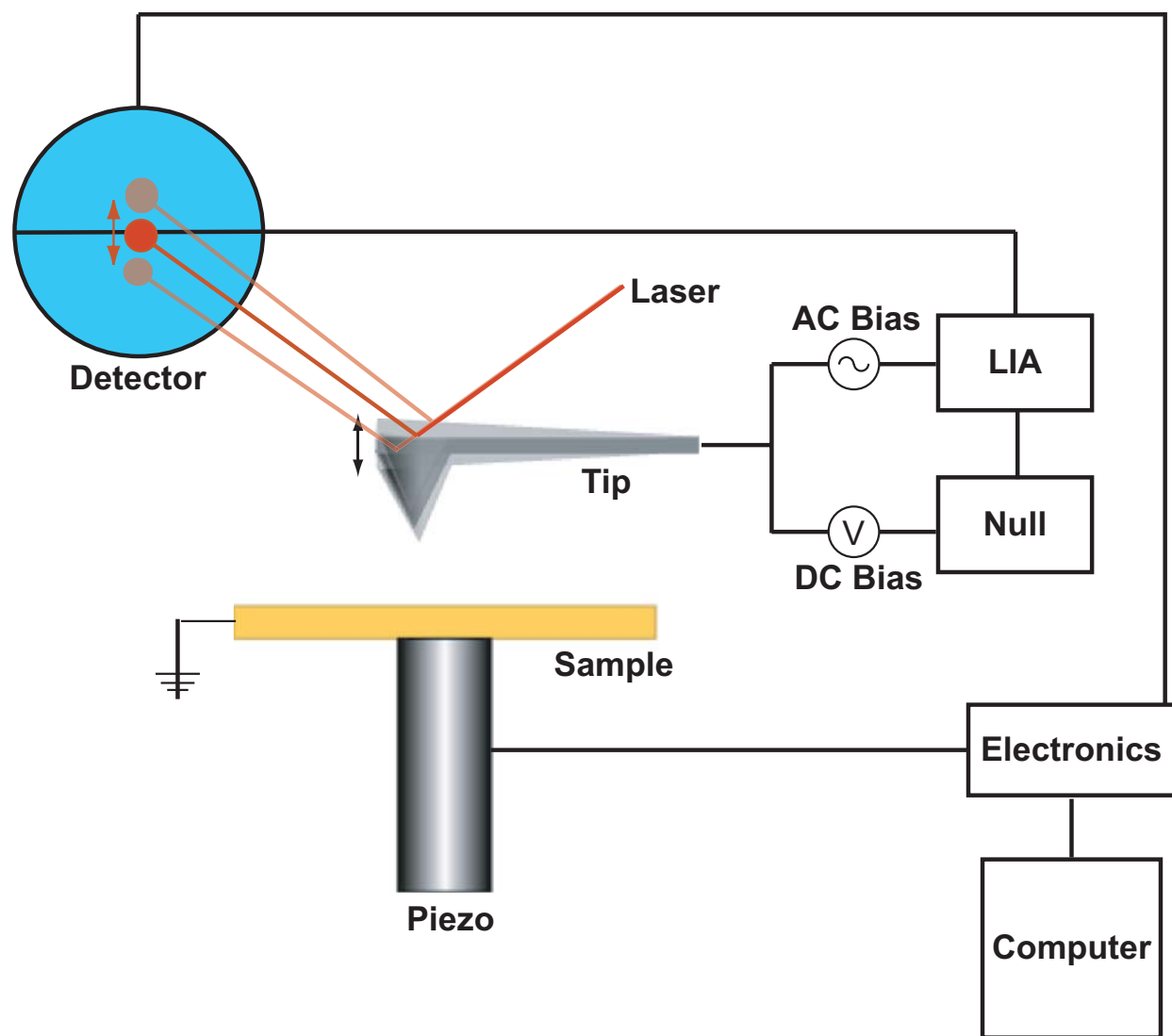
Figure 6.2.   A schematic of kelvin probe microscopy with the additional feedback loop used to null the surface potential.

where C is the capacitance and z is the tip-sample distance. Using the lock-in amplifier to measure the ω term, the sample potential can be determined by varying the DC bias. When the DC bias exactly matches the sample potential such that $V_{DC} - V_{Sample} = 0$, the ω term is zero. In this manner, an image is created from the variation of the DC bias as the ω term in equation 6.2 is nulled. The advantage of this measurement is that it is possible to define the surface potential quantitatively.

6.3 Experimental Procedure

6.3.1 Sample preparation

The experimental processes for μCP and μDP are shown in Figures 6.3 and 6.4, respectively. All the SAMs were assembled on Au{111} via solution deposition in argon-sparged ethanol. Commercially available Au{111} on mica substrates (Molecular Imaging, Tempe, AZ) were annealed using a hydrogen flame or UV/ozone cleaned just prior to deposition. AD (synthesized by methods previously described [133,134,157,238]) SAMs were prepared by immersing the annealed substrates in a 10 mM ethanolic solution for 24 h. Post deposition, each sample was rinsed in neat ethanol and blown dry with inert gas twice.

The polydimethylsiloxane (PDMS) polymer was made by combining a 10:1 ratio of PDMS Sylgard 184 Base and PDMS Sylgard 184 Cure (Dow Corning, Midland, MI) and stirring rigorously until they were thoroughly combined. Unpatterned stamps (stamps with no relief pattern) were fabricated by pouring the uncured polymer into empty plastic Petri dishes (VWR International, West Chester, PA) and deaerating them in a vacuum desiccator until degassing was no longer observed. The PDMS was then cured at 90 °C for 2 h. Patterned stamps were formed from diffraction grating masters (Optometrics LLC, Ayer, MA) or photolithographically defined silicon masters. The diffraction gratings were used as is; no additional steps were necessary to keep the PDMS from binding to the surface. For the silicon masters, prior to stamp fabrication, a (heptadecafluoro-1,1,2,2-tetra-hydrodecyl) trichlorosilane (Gelest, Morrisville, PA) SAM was formed on the silicon surface to prevent PDMS adhesion to the silicon. The PDMS pre-polymer was poured over the masters and was treated similarly to the unpatterned stamps. Examples of the resulting stamps created by this process and used for the printing experiments discussed below are shown in Figure 6.5.
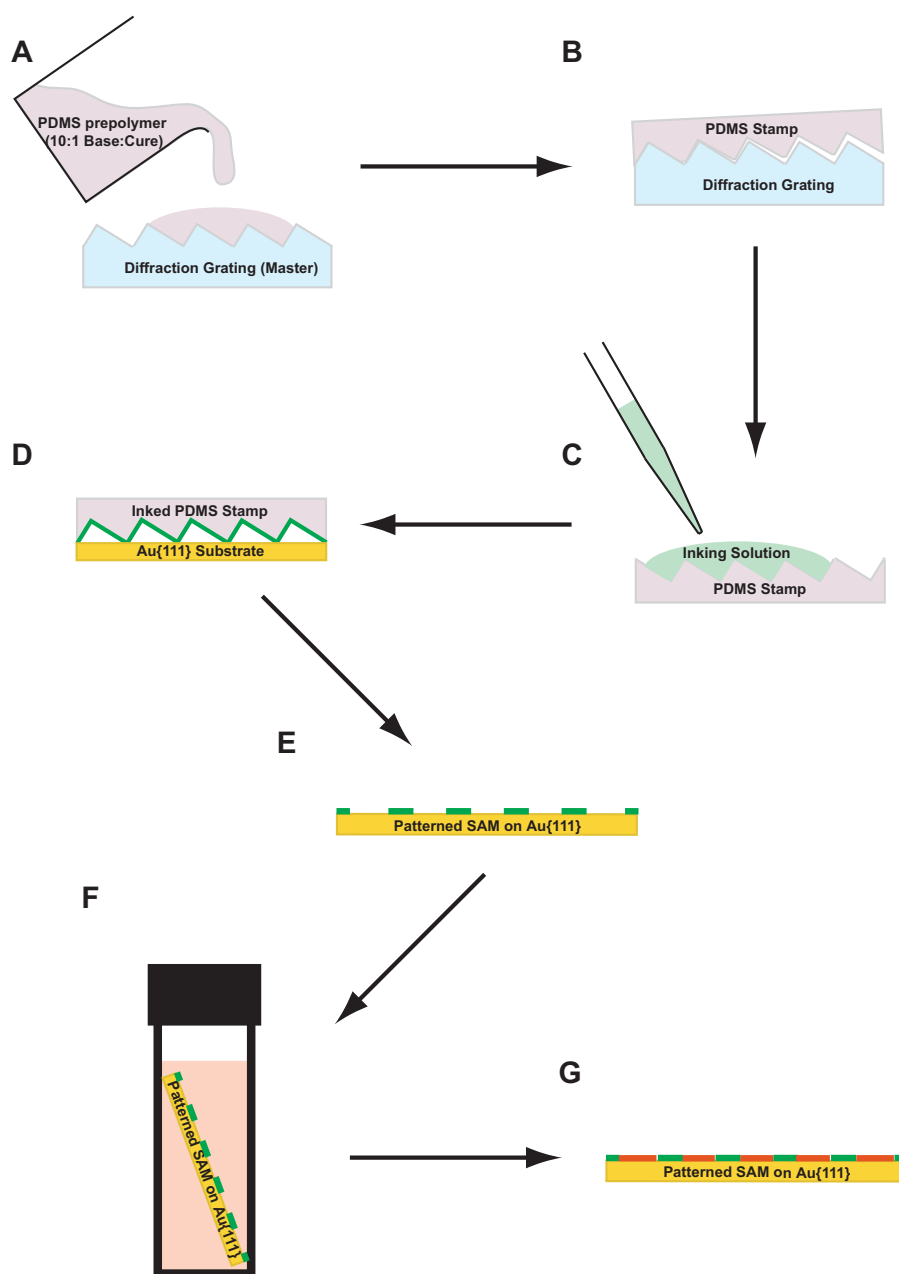
Figure 6.3. A schematic of the microcontact printing process. A) The PDMS prepolymer was poured over a previously prepared master and was then cured for a minimum of 2 h at 90 °C. B) The PDMS stamp was peeled off the master and was thoroughly cleaned. C) An inking solution was pipetted onto the PDMS stamp and subsequently dried with inert gas. D) The inked stamp was contacted on clean, dry Au{111} substrate and (E) upon removal of the stamp a patterned SAM of the ink was formed on the Au{111}. F) By submerging the patterned sample in another ink the bare areas between the patterned SAM were filled, (G) creating a two-component patterned SAM.
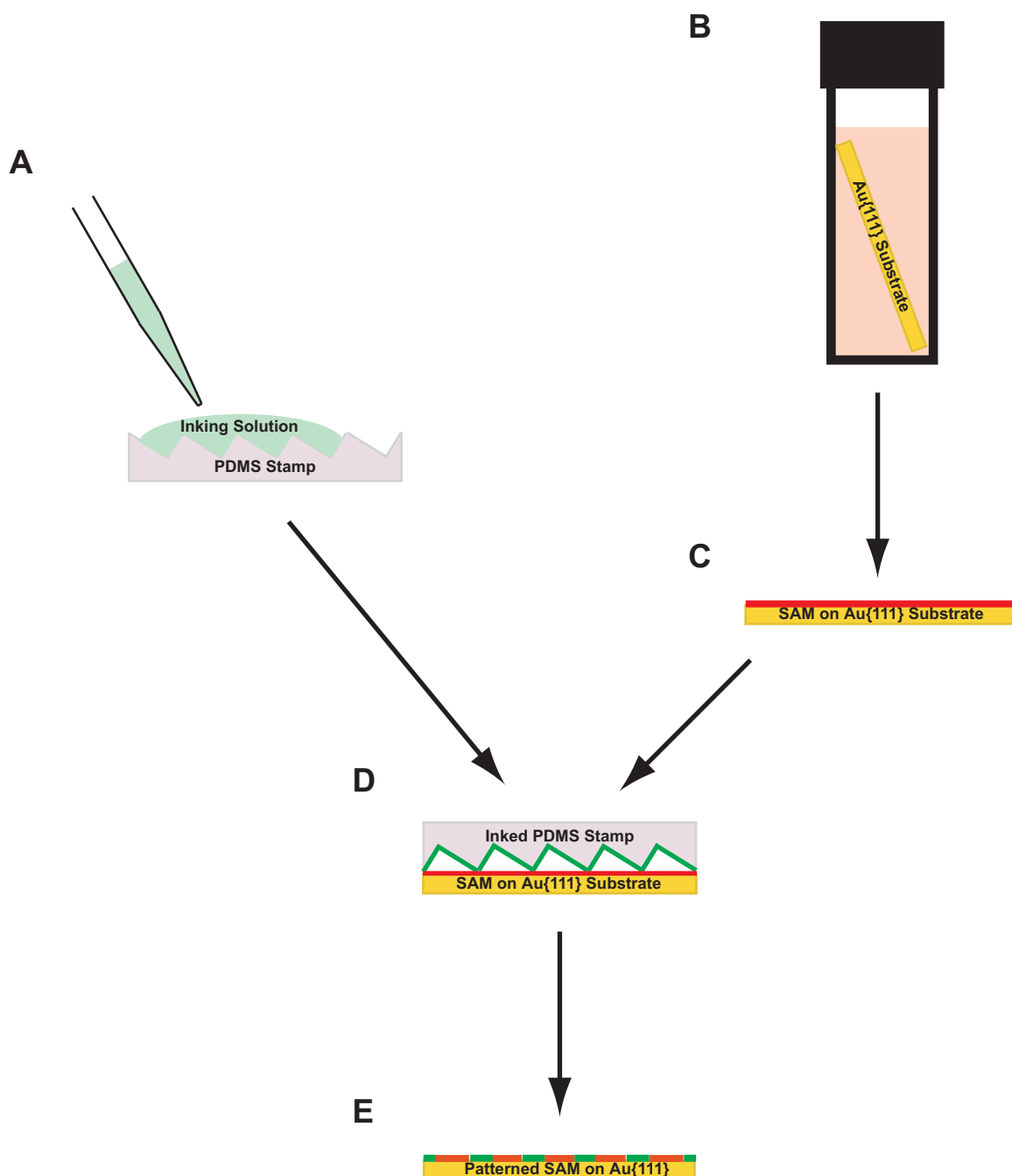
Figure 6.4. A schematic of the microdisplacement printing process. A) The PDMS stamp was fabricated and prepared in the same fashion as for microcontact printing (Figure 6.3 A–C). B and C) Prior to stamping, a 1-admantanethiolate SAM was fabricated by solution deposition as described in Chapter 3. D) The inked and dried PDMS stamp was contacted directly to the SAM. E) Displacement of 1-admantanethiolate occurred only in the areas where the PDMS surface touches the SAM surface, creating a patterned two-component SAM.
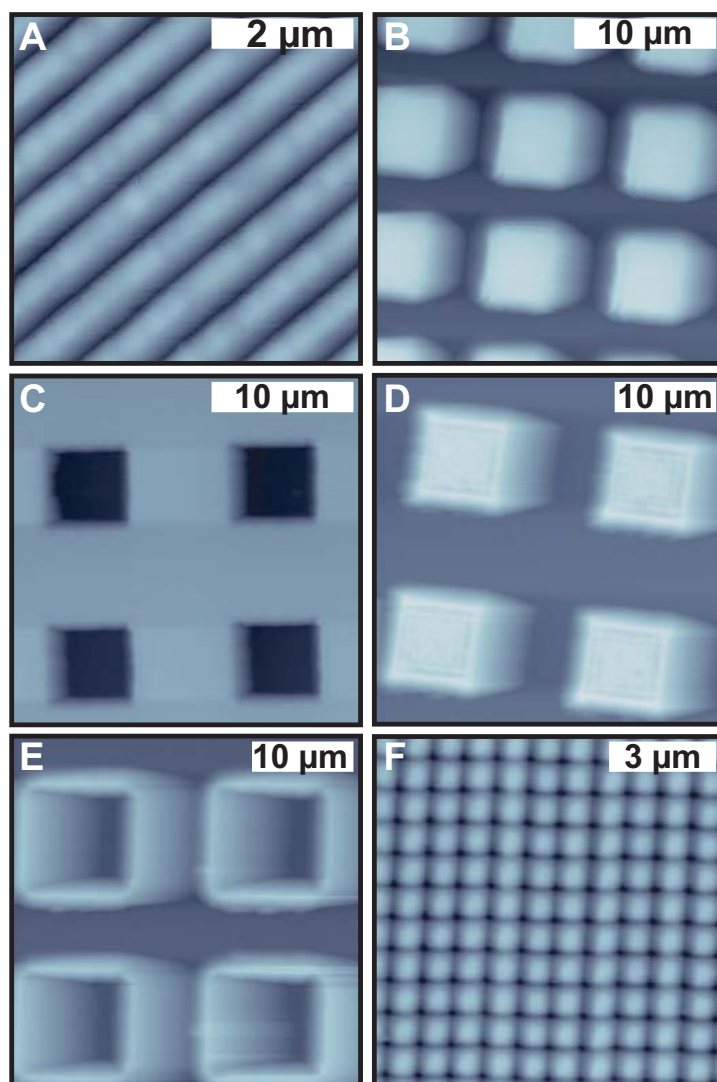
Figure 6.5. Atomic force microscopy images of some example PDMS stamps used for micro-contact and microdisplacement printing. A) A lined stamp created from a 1200 grooves/mm glass grating master. Imaging parameters: Force setpoint: 50 nN; Scan rate: 1 Hz; 5 μm × 5 μm. B) An image of a stamp with 5 μm by 5 μm pillars at a 10 μm pitch made from a silicon master. Imaging parameters: Force setpoint: 50 nN; Scan rate: 1 Hz; 25 μm × 25 μm. C) An image of a stamp with 5 μm by 5 μm wells at a 10 μm pitch made from a silicon master. Imaging parameters: Force setpoint: 50 nN; Scan rate: 1 Hz; 25 μm × 25 μm. D) An image of a stamp with 10 μm by 10 μm pillars at a 20 μm pitch made from a silicon master. Imaging parameters: Force setpoint: 50 nN; Scan rate: 1 Hz; 35 μm × 35 μm. E) An image of a stamp with 10 μm by 10 μm square cylinders at a 20 μm pitch made from an overly etched silicon master of 10 μm by 10 μm pillars. Imaging parameters: Force setpoint: 50 nN; Scan rate: 1 Hz; 35 μm × 35 μm. F) An image of a stamp with 1 μm by 1 μm pillars at a 2 μm pitch made from a silicon master. Imaging parameters: Force setpoint: 50 nN; Scan rate: 1 Hz; 20 μm × 20 μm. All the features are approximately 1 μm high.

To remove any uncured or low-molecular-weight PDMS, once cured, the stamps were excised from the Petri dish and cleaned using a method modified from that of Graham *et al.* [246]. The stamps were sonicated in hexanes for 30 min, dried with inert gas, heated at 90 °Cuntil the PDMS returned to its original size, and sonicated for 5 min in 2:1 ethanol and water and dried with inert gas three times. The whole procedure was then repeated three times, and finally the stamps were dried in the oven for 15 min. Between uses, each stamp was cleaned with one cycle of the above cleaning method.

An ethanolic solution of the molecule to be stamped ('ink') was pipetted directly onto the stamp, allowed to adsorb to the PDMS surface for 10 s and subsequently dried off with inert gas. The *n*-alkanethiols, 1-octadecanethiol (ODT), 1-tetradecanethiol (C14), C12, C10, and C8, were purchased from either Lancaster (Pelham, NH) or Sigma-Aldrich (St. Louis, MO). 11-Mercaptoundecanoic acid (MUDA) and 16-mercaptohexadecanoic acid (MHDA) were purchased from Sigma-Aldrich (St. Louis, MO). 11-amino-1-undecanethiol (AUDT) was purchased from Dojindo (Kumamoto, Japan).

Microcontact printed samples were fabricated using bare, clean Au{111} on mica substrates (Molecular Imaging, Tempe, AZ) by applying an inked stamp to the gold surface for the specified amount of time and subsequently backfilled using a 1 mM ethanolic solution of a different molecule for 5 min [6, 225]. In contrast, μDP samples were prepared using AD SAMs on Au{111} as substrates. The inked stamp was applied to the SAM surface for the specified time and the samples were then rinsed thoroughly with ethanol (rinsing is not necessary, but removes molecules not bound to the surface, making imaging considerably easier) and dried with inert gas. No backfill was performed.

Additional solution processing steps were performed on AD-containing μCP and μDP samples. In the μCP cases, after the initial backfill with AD, the sample was rinsed with ethanol, dried with inert gas, and then immersed in another thiol solution. In the μDP cases, after the displacement patterning, the sample was immersed in another thiol solution without rinsing.

Additional patterning steps were also performed on AD-containing μCP and μDP samples. After the initial patterning steps, a second pattern was fabricated directly on top of the first pattern by the μDP method.

Within min of preparation, each sample was imaged using either ambient STM (discussed in Chapters 1 and 2) or one of the ambient AFM methods discussed above. The AFM used

for collection of the data herein is a Thermo Microscopes Autoprobe CP Research AFM (Veeco Instruments, Santa Barbara, CA) with both contact mode and noncontact mode capabilities.

Lateral force measurements were made under ambient conditions using silicon-nitride-coated plank-style AFM tips with a force constant of 0.03 N/m. Phase imaging was performed under ambient conditions using silicon-nitride-coated plank-style AFM tips with a force constant of 0.03 N/m or platinum-coated V-style non-contact AFM tips with a force constant of 17.2 N/m. For KPM measurements, in addition to the AFM, an SR830 DSP lock-in amplifier (Stanford Research Instruments Inc, Sunnyvale, CA) and custom-built summing and nulling circuits were used for the additional potential nulling feedback. All measurements were performed applying 500 mV to the tip at a frequency of 10 kHz and using a lock-in time constant of 3 ms and a sensitivity of 1 mV. Electrical contact between the sample and the sample puck was provided by a dab of nickel print (Newark InOne, Chicago, IL). Imaging was performed under ambient conditions using platinum-coated V-style non-contact AFM tips with a force constant of 17.2 N/m. All the AFM tips were purchased from Mikromasch (Portland, OR).

6.3.2   Image analysis

6.3.2.1   Determining the microdisplacement printed fractional coverage

Using Matlab (MathWorks, Natick, MA), the fractional coverage was calculated from representative STM images of each sample. Binary images were generated from the STM images using a user-defined threshold based on the apparent height of the molecular features (similar to the analysis determining the fractional coverage from STM images used in Chapter 5). The pixel fraction of the image covered by each apparent height was calculated, grouped by type, and then divided by the total lattice coverage. Defects in the substrates were not included. All the coverages were calculated from images either 1000 AA × 1000 Å or 500 Å × 500 Å in area that included only one substrate terrace. Images were taken from different (independent) areas across the samples and the resulting fractional coverages were averaged. Unless otherwise indicated, the associated error for all the percentages shown is ±2 %.

6.3.2.2   Contact potential difference analysis

The potential difference between the molecular pair in each patterned SAM was calculated from the KPM images using Matlab (MathWorks, Natick, MA). A binary image was generated from

the KPM image and a user-defined threshold. Using masks based on user-defined thresholds, the patterned regions of the image were separated from the background. The regions of the patterned features and the background were then collated separately and the average and standard deviation of the values were calculated. The potential difference between the molecular pair in the patterned SAM was equal to the average potential of the (stamped) features minus the average potential of the background. These individual histrograms were checked against a sum of two Gaussians fit to a histogram of the entire image.

6.4   Results and Discussion

6.4.1   Mircocontact printing

As discussed in Chapter 4, AD films are labile, in that it is possible to displace the AD molecules from the surface by submersion of the sample into a solution of a different thiolated molecule such as an ALK. However, submersion of a pre-assembled ALK SAM into an AD solution results in little or no displacement. This property can be applied to backfilling of traditional μCP samples. Lateral force microscopy imaging of a Au{111} substrate that has been patterned using μCP methods and then backfilled with AD shows a distinct pattern, as shown in Figure 6.6. After printing, the AD molecules adsorb to the gold substrate between the patterned features, in the areas where the patterned molecules are not present without disturbing the pre-existing molecules.

6.4.2   Microdisplacement printing

Using the lability of the AD SAMs it is also possible to 'fill in' the space between the patterned features *before* patterning via μDP, thus preventing pattern dissolution, even for molecules that would normally diffuse rapidly across the substrate surface. During μDP, as shown in Figure 6.4, thiolated molecules are stamped onto an existing SAM, displacing the SAM only where the stamp meets the surface. Within the contacted area, similar to that observed for the solution displacement in Chapter 4, the displacement is observed first at film and substrate defects in the SAM and then as patches of ordered molecular lattice that increase in size from their origins at defects. Figure 6.7 shows a 175 Å$\times$ 175 Å STM image of a sample created by μDP on an AD SAM with an unpatterned PDMS stamp inked with 100 mM C10 (3.5 min stamp-substrate contact time). Large ordered areas of each lattice type are observed where previously there was only AD. It is the two

A Patterned SAM on Au{111}

LFM   1 µm

B Patterned SAM on Au{111}

LFM   1 µm
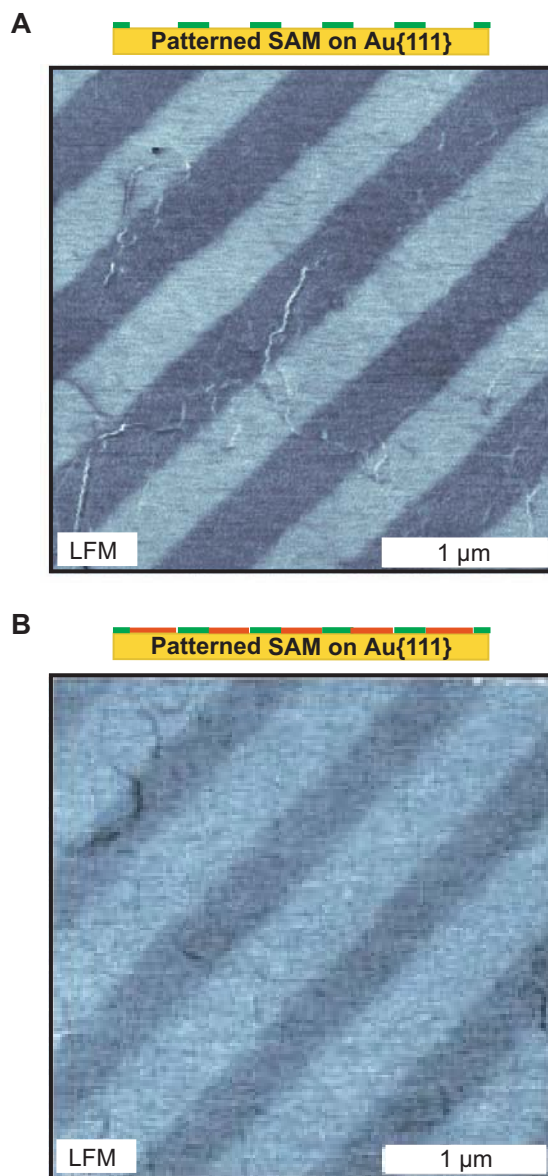
Figure 6.6. A) A LFM image, and shown schematically above, of a striped microcontact printed sample created on Au{111} using the stamp with 1200 lines/mm, shown in Figure 6.5A, inked with 5 mM 11-mercaptoundecanioc acid solution. The high-friction stripes are the MUDA regions, and the low-friction stripes are the bare Au{111}. Imaging parameters: Force setpoint: 1 nN; Scan rate: 2 Hz; 3 μm × 3 μm. B) A LFM image, and shown schematically above, of the same sample after backfilling with 10 mM 1-admantanethiol. The high-friction stripes are the 11-mercaptoundecanioc acid regions, and the low-friction stripes are 1-admantanethiolate regions. Imaging parameters: Force setpoint: 1 nN; Scan rate: 2 Hz; 3 μm × 3 μm.

adsorbed molecules can be distinguished because of the differences in lattice size, lattice spacing, and apparent height ($\Delta h \approx 2.5$ Å) between them (discussed in detail in Chapter 4). The more protruding lattice (lower right indicated by the arrow), juxtaposing two substrate defects, is C10, while the less protruding lattice (the majority of the image) is AD.

6.4.2.1   Stamping time and concentration dependence

The extent of displacement can be controlled by tuning the stamping duration and the ink concentration during sample fabrication. Figure 6.8 shows a matrix of STM images of AD SAMs contacted with an unpatterned C10-inked stamp using different combinations of stamping time and stamping ink concentration. In this matrix, the stamping duration increases to the right and the C10-inking solution concentration increases downwards. Each sample was imaged with STM and a representative 1000 Å× 1000 Å image was selected for each time and concentration pair. Although there is some variation across each sample due to concentration gradients across the stamp, degree of contact between the stamp and sample, etc., the increasing trends are reproducible. As observed and discussed in Chapter 4, it can be seen in the figure that both increasing the stamp duration and increasing the ink concentration increase the displacement. However, it should also be noted that, as in solution displacement, the degree of order of the C10 lattice also increases with increased displacement. For example, at an ink concentration of 100 mM, a 10 s stamping time results in randomly dispersed small clusters of C10 molecules. With increased stamping time, these clusters grow and order into larger patches, and finally C10 domains nearly cover the surface for a 180 s stamping time.

The extent of displacement is quantitatively shown in Figure 6.9, where the mean fractional coverage of C10 lattice is plotted as a function of stamping time (A) and ink concentration (B). The mean fractional coverages were extracted from a set of STM images for each sample as described above. As observed in Figure 6.8, the coverage increases with both stamp time and ink concentration. Furthermore, for each concentration there is a time below which there is little displacement. This time decreases with increasing concentration (i.e. for each stamping time there is also a concentration below which there is little displacement). This behavior is likely due to the ink transport from the stamp to the surface through the existing monolayer. Although the unpatterned stamp contacts the surface everywhere, the C10-ink adsorption is limited by the existing AD SAM, initially resulting in C10 patches at and about AD SAM defects. The longer the
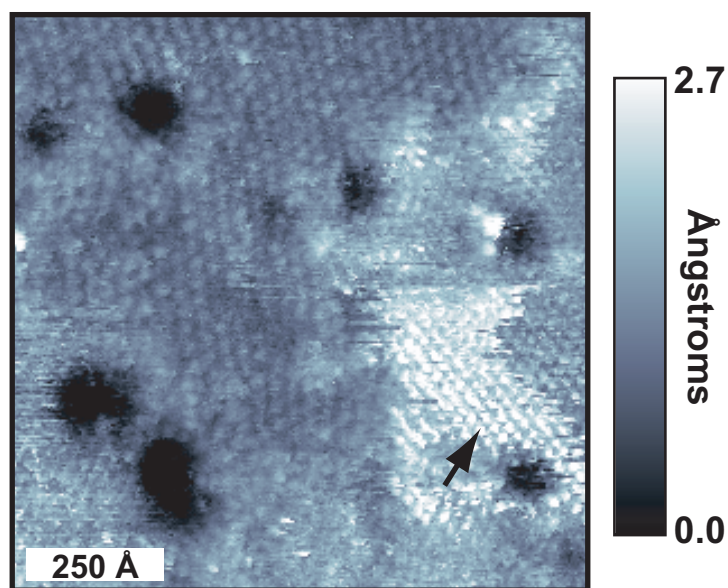
Figure 6.7. A molecularly resolved STM image of a two-component SAM of 1-decanethiolate and 1-adamantanethiolate fabricated by microdisplacement printing using an unpatterned PDMS stamp. The ordered lattice of both components can be seen; the more protruding SAM with the smaller lattice spacing (arrow) is 1-decanethiolate. Imaging parameters: V_{sample}: 1 V; I_{tunnel}: 4 pA; 175 Å $\times$ 175 Å.

Stamp Dwell Time (s)
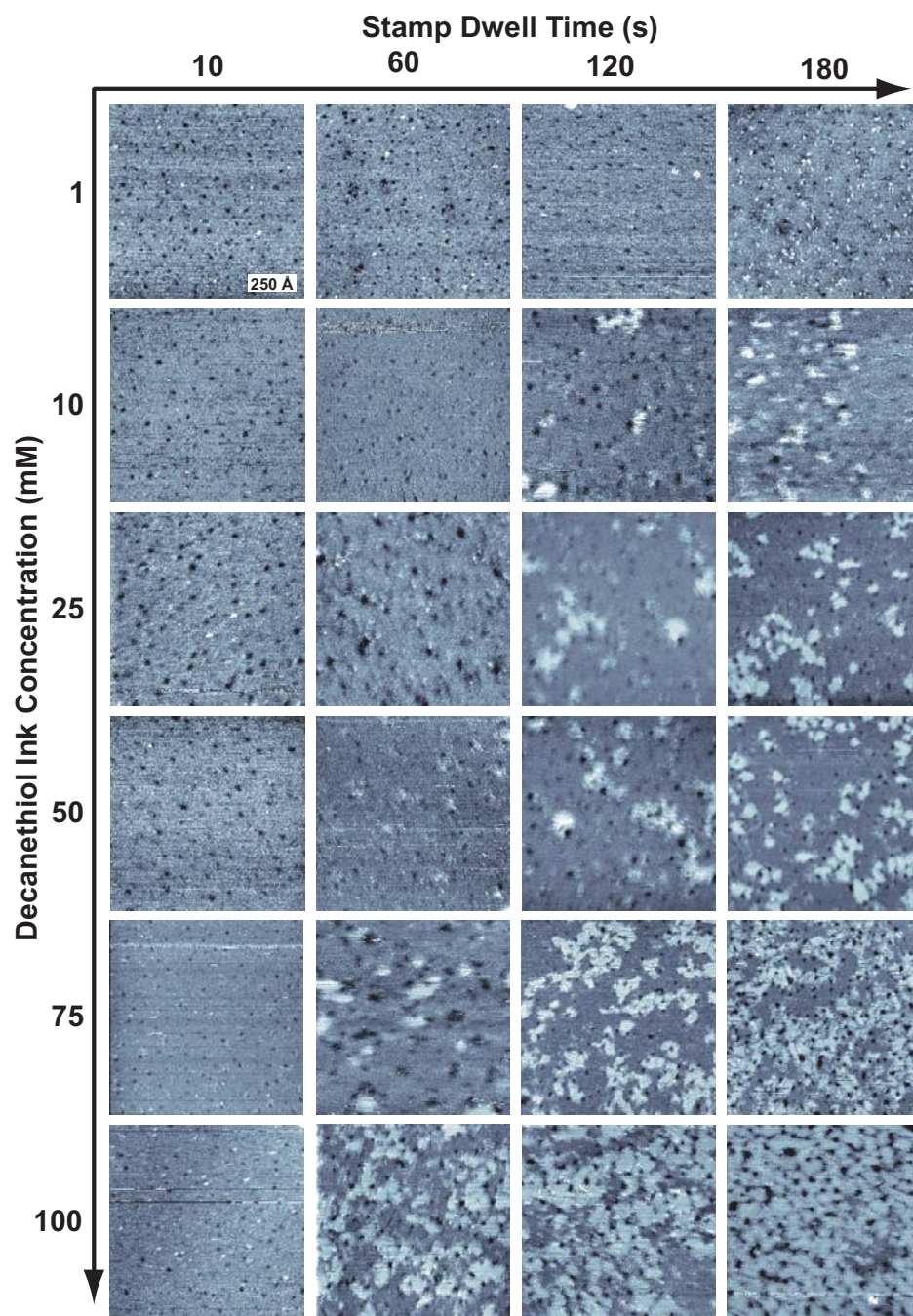
Figure 6.8. A matrix of STM images of microdisplacement printed 1-adamantanethiolate SAMs stamped with an unpatterned PDMS stamp inked with 1-decanethiol (imaged as protruding features). The concentration of the 1-decanethiol solution used was increased top to bottom, while the duration that the stamp was in contact with the sample was increased left to right. Imaging parameters (all images): V_{sample}: 1 V; I_{tunnel}: between 1 and 2 pA; 1000 Å × 1000 Å.

stamp contacts the surface and the higher the concentration of the ink on the stamp, the more the ink molecules have a chance to disrupt the AD SAM. As observed in other displacement studies, the limiting step is the initial removal and replacement of the pre-existing monolayer [238, 247]. Using these observed trends, we are able to optimize μDP; determining the detailed kinetics of the displacement stamping process from the STM data requires substantially greater statistics so as to be comparable with ensemble-averaging methods such as those used for determining the kinetics of solution displacement in Chapter 5 [33, 214, 218, 248, 249].

6.4.2.2 Patterned self-assembled monolayers

Using the data shown in Figures 6.8 and 6.9 for stamping with an unpatterned stamp, the stamping times and ink concentrations for analogous stamping with a patterned stamp can be estimated. Furthermore, kinetics studies of stamping displacement, similar to those for solution displacement (Chapter 5), are needed for each molecule to determine the degree of displacement more precisely. Displacement of AD by stamping of the molecules discussed here is expected to follow similar trends to those observed for AD and C10 in Figures 6.8 and 6.9.

Figure 6.10 demonstrates μDP patterning using 25 mM MUDA on a PDMS stamp with 1200 lines/mm for a stamp contact time of 3 min (A) and 50 mM ODT on a PDMS stamp with 5 μm by 5 μm square wells at a 10 μm pitch for a stamp contact time of 3 min (B). As in the unpatterned case, the stamp was contacted directly to a previously-assembled AD SAM. In Figure 6.10A, the MUDA molecules displaced the AD molecules where the stamp contacted the sample (along the lines in the PDMS stamp), creating patterned lines of MUDA. Similarly in Figure 6.10B, the ODT displaced the AD SAM everywhere except where the stamp wells were located, leaving squares of AD SAM surrounded by ODT SAM. The varying contrast observed between the AD and stamped molecule regions are likely caused by incomplete displacement of the AD SAM by the MUDA or ODT.

6.4.2.3 Patterning of low-molecular-weight molecules

We have successfully extended this technique to other molecules, including molecules that are too mobile on the surface to pattern by conventional μCP, specifically short chain ALKs. These low-molecular-weight molecules will laterally diffuse across the Au{111} surface during the patterning procedure, before backfilling is possible [231–233]. Figure 6.11 shows a patterned SAM
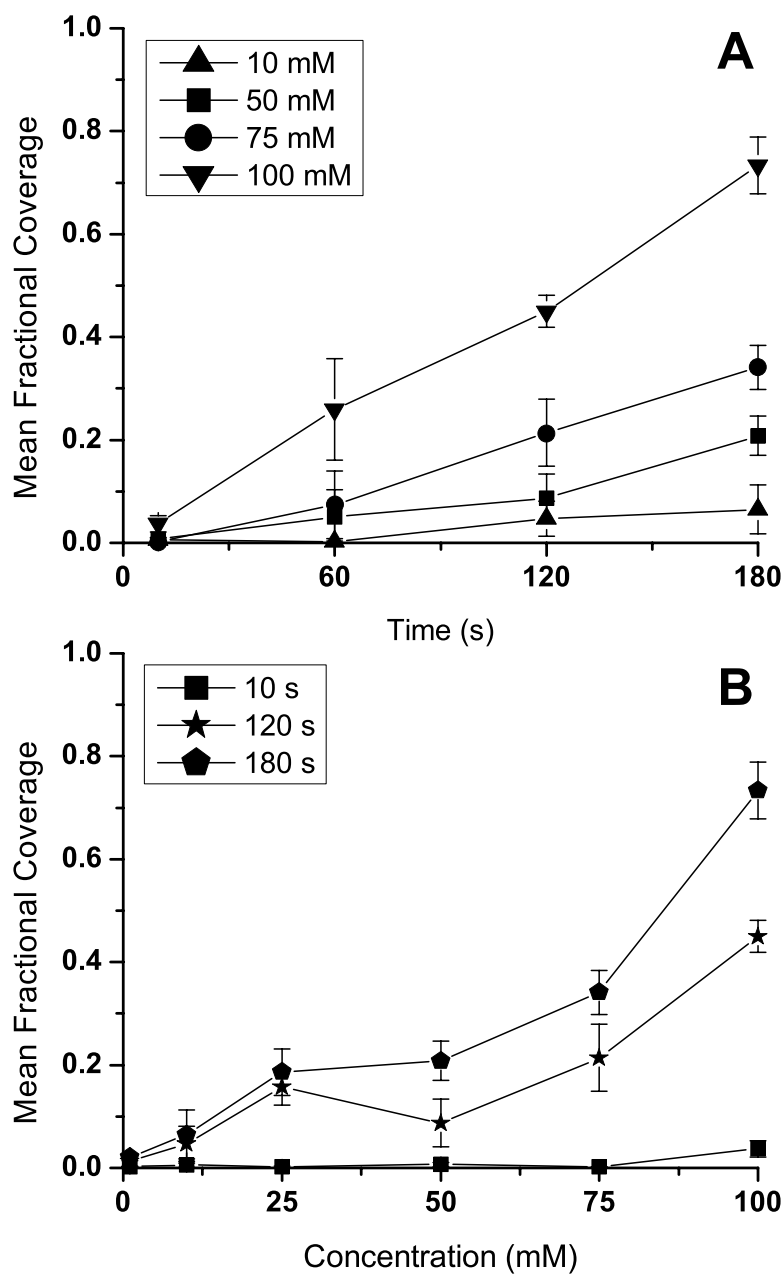
Figure 6.9. Plots of the mean fractional 1-decanethiolate coverage from STM images of microdisplacement printed samples as a function of stamp contact time (A) and as a function of ink concentration (B). Each point was averaged from a series of images that were 1000 Å × 1000 Å, with a V_{sample} of 1 V, and a I_{tunnel} between 1 pA and 2 pA.
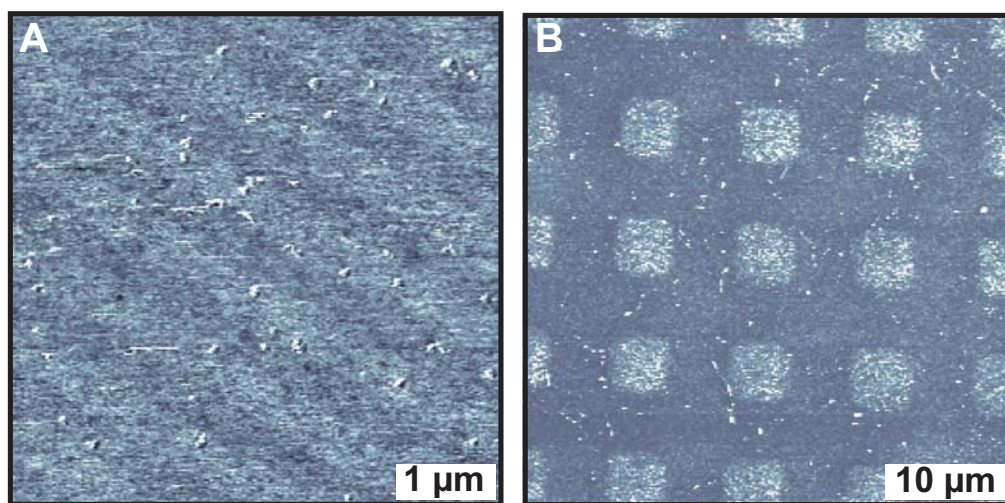
Figure 6.10. Images of patterned SAMs composed of 1-adamantanethiolate and 11-mercapto-undecanoic acid lines (A) and 1-adamantanethiolate squares surrounded by 1-octadecanethiolate (B) fabricated by microdisplacement printing. (A) Lateral force microscopy micrograph of a pattern made using a stamp with 1200 lines/mm inked with a 25 mM 11-mercaptoundecanoic acid solution (3 min contact time). The high-friction stripes are the stamped 11-mercaptoundecanoic acid and the low-friction stripes are the 1-adamantanethiolate SAM. Imaging parameters: Force setpoint: 0.5 nN; Scan rate: 2 Hz; 10 μm $\times$ 10 μm. (B) Non-contact phase micrograph of a pattern made using a stamp with 5 μm by 5 μm square wells at a 10 μm pitch that was inked with a 50 mM 1-octadecanethiol solution (3 min contact time). The high-contrast squares are the 1-adamantanethiolate SAM and the low-contrast background is the stamped 1-octadecanethiolate. Imaging parameters: Amplitude setpoint: -0.05 μm; Scan rate: 1 Hz; 40 μm $\times$ 40 μm.

created by μDP using 25 mM C10 on a PDMS stamp with 10 μm by 10 μm square posts at a 5 μm pitch (A) and 25 mM C8 on a PDMS stamp with 5 μm by 5 μm square posts at a 10 μm pitch (B). In both cases square regions of C10 and C8, respectively, that replicate the stamp geometry can be seen. The existence of the AD SAM blocks this diffusion *during* patterning, holding the molecules in place, making patterning of these molecules possible.

6.4.2.4 Further pattern processing to remove 1-adamantanethiolate molecules

To create more complex patterns, or patterns composed of more than one low-molecular-weight molecule, it is possible to replace the AD regions via a further solution deposition or patterning step [238]. To demonstrate this process, a number of LFM and KPM measurements were made.

The lateral forces in LFM images are all relative measurements, and therefore LFM was insufficient to show a change in molecular species. To distinguish one molecular species from another, both must be present in the same image, or some unchanging frictional reference must be available within the image, both of which were unfeasible for the solution processing experiments. Kelvin probe microscopy was used to identify and to quantify the molecular species present without the need for a molecular reference.

Microcontact printed samples were made by stamping one molecule and backfilling with another molecule and then measuring their potential difference with KPM. The measured potential differences are given for a variety of molecules in Table 6.1. In the table, the columns represent the stamped molecules and the rows are the molecules that were used to backfill. The potential difference is given as the stamped molecule minus the backfilled molecule, and therefore, a negative potential indicates that the backfilled molecular regions have a more positive surface potential than the stamped molecular regions.

It has been shown previously that with respect to MHDA, there is a potential shift with decreasing chain length for ALK molecules [250,251]. We see a similar trend; however, the standard deviation of the measurement is much higher than the actual shift in potential due to a different molecular species. The high standard deviation can be attributed to a few factors. Firstly, the inherent signal-to-noise for the KPM setup was measured to be ~200 mV. Secondly, because the second patterning step is a backfilling process, the stamped molecular regions are a mixture of more
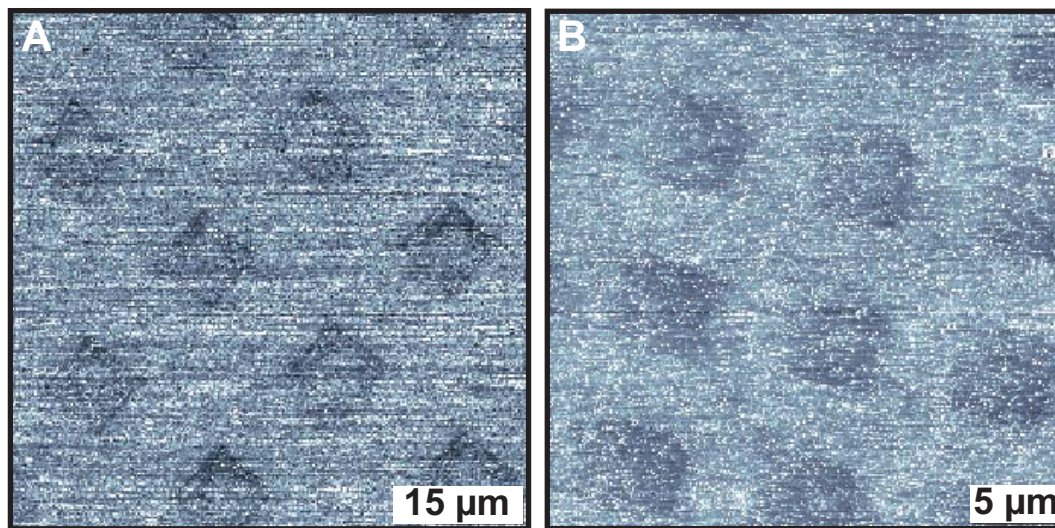
Figure 6.11. Images of patterned SAMs composed of molecules that are not patternable by traditional microcontact printing methods that were fabricated by microdisplacement printing. A) Lateral force microscopy micrograph of a pattern of squares of 1-decanethiolate surrounded by 1-adamantanethiolate made using a stamp with 10 μm by 10 μm square posts at a 20 μm pitch that was inked with a 25 mM 1-decanethiol solution (5 min stamp-substrate contact time). The low-friction squares are the stamped 1-decanethiolate and the high-friction background is the 1-adamantanethiolate SAM. Imaging parameters: Force setpoint: 2 nN; Scan rate: 2 Hz; 60 μm × 60 μm. (B) Lateral force microscopy micrograph of a pattern of squares of 1-octanethiolate surrounded by 1-adamantanethiolate made using a stamp with 5 μm by 5 μm square posts at a 10 μm pitch that was inked with a 25 mM 1-octanethiol solution (5 min stamp-substrate contact time). The low-friction squares are the stamped 1-octanethiolate and the high-friction background is the 1-adamantanethiolate SAM. Imaging parameters: Force setpoint: 1 nN; Scan rate: 1 Hz; 30 μm × 30 μm.

than one molecular component. This problem is compounded by the amount of contact made during stamping. Although care is taken to follow the same stamping procedure, it cannot be assured that the contact between the sample and the stamp is the same every time and is homogeneous over the whole sample. This is especially the case at the interfaces. Removing the interface region from the analysis improves the standard deviation slightly, but not significantly. Additionally, the molecular order of a particular region (which in turn is also affected by other molecular species and the degree of stamp homogeneity) should have a large impact on the measured potential. This is shown by the observation that stamping with molecule A and backfilling with molecule B does not yield the same potential difference as stamping with molecule B and backfilling with molecule A, as seen for example with the ODT/MUDA molecular pair.

Backfilled Molecule	Stamped Molecule	
	MUDA	ODT
AD	-0.38 ± 0.17 V	0.21 ± 0.14 V
ODT	-0.18 ± 0.19 V	–
C12	-0.24 ± 0.13V	0.12 ± 0.11 V
C10	-0.15 ± 0.16 V	0.22 ± 0.17 V
C8	0.02 ± 0.11 V	0.23 ± 0.13 V
C6	-0.09 ± 0.11 V	0.31 ± 0.16 V
MUDA	–	0.25 ± 0.16 V
MHDA	-0.08 ± 0.12 V	0.32 ± 0.16 V
AUDT	N/A*	0.23 ± 0.11 V

Table 6.1. The measured potential differences between the patterned molecular regions in μCP samples. The columns are the molecules used for the stamped regions and the columns are the molecules used for backfilling. *Although a pattern was visually discernable, the potential difference was too small to be measured.

The same procedure was used to determine the potential difference between stamped areas and the AD SAM in μDP fabricated samples for MUDA and ODT. In this case the molecules were stamped onto an AD SAM and the potential was measured between the stamped regions and the AD regions (stamped molecule potential minus AD potential). The potential differences were

measured as 0.11 ± 0.1 V and 0.06 ± 0.1 V for MUDA and ODT μDP, respectively. Neither of these values match those measured for the μCP samples.

Despite the ambiguous quantitative data, it has been observed that both the relative frictional and potential differences are consistent for LFM and KPM measurements, respectively. It should be possible to pick a molecular combination in which the contrast of an image for these two measurements will invert after the solution displacement step. For this to be the case, the patterned molecular regions must have frictional (or potential) properties that are between AD and the molecule used for solution displacement. In this case, the displacement of AD by the molecule in solution can be seen by the change in frictional (potential) properties of the regions surrounding the pattern from high (low) to low (high) relative to the patterned regions. This inversion of contrast experiment was attempted using both LFM and KPM. For LFM, MUDA was patterned and AUDT was used to displace the AD, and for KPM, AUDT was patterned and ODT was used to displace the AD (the measured potential difference between stamped AUDT and backfilled AD was 0.10 ± 0.10 V). However, no case of contrast inversion was observed for any molecular combination using either characterization technique. This could be due to incomplete displacement, leading to a mixed SAM with different frictional or potential properties. Additionally, the orientation of the molecules on the surface after displacement may be different (see Chapter 5), also causing different frictional or potential properties. Another possibility is that the displacing solution is also displacing the pattern molecules, although (as discussed below) phase images indicate no significant pattern displacement.

Figure 6.12 shows phase images of a MUDA-patterned μDP sample before (A) and after (B) it has been immersed in a C8 solution for 2 h. Each image in Figure 6.12 was taken at the same location on the sample, within a few tens of microns. Although it is not obvious from the images that the AD has been displaced, previous studies have shown that this is a sufficiently long exposure to completely replace the AD monolayer with C8 (see Chapters 4 and 5) [238]. It can be seen, however, that the pattern did not degrade after 2 h in solution. Additionally, such patterns remain after exposure to a thiolated solution for up to 9 h.

Further evidence that the AD in μDP samples is susceptible to further processing steps is shown in Figure 6.13, where a second patterning step was performed. Here, a patterned sample containing regions of 1-adamantanethiol is created by either μCP or μDP processes. This sample is then subjected to a second μDP step, during which only the AD regions are (further) displaced. As
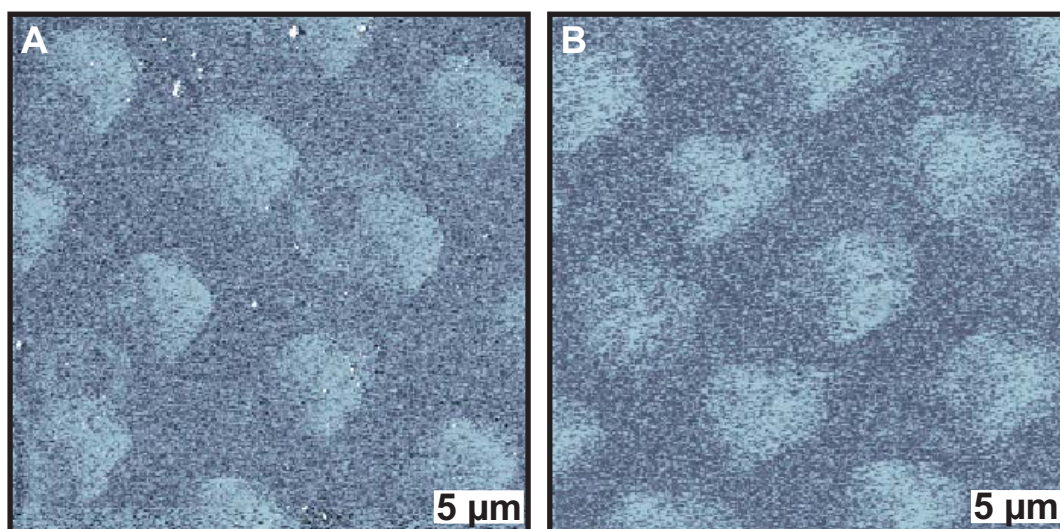
Figure 6.12. Non-contact phase micrographs of Au{111} patterned by microdisplacement printing using a PDMS stamp with 5 μm by 5 μm square posts at a 10 μm pitch that was inked with a 50 mM 11-mercaptoundecanoic acid solution (5 min contact time) before (A) and after (B) the sample was immersed in a 1 mM 1-octanethiol solution for 2 h. The high-contrast squares are the stamped 11-mercaptoundecanoic acid. A) Imaging parameters: Amplitude setpoint: -0.06 μm; Scan rate: 1 Hz; 30 μm $\times$ 30 μm. B) Imaging parameters: Amplitude setpoint: -0.1 μm; Scan rate: 1 Hz; 30 μm $\times$ 30 μm.

shown schematically in Figure 6.13A, this process results in a three component SAM made up of, in this case, large squares of one molecule, small squares of a second molecule, and the remaining AD in the background. Figure 6.13B shows a phase image of a MUDA-patterned μCP sample (large squares) that was backfilled with AD and then patterned a second time with C8 using μDP (small squares). The figure shows two sets of squares with different contrast rotated by $\sim45°$. A higher resolution LFM image of the same sample is shown in Figure 6.13C. In this image, as in the schematic, the small squares only displace the AD regions, resulting in parts of these squares and leaving the original large square pattern intact.

Using these complex patterning techniques, registration issues of placing two types of molecules in close proximity are avoided. Starting with the transient AD film and then patterning the molecular features sequentially, in order from the most interacting, to the least interacting (i.e. the least displaceable first), assures that the patterns are proximally placed, while maintaining intact features that do not laterally diffuse across the surface, at each step.

By these methods, it is also possible to pattern two low-molecular-weight molecules. Figure 6.14 shows an LFM image of an AD SAM that was patterned with C10 using μDP (large squares sample shown in Figure 6.11A), which was then further patterned with C8 using μDP (small squares). By this method a two-component, low-molecular-weight, separated, patterned sample was created via a solutionless, two-step process. This complex patterning is not possible using other soft lithography methods.

6.5   Conclusions

Microdisplacement printing increases the sophistication of traditional μCP by hindering the mobility of stamped molecules on the substrate surface both during and following the stamping process. The existence of the SAM before stamping blocks lateral movement of the stamped molecules during patterning, something that is not possible by secondary backfilling techniques. As a result, the number of patternable molecules is increased by adding molecules that are too mobile to pattern by other methods. Traditional μCP methods often require a solution deposition step, thereby degrading the resolution of the pattern interfaces as well as the composition of the patterns themselves due to molecular exchange. Microdisplacement printing eliminates the need for solvent exposure after stamping because no backfilling step is required. Additionally, the remaining AD regions can be displaced from μDP samples without pattern dissolution and with additional
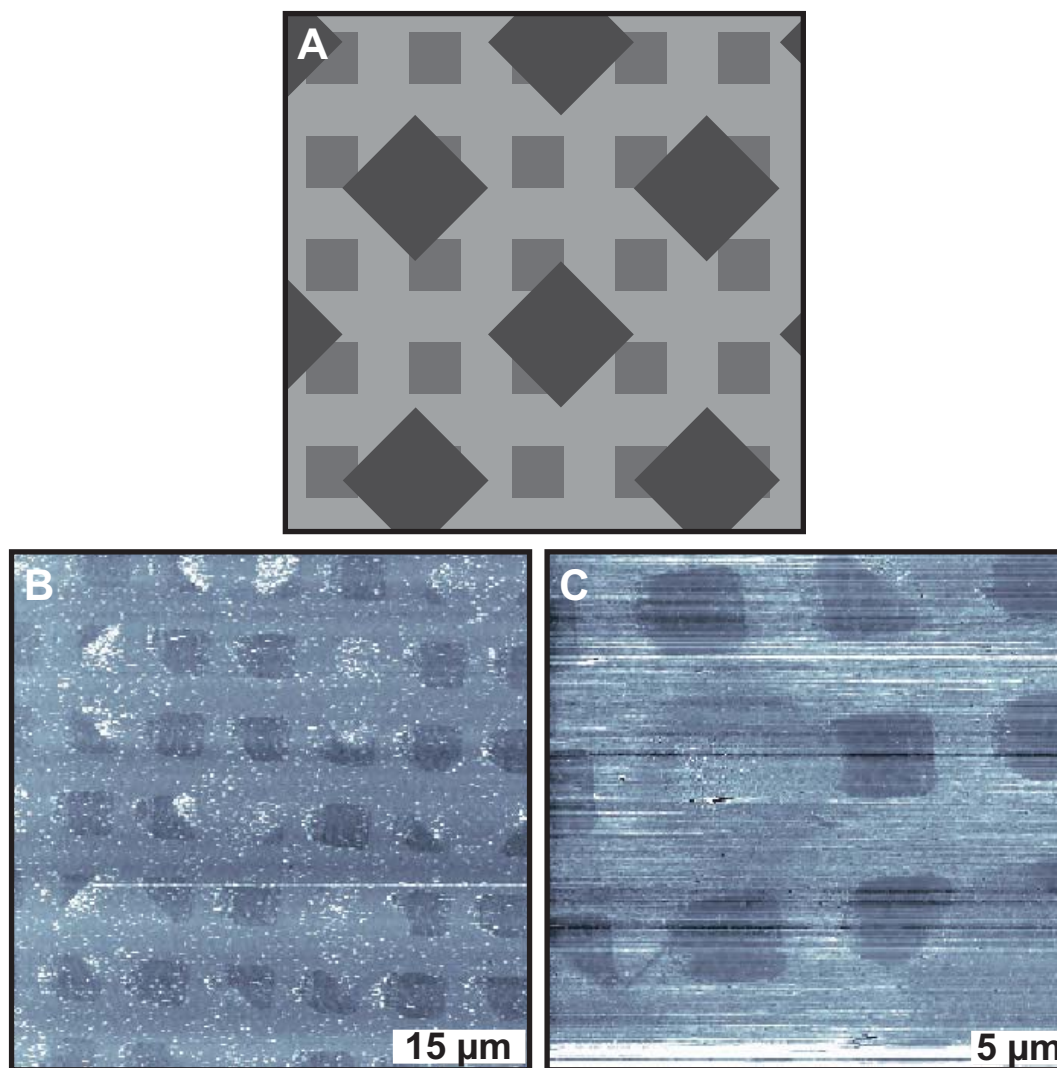
Figure 6.13. Examples of complex patterning by microdisplacement printing. A) Schematic depicting the result of two patterning steps using a stamp with large squares first and small squares (with a ~45°rotation) second. The light gray, black, and dark gray represent the 1-adamantanethiolate monolayer, the first patterned molecule (large squares), and the second patterned molecule (small squares), respectively. B and C) Non-contact phase and LFM micrographs a sample patterned by microcontact printing using a PDMS stamp with 10 μm by 10 μm square wells at a 20 μm pitch that was inked with a 5 mM solution of 11-mercaptoundecanoic acid (10 s contact time), backfilled with a 10 mM solution of 1-adamantanethiol for 5 min, and subsequently patterned by microdisplacement printing using a PDMS stamp with 5 μm by 5 μm square wells at a 10 μm pitch that was inked with a 25 mM 1-octanethiol solution (5 min contact time). B) Imaging parameters: Amplitude setpoint: -0.05 μm; Scan rate: 1 Hz; 60 μm × 60 μm. C) Because the 1-octanethiol displaces the 1-adamantanethiolate but does not displace the 11-mercaptoundecanoic acid, the result of the second pattern step is partial squares. Imaging parameters: Force setpoint: 50 nN; Scan rate: 1 Hz; 30 μm × 30 μm.
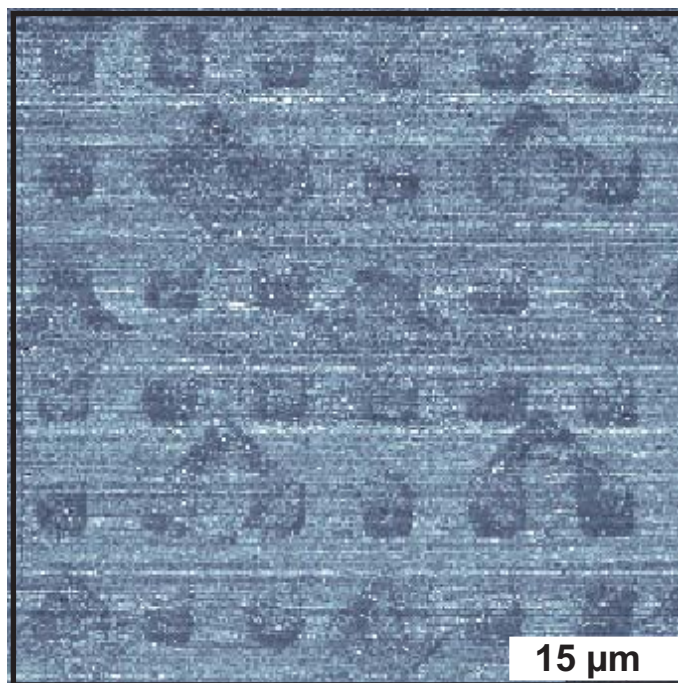
Figure 6.14. An example of complex patterning of two low-molecular-weight molecules by microdisplacement printing (refer to Figure 6.13 for a schematic). Lateral force microscopy micrograph of a sample patterned by microdisplacement printing using a PDMS stamp with 10 μm by 10 μm square wells at a 20 μm pitch that was inked with a 25 mM 1-decanethiol solution (5 min contact time), and subsequently patterned by microdisplacement printing using a PDMS stamp with 5 μm by 5 μm square wells at a 10 μm pitch that was inked with a 25 mM solution of 1-octanethiol (5 min contact time). Imaging parameters: Force setpoint: 1 nN; Scan rate: 2 Hz; 60 μm $\times$ 60 μm.

processing steps, complex multi-component patterns can be created. Microdisplacement printing extends the inexpensive and simple alternatives to traditional lithographic techniques. It may be possible to extend this exploitation of competitive adsorption for patterning of SAMs to other self-assembly patterning techniques.

Chapter 7

Nanoscale Patterning II: Dip-Pen Nanolithography and Displacement Dip-Pen Nanolithography

7.1 Introduction

The direct writing of material from the tip of an atomic force microscope to a substrate was first shown in 1995 by Jaschke and Butt [252]. This observation was then developed by Mirkin and co-workers into a robust patterning technique, which has come to be known as dip-pen nanolithography [77, 78]. The first DPN experiments used ALK as an "ink" (the molecules on the tip used for patterning) on a gold substrate [78]; however, the technique has since been extended to a variety of ink-substrate combinations, including polymers, biological molecules, and colloidal particles on semiconductors, oxides, and noble metals [77]. To date, the applications of DPN range from lithographic resists [82, 85, 253] to biologically compatible surfaces [6, 83, 254].

The most studied DPN system uses thiol-containing molecules, in particular ODT and MHDA, on gold surfaces. These two inks have been the subject of many investigations, in particular looking at the influence of the environmental conditions, such as relative humidity and temperature, on the writing process [255–259]. However, there have been comparatively few studies of the effect of the *surface* on both DPN ink transport from the tip to the surface and the ink diffusion across the surface.

The measured transport rate of the molecular ink depends sensitively on both the environmental conditions and the exact nature of the inked cantilever and the substrate surface. Therefore, the first step in any patterning by DPN is measurements of the molecular transport rate of the ink by patterning 'dots' (the shape defined by static tip ink deposition) with varying tip dwell times or 'lines' (the shape defined by moving tip ink deposition) with varying tip speeds. Assuming a constant flux of molecules from the molecularly coated cantilever to the surface, the patterned area is proportional to the tip dwell time. The assumption of a constant transport rate generally has been found to be valid; however, the rate constant can vary significantly from experiment to experiment [257–262].

Generally, the stationary tip measurements reported in the literature have had dwell times ranging from a few s to a few min [255, 257–259, 261, 262]. However, the transport rate measured with these short tip dwell times may not be valid when extrapolated to longer dwell times. In particular, the assumption of a constant transport rate does not take into account any effect of the already-deposited ink on the transport of subsequent ink. Small changes in the molecular transport rate as a result of the previously-patterned ink would not be evident in short time transport rate measurements.

In order to extend the displacement techniques discussed in the previous chapter to DPN, we must first understand ink transport. In particular, how do the ink molecules move from the inked tip through the water meniscus, across or through any existing molecules on the surface, to the substrate surface? In this chapter, we present results from extended time measurements of MHDA and ODT on Au{111} surfaces, and show that the dot dwell time affects the transport rate. Then we present the results of DPN experiments where both MHDA and ODT were written on the same area of a Au{111} substrate. By patterning the surface with one ink and subsequently writing on top of that structure with a second ink, we have examined the role that surface hydrophobicity plays in determining ink transport in DPN. In addition, we have established that during DPN, inks flow across a pre-existing surface monolayer and adsorb at the edge of the pattern rather than diffuse through the existing SAM. Finally, we show the adverse implications of these transport phenomena on displacement DPN.

7.2 Experimental Procedure

7.2.1 Sample and tip preparation

Commercially available Au{111} on mica substrates (Molecular Imaging, Tempe, AZ) were cleaned with UV/ozone just prior to use. The MHDA and ODT, used as ink, were purchased from Sigma-Aldrich (St. Louis, MO) and used as received. Silicon-nitride-coated plank-style cantilevers with a force constant of 0.05 N/m (Mikromasch, Portland, OR) were used both to write the desired patterns (molecularly coated, hereafter referred to as "inked," cantilevers) and to image the resulting structures (un-inked cantilevers). All cantilevers were cleaned with UV/ozone just prior to inking. Inking was performed in base bath-cleaned (KOH/saturated ethanol) glass vials.

Cantilevers inked with ODT were prepared by vapor deposition. The cantilever was exposed to sublimed ODT at 78 °C for ~10 min and then left in the sealed container at room temperature until the ODT recrystallized (~5 min). Cantilevers inked with MHDA were prepared following the "double dipping" procedure from a 5 mM acetonitrile solution of MHDA [263]. The cantilevers were dipped in the MHDA solution for ~5 s, dried with inert gas, exposed to 18 MΩ water vapor for 5 min, allowed to air dry for an additional 5 min, re-dipped in the MHDA solution for ~5 s, and dried with inert gas.

7.2.2 Nanolithography with the atomic force microscope

All DPN experiments were performed using a ThermoMicroscopes Autoprobe CP Research AFM (Veeco Instruments, Santa Barbara, CA) in contact mode. The AFM was enclosed in a glove bag (Spilfyter, VWR, West Chester, PA) for environmental control. Before each experiment and during tip or sample exchange, the glove bag was purged with dry inert gas to maintain constant atmospheric conditions. All experiments were performed at a relative humidity of $21 \pm 1\%$ and temperature of 24 ± 1 °C.

Dip-pen nanolithography writing was performed using the Nanolithography module in the ProScan software package (Veeco Instruments, Santa Barbara, CA). For double-ink experiments, an alignment mark was written along with the first structure (a few tens of μm away) for nanoscale alignment of subsequent cantilevers.

7.2.3 Lateral force microscopy imaging

Imaging of the DPN-generated structures was performed with un-inked cantilevers in lateral force microscopy (LFM) mode (see chapter 6 for an explanation of the LFM technique). Areas patterned with MHDA image with higher friction than the surrounding gold because of the protruding carboxylic acid groups, while ODT areas image with lower friction than the surrounding gold. In the LFM images presented in this paper, lighter contrast represents areas of higher frictional force between the tip and the sample, while darker contrast represents lower friction.

7.2.4 Image analysis

Using Matlab, the pattern areas were determined from the LFM images by one of two methods. The two methods are demonstrated in Figure 7.1. In one method (Figure 7.1C), a binary
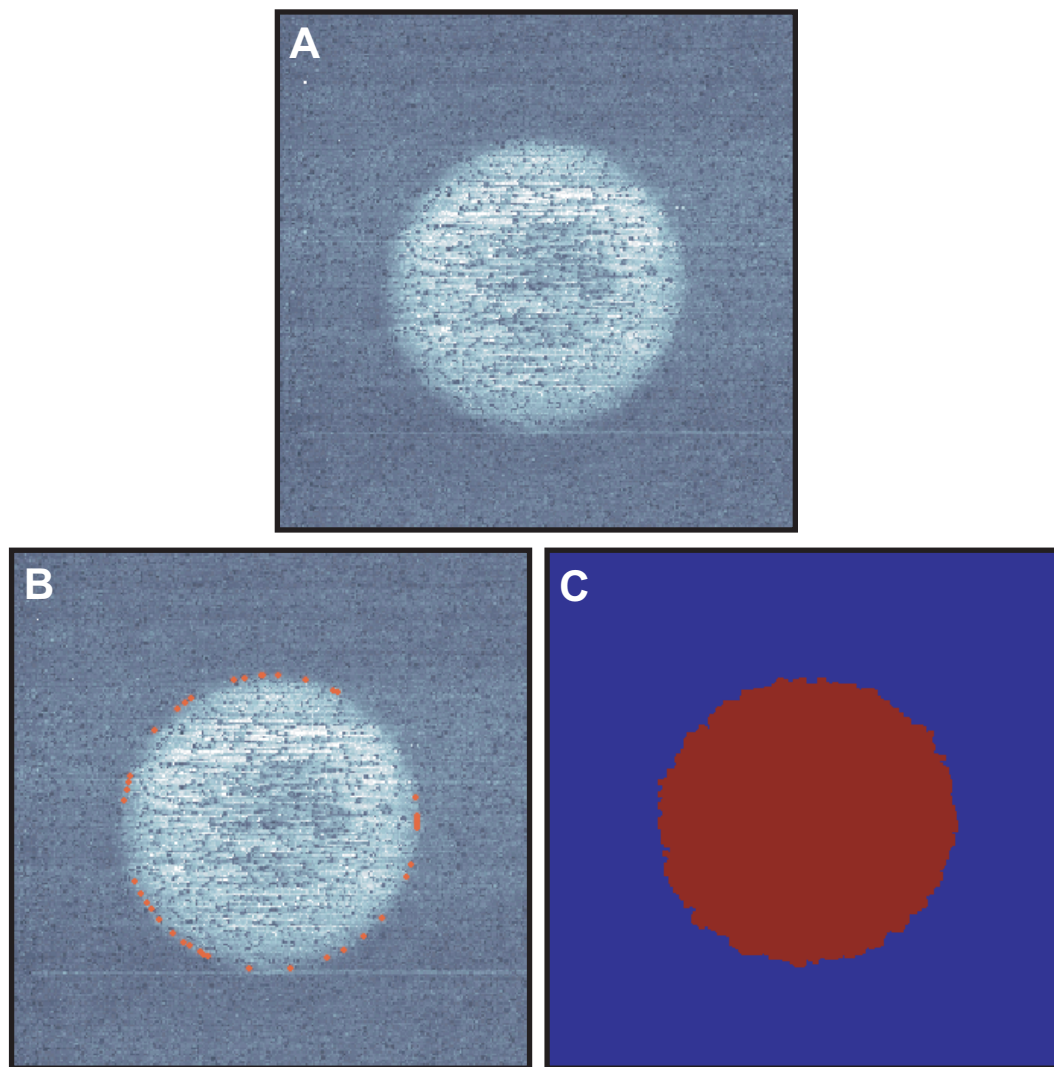
Figure 7.1. Images demonstrating the analyis techniques used to determine the areas of the DPN pattern features. A) An LFM image of a 16-mercaptohexadecanoic acid dot on Au{111}. Imaging parameters: Force setpoint: 1 nN; Scan rate: 4 Hz; 8 μm $\times$ 8 μm. B) An image generated by the circle analysis technique showing the proposed circumference of the dot based on three user-defined points. C) An image generated by the threshholding technique showing the area above a user-defined threshold that was then labeled as a patterned feature.

image was generated from a user-defined threshold of the AFM image of the pattern. Each distinct feature in the binary image was then labeled separately. The number of pixels in each feature was then counted and the area of each was determined based on the size of the image (Å/pixel).

The other method (Figure 7.1B) was used for the dot features only. In this case, three points $(P1 : (X1, Y1)$, $P2 : (X2, Y2)$, and $P3 : (X3, Y3))$ were defined along the perimeter of the dot. From these points, a circle defining the dot was generated. The center of the circle was determined by the equations,

$$X_{center} = \frac{m_a m_b (Y1 - Y3) + m_b (X1 + X2) - m_a (X2 + X3)}{2(m_b - m_a)},$$ (7.1)

and

$$Y_{center} = -\frac{1}{m_b}(X_{center} - \frac{X2 - X3}{2}) + \frac{Y2 + Y3}{2},$$ (7.2)

where (X_{center}, Y_{center}) are the coordinates for the center, and m_a and m_b are the slopes of lines from $P1$ to $P2$ and $P2$ to $P3$, respectively. The radius of the circle was then the distance between the center point and any of the three user-defined points. The number of pixels that fell within the defined circle was counted and the area was determined in the same manner as the first method. The advantage of the first method is that it measures the exact areas of the pattern, inclusive of small defects in the pattern. The second method can only be used for nearly perfect dot features but streaks and lines within the images from changes in the tip morphology do not influence the analysis. Both methods gave the same areas within a few pixels.

7.2.5 Determining writing coefficients

Before starting each of the experiments (and often several times during the experiments), each sample and tip combination was calibrated by determining the ink transport rate. The extended time ink transport experiments are an extension of this same principle.

To determine the ink transport, dots or lines were drawn with defined tip dwell times (in the case of dots) or tip speeds (in the case of lines). The diameters of the dots and the widths of the lines were determined from the images. The dot diameter squared was plotted against dwell time and the line widths were plotted against the inverse of the tip speed. From a liner fit to these plots the ink transport rate was estimated. It should be noted, however, that the ink transport rate changes with time and molecular presence (as explained below).
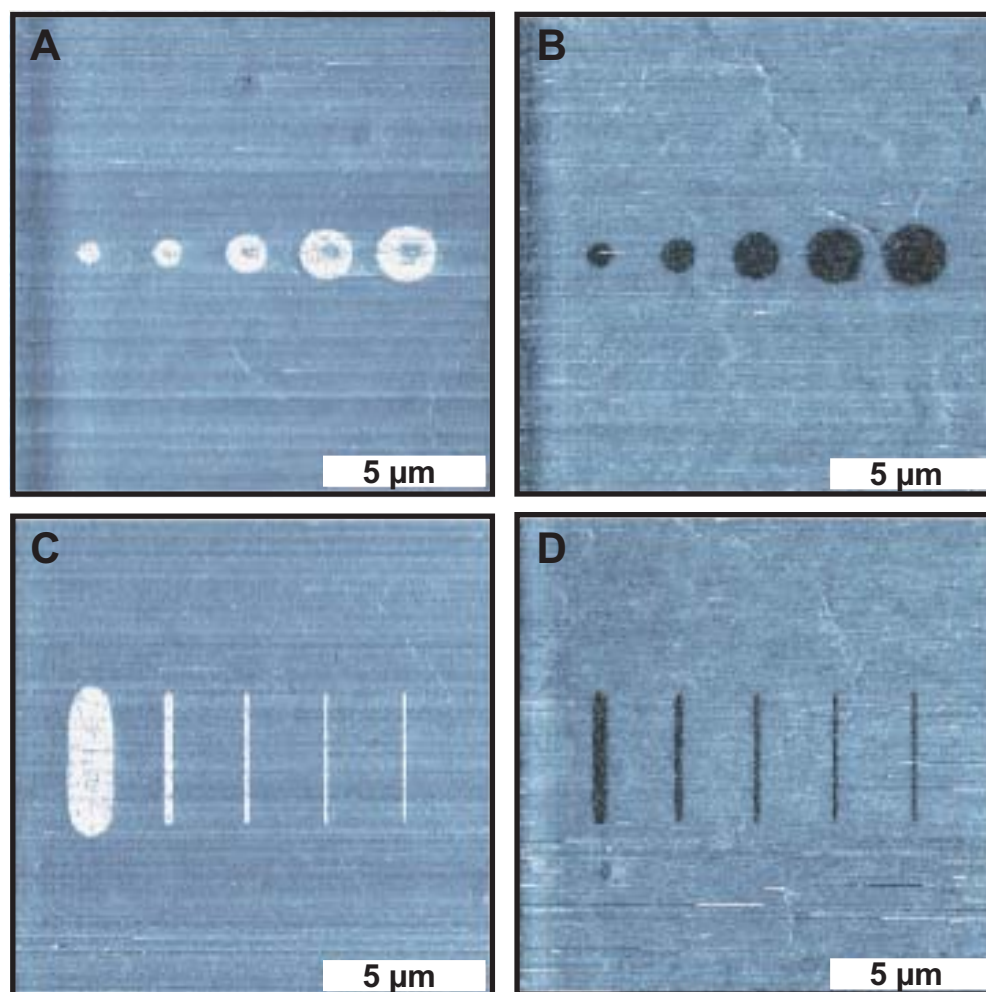
Figure 7.2. Lateral force microscopy images of ink transport measurements using DPN defined dots and lines of 16-mercaptohexadecanoic acid (A and C) and 1-octadecanethiolate (B and D) on Au{111}. A) 16-Mercaptohexadecanoic acid dots fabricated using dwell times, from left to right, of 30 s, 60 s, 120 s, 180 s, and 240 s. Imaging parameters: Force setpoint: 1 nN; Scan rate: 6 Hz; 15 μm $\times$ 15 μm. B) 1-Octadecanethiolate dots fabricated using dwell times, from left to right, of 30 s, 60 s, 120 s, 180 s, and 240 s. Imaging parameters: Force setpoint: 1 nN; Scan rate: 4 Hz; 15 μm $\times$ 15 μm. C) 16-Mercaptohexadecanoic acid lines fabricated using tip speeds, from left to right, of 0.005 μm/s, 0.0288 μm/s, 0.0525 μm/s, 0.0763 μm/s, and 0.1 μm/s. Imaging parameters: Force setpoint: 1 nN; Scan rate: 4 Hz; 15 μm $\times$ 15 μm. D) 1-Octadecanethiolate lines fabricated using tip speeds, from left to right, of 0.025 μm/s, 0.0438 μm/s, 0.0625 μm/s, 0.0813 μm/s, and 0.1 μm/s. Imaging parameters: Force setpoint: 1 nN; Scan rate: 4 Hz; 15 μm $\times$ 15 μm.

Images of example ink transport measurements for MHDA and ODT on a bare Au{111} surface are shown in Figure 7.2. The determined transport rates for these calibrations were 0.014 μm^2/s, 0.071 μm^2/s, 0.0169 μm^2/s, and 0.010 μm^2/s for the MHDA dots, MHDA lines, ODT dots, and ODT lines, respectively. However, these rates are not representative of all the transport rates; there was a large deviation of transport rates from experiment to experiment. The average transport rates on bare Au{111} from all the experiments were 0.033 $\pm$ 0.021 μm^2/s, 0.041 $\pm$ 0.027 μm^2/s, 0.014 $\pm$ 0.013 μm^2/s, and 0.015 $\pm$ 0.014 μm^2/s, for the MHDA dots, MHDA lines, ODT dots, and ODT lines, respectively.

7.3 Results and Discussion

7.3.1 Extended Time Ink Transport Measurements in Dip-pen nanolithography

Long-time measurements were performed for ODT and MHDA by writing a set of 11 dots with dwell times ranging from 15 s to 2 h. The use of dot features allowed for the determination of the ink transport rate without the added influence of the tip velocity that would be present if line features were used. In each case, the set of 11 dots was repeated two additional times, resulting in three copies of the sets of dots in a total writing time of 19 h. For the first set of dots, the dot dwell times started at 15 s and increased to 2 h, while for the final two sets, the dwell times were reversed and started with 2 h and decreased to 15 s. By reversing the order of the dot dwell times for Sets 2 and 3, the writing behavior could be broken down into two independent contributions, a dependence on the total writing time and a dependence on the dot dwell time.

The areas of each of the 33 patterned dots were calculated from LFM images, and the transport rate for each dot was determined by dividing the dot area by the corresponding dot dwell time.

Figure 7.3 shows the results of these long time transport experiments, plotted as the molecular transport rate for both ODT (A) and MHDA (B) as a function of the *total writing time* (the length of time from the beginning of the experiment when the particular dot was written). For ODT, the transport rate is nearly constant except for sharp increases around 0 s, 4.6×10^4 s ($\sim$12.8 h), and 6.9×10^4 s ($\sim$19.1 h) total writing time. These three times correspond to the beginning of Set 1 and the ends of Sets 2 and 3, when dots with short dwell times were being written. In the case of MHDA, the measured transport rate decreases significantly during the course of the

entire experiment. In addition to this overall decrease, similar to the results for ODT, the transport rate for MHDA increases at the beginning of Set 1 and the ends of Sets 2 and 3, when the dots with short dwell times were being patterned.

Consistent with the results shown in Figure 7.3A, Sheehan and Whitman observed no significant change in the transport rate of ODT throughout 24 h of continuous writing in a dry nitrogen atmosphere [258]. In contrast, Schwartz and co-workers reported decreases in MHDA transport rate over several h of writing [255], similar to Figure 7.3B. They observed roughly exponential decreases in the molecular transport rates with relaxation times ranging from tens of min to a few h for cantilevers with various inking protocols. They attributed this phenomenon to depletion of the ink from the region of the cantilever near the surface as a result of extended periods of writing. In addition, solution-deposited cantilevers tended to have longer equilibration times and higher stready-state transport rates than those deposited by solutionless methods, indicating that solvent plays a critical role in determining the mobility and distribution of ink on (and from) the cantilever.

The data in Figure 7.3 for both ODT and MHDA were fit to exponential curves. As seen in Figure 7.3A, the exponential curve does not fit the ODT data ($R^2 = 0.18$). However, for MHDA (Figure 7.3B), the exponential curve agrees reasonably with the data except at the beginning of Set 1 and the ends of Sets 2 and 3, when the dots with short dwell times were patterned ($R^2 = 0.94$). The observed relaxation time ($1/k$ from the equation $A \exp(-kt)$) of 7.5 ± 1.0 h is longer than that reported by Schwartz and co-workers. The different inking protocols used as well as the variability from tip to tip observed by Schwartz even for nominally identical inking protocols [257] offer an explanation for this difference.

Ink transport as a function of *dwell time* can be observed from the residual transport rate (measured transport rate minus fit). Figure 7.4 shows these residual transport rates for both ODT (A) and MHDA (B) plotted as a function of the dot dwell time for each set of dots. When corrected for the overall trend with writing time in this way, the data for each set of dots are consistent. For both ODT (Figure 7.4A) and MHDA (Figure 7.4B), the residual transport rate was highest for small dot dwell times and decreased to a relatively constant value for tip dwell times greater than 300 s.

This behavior highlights the fact that patterning small features (i.e. short dwell times) gives different results than patterning large features (long dwell times). In particular, the transport rate for small dwell times, when the inked cantilever writes on an unpatterned substrate, is higher. For

longer dwell times, when the cantilever continues to pattern a region that already has ink patterned on it, the transport rate is lower. Thus, short-time measurements are inaccurate in determining the transport rates for features patterned with longer dwell times. To ensure that large DPN features have the desired sizes, pre-patterning transport rate measurements need to be on the same time scale (and thus size scale) as those features.

For all the extended time studies performed in our laboratory, we observed both overall decreases in the MHDA transport rate with writing time and that the writing for small dot dwell times differed from those for long dwell times. However, quantitatively, the writing showed large variability from experiment to experiment.

7.3.2   Dual-Ink Dip-Pen Nanolithography Studies to Elucidate Ink Transport

Figure 7.5 illustrates the stages of an example double-ink experiment, where ODT dots were patterned on top of MHDA dots. At each stage in the experiment, the patterned features were imaged in LFM mode with a clean un-inked cantilever, and these images are shown in the figure. Figure 7.5A shows five MHDA dots (patterned with identical dwell times of 356 s, chosen to pattern nominally 2 μm diameter dots) after the MHDA patterning step. Dots M1 and M3 are the dots on which ODT was subsequently written, and Dots M2 and M4 are dots that were used for reference after ODT patterning. Dot M5 is an additional alignment dot closer to the experimental pattern, used for final alignment verification. Figure 7.5B shows the full structure after ODT was patterned. Here, ODT was patterned on top of Dots M1 and M3 (Dots O*1 and O*3) using two different dwell times of 236 s and 943 s (chosen to pattern nominally 2 μm and 4 μm diameter dots, respectively). The same dwell times were used to pattern additional reference dots of ODT (Dots O*2 and O*4). For the rest of the paper, all DPN-generated objects are labeled in a similar manner. 'M' ('O') indicates the structure was patterned with MHDA (ODT); no asterisk (asterisk) indicates the structure was patterned in the first (second) step.

This same general procedure was used for all the double-ink experiments discussed below. Single-ink control experiments were also performed using the same method, but without switching inks between the two patterning steps.
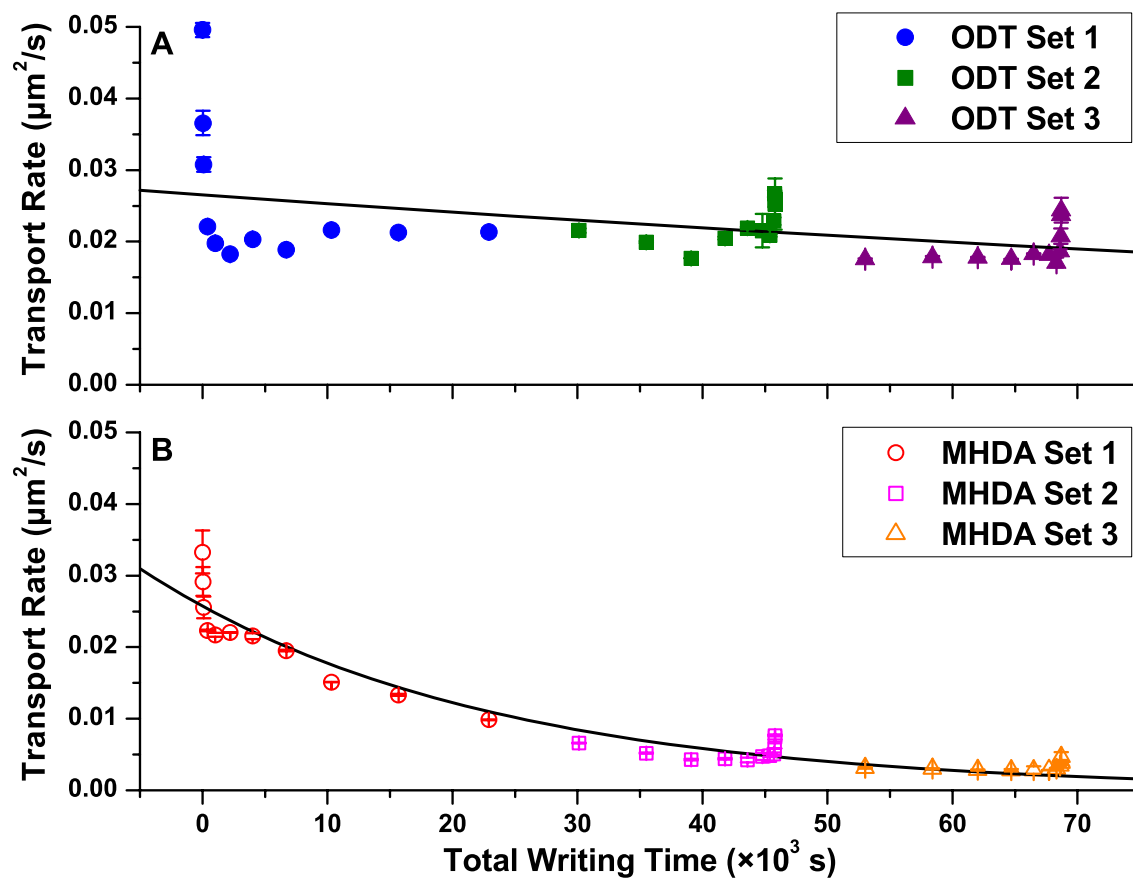
Figure 7.3. Plots of the transport rate (dot area divided by tip dwell time) as a function of the total writing time for long time transport measurements with 1-octadecanethiol (A) and 16-mercaptohexadecanoic acid (B) with exponential fits.
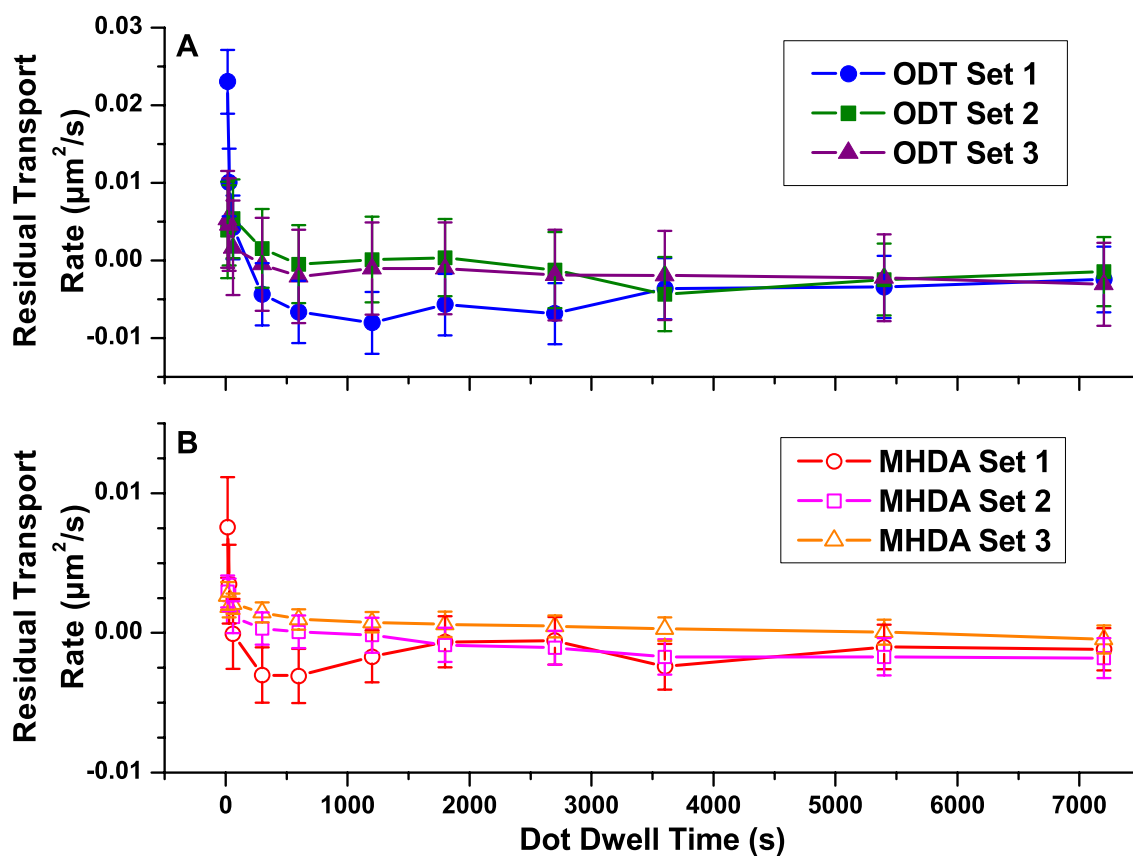
Figure 7.4. Plots of the residual transport rate (measured transport rate − exponential fit in Figure 7.3) as a function of tip dwell time for 1-octadecanethiol (A) and 16-mercaptohexadecanoic acid (B).
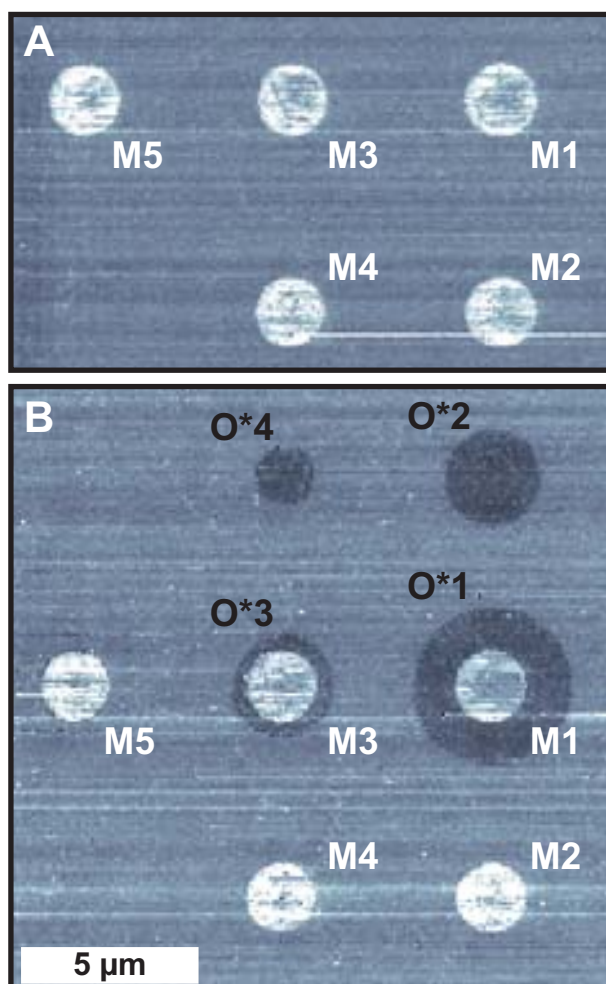
Figure 7.5. Extracts from two 20 μm × 20 μm LFM images showing the stages of a double-ink DPN experiment. A) Five dots of 16-mercaptohexadecanoic acid (M1–M5), patterned with identical dwell times 356 s. B) Four dots of 1-octadecanethiolate (O*1–O*4), two of which (O*1 and O*3) were patterned on top of the previously-patterned 16-mercaptohexadecanoic acid dots (M1 and M3). Dots O*1 and O*2 were patterned with the same dwell time of 943 s, and dots O*3 and O*4 were patterned with the same (shorter) dwell time of 236 s. Imaging parameters: Force setpoint: 1 nN; Scan rate: 4 Hz; 20 μm × 20 μm.

7.3.3 Double-Ink stationary tip experiment

Figure 7.6 shows the results of two double-ink dot-on-top-of-dot experiments of the type shown in Figure 7.5, where ODT was patterned on top of MHDA (A) and MHDA was patterned on top of ODT (B). Dots M1 and M2 (O1 and O2) were patterned in the first step with identical dwell times of 356 s (236 s), chosen to pattern nominally 2 μm diameter dots, and then Dots O*1 and O*2 (M*1 and M*2) were patterned in the second step, again with identical dwell times of 943 s (1146 s), chosen to pattern nominally 4 μm diameter dots. In both cases, the result of the second patterning step (O*1 or M*1) was a region of the second ink on the outside of the previously-patterned feature (M1 or O1, respectively). From this observation, we conclude that for DPN of MHDA and ODT, both inks diffuse from the AFM tip on the top of the pre-existing SAM and adsorb to the bare surface at the periphery of the feature.

For each experiment, the areas of the patterned regions of MHDA and ODT were calculated. Because the ink transport rate in DPN varies from experiment to experiment, the areas of the patterned regions are not useful by themselves. Instead, we define a relative transport rate, $R_{I*|I}$, which compares the transport for the ink I^* (O* for ODT or M* for MHDA) on a surface patterned with the ink I (M or O respectively) to the transport of I^* on the bare Au{111} surface during the same experiment. For each ink combination,

$$R_{I*|I} = \frac{A_{I*|I}}{A_{I*|\text{Au}}}, \tag{7.3}$$

where $A_{I*|I}$ is the area of I^* that was patterned on top of I and $A_{I*|\text{Au}}$ is the area of the reference dot of I^* patterned on bare Au{111} using the same dwell time in the same experiment. If ink transport were not affected by the presence of the patterned feature already on the surface, the relative transport rate calculated in this way would be equal to 1.

For ODT writing on MHDA, $R_{O*|M} = 1.8 \pm 0.6$. In contrast, from MHDA writing on ODT, $R_{M*|O} = 0.39 \pm 0.14$. This large difference in relative transport rates is strong evidence that the nature of the substrate plays a crucial role in determining the ink transport in DPN. In particular, ODT transport is sped up when writing on MHDA compared to writing on bare Au{111}, while MHDA transport is slowed down when writing on ODT.

This conclusion helps explain why the O1/M*1 structure in Figure 7.6B is not symmetric. The two dotted lines in Figure 7.6B show the horizontal locations of the center of the M*2 dot
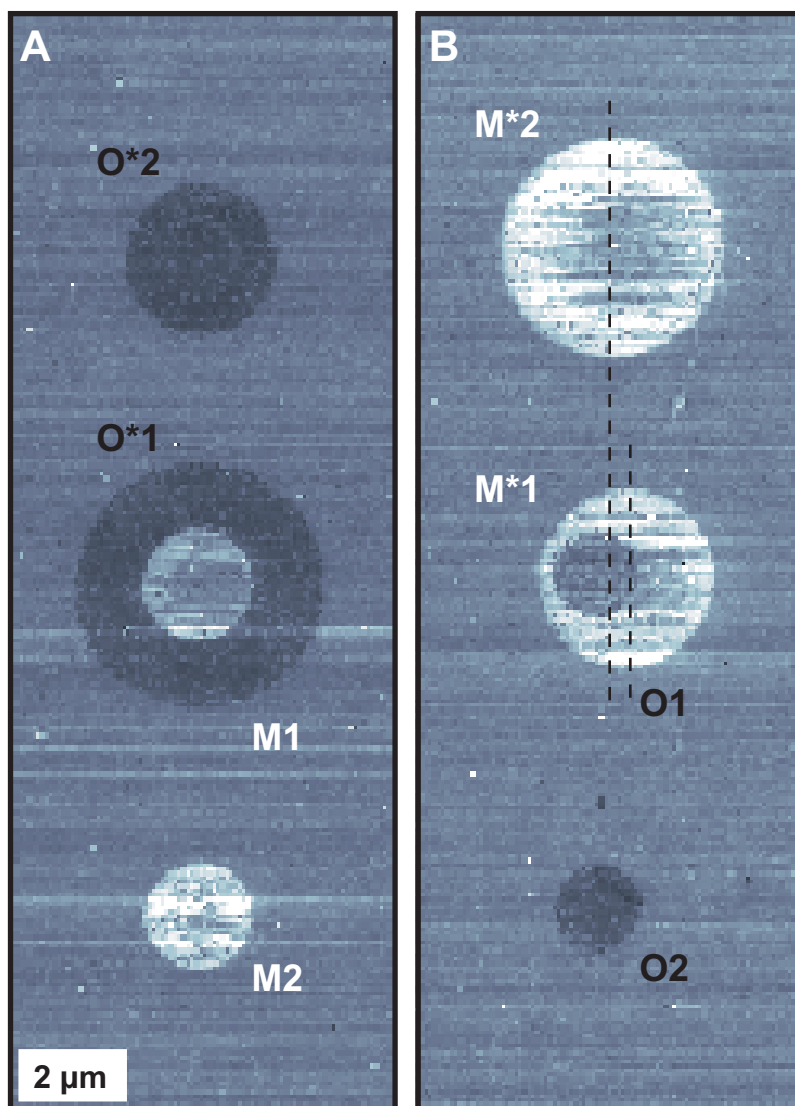
Figure 7.6. Extracts from two 20 μm × 20 μm LFM images from double-ink DPN experiments. A) First, the middle (M1) and lower (M2) dots were patterned with identical dwell times of 356 s. Then, the middle (O*1) on top of M1, and upper (O*2) dots were patterned with identical dwell times of 943 s. B) First the middle (O1) and lower (O2) dots were patterned with identical dwell times of 236 s. Then the middle (M*1) on top of O1, and upper (M*2) dots were patterned with identical dwell times of 1146 s. The two vertical dotted lines show the horizontal locations of the center of the M*2 dot (longer line) and the M*1 dot (shorter line). Imaging parameters: Force setpoint: 1 nN; Scan rate: 4 Hz; 20 μm × 20 μm.

(longer line) and the M*1 dot (shorter line). The longer dotted line does not pass through the center of the O1 dot, indicating there was a small shift to the right in the registration between the patterning of ODT in the first step and the patterning of MHDA in the second step. However, the shorter line is even farther to the right of the center of the O1 dot, showing that the small shift in registration of the patterning locations was amplified in the results of that patterning. Because transport of MHDA was inhibited when patterning on the ODT, small differences in the symmetry of the pattern were increased.

7.3.3.1   Single-ink stationary tip control experiment

As a control experiment for the double-ink dot-on-top-of-dot experiments, analogous single-ink experiments were performed using the method shown in Figure 7.5 but without changing the ink between the two patterning steps. Figure 7.7 shows the results of this two step patterning with MHDA (A) and ODT (B). Dots M3 and M4 (O3 and O4) were patterned in the first step with identical dwell times of 404 s (217 s), chosen to pattern nominally 2 μm diameter dots. Then Dots M*3 and M*4 (O*3 and O*4) were patterned in the second step, again with identical dwell times of 404 s (217 s), chosen to pattern nominally 2 μm diameter dots.

For each single-ink experiment, the areas of the individual patterned features were calculated. In each case, the area of the reference dot from the first patterning step (Dot 4 in Figure 7.7) was subtracted from the area of the dot patterned in two steps (Dot 3/*3). The result represents the additional ink patterned in the second step on top of the already-patterned ink, $A_{I*|I}$. This area was compared to the area, $A_{I*|\mathrm{Au}}$, of the reference dot from the second patterning step (Dot *4). For each single-ink experiment, the relative transport rate was calculated from these areas using equation 7.3. If transport were not affected by the ink already on the surface, then the sum of the areas of Dot 4 and Dot *4 would be equal to the area of Dot 3/*3, and $R_{I*|I}$ would be equal to 1.

For MHDA writing on already-patterned MHDA, $R_{\mathrm{M}*|\mathrm{M}} = 1.02 \pm 0.04$, indicating that MHDA transport is not affected by MHDA already on the surface, within the error of the measurement. In contrast, $R_{\mathrm{O}*|\mathrm{O}} = 0.82 \pm 0.08$, indicating that ODT transport is slowed down slightly by the presence of the already-patterned ODT.
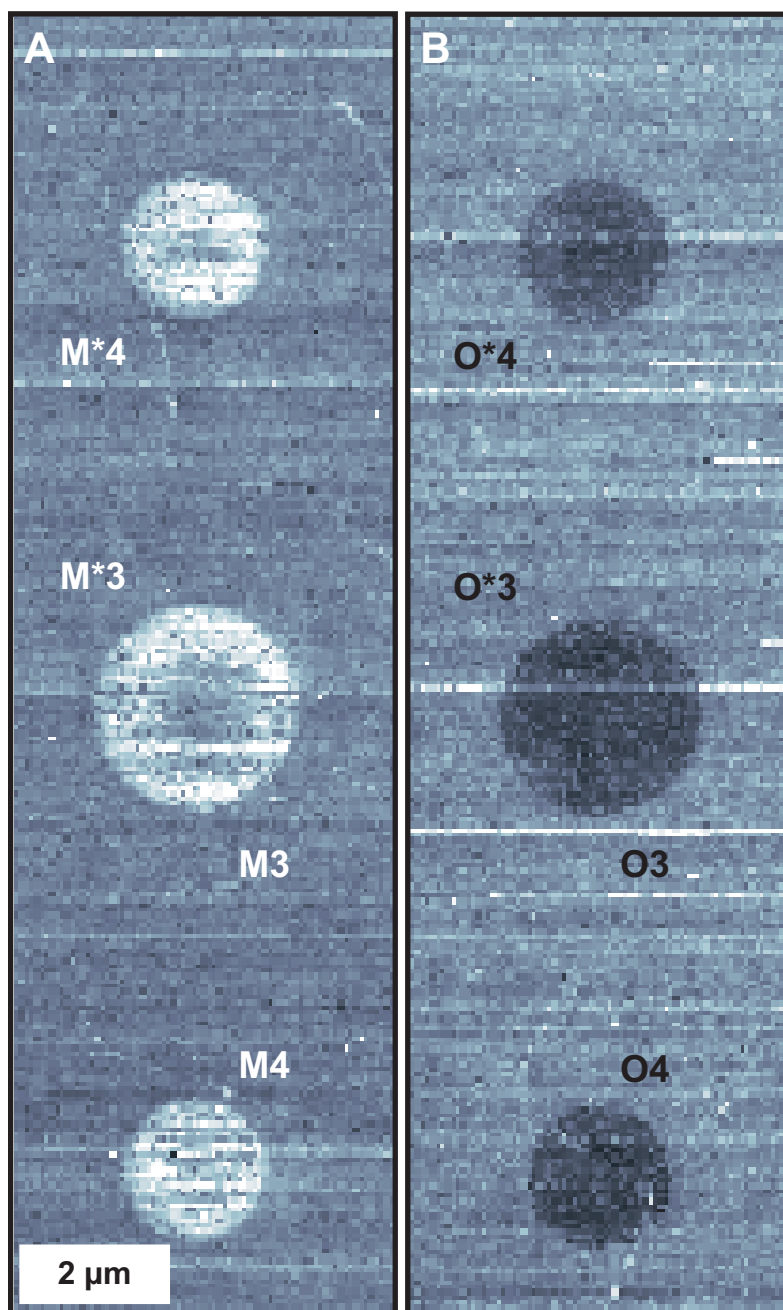
Figure 7.7. Extracts from two 17 μm $\times$ 17 μmLFM images from two single-ink DPN experiments. Four dots of 16-mercaptohexadecanoic acid (A) and 1-octadecanethiolate (B) were patterned in two steps. First, the middle (M3 or O3) and lower (M4 or O4) dots were patterned with identical dwell times of 404 s and 217 s for the 16-mercaptohexadecanoic acid and 1-octadecanethiolate dots, respectively. Then, the middle (M*3 or O*3), on top of M3 or O3, and upper (M*4 or O*4) dots were patterned with identical dwell times of 404 s and 217 s for the 16-mercaptohexadecanoic acid and 1-octadecanethiolate dots, respectively. Imaging parameters: Force setpoint: 1 nN; Scan rate: 4 Hz; 17 μm $\times$ 17 μm.

7.3.3.2 Double-ink mobile ink experiment

Figure 7.8 shows results from double-ink experiments where an ODT cross was patterned on top of an MHDA dot (A) and an MHDA cross was patterned onto an ODT dot (B). This geometry was similar to the dot-on-top-of-dot geometry, except that in the second patterning step, the tip moved across the patterned feature, rather than being stationary. In the case of ODT patterning on top of MHDA (Figure 7.8A), the ODT deposited in a ring around the outside of the MHDA dot in addition to the periphery cross structure. In the opposite case (Figure 7.8B), the MHDA deposited only as the specified cross feature.

This difference is consistent with the results seen in the double-ink dot-on-top-of-dot experiments, where the relative transport rate for ODT patterning on MHDA, $R_{O^*,M}$, was larger than 1 while the reverse relative transport rate, $R_{M^*,O}$, was smaller than 1. When the ODT-inked tip encountered the already-patterned MHDA feature, the transport rate increased and the ink diffused in all directions across the top of the existing MHDA, resulting in ODT around the periphery of the dot. In the opposite case, the MHDA transport decreased when patterning on the ODT dot, resulting in no MHDA at the outside of the ODT dot, except in the directions of the cross structure. However, in both cases the ink deposited during the cross patterning steps is not observed inside the area of the dot, which is consistent with the above dot on dot experiments.

7.3.3.3 Double-ink corrals

Figure 7.9 shows results from double-ink experiments where an ODT dot was patterned inside an MHDA star-shaped corral (A) and an MHDA dot was patterned inside an ODT star-shaped corral (B). In this geometry, the second ink was not patterned on top of the first ink, as in the previous geometries. Instead, the geometry was designed to determine how the ink behaves when it encounters an area of the other ink. In both cases, the dot was patterned on a bare Au{111} surface, but it was large enough that the ink encountered the corral during the course of the deposition.

In Figure 7.9A, the ODT did not deposit in a radially symmetric fashion. Instead, the transport was inhibited in the directions of the MHDA corral and deposited preferentially in the directions of bare Au{111} substrate (where the corral was farther away). The interaction of the ODT with the MHDA corral did not change the shape of the corral. However, a small amount of ODT was also deposited on the outside of the corral. Similar conclusions can be drawn from
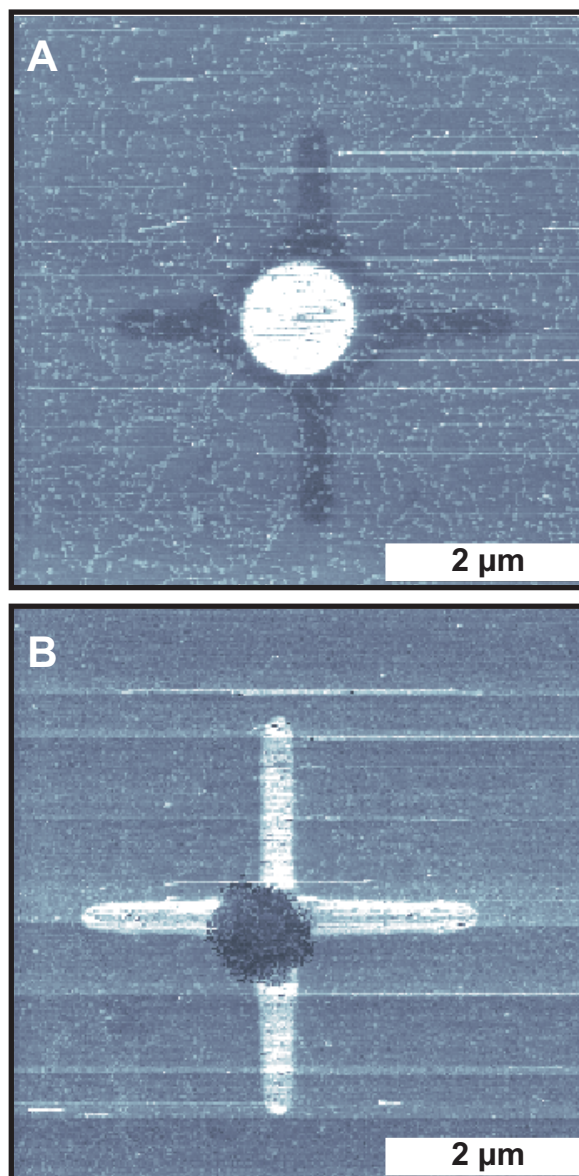
Figure 7.8. Two 6 μm $\times$ 6 μm LFM images from double-ink mobile tip DPN experiments. A) 1-Octadecanethiolate cross patterned on an 16-mercaptohexadecanoic acid dot. B) 16-mercaptohexadecanoic acid cross patterned on an 1-octadecanethiolate dot. Imaging parameters: Force setpoint: 1 nN; Scan rate: 4 Hz; 6 μm $\times$ 6 μm.
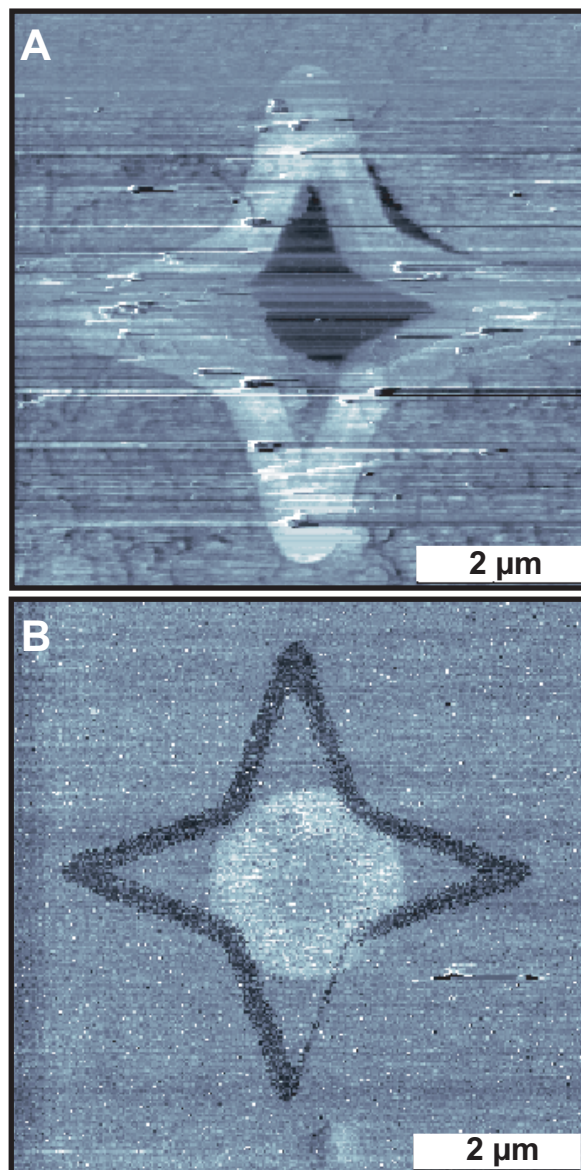
Figure 7.9. Two 7 μm $\times$ 7 μm LFM images from double-ink corral DPN experiments. A) 1-Octadecanethiolate dot patterned in an 16-mercaptohexadecanoic acid corral. B) 16-Mercapto-hexadecanoic acid dot patterned in an 1-octadecanethiolate corral. Imaging parameters: Force setpoint: 1 nN; Scan rate: 4 Hz; 7 μm $\times$ 7 μm.

Figure 7.9B. The MHDA deposited preferentially in the directions with the longest distance to the ODT corral. In addition, a small amount of MHDA deposited at the exterior of the ODT corral. The ODT corral shape was not altered as a result of the MHDA deposition. In both cases shown in Figure 7.9 there is no indication that the inks mixed within the lines of the corrals.

The double-ink experiments shown here give a comprehensive picture of ink transport for the most common inks used in DPN. In particular, these results establish that during DPN, ink molecules travel from the molecularly coated tip to the surface and across any pre-existing SAM where they deposit at the periphery of the structure. In this respect, the results for all the geometries investigated are consistent. When one ink is deposited on top of the other, as in Figures 7.6 and 7.8, the new ink deposits on the edge of the pre-existing structure. When one ink encounters an obstacle of the other, as in Figure 7.9, the ink eventually deposits on the other side of the obstacle. In both cases, there is no evidence of mixing between the two inks or of one ink pushing the other ink out of the way.

By measuring the relative transport rates from the dot-on-top-of-dot experiments, we have shown that ODT transport is increased when patterning on MHDA and that MHDA transport is inhibited when patterning on ODT. The asymmetries in transport evident in the other double-ink experiments can be explained by the differences in transport rates when patterning on a surface with an existing SAM and when patterning on a bare surface.

The advancing contact angle for water on a bare Au surface is 30-70° [264], while on single component ODT and MHDA SAMs formed on Au the contact angles are 115° and less than 15°, respectively [161]. Thus, in a DPN experiment, a region patterned with MHDA is more hydrophilic than the surrounding Au, while a region patterned with ODT is more hydrophobic. These differences in hydrophobicity between the three surfaces affect the size and shape of the water meniscus that can form between an AFM tip and the surface during DPN [265, 266]. On a surface patterned with MHDA, the water meniscus spreads out, while on a surface with ODT, the water meniscus is compact, if it exists at all.

Mercaptohexadecanoic acid is over 100 times more soluble in water than ODT due to the carboxylic acid terminal group [267, 268]. Thus, the ink molecules on an AFM cantilever interact with the water meniscus differently in these two systems. In particular, when patterning with MHDA, the ink molecules interact favorably with the water meniscus, especially in the case of a hydrophobic surface. When patterning with ODT, however, the ink molecules are less likely to be

in the meniscus and prefer to be either on the tip or the surface, forming micelles to minimize water exposure (decreasing the energy of the system) in the interim.

The concentration of the molecules in the meniscus is unknown. However, considering that the ODT crystals are visible on the microscale, while the water meniscus is not, the ODT concentration is assumed to be higher than the critical micelle concentration. Additionally, the MHDA concentration may also be above the critical micelle concentration, in which case these molecules would also form micelles in the meniscus. [269–271].

Combining these two facts, we propose a mechanism for the differences in transport rate of these two molecules when patterning on the other. When ODT is patterned on top of MHDA, the water meniscus spreads out, and the insoluble ink molecules are transported more easily, resulting in a higher transport rate. When MHDA is patterned on top of ODT, the water meniscus is compact, and transport of the more soluble ink molecules is inhibited, resulting in a lower transport rate. This proposed mechanism is shown schematically in Figure 7.10.

This mechanism is consistent with the recent results by Mirkin and co-workers where both ODT and MHDA were deposited simultaneously from a doubly-inked DPN tip. [272] In that case, MHDA, which interacts strongly with the water meniscus, deposits more quickly than ODT, resulting in MHDA at the center of the structure. The deposition of ODT then occurs at the periphery.

7.3.4 Displacement dip-pen nanolithography

Figure 7.11 shows the comparison of MHDA dots written on a bare Au {111} substrate and on a preformed AD SAM. Both sets of dots were fabricated using the same dwell times of 2 min, 5 min, 7 min and 10 min. It can be seen in the figure that the dots on the bare Au{111} are smaller and more resolved than the dots on the AD SAM. During imaging it is apparent that the ink deposited on the AD SAM can be moved around by the tip and after a few images, the ink that is not bound to the surface is swept out of and collects around the imaged region. Both these observations are consistent with a system in which the deposited ink flows across the surface of the preexisting film until it comes to a part of the surface that does not already have a SAM on it (SAM defect), as was observed in all the above double-ink experiments. As in the case of microdisplacement printing, the AD SAM is weak enough that eventually the ink penetrates the SAM surface and can form regions of the ink molecule. However, this process greatly hinders the DPN process, making DDPN infeasible as attempted here.
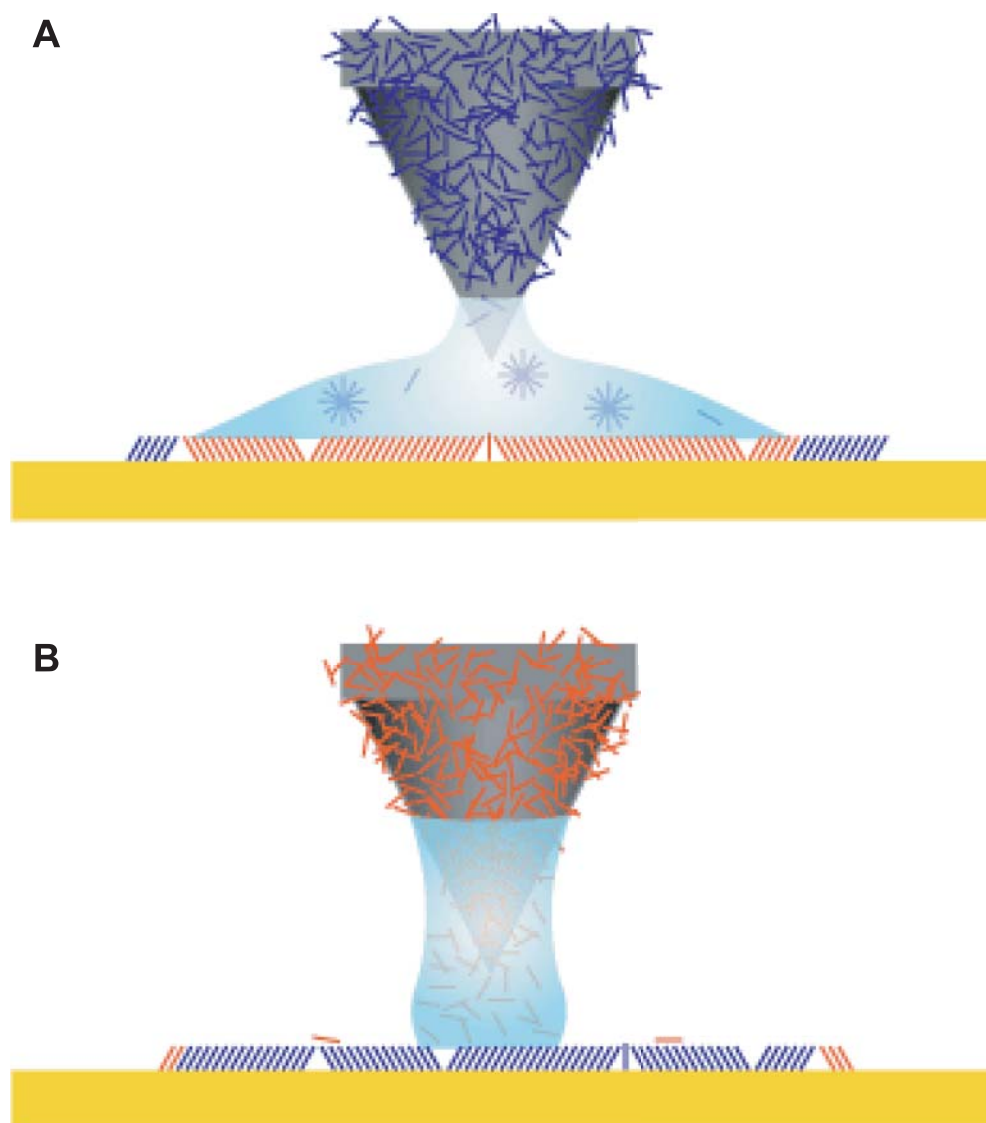
Figure 7.10. Schematic depicting the proposed mechanisms for the subsequent deposition of ink on preexisting patterns during double-ink DPN. A) 1-Octadecanethiolate patterned onto 16-mercaptohexadecanoic acid. The water meniscus spreads out on the 16-mercaptohexadecanoic acid surface, facilitating 1-octadecanethiol transport. B) 16-Mercaptohexadecanoic acid patterned onto 1-octadecanethiolate. The water meniscus beads up on the on 1-octadecanethiolate surface, hindering 16-mercaptohexadecanoic acid transpoirt.
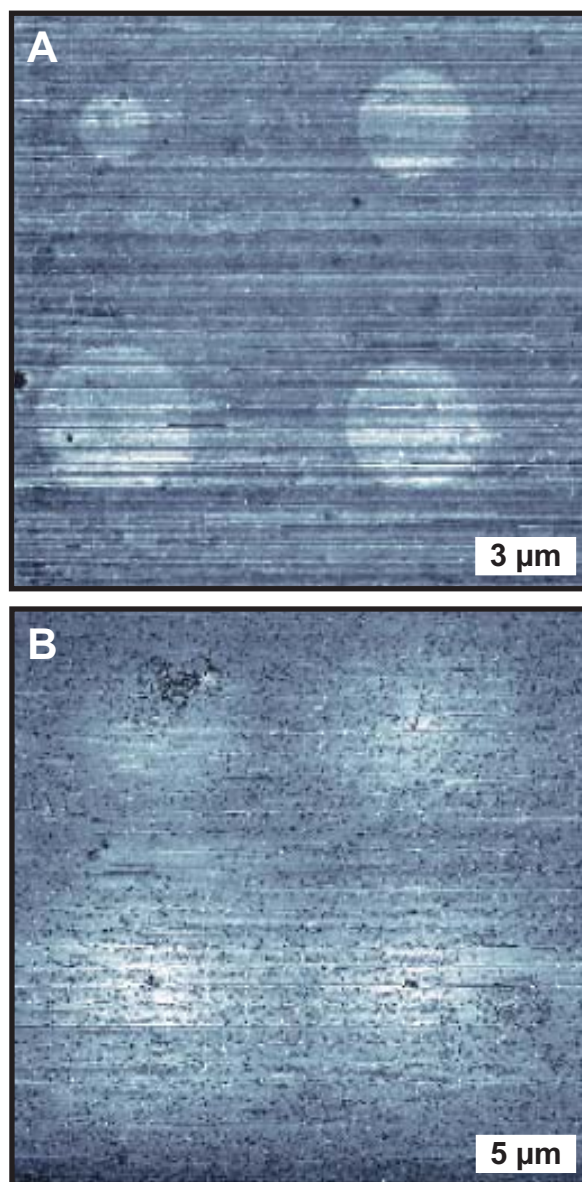
Figure 7.11. Lateral force microscopy images of (A) 16-mercaptohexadecanoic acid dots written on a bare Au{111} surface and (B) a preformed 1-adamantanethiolate SAM using the same tip dwell times of 2 min, 5 min, 7 min and 10 min (clockwise from upper left dot). A) Imaging parameters: Force setpoint: 1 nN; Scan rate: 4 Hz; 20 μm $\times$ 20 μm. B) Imaging parameters: Force setpoint: 1 nN; Scan rate: 4 Hz; 40 μm $\times$ 40 μm.

7.4 Conclusions

The extended time results presented here demonstrate that the transport of thiol inks such as MHDA and ODT can be affected significantly by the state of the substrate. The presence of ink already on the surface can slow down the transport rate for additional ink. Additionally, the double-ink DPN experiments showed that surface adsorbates affect the direction of transport of subsequent ink. A further consequence of this observation is that the exact nature of the substrate used for a particular DPN experiment can affect the behavior of the ink during patterning. Any adsorbates on the substrate (whether placed there intentionally by earlier patterning steps or present unintentionally due to insufficient cleaning or ambient contamination) can affect the ink transport rate or even cause the patterning to fail. Uncontrolled surface chemistry may be the source of much of the variation found in the literature for dip-pen nanolithography of thiol inks on gold surfaces [257–261].

In our proposed mechanism for the changes in ink transport rate, both the water solubility of the ink molecules and the hydrophobicity of the surface (which governs the size of the meniscus on the patterned features) affect the resulting transport. Thus, the interactions of the water meniscus that forms between the AFM tip and the sample with both the ink molecules and the substrate play important roles in determining the ink transport.

DPN has been touted as an ideal patterning tool for high density structures, particularly for biological materials [77]. The results shown here indicate that the presence of one ink affect the patterning of additional inks, especially for molecules with different functional groups in close proximity. In order for DPN to be technologically viable, fundamental understanding of the roles of the interactions between the materials patterned with DPN will be required.

Chapter 8

Conclusions and Future Prospects

This thesis describes the design, synthesis and characterization of molecules with varied supramolecular structure, interaction strengths, and electronic function to test and to extend our control of nanoscale patterning and function.

8.1 Molecular Conductance

The research we have conducted, self-assembling two structurally similar molecules, has given us insight into the influence of molecular structure on molecular conductance. From this work we found that the addition of one phenyl to biphenyl adversely influences the order of the film, and slightly manipulates electron transport through films of these molecules. Additionally, these studies contribute to a large body of work examining the origins of stochastic switching on single molecules inserted in SAMs [2, 47, 115]. By hindering the degrees of freedom afforded to a molecule, and demonstrating that it is still capable of switching, we have shown that internal ring rotation is not a primary mechanism of stochastic switching.

The work described in Chapter 2 on the difference between 2-thiophenanthrene and 4-thiobiphenyl SAMs and their respective conductances has resulted in the following publications:

Effects of hindered internal rotation on packing and conductance of self-assembled mono-layers, A. A. Dameron, J. W. Ciszek, J. M. Tour and P. S. Weiss, *Journal of Physical Chemistry B* **108**, 16761 (2004).

Molecular engineering and measurements to test hypothesized mechanisms in single molecule conductance switching, A. M. Moore, A. A. Dameron, B. A. Mantooth, Y. Yao, J. W. Ciszek, F. Maya, J. M. Tour and P. S. Weiss, *Journal of the American Chemical Society* **in press**.

The first paper explains the experiments and results described in Chapter 2, while the second paper discusses these experiments within the framework of other experiments we have used to decipher the switching mechanism.

Rather than elucidating the exact conductance switching mechanism, many studies have demonstrated that the majority of thiolated molecules exhibit conductive switching when examined in the appropriate testbed. It has become increasingly clear that the molecule-metal interface is the key to electron transport through and conductance switching of inserted molecules. Extensive research has been done to elucidate the properties of the metal-molecule interface that influence electron transport, with minimal success [48, 273, 274]. Further experiments will require the development of new systems to probe the metal-molecule interface selectively.

8.2 1-Adamantanethiolate Self-Assembled Monolayers and Displacement

In Chapters 3 through 5 we further investigated the influence of molecular structure and intermolecular interaction strengths on the properties of SAMs. In Chapter 3, we demonstrated that by manipulating the intermolecular spacing, thus tuning the strength of the intermolecular forces, we can influence the stability of the SAMs. Using bulky AD molecules, we created a SAM that had strong enough intermolecular interaction strengths to form an ordered monolayer, but had weak enough intermolecular interactions such that the AD SAMs were susceptible to replacement by the presence of another thiolated species. The work discussed in Chapters 4 and 5 showed that AD SAMs are labile with respect to replacement and can be replaced completely upon exposure to ALK molecules. Extensive characterization by STM, FTIR, XPS, and electrochemical methods of the mixed films, created by solution and vapor displacement, revealed that the displacement mechanism is a nucleation and growth mechanism, starting from inserted molecules in the AD SAM defect sites. Furthermore, the structure of the resulting two-component SAM depends strongly on the chain length of the molecule used for displacement. Because of these observations, in combination with photoemission experiments, it was hypothesized that the displacement was not caused by a weakened S-Au bond, but was instead caused by a combination of enthalpic contributions from a higher S-Au density and increased VDW forces after displacement. Manipulation of these enthalpic contributions could result in a variety of removable monolayers, each with a specific susceptibility to displacement range.

The work characterizing AD SAMs described in Chapter 3 resulted in the following publication:

Structure and displacement of 1-adamantanethiol self-assembled monolayers, A. A. Dameron, L. F. Charles and P. S. Weiss, *Journal of the American Chemical Society* **127**, 8697 (2005).

This paper describes AD SAM preparation, STM studies of AD SAM structure, and the initial experiments investigating the structure of ALK-displaced AD SAMs.

The work characterizing the origins and kinetics of AD SAM displacement, described in Chapters 4 and 5 resulted in the following manuscripts:

Origins of 1-Adamantanethiolate Displacement, A. A. Dameron, T. J. Mullen, R. W. Hengstebeck, H. M Saavedra and P. S.Weiss, *in preparation.*

Kinetics of 1-Adamantanethiolate Displacement, T. J. Mullen, A. A. Dameron, H. M. Saavedra and P. S. Weiss, *in preparation.*

The first paper describes the reasons for AD displacement with C12 and demonstrates that displacement is not the result of a weakened molecule-surface bond. The observed dynamics of AD displacement and experimental parameters hypothesized to influence them are discussed in the second paper.

Further studies of AD SAMs should include electronic measurements to characterize the conductance of the AD molecules, especially if further patterning techniques are developed using AD for molecular electronics applications. Because of the ease of making two-component, separated SAMs, barrier height (the change in current as a function of tip-sample separation) measurements of an ALK displaced AD SAM would garner information about electron transport through both the AD and the ALK regions simultaneously.

Structural modifications of AD should include the addition of functional groups to maximize the lateral intermolecular interactions, thus tuning the interactions of the AD SAMs from weak to strong. Additionally, there is precedence for optimizing a molecule with incorporated functional groups, similar to the ADtether, to move the bulky headgroup farther from the surface to explore the influence of the bulky headgroup on SAM lattice packing and long-range order [135].

Alternatively, future experiments may include investigating the structural and electronic properties of 2-admantanethiolate SAMs. Although these molecules are not chiral by themselves, the required proximity of one portion of the molecule to the surface after adsorption will induce chirality to the system. It may be possible to assemble ordered regions of 2-adamantanethiolate with

either left or right chirality. Additionally the orientation of the C-S-Au bond should be influenced by the additional hydrogen on this carbon. This should dramatically impact the conductance properties of the 2-admanatanethiolate SAMs, as compared to 1-adamantanethiolate SAMs.

Currently, thermal programmed desorption studies of AD SAM are underway to deduce the adsorption energy of the AD molecules to the surface. Provided there is a difference in energies between AD and ALK SAMs, molecular modeling would be useful to decipher what structural elements of the SAM have influenced this energy.

In retrospect, characterizing the kinetics of displacement from vacuum may have been an easier system to analyze, because it eliminates environmental effects. However, this would involve a significant experimental redesign of both the instrumentation and the methods. Studies of displacement as a function of concentration and temperature should be preformed to optimize thoroughly the system for one molecule type. Additionally, the influence of structural parameters, such as the chain length of the displacing molecule should be performed to be able to model molecules other than ALKs. Finally, based on our hypothesis of displacement origins, other molecules should also be displaceable provided they have low enough intermolecular interaction strengths. Initial experiments displacing short chain ALKs such as ethanethiol or butanethiol, with longer chain ALKs could be fruitful.

8.3   Molecular Patterning

Building on existing μCP techniques [34,35,76] and exploiting the labile nature of AD SAMs, we developed a new technique for molecular patterning, called microdisplacement printing. Using μDP, we have combated lateral surface diffusion of patterned molecules, extending the library of molecules that are patternable by μCP techniques. We have also demonstrated that further processing steps can be performed to remove the labile AD SAM selectively, creating complex patterns, and combating issues with pattern registry. Additionally, we have demonstrated that the exploitation of transient films and competitive adsorption processes has applications in patterning technologies.

The microcontact printing and microdisplacement printing studies (Chapter 6) resulted in the following publications:

Microdisplacement printing, A. A. Dameron, J. R. Hampton, R. K. Smith, T. J. Mullen, S. D. Gillmor and P. S. Weiss, *Nano Letters* **5**, 1834 (2005).

Enhanced molecular patterning via microdisplacement printing, A. A. Dameron, J. R. Hampton, S. D. Gillmor, J. N. Hohman and P. S. Weiss, *Journal of Vacuum Science and Technology* **23**, 2929 (2005).

The first paper describes the microdisplacement patterning process, using AD SAMs as the transient monolayers. The second paper describes further processing techniques after microdisplacement patterning used to remove the remaining AD molecules, and to create complex patterns.

Pertinent future experiments include determining the limit of resolution achievable by μDP, and exploration of the molecular structure of the printed films, especially at the edges of the patterns. Additionally, it may be possible to improve chemical patterning using molecules with high intermolecular interaction strengths to straighten pattern interfaces.

In Chapter 7, we discussed the fundamental properties of ink transport during DPN using two commonly used molecular inks. Despite the volumes of work applying DPN [77, 78, 275], there are few studies of the fundamental properties of DPN [255, 257–259, 262, 272], particularly how the ink moves from the AFM tip down to the sample surface, especially if there is a SAM already present on the surface. Exploring the influence of deposition time and the presence of substrate species on ink transport rates, we have found that the transport rate was different for smaller features than for larger features, and slowed as a function of total deposition time. Additionally, the ink transport was greatly influenced by the molecular presence on the surface; the ink molecules do not go from the tip down to the surface without first interacting with the preexisting SAM on the surface. These findings impact both sequential patterning and pattern alignment with DPN and must be addressed to make DPN an industrially viable technique.

The research discussed in Chapter 7 on molecular transport rates in dip-pen nanolithography resulted in the following publications:

Transport rates vary with deposition time in dip-pen nanolithography, J. R. Hampton, A. A. Dameron and P. S. Weiss, *Journal of Physical Chemistry B* **109**, 23118 (2005).

Double ink dip-pen nanolithography to elucidate molecular transport, J. R. Hampton, A. A. Dameron and P. S. Weiss, *Journal of the American Chemical Society* **in press**.

The first paper investigates the effects of time (both total experimental time and single pattern deposition time) on the transport rates of molecules from the tip to the sample in DPN. Analogously, the second paper explores the influence of surface adsorbates on the transport of molecules by DPN.

8.4   Final Thoughts

These studies highlight the importance of tailoring the supramolecular structure, intermolecular interaction strengths and electronic properties of the individual molecules in both pure and patterned SAMs. Manipulation of each (or the combination) of these properties impacts the existence of phase-separated or displaceable domains, and the molecular mobility of and electron transport through these regions in the assembled 2-D films of molecules. This, in turn, can help or hinder successful patterning of a SAM. These fundamental studies extend our control and understanding of complex nanoscale assemblies that are constructed from individual molecules upward, and further our ability to design new patterning strategies intelligently.

References

[1] A. Ulman, *Self-Assembled Monolayers of 4-Mercaptobiphenyls*, Accounts of Chemical Research **34**, 855 (2001).

[2] D. L. Allara, T. D. Dunbar, P. S. Weiss, L. A. Bumm, M. T. Cygan, J. M. Tour, W. A. Reinerth, Y. Yao, M. Kozaki, and L. Jones, *Molecular Electronics: Science and Technology*, Vol. 852 of *Annals of the New York Academy of Sciences* (New York Academy of Sciences, New York, NY, 1998), pp. 349–370.

[3] W. Azzam, P. Cyganik, G. Witte, M. Buck, and C. Woll, *Pronounced Odd-Even Changes in the Molecular Arrangement and Packing Density of Biphenyl-Based Thiol SAMs: A Combined STM and LEED Study*, Langmuir **19**, 8262 (2003).

[4] J. F. Kang, A. Ulman, S. Liao, R. Jordan, G. H. Yang, and G. Y. Liu, *Self-Assembled Rigid Monolayers of 4'-Substituted-4-Mercaptobiphenyls on Gold and Silver Surfaces*, Langmuir **17**, 95 (2001).

[5] K. F. Kelly, Y. S. Shon, T. R. Lee, and N. J. Halas, *Scanning Tunneling Microscopy and Spectroscopy of Dialkyl Disulfide Fullerenes Inserted into Alkanethiolate SAMs*, Journal of Physical Chemistry B **103**, 8639 (1999).

[6] R. K. Smith, P. A. Lewis, and P. S. Weiss, *Patterning Self-Assembled Monolayers*, Progress in Surface Science **75**, 1 (2004).

[7] L. A. Bumm, J. J. Arnold, M. T. Cygan, T. D. Dunbar, T. P. Burgin, L. Jones, D. L. Allara, J. M. Tour, and P. S. Weiss, *Are Single Molecular Wires Conducting?*, Science **271**, 1705 (1996).

[8] M. T. Cygan, T. D. Dunbar, J. J. Arnold, L. A. Bumm, N. F. Shedlock, T. P. Burgin, L. Jones, D. L. Allara, J. M. Tour, and P. S. Weiss, *Insertion, Conductivity, and Structures of Conjugated Organic Oligomers in Self-Assembled Alkanethiol Monolayers on Au{111}*, Journal of the American Chemical Society **120**, 2721 (1998).

[9] A. A. Dameron, J. W. Ciszek, J. M. Tour, and P. S. Weiss, *Effects of Hindered Internal Rotation on Packing and Conductance of Self-Assembled Monolayers*, Journal of Physical Chemistry B **108**, 16761 (2004).

[10] Z. J. Donhauser, B. A. Mantooth, K. F. Kelly, L. A. Bumm, J. D. Monnell, J. J. Stapleton, D. W. Price, A. M. Rawlett, D. L. Allara, J. M. Tour, and P. S. Weiss, *Conductance Switching in Single Molecules through Conformational Changes*, Science **292**, 2303 (2001).

[11] T. D. Dunbar, M. T. Cygan, L. A. Bumm, G. S. McCarty, T. P. Burgin, W. A. Reinerth, L. Jones, J. J. Jackiw, J. M. Tour, P. S. Weiss, and D. L. Allara, *Combined Scanning Tunneling Microscopy and Infrared Spectroscopic Characterization of Mixed Surface Assemblies of Linear Conjugated Guest Molecules in Host Alkanethiolate Monolayers on Gold*, Journal of Physical Chemistry B **104**, 4880 (2000).

[12] P. A. Lewis, C. E. Inman, Y. Yao, J. M. Tour, J. E. Hutchison, and P. S. Weiss, *Molecular Engineering of the Polarity and Interactions of Molecular Electronic Switches*, Journal of the American Chemical Society **127**, 17421 (2005).

[13] S. R. Forrest, *Ultrathin Organic Films Grown by Organic Molecular Beam Deposition and Related Techniques*, Chemical Reviews **97**, 1793 (1997).

[14] A. Koma, *Molecular-Beam Epitaxial-Growth of Organic Thin-Films*, Progress in Crystal Growth and Characterization of Materials **30**, 129 (1995).

[15] H. B. Li, R. K. Sharma, Y. Zhang, A. A. O. Tay, E. T. Kang, and K. G. Neoh, *Surface Modification of Polyimide Films Via Plasma-Enhanced Chemical Vapor Deposition of Thin Silica and Nitride Films*, Langmuir **19**, 6845 (2003).

[16] S. Takeishi, H. Kudo, R. Shinohara, M. Hoshino, S. Fukuyama, J. Yamaguchi, and M. Yamada, *Plasma-Enhanced Chemical Vapor Deposition of Fluorocarbon Films with High Thermal Resistance and Low Dielectric Constants*, Journal of the Electrochemical Society **144**, 1797 (1997).

[17] A. A. Dhirani, R. W. Zehner, R. P. Hsung, P. GuyotSionnest, and L. R. Sita, *Self-Assembly of Conjugated Molecular Rods: A High-Resolution STM Study*, Journal of the American Chemical Society **118**, 3319 (1996).

[18] S. Frey, A. Shaporenko, M. Zharnikov, P. Harder, and D. L. Allara, *Self-Assembled Monolayers of Nitrile-Functionalized Alkanethiols on Gold and Silver Substrates*, Journal of Physical Chemistry B **107**, 7716 (2003).

[19] T. Ishida, W. Mizutani, H. Azehara, K. Miyake, Y. Aya, S. Sasaki, and H. Tokumoto, *Molecular Arrangement and Electrical Conduction of Self-Assembled Monolayers Made from Terphenyl Thiols*, Surface Science **514**, 187 (2002).

[20] T. Y. B. Leung, P. Schwartz, G. Scoles, F. Schreiber, and A. Ulman, *Structure and Growth of 4-Methyl-4'-Mercaptobiphenyl Monolayers on Au{111}: A Surface Diffraction Study*, Surface Science **458**, 34 (2000).

[21] E. Sabatani and I. Rubinstein, *Organized Self-Assembling Monolayers on Electrodes. 2. Monolayer-Based Ultramicroelectrodes for the Study of Very Rapid Electrode Kinetics*, Journal of Physical Chemistry **91**, 6663 (1987).

[22] E. Sabatani, I. Rubinstein, R. Maoz, and J. Sagiv, *Organized Self-Assembling Monolayers on Electrodes. 1. Octadecyl Derivatives on Gold*, Journal of Electroanalytical Chemistry **219**, 365 (1987).

[23] J. J. Stapleton, P. Harder, T. A. Daniel, M. D. Reinard, Y. X. Yao, D. W. Price, J. M. Tour, and D. L. Allara, *Self-Assembled Oligo(Phenylene-Ethynylene) Molecular Electronic Switch Monolayers on Gold: Structures and Chemical Stability*, Langmuir **19**, 8245 (2003).

[24] K. Edinger, A. Golzhauser, K. Demota, C. Woll, and M. Grunze, *Formation of Self-Assembled Monolayers of n-Alkanethiols on Gold – a Scanning Tunneling Microscopy Study on the Modification of Substrate Morphology*, Langmuir **9**, 4 (1993).

[25] K. Kobayashi, H. Yamada, T. Horiuchi, and K. Matsushige, *The Molecular Arrangements of Alkanethiol Self-Assembled Monolayers on Au{111} Studied by Scanning Tunneling Microscopy*, Japanese Journal of Applied Physics, Part I: Regular Papers and Short Notes **37**, 6183 (1998).

[26] J. Noh and M. Hara, *Molecular-Scale Desorption Processes and the Alternating Missing-Row Phase of Alkanethiol Self-Assembled Monolayers on Au{111}*, Langmuir **17**, 7280 (2001).

[27] R. G. Nuzzo, E. M. Korenic, and L. H. Dubois, *Studies of the Temperature-Dependent Phase-Behavior of Long-Chain Normal-Alkyl Thiol Monolayers on Gold*, Journal of Chemical Physics **93**, 767 (1990).

[28] H. Ogawa, T. Takamura, and Y. Shimoyama, *Self-Assembly Process of Alkanethiol Monolayers*, Japanese Journal of Applied Physics, Part I: Regular Papers and Short Notes **38**, 6019 (1999).

[29] G. E. Poirier and E. D. Pylant, *The Self-Assembly Mechanism of Alkanethiols on Au{111}*, Science **272**, 1145 (1996).

[30] A. Ulman, S. D. Evans, and R. G. Snyder, *Self-Assembled Monolayers of Alkanethiols on Gold – Sulfone Groups Enhancing 2-Dimensional Organization*, Thin Solid Films **210**, 806 (1992).

[31] A. Ulman, *Formation and Structure of Self-Assembled Monolayers*, Chemical Reviews **96**, 1533 (1996).

[32] G. E. Poirier, *Characterization of Organosulfur Molecular Monolayers on Au{111} Using Scanning Tunneling Microscopy*, Chemical Reviews **97**, 1117 (1997).

[33] D. K. Schwartz, *Mechanisms and Kinetics of Self-Assembled Monolayer Formation*, Annual Review of Physical Chemistry **52**, 107 (2001).

[34] M. Mrksich and G. M. Whitesides, *Patterning Self-Assembled Monolayers Using Microcontact Printing: A New Technology for Biosensors*, Trends in Biotechnology **13**, 228 (1995).

[35] Y. N. Xia and G. M. Whitesides, *Soft Lithography*, Angewandte Chemie, International Edition **37**, 551 (1998).

[36] E. Barrena, E. Palacios-Lidon, C. Munuera, X. Torrelles, S. Ferrer, U. Jonas, M. Salmeron, and C. Ocal, *The Role of Intermolecular and Molecule-Substrate Interactions in the Stability of Alkanethiol Nonsaturated Phases on Au{111}*, Journal of the American Chemical Society **126**, 385 (2004).

[37] E. Delamarche and B. Michel, *Structure and Stability of Self-Assembled Monolayers*, Thin Solid Films **273**, 54 (1996).

[38] L. H. Dubois, B. R. Zegarski, and R. G. Nuzzo, *The Chemisorption of Organosulfur Compounds on Gold Surfaces: Construction of Well-Defined Organic-Solids*, Journal of Vacuum Science and Technology A **5**, 634 (1987).

[39] G. E. Poirier, *Coverage-Dependent Phases and Phase Stability of Decanethiol on Au{111}*, Langmuir **15**, 1167 (1999).

[40] W. W. Zhang, X. M. Ren, H. F. Li, C. S. Lu, C. J. Hu, H. Z. Zhu, and Q. J. Meng, *Study on Self-Assembled Monolayers of Functionalized Azobenzene Thiols on Gold: XPS, Electrochemical Properties, and Surface-Enhanced Raman Spectroscopy*, Journal of Colloid and Interface Science **255**, 150 (2002).

[41] L. V. Protsailo, W. R. Fawcett, D. Russell, and R. L. Meyer, *Electrochemical Characterization of the Alkaneselenol-Based SAMs on Au{111} Single Crystal Electrode*, Langmuir **18**, 9342 (2002).

[42] S. Reese and M. A. Fox, *Self-Assembled Monolayers on Gold of Thiols Incorporating Conjugated Terminal Groups*, Journal of Physical Chemistry B **102**, 9820 (1998).

[43] R. Schweiss, C. Werner, and W. Knoll, *Impedance Spectroscopy Studies of Interfacial Acid-Base Reactions of Self-Assembled Monolayers*, Journal of Electroanalytical Chemistry **540**, 145 (2003).

[44] J. Chen, L. C. Calvet, M. A. Reed, D. W. Carr, D. S. Grubisha, and D. W. Bennett, *Electronic Transport through Metal – 1,4-Phenylenediisocyanide – Metal Junctions*, Chemical Physics Letters **313**, 741 (1999).

[45] M. A. Reed, C. Zhou, C. J. Muller, T. P. Burgin, and J. M. Tour, *Conductance of a Molecular Junction*, Science **278**, 252 (1997).

[46] C. Zhou, M. R. Deshpande, M. A. Reed, L. Jones, and J. M. Tour, *Nanoscale Metal Self-Assembled Monolayer Metal Heterostructures*, Applied Physics Letters **71**, 611 (1997).

[47] M. A. Reed, C. Zhou, M. R. Deshpande, C. J. Muller, T. P. Burgin, L. Jones, and J. M. Tour, *Molecular Electronics: Science and Technology*, Vol. 852 of *Annals of the New York Academy of Sciences* (New York Academy of Sciences, New York, NY, 1998), pp. 133–144.

[48] M. A. Rampi and G. M. Whitesides, *A Versatile Experimental Approach for Understanding Electron Transport through Organic Materials*, Chemical Physics **281**, 373 (2002).

[49] K. Slowinski, H. K. Y. Fong, and M. Majda, *Mercury-Mercury Tunneling Junctions. 1. Electron Tunneling across Symmetric and Asymmetric Alkanethiolate Bilayers*, Journal of the American Chemical Society **121**, 7257 (1999).

[50] K. Slowinski and M. Majda, *Mercury-Mercury Tunneling Junctions. 2. Structure and Stability of Symmetric Alkanethiolate Bilayers and Their Effect on the Rate of Electron Tunneling*, Journal of Electroanalytical Chemistry **491**, 139 (2000).

[51] C. J. Chen, *Introduction to Scanning Tunneling Microscopy*, Oxford Series in Optical and Imaging Sciences (Oxford University Press, New York, 1993).

[52] D. A. Bonnell, *Scanning Probe Microscopy and Spectroscopy: Theory, Techniques, and Applications*, 2nd ed. (Wiley–VCH, Inc., New York, 2001).

[53] J. N. Israelachvili, *Intermolecular and Surface Forces*, 2nd ed. (Academic Press, San Diego, CA, 1992).

[54] L. Bergstrom, *Hamaker Constants of Inorganic Materials*, Advances In Colloid And Interface Science **70**, 125 (1997).

[55] H. C. Hamaker, *The London-Van Der Waals Attraction between Spherical Particles.*, Physica **4**, 1058 (1937).

[56] S. W. Lee and W. M. Sigmund, *Afm Study of Repulsive Van Der Waals Forces between Teflon AF^{TM} Thin Film and Silica or Alumina*, Colloids and Surfaces A: Physicochemical and Engineering Aspects **204**, 43 (2002).

[57] A. Meurk, P. F. Luckham, and L. Bergstrom, *Direct Measurement of Repulsive and Attractive van der Waals Forces between Inorganic Materials*, Langmuir **13**, 3896 (1997).

[58] Refers to a special class of non-photolithographic patterning techniques that use an elastomeric stamp or mold to transfer a pattern to a substrate and uses flexible organic materials for fabrication.

[59] A. Kumar and G. M. Whitesides, *Features of Gold Having Micrometer to Centimeter Dimensions Can Be Formed through a Combination of Stamping with an Elastomeric Stamp and an Alkanethiol Ink Followed by Chemical Etching*, Applied Physics Letters **63**, 2002 (1993).

[60] A. Bernard, J. P. Renault, B. Michel, H. R. Bosshard, and E. Delamarche, *Microcontact Printing of Proteins*, Advanced Materials **12**, 1067 (2000).

[61] C. S. Chen, M. Mrksich, S. Huang, G. M. Whitesides, and D. E. Ingber, *Micropatterned Surfaces for Control of Cell Shape, Position, and Function*, Biotechnology Progress **14**, 356 (1998).

[62] A. T. A. Jenkins, R. J. Bushby, S. D. Evans, W. Knoll, A. Offenhausser, and S. D. Ogier, *Lipid Vesicle Fusion on MCP Patterned Self-Assembled Monolayers: Effect of Pattern Geometry on Bilayer Formation*, Langmuir **18**, 3176 (2002).

[63] R. S. Kane, S. Takayama, E. Ostuni, D. E. Ingber, and G. M. Whitesides, *Patterning Proteins and Cells Using Soft Lithography*, Biomaterials **20**, 2363 (1999).

[64] N. L. Jeon, R. G. Nuzzo, Y. N. Xia, M. Mrksich, and G. M. Whitesides, *Patterned Self-Assembled Monolayers Formed by Microcontact Printing Direct Selective Metallization by Chemical Vapor Deposition on Planar and Nonplanar Substrates*, Langmuir **11**, 3024 (1995).

[65] J. L. Wilbur, A. Kumar, H. A. Biebuyck, E. Kim, and G. M. Whitesides, *Microcontact Printing of Self-Assembled Monolayers: Applications in Microfabrication*, Nanotechnology **7**, 452 (1996).

[66] J. L. Wilbur, A. Kumar, E. Kim, and G. M. Whitesides, *Microfabrication by Microcontact Printing of Self-Assembled Monolayers*, Advanced Materials **6**, 600 (1994).

[67] Y. N. Xia, E. Kim, M. Mrksich, and G. M. Whitesides, *Microcontact Printing of Alkanethiols on Copper and Its Application in Microfabrication*, Chemistry of Materials **8**, 601 (1996).

[68] Y. N. Xia, X. M. Zhao, and G. M. Whitesides, *Pattern Transfer: Self-Assembled Monolayers as Ultrathin Resists*, Microelectronic Engineering **32**, 255 (1996).

[69] R. M. Crooks, *Patterning of Hyperbranched Polymer Films*, Chemistry and Physical Chemistry **2**, 644 (2001).

[70] P. C. Hidber, W. Helbig, E. Kim, and G. M. Whitesides, *Microcontact Printing of Palladium Colloids: Micron-Scale Patterning by Electroless Deposition of Copper*, Langmuir **12**, 1375 (1996).

[71] N. L. Jeon, I. S. Choi, G. M. Whitesides, N. Y. Kim, P. E. Laibinis, Y. Harada, K. R. Finnie, G. S. Girolami, and R. G. Nuzzo, *Patterned Polymer Growth on Silicon Surfaces Using Microcontact Printing and Surface-Initiated Polymerization*, Applied Physics Letters **75**, 4201 (1999).

[72] W. K. Ng, L. Wu, and P. M. Moran, *Microcontact Printing of Catalytic Nanoparticles for Selective Electroless Deposition of Metals on Nonplanar Polymeric Substrates*, Applied Physics Letters **81**, 3097 (2002).

[73] S. Palacin, P. C. Hidber, J. P. Bourgoin, C. Miramond, C. Fermon, and G. M. Whitesides, *Patterning with Magnetic Materials at the Micron Scale*, Chemistry of Materials **8**, 1316 (1996).

[74] V. Santhanam and R. P. Andres, *Microcontact Printing of Uniform Nanoparticle Arrays*, Nano Letters **4**, 41 (2004).

[75] H. S. Shin, H. J. Yang, Y. M. Jung, and S. Bin Kim, *Direct Patterning of Silver Colloids by Microcontact Printing: Possibility as SERS Substrate Array*, Vibrational Spectroscopy **29**, 79 (2002).

[76] X. M. Zhao, Y. N. Xia, and G. M. Whitesides, *Soft Lithographic Methods for Nano-Fabrication*, Journal of Materials Chemistry **7**, 1069 (1997).

[77] D. S. Ginger, H. Zhang, and C. A. Mirkin, *The Evolution of Dip-Pen Nanolithography*, Angewandte Chemie, International Edition **43**, 30 (2004).

[78] R. D. Piner, J. Zhu, F. Xu, S. H. Hong, and C. A. Mirkin, *"Dip-Pen" Nanolithography*, Science **283**, 661 (1999).

[79] A. Noy, A. E. Miller, J. E. Klare, B. L. Weeks, B. W. Woods, and J. J. DeYoreo, *Fabrication of Luminescent Nanostructures and Polymer Nanowires Using Dip-Pen Nanolithography*, Nano Letters **2**, 109 (2002).

[80] L. M. Demers and C. A. Mirkin, *Combinatorial Templates Generated by Dip-Pen Nano-lithography for the Formation of Two-Dimensional Particle Arrays*, Angewandte Chemie, International Edition **40**, 3069 (2001).

[81] M. Su, X. G. Liu, S. Y. Li, V. P. Dravid, and C. A. Mirkin, *Moving Beyond Molecules: Patterning Solid-State Features Via Dip-Pen Nanolithography with Sol-Based Inks*, Journal of the American Chemical Society **124**, 1560 (2002).

[82] D. A. Weinberger, S. Hong, C. A. Mirkin, B. W. Wessels, and T. B. Higgins, *Combinatorial Generation and Analysis of Nanometer- and Micrometer-Scale Silicon Features Via "Dip-Pen" Nanolithography and Wet Chemical Etching*, Advanced Materials **12**, 1600 (2000).

[83] K. B. Lee, S. J. Park, C. A. Mirkin, J. C. Smith, and M. Mrksich, *Protein Nanoarrays Generated by Dip-Pen Nanolithography*, Science **295**, 1702 (2002).

[84] J. C. Smith, K. B. Lee, Q. Wang, M. G. Finn, J. E. Johnson, M. Mrksich, and C. A. Mirkin, *Nanopatterning the Chemospecific Immobilization of Cowpea Mosaic Virus Capsid*, Nano Letters **3**, 883 (2003).

[85] H. Zhang, K. B. Lee, Z. Li, and C. A. Mirkin, *Biofunctionalized Nanoarrays of Inorganic Structures Prepared by Dip-Pen Nanolithography*, Nanotechnology **14**, 1113 (2003).

[86] L. A. Bumm, J. J. Arnold, T. D. Dunbar, D. L. Allara, and P. S. Weiss, *Electron Transfer through Organic Molecules*, Journal of Physical Chemistry B **103**, 8122 (1999).

[87] S. M. Dirk and J. M. Tour, *Synthesis of Nitrile-Terminated Potential Molecular Electronic Devices*, Tetrahedron **59**, 287 (2003).

[88] A. K. Flatt and J. M. Tour, *Synthesis of Thiol Substituted Oligoanilines for Molecular Device Candidates*, Tetrahedron Letters **44**, 6699 (2003).

[89] J. J. Hwang and J. M. Tour, *Combinatorial Synthesis of Oligo(Phenylene Ethynylene)s*, Tetrahedron **58**, 10387 (2002).

[90] D. W. Price, S. M. Dirk, F. Maya, and J. M. Tour, *Improved and New Syntheses of Potential Molecular Electronics Devices*, Tetrahedron **59**, 2497 (2003).

[91] D. W. Price and J. M. Tour, *Biphenyl- and Fluorenyl-Based Potential Molecular Electronic Devices*, Tetrahedron **59**, 3131 (2003).

[92] M. A. Reed, J. Chen, A. M. Rawlett, D. W. Price, and J. M. Tour, *Molecular Random Access Memory Cell*, Applied Physics Letters **78**, 3735 (2001).

[93] J. M. Tour, A. M. Rawlett, M. Kozaki, Y. X. Yao, R. C. Jagessar, S. M. Dirk, D. W. Price, M. A. Reed, C. W. Zhou, J. Chen, W. Y. Wang, and I. Campbell, *Synthesis and Preliminary Testing of Molecular Wires and Devices*, Chemistry – A European Journal **7**, 5118 (2001).

[94] H. Sellers, A. Ulman, Y. Shnidman, and J. E. Eilers, *Structure and Bonding of Alkanethiolates on Gold and Silver Surfaces: Implications for Self-Assembled Monolayers*, Journal of the American Chemical Society **115**, 9389 (1993).

[95] J. Chen, M. A. Reed, A. M. Rawlett, and J. M. Tour, *Large on–Off Ratios and Negative Differential Resistance in a Molecular Electronic Device*, Science **286**, 1550 (1999).

[96] P. A. Lewis, Z. J. Donhauser, B. A. Mantooth, R. K. Smith, L. A. Bumm, K. F. Kelly, and P. S. Weiss, *Control and Placement of Molecules Via Self-Assembly*, Nanotechnology **12**, 231 (2001).

[97] Z. J. Donhauser, B. A. Mantooth, T. P. Pearl, K. F. Kelly, S. U. Nanayakkara, and P. S. Weiss, *Matrix-Mediated Control of Stochastic Single Molecule Conductance Switching*, Japanese Journal of Applied Physics, Part I: Regular Papers and Short Notes **41**, 4871 (2002).

[98] J. W. Ciszek and J. M. Tour, *Synthesis of Ladder Polyaromatics as New Molecular Device Candidates*, Tetrahedron Letters **45**, 2801 (2004).

[99] B. A. Mantooth, *Nanoscopic Analyses: Single Molecule Characterization in Molecular Electronics and Surface Science*, Ph. D. Thesis, The Pennsylvania State University, May 2005.

[100] B. A. Mantooth, Z. J. Donhauser, K. F. Kelly, and P. S. Weiss, *Cross-Correlation Image Tracking for Drift Correction and Adsorbate Analysis*, Review of Scientific Instruments **73**, 313 (2002).

[101] A. M. Moore, B. A. Mantooth, Z. J. Donhauser, F. Maya, J. D. W. Price, Y. Yao, J. M. Tour, and P. S. Weiss, *Cross-Step Place-Exchange of Oligo(Phenylene-Ethynylene) Molecules*, Nano Letters **5**, 2292 (2005).

[102] In a crystal packing conformation, biphenyl is planar because the packing forces offset the steric hindrances. As a SAM, the barrier to rotation may differ from that in solution.

[103] I. Cacelli, G. Cinacchi, C. Geloni, G. Prampolini, and A. Tani, *Computer Simulation of P-Phenyls with Interaction Potentials from Ab-Initio Calculations*, Molecular Crystals and Liquid Crystals **395**, 171 (2003).

[104] I. Cacelli and G. Prampolini, *Torsional Barriers and Correlations between Dihedrals in P-Polyphenyls*, Journal of Physical Chemistry A **107**, 8665 (2003).

[105] N. Sadlej-Sosnowska, *Energy Barriers to Internal Rotation: Hyperconjugation and Electrostatic Description*, Journal of Physical Chemistry A **107**, 8671 (2003).

[106] J. M. Tour, L. Jones II, D. L. Pearson, J. J. S. Lamba, T. P. Burgin, G. M. Whitesides, D. L. Allara, A. N. Parikh, and S. V. Atre, *Self-Assembled Monolayers and Multilayers of Conjugated Thiols, α, ω-Dithiols, and Thioacetyl-Containing Adsorbates: Understanding Attachments between Potential Molecular Wires and Gold Surfaces*, Journal of the American Chemical Society **117**, 9529 (1995).

[107] S. W. Hla, G. Meyer, and K. H. Rieder, *Selective Bond Breaking of Single Iodobenzene Molecules with a Scanning Tunneling Microscope Tip*, Chemical Physics Letters **370**, 431 (2003).

[108] L. J. Lauhon and W. Ho, *Single-Molecule Chemistry and Vibrational Spectroscopy: Pyridine and Benzene on Cu{001}*, Journal of Physical Chemistry A **104**, 2463 (2000).

[109] R. Benassi and F. Taddei, *Ground-State Molecular Stabilization of Substituted Ethylenes. A Theoretical MO Ab-Initio Thermochemical Study*, Journal of Molecular Structure: THEOCHEM **572**, 169 (2001).

[110] F. Taddei, *Effect of Heteroatoms in Determining the Rotational Barrier around Carbon-Carbon Double Bond in Substituted Ethylenes. An MO Ab Initio Theoretical Study*, Journal of Molecular Structure: THEOCHEM **544**, 141 (2001).

[111] E. Sabatani, J. Cohenboulakia, M. Bruening, and I. Rubinstein, *Thioaromatic Monolayers on Gold: A New Family of Self-Assembling Monolayers*, Langmuir **9**, 2974 (1993).

[112] Z. J. Donhauser, *Probing Nanoscale Electronics Using Scanning Tunneling Microscopy*, Ph.D. Thesis, The Pennsylvania State University, 2003.

[113] G. H. Yang, Y. L. Qian, C. Engtrakul, L. R. Sita, and G.-Y. Liu, *Arenethiols Form Ordered and Incommensurate Self-Assembled Monolayers on Au{111} Surfaces*, Journal of Physical Chemistry B **104**, 9059 (2000).

[114] J. G. Kushmerick, D. B. Holt, J. C. Yang, J. Naciri, M. H. Moore, and R. Shashidhar, *Metal-Molecule Contacts and Charge Transport across Monomolecular Layers: Measurement and Theory*, Physical Review Letters **89**, (2002).

[115] B. A. Mantooth and P. S. Weiss, *Fabrication, Assembly, and Characterization of Molecular Electronic Components*, Proceedings of the IEEE **91**, 1785 (2003).

[116] J. M. Seminario, C. E. de la Cruz, and P. A. Derosa, *A Theoretical Analysis of Metal–Molecule Contacts*, Journal of the American Chemical Society **123**, 5616 (2001).

[117] J. M. Seminario, A. G. Zacarias, and P. A. Derosa, *Theoretical Analysis of Complementary Molecular Memory Devices*, Journal of Physical Chemistry A **105**, 791 (2001).

[118] E. G. Emberly and G. Kirczenow, *The Smallest Molecular Switch*, Physical Review Letters **91**, (2003).

[119] P. E. Kornilovitch and A. M. Bratkovsky, *Orientational Dependence of Current through Molecular Films*, Physical Review B **6419**, (2001).

[120] S. D. Evans, E. Urankar, A. Ulman, and N. Ferris, *Self-Assembled Monolayers of Alkanethiols Containing a Polar Aromatic Group - Effects of the Dipole Position on Molecular Packing, Orientation, and Surface Wetting Properties*, Journal of the American Chemical Society **113**, 4121 (1991).

[121] P. A. Lewis, R. K. Smith, K. F. Kelly, L. A. Bumm, S. M. Reed, R. S. Clegg, J. D. Gunderson, J. E. Hutchison, and P. S. Weiss, *The Role of Buried Hydrogen Bonds in Self-Assembled Mixed Composition Thiols on Au{111}*, Journal of Physical Chemistry B **105**, 10630 (2001).

[122] R. K. Smith, S. M. Reed, P. A. Lewis, J. D. Monnell, R. S. Clegg, K. F. Kelly, L. A. Bumm, J. E. Hutchison, and P. S. Weiss, *Phase Separation within a Binary Self-Assembled Monolayer on Au{111} Driven by an Amide-Containing Alkanethiol*, Journal of Physical Chemistry B **105**, 1119 (2001).

[123] G. E. Poirier and M. J. Tarlov, *The c(4×2) Superlattice of n-Alkanethiol Monolayers Self-Assembled on Au{111}*, Langmuir **10**, 2853 (1994).

[124] L. F. Charles, M.S. Thesis, The Pennsylvania State University, 1999.

[125] L. M. Molina and B. Hammer, *Theoretical Study of Thiol-Induced Reconstructions on the Au{111} Surface*, Chemical Physics Letters **360**, 264 (2002).

[126] G. E. Poirier, *Mechanism of Formation of Au Vacancy Islands in Alkanethiol Monolayers on Au{111}*, Langmuir **13**, 2019 (1997).

[127] Y. H. Hu and S. B. Sinnott, *A Molecular Dynamics Study of Thin-Film Formation Via Molecular Cluster Beam Deposition: Effect of Incident Species*, Surface Science **526**, 230 (2003).

[128] W. Nowacki, *Die Krystallstrucktur Von Adamantan (Symm. Tri-Cyclo-Decan)*, Helvetica Chimica Acta **28**, 1233 (1945).

[129] W. Nowacki and K. W. Hedberg, *An Electron Diffraction Study of the Structure of Adaman-tane*, Journal of the American Chemical Society **70**, 1497 (1948).

[130] P. v. R. Schleyer and M. M. Donaldson, *The Relative Stability of Bridged Hydrocarbons. 2. endo- and exo-Trimethylenenorbornane. The Formation of Adamantane*, Journal of the American Chemical Society **82**, 4645 (1960).

[131] P. v. R. Schleyer, J. E. Williams, and K. R. Blanchard, *The Evaluation of Strain in Hydrocar-bons. The Strain in Adamantane and Its Origin*, Journal of the American Chemical Society **92**, 2377 (1970).

[132] M. Shen, H. F. S. III, C. Liang, J.-H. Lii, N. L. Allinger, and P. v. R. Schleyer, *Finite T_D Symmetry Models for Diamond: From Adamantane to Superadamantane ($C_{35}H_{36}$)*, Journal of the American Chemical Society **114**, 497 (1992).

[133] K. K. Khullar and J. Bauer, *Carbon-Sulfur Cleavage of 1-Adamantyl Sulfides*, Journal of Organic Chemistry **36**, 3038 (1971).

[134] B. J. Mair, M. Shamaiengar, N. C. Krouskop, and F. D. Rossini, *Isolation of Adamantane from Petroleum*, Analytical Chemistry **31**, 2082 (1959).

[135] S. Fujii, U. Akiba, and M. Fujihira, *Geometry for Self-Assembling of Spherical Hydrocarbon Cages with Methane Thiolates on Au{111}*, Journal of the American Chemical Society **124**, 13629 (2002).

[136] S. Wakamatsu, S. Fujii, U. Akiba, and M. Fujihira, *Motions of Single Molecules Inserted in a Self-Assembled Monolayer Matrix of a Bicyclo [2.2.2] Octane Derivative on Au{111}*, Nanotechnology **14**, 258 (2003).

[137] A. J. Bard and L. R. Faulkner, *Electrochemical Methods: Fundamentals and Applications*, 2nd ed. (John Wiley and Sons, Inc., New York, NY, 2001).

[138] D. C. Harris, *Quantitative Chemical Analysis*, 5th ed. (W.H. Freeman, Ney York, NY, 1999).

[139] D. A. Skoog, W. D. M., H. F. J., and S. R. Crouch, *Analytical Chemistry: An Introduction* (Harcourt, Inc., Orlando, FL, 2000).

[140] B. C. Smith, *Fundamentals of Fourier Transform Infrared Spectroscopy* (CRC Press, Boca Raton, FL, 1996).

[141] H. G. Tompkins and E. A. Irene, *Handbook of Ellipsometry* (Academic Press, Boston, MA, 2003).

[142] H. G. Tompkins and W. A. McGahan, *Spectroscopic Ellipsometry and Reflectometry: A User's Guide* (John Wiley and Sons, Inc., New York, NY, 1999).

[143] J. Wang, *Analytical Electrochemistry*, 2nd ed. (John Wiley and Sons, Inc., New York, NY, 2000).

[144] M. D. Porter, T. B. Bright, D. L. Allara, and C. E. D. Chidsey, *Spontaneously Organized Molecular Assemblies. 4. Structural Characterization of Normal-Alkyl Thiol Monolayers on Gold by Optical Ellipsometry, Infrared Spectroscopy, and Electrochemistry*, Journal of the American Chemical Society **109**, 3559 (1987).

[145] N. Sandhyarani and T. Pradeep, *Current Understanding of the Structure, Phase Transitions and Dynamics of Self-Assembled Monolayers on Two- and Three-Dimensional Surfaces*, International Reviews in Physical Chemistry **22**, 221 (2003).

[146] R. G. Nuzzo, L. H. Dubois, and D. L. Allara, *Fundamental-Studies of Microscopic Wetting on Organic-Surfaces. 1. Formation and Structural Characterization of a Self-Consistent Series of Polyfunctional Organic Monolayers*, Journal of the American Chemical Society **112**, 558 (1990).

[147] A. N. Parikh, D. L. Allara, I. B. Azouz, and F. Rondelez, *An Intrinsic Relationship between Molecular-Structure in Self-Assembled n-Alkylsiloxane Monolayers and Deposition Temperature*, Journal of Physical Chemistry **98**, 7577 (1994).

[148] A. N. Parikh, B. Liedberg, S. V. Atre, M. Ho, and D. L. Allara, *Correlation of Molecular-Organization and Substrate Wettability in the Self-Assembly of n-Alkylsiloxane Monolayers*, Journal Of Physical Chemistry **99**, 9996 (1995).

[149] T. Kakiuchi, K. Sato, M. Iida, D. Hobara, S. Imabayashi, and K. Niki, *Phase Separation of Alkanethiol Self-Assembled Monolayers During the Replacement of Adsorbed Thiolates on Au{111} with Thiols in Solution*, Langmuir **16**, 7238 (2000).

[150] T. Kakiuchi, H. Usui, D. Hobara, and M. Yamamoto, *Voltammetric Properties of the Reductive Desorption of Alkanethiol Self-Assembled Monolayers from a Metal Surface*, Langmuir **18**, 5231 (2002).

[151] C. A. Widrig, C. Chung, and M. D. Porter, *The Electrochemical Desorption of n-Alkanethiol Monolayers from Polycrystalline Au and Ag Electrodes*, Journal of Electroanalytical Chemistry **310**, 335 (1991).

[152] C. J. Zhong and M. D. Porter, *Fine Structure in the Voltammetric Desorption Curves of Alkanethiolate Monolayers Chemisorbed at Gold*, Journal of Electroanalytical Chemistry **425**, 147 (1997).

[153] C. J. Zhong, J. Zak, and M. D. Porter, *Voltammetric Reductive Desorption Characteristics of Alkanethiolate Monolayers at Single Crystal Au{111} and {110} Electrode Surfaces*, Journal of Electroanalytical Chemistry **421**, 9 (1997).

[154] S.-I. Imabayashi, N. Gon, T. Sasaki, D. Hobara, and T. Kakiuchi, *Effect of Nanometer-Scale Phase Separation on Wetting of Binary Self-Assembled Thiol Monolayers on Au{111}*, Langmuir **14**, 2348 (1998).

[155] S.-I. Imabayashi, D. Hobara, and T. Kakiuchi, *Selective Replacement of Adsorbed Alkanethiols in Phase-Separated Binary Self-Assembled Monolayers by Electrochemical Partial Desorption*, Langmuir **13**, 4502 (1997).

[156] S.-I. Imabayashi, D. Hobara, and T. Kakiuchi, *Voltammetric Detection of the Surface Diffusion of Adsorbed Thiolate Molecules in Artificially Phase-Separated Binary Self-Assembled Monolayers on a Au{111} Surface*, Langmuir **17**, 2560 (2001).

[157] J. R. Geigy, *Alpha-(Adamant-Ylthio)Carboxylic Acids*, Chemical Abstracts **60**, 9167 (1964).

[158] S. Dingman, and P. Gao, Sigma-Aldrich Co., Personal communication, 2005.

[159] S.-W. Tam-Chang, H. Biebuyck, G. M. Whitesides, N. Jeon, and R. G. Nuzzo, *Self-Assembled Monolayers on Gold Generated from Alkanethiols with the Structure RnHCOCH$_2$SH*, Langmuir **11**, 4371 (1995).

[160] L. A. Bumm, J. J. Arnold, L. F. Charles, T. D. Dunbar, D. L. Allara, and P. S. Weiss, *Directed Self-Assembly to Create Molecular Terraces with Molecularly Sharp Boundaries in Organic Monolayers*, Journal of the American Chemical Society **121**, 8017 (1999).

[161] P. E. Laibinis, R. G. Nuzzo, and G. M. Whitesides, *Structure of Monolayers Formed by Coadsorption of Two n-Alkanethiols of Different Chain Lengths on Gold and Its Relation to Wetting*, Journal of Physical Chemistry **96**, 5097 (1992).

[162] E. Delamarche, B. Michel, C. Gerber, D. Anselmetti, H.-J. Gntherodt, H. Wolf, and H. Ringsdorf, *Real-Space Observation of Nanoscale Molecular Domains in Self-Assembled Monolayers*, Langmuir **10**, 2869 (1994).

[163] L. H. Dubois and R. G. Nuzzo, *Synthesis, Structure, and Properties of Model Organic Surfaces*, Annual Review of Physical Chemistry **43**, 437 (1992).

[164] A. Ulman, J. E. Eilers, and N. Tillman, *Packing and Molecular Orientation of Alkanethiol Monolayers on Gold Surfaces*, Langmuir **5**, 1147 (1989).

[165] G. Maroulis, D. Xenides, U. Hohm, and A. Loose, *Dipole, Dipole-Quadrupole, and Dipole-Octopole Polarizability of Adamantane, C$_{10}$H$_{16}$, from Refractive Index Measurements, Depolarized Collision-Induced Light Scattering, Conventional Ab Initio and Density Functional Theory Calculations*, Journal Of Chemical Physics **115**, 7957 (2001).

[166] Y. Watanabe, Y. Shibasaki, S. Ando, and M. Ueda, *Synthesis of Semiaromatic Polyimides from Aromatic Diamines Containing Adamantyl Units and Alicyclic Dianhydrides*, Journal of Polymer Science Part A: Polymer Chemistry **42**, 144 (2004).

[167] P. E. Laibinis, M. A. Fox, J. P. Folkers, and G. M. Whitesides, *Comparisons of Self-Assembled Monolayers on Silver and Gold: Mixed Monolayers Derived from Hs(CH$_2$)$_{21}$X and HS(CH$_2$)$_{10}$Y (X, Y = CH$_3$, CH$_2$OH) Have Similar Properties*, Langmuir **7**, 3167 (1991).

[168] W. J. Miller and N. L. Abbott, *Influence of Van Der Waals Forces from Metallic Substrates on Fluids Supported on Self-Assembled Monolayers Formed from Alkanethiols*, Langmuir **13**, 7106 (1997).

[169] R. K. Smith, *Precise Nano-Scale Assemblies: Undecagold Clusters and Self-Assembled Monolayers*, Ph.D. Thesis, The Pennsylvania State University, 2005.

[170] J. O. Jensen, *Vibrational Frequencies and Structural Determination of Adamantane*, Spectrochimica Acta Part A-Molecular And Biomolecular Spectroscopy **60**, 1895 (2004).

[171] N. Polfer, B. G. Sartakov, and J. Oomens, *The Infrared Spectrum of the Adamantyl Cation*, Chemical Physics Letters **400**, 201 (2004).

[172] Hereafter only the sweep in the negative direction (cathodic portion) of the cyclic voltammogram will be shown. However, in all cases both sweeps were acquired.

[173] A. Bard, K. K. Berggren, J. L. Wilbur, J. D. Gillaspy, S. L. Rolston, J. J. McClelland, W. D. Phillips, M. Prentiss, and G. M. Whitesides, *Self-Assembled Monolayers Exposed by Metastable Argon and Metastable Helium for Neutral Atom Lithography and Atomic Beam Imaging*, Journal of Vacuum Science and Technology B **15**, 1805 (1997).

[174] E. Delamarche, A. C. F. Hoole, B. Michel, S. Wilkes, M. Despont, M. E. Welland, and H. Biebuyck, *Making Gold Nanostructures Using Self-Assembled Monolayers and a Scanning Tunneling Microscope*, Journal of Physical Chemistry B **101**, 9263 (1997).

[175] J. C. Love, D. B. Wolfe, M. L. Chabinyc, K. E. Paul, and G. M. Whitesides, *Self-Assembled Monolayers of Alkanethiolates on Palladium Are Good Etch Resists*, Journal of the American Chemical Society **124**, 1576 (2002).

[176] C. S. Whelan, M. J. Lercel, H. G. Craighead, K. Seshadri, and D. L. Allara, *Improved Eectron-Beam Patterning of Si with Self-Assembled Monolayers*, Applied Physics Letters **69**, 4245 (1996).

[177] V. I. Nefedov, *X-Ray Photoelectron Spectroscopy of Solid Surfaces* (VSP BV, Utrecht, Netherlands, 1988).

[178] G. A. Somorjai, *Introduction to Surface Chemistry and Catalysis* (John Wiley and Sons, New York, NY, 1994).

[179] N. Fairley, CasaXPS version 2.3.5, Freeware: http://www.casaxps.com/

[180] P. Fenter, A. Eberhardt, K. S. Liang, and P. Eisenberger, *Epitaxy and Chainlength Dependent Strain in Self-Assembled Monolayers*, Journal of Chemical Physics **106**, 1600 (1997).

[181] J. Noh, T. Araki, K. Nakajima, and M. Hara, *Molecular Decomposition Via Striped Phase in Self-Assembled Monolayers of Alkanethiols Adsorbed on Au{111}*, Molecular Crystals and Liquid Crystals **371**, 95 (2001).

[182] J. Noh and M. Hara, *Surface Structures in Spatio-Temporal Ordering of Alkanethiol Self-Assembled Monolayers on Au{111}*, Molecular Crystals and Liquid Crystals **349**, 223 (2000).

[183] J. Noh, K. Nakajima, M. Hara, H. Sasabe, W. Knoll, and H. Lee, *Adsorption and Desorption Processes of Hexanethiol Self-Assembled Monolayers on Au{111} Studied by Scanning Tunneling Microscopy*, Korea Polymer Journal **6**, 307 (1998).

[184] G. E. Poirier and M. J. Tarlov, *Molecular Ordering and Gold Migration Observed in Butanethiol Self-Assembled Monolayers Using Scanning-Tunneling-Microscopy*, Journal of Physical Chemistry **99**, 10966 (1995).

[185] G. E. Poirier, M. J. Tarlov, and H. E. Rushmeier, *2-Dimensional Liquid-Phase and the P×$\sqrt{3}$-Phase of Alkanethiol Self-Assembled Monolayers on Au{111}*, Langmuir **10**, 3383 (1994).

[186] Z. J. Donhauser, D. W. Price II, J. M. Tour, and P. S. Weiss, *Control of Alkanethiolate Monolayer Structure Using Vapor-Phase Annealing*, Journal of the American Chemical Society **125**, 11462 (2003).

[187] K. Andersson, A. Nikitin, L. G. M. Pettersson, A. Nilsson, and H. Ogasawara, *Water Dissociation on Ru{001}:An Activated Process*, Physical Review Letters **93**, 196101 (2004).

[188] J. F. Moulder, *Handbook of X-Ray Photoelectron Spectroscopy: A Reference Book of Standard Spectra for Identification and Interpretation of XPS Data* (Perkin-Elmer Corporatioon, Physical Electronics Division, Eden Prairie, MN, 1999).

[189] J. J. Pireaux, M. Chtaib, J. P. Delrue, P. A. Thiry, M. Liehr, and R. Caudano, *Electron Spectroscopic Characterization of Oxygen Adsorption on Gold Surfaces: I. Substrate Impurity Effects on Molecular Oxygen Adsorption in Ultra High Vacuum*, Surface Science **141**, 211 (1984).

[190] J. J. Pireaux, M. Liehr, P. A. Thiry, J. P. Delrue, and R. Caudano, *Electron Spectroscopic Characterization of Oxygen Adsorption on Gold Surfaces: II. Production of Gold Oxide in Oxygen DC Reactive Sputtering*, Surface Science **141**, 221 (1984).

[191] H. Ron and I. Rubinstein, *Alkanethiol Monolayers on Preoxidized Gold – Encapsulation of Gold Oxide under an Organic Monolayer*, Langmuir **10**, 4566 (1994).

[192] C. Yan, A. Golzhauser, M. Grunze, and C. Woll, *Formation of Alkanethiolate Self-Assembled Monolayers on Oxidized Gold Surfaces*, Langmuir **15**, 2414 (1999).

[193] A. S. Duwez, *Exploiting Electron Spectroscopies to Probe the Structure and Organization of Self-Assembled Monolayers: A Review*, Journal of Electron Spectroscopy and related Phenomena **134**, 97 (2004).

[194] P. E. Laibinis, C. D. Bain, and G. M. Whitesides, *Attenuation of Photoelectrons in Monolayers of Normal-Alkanethiols Adsorbed on Copper, Silver, and Gold*, Journal of Physical Chemistry **95**, 7017 (1991).

[195] M. T. Lee, C. C. Hsueh, M. S. Freund, and G. S. Ferguson, *Air Oxidation of Self-Assembled Monolayers on Polycrystalline Gold: The Role of the Gold Substrate*, Langmuir **14**, 6419 (1998).

[196] T. M. Willey, A. L. Vance, T. van Buuren, C. Bostedt, L. J. Terminello, and C. S. Fadley, *Rapid Degradation of Alkanethiol-Based Self-Assembled Monolayers on Gold in Ambient Laboratory Conditions*, Surface Science **576**, 188 (2005).

[197] M. C. Bourg, A. Badia, and R. B. Lennox, *Gold-Sulfur Bonding in 2-D and 3-D Self-Assembled Monolayers: XPS Characterization*, Journal of Physical Chemistry B **104**, 6562 (2000).

[198] P. Kohli, K. K. Taylor, J. J. Harris, and G. J. Blanchard, *Assembly of Covalently-Coupled Disulfide Multilayers on Gold*, Journal of the American Chemical Society **120**, 11962 (1998).

[199] C. D. Bain, H. A. Biebuyck, and G. M. Whitesides, *Comparison of Self-Assembled Monolayers on Gold – Coadsorption of Thiols and Disulfides*, Langmuir **5**, 723 (1989).

[200] T. Ishida, N. Choi, W. Mizutani, H. Tokumoto, I. Kojima, H. Azehara, H. Hokari, U. Akiba, and M. Fujihira, *High-Resolution X-Ray Photoelectron Spectra of Organosulfur Monolayers on Au{111}: S(2p) Spectral Dependence on Molecular Species*, Langmuir **15**, 6799 (1999).

[201] M. Wirde, U. Gelius, T. Dunbar, and D. L. Allara, *Modification of Self-Assembled Monolayers of Alkanethiols on Gold by Ionizing Radiation*, Nuclear Instruments and Methods in Physics Research, Section B: Beam Interactions with Materials and Atoms **131**, 245 (1997).

[202] D. G. Castner, K. Hinds, and D. W. Grainger, *X-Ray Photoelectron Spectroscopy Sulfur 2p Study of Organic Thiol and Disulfide Binding Interactions with Gold Surfaces*, Langmuir **12**, 5083 (1996).

[203] G. Gonella, O. Cavalleri, S. Terreni, D. Cvetko, L. Floreano, A. Morgante, M. Canepa, and R. Rolandi, *High Resolution X-Ray Photoelectron Spectroscopy of 3-Mercaptopropionic Acid Self-Assembled Films*, Surface Science **566**, 638 (2004).

[204] D. E. Weisshaar, M. M. Walczak, and M. D. Porter, *Electrochemically Induced Transformations of Monolayers Formed by Self-Assembly of Mercaptoethanol at Gold*, Langmuir **9**, 323 (1993).

[205] C.-J. Zhong and M. D. Porter, *Evidence for Carbon-Sulfur Bond Cleavage in Spontaneously Adsorbed Organosulfide-Based Monolayers at Gold*, Journal of the American Chemical Society **116**, 11616 (1994).

[206] D. Hobara, O. Miyake, S. Imabayashi, K. Niki, and T. Kakiuchi, *In Situ Scanning Tunneling Microscopy Imaging of the Reductive Desorption Process of Alkanethiols on Au{111}*, Langmuir **14**, 3590 (1998).

[207] D. Hobara, M. Ota, S. Imabayashi, K. Niki, and T. Kakiuchi, *Phase Separation of Binary Self-Assembled Thiol Monolayers Composed of 1-Hexadecanethiol and 3-Mercaptopropionic Acid on Au{111} Studied by Scanning Tunneling Microscopy and Cyclic Voltammetry*, Journal of Electroanalytical Chemistry **444**, 113 (1998).

[208] D. Hobara, K. Ueda, S. Imabayashi, M. Yamamoto, and T. Kakiuchi, *Phase Separation of Binary Self-Assembled Thiol Monolayers of 2Mercaptoethanesulfonic Acid and 1Octadecanethiol on Au{111}*, Electrochemistry **67**, 1218 (1999).

[209] F. Schreiber, *Structure and Growth of Self-Assembling Monolayers*, Progress in Surface Science **65**, 151 (2000).

[210] H. C. Kang and W. H. Weinberg, *Kinetic Modeling of Surface Rate-Processes*, Surface Science **300**, 755 (1994).

[211] S. J. Lombardo and A. T. Bell, *A Review of Theoretical-Models of Adsorption, Diffusion, Desorption, and Reaction of Gases on Metal-Surfaces*, Surface Science Reports **13**, 1 (1991).

[212] G. F. Cerofolini, *Theory of Localized Adsorption on Surfaces Undergoing Reversible Reconstruction*, Physical Review E **67**, (2003).

[213] O. Dannenberger, M. Buck, and M. Grunze, *Self-Assembly of n-Alkanethiols: A Kinetic Study by Second Harmonic Generation*, Journal of Physical Chemistry B **103**, 2202 (1999).

[214] K. A. Peterlinz and R. Georgiadis, *In Situ Kinetics of Self-Assembly by Surface Plasmon Resonance Spectroscopy*, Langmuir **12**, 4731 (1996).

[215] A. M. Bowler and E. S. Hood, *Time-Dependent Monte-Carlo Studies of Diffusion with Surface Steps*, Journal of Chemical Physics **97**, 1257 (1992).

[216] A. M. Bowler and E. S. Hood, *Time-Dependent Monte-Carlo Studies of Diffusion with Surface Traps*, Journal of Chemical Physics **97**, 1250 (1992).

[217] H. C. Kang, C. B. Mullins, and W. H. Weinberg, *Molecular Adsorption of Ethane on the Ir{110}-(1×2) Surface – Monte-Carlo Simulations and Molecular-Beam Reflectivity Measurements*, Journal of Chemical Physics **92**, 1397 (1990).

[218] R. Subramanian and V. Lakshminarayanan, *A Study of Kinetics of Adsorption of Alkanethiols on Gold Using Electrochemical Impedance Spectroscopy*, Electrochimica Acta **45**, 4501 (2000).

[219] J. B. Schlenoff, M. Li, and H. Ly, *Stability and Self-Exchange in Alkanethiol Monolayers*, Journal of the American Chemical Society **117**, 12528 (1995).

[220] A. L. Bross, A. E. Hooper, L. A. Bumm, D. L. Allara, and P. S. Weiss, *Directing Assembly in Monolayers by Controlling the Exchange Kinetics*, Unpublished manuscript .

[221] S. S. Wong and M. D. Porter, *Origin of the Multiple Voltammetric Desorption Waves of Long-Chain Alkanethiolate Monolayers Chemisorbed on Annealed Gold Electrodes*, Journal of Electroanalytical Chemistry **485**, 135 (2000).

[222] L. S. Jung and C. T. Campbell, *Sticking Probabilities in Adsorption of Alkanethiols from Liquid Ethanol Solutions onto Gold*, Journal of Physical Chemistry B **104**, 11168 (2000).

[223] E. Mishina, T. Tamura, H. Sakaguchi, and S. Nakabayashi, *Kinetics of Adsorption and Self-Assembling of Thiophene and Dodecanethiol Studied by Optical Second Harmonic Generation*, Chemistry Letters **32**, 652 (2003).

[224] A. Eberhardt, P. Fenter, and P. Eisenberger, *Growth Kinetics in Self-Assembling Monolayers: A Unique Adsorption Mechanism*, Surface Science **397**, L285 (1998).

[225] A. Kumar, H. A. Biebuyck, and G. M. Whitesides, *Patterning Self-Assembled Monolayers: Applications in Materials Science*, Langmuir **10**, 1498 (1994).

[226] M. R. Dusseiller, D. Schlaepfer, M. Koch, R. Kroschewski, and M. Textor, *An Inverted Microcontact Printing Method on Topographically Structured Polystyrene Chips for Arrayed Micro-3-D Culturing of Single Cells*, Biomaterials **26**, 5917 (2005).

[227] M. J. Park, W. M. Choi, and O. O. Park, *Fabrication of Patterned Electroluminescent Polymers with Microcontact Printing*, Journal of Nonlinear Optical Physics and Materials **13**, 643 (2004).

[228] W. Prissanaroon, N. Brack, P. J. Pigram, P. Hale, P. Kappen, and J. Liesegang, *Microcontact Printing of Copper and Polypyrrole on Fluoropolymers*, Thin Solid Films **477**, 131 (2005).

[229] J. I. Park, W. R. Lee, S. S. Bae, Y. J. Kim, K. H. Yoo, J. Cheon, and S. Kim, *Langmuir Monolayers of Co Nanoparticles and Their Patterning by Microcontact Printing*, Journal of Physical Chemistry B **109**, 13119 (2005).

[230] D. J. Zhou, A. Bruckbauer, C. Abell, D. Klenerman, and D. J. Kang, *Fabrication of Three-Dimensional Surface Structures with Highly Fluorescent Quantum Dots by Surface-Templated Layer-by-Layer Assembly*, Advanced Materials **17**, 1243 (2005).

[231] E. Delamarche, H. Schmid, A. Bietsch, N. B. Larsen, H. Rothuizen, B. Michel, and H. Biebuyck, *Transport Mechanisms of Alkanethiols During Microcontact Printing on Gold*, Journal of Physical Chemistry B **102**, 3324 (1998).

[232] N. B. Larsen, H. Biebuyck, E. Delamarche, and B. Michel, *Order in Microcontact Printed Self-Assembled Monolayers*, Journal of the American Chemical Society **119**, 3017 (1997).

[233] L. Libioulle, A. Bietsch, H. Schmid, B. Michel, and E. Delamarche, *Contact-Inking Stamps for Microcontact Printing of Alkanethiols on Gold*, Langmuir **15**, 300 (1999).

[234] E. Delamarche, M. Geissler, H. Wolf, and B. Michel, *Positive Microcontact Printing*, Journal of the American Chemical Society **124**, 3834 (2002).

[235] S. J. Stranick, A. N. Parikh, D. L. Allara, and P. S. Weiss, *A New Mechanism for Surface Diffusion: Motion of a Substrate-Adsorbate Complex*, Journal of Physical Chemistry **98**, 11136 (1994).

[236] R. T. Baker, J. D. Mougous, A. Brackley, and D. L. Patrick, *Competitive Adsorption, Phase Segregation, and Molecular Motion at a Solid-Liquid Interface Studied by Scanning Tunneling Microscopy*, Langmuir **15**, 4884 (1999).

[237] L. M. Sun and J. A. Gardella, *Oxidation-Assisted Secondary Ion Mass Spectrometry Methodology to Quantify Mixed Alkylthiol Self-Assembled Monolayers on Gold: Applications to Competitive Chemical Adsorption*, Langmuir **18**, 9289 (2002).

[238] A. A. Dameron, L. F. Charles, and P. S. Weiss, *Structures and Displacement of 1-Ada-ManTaneThiol Self-Assembled Monolayers on Au{111}*, Journal of the American Chemical Society **127**, 8697 (2005).

[239] A. A. Dameron, J. R. Hampton, R. K. Smith, T. J. Mullen, S. D. Gillmor, and P. S. Weiss, *Microdisplacement Printing*, Nano Letters **5**, 1834 (2005).

[240] G. Bar, R. Brandsch, and M. H. Whangbo, *Correlation between Frequency-Sweep Hysteresis and Phase Imaging Instability in Tapping Mode Atomic Force Microscopy*, Surface Science **436**, L715 (1999).

[241] G. Bar, S. Rubin, A. N. Parikh, B. I. Swanson, T. A. Zawodzinski, and M. H. Whangbo, *Scanning Force Microscopy Study of Patterned Monolayers of Alkanethiols on Gold. Importance of Tip-Sample Contact Area in Interpreting Force Modulation and Friction Force Microscopy Images*, Langmuir **13**, 373 (1997).

[242] G. Bar, Y. Thomann, R. Brandsch, H. J. Cantow, and M. H. Whangbo, *Factors Affecting the Height and Phase Images in Tapping Mode Atomic Force Microscopy. Study of Phase-Separated Polymer Blends of Poly(Ethene-Co-Styrene) and Poly(2,6-Dimethyl-1,4-Phenylene Oxide)*, Langmuir **13**, 3807 (1997).

[243] R. Brandsch, G. Bar, and M. H. Whangbo, *On the Factors Affecting the Contrast of Height and Phase Images in Tapping Mode Atomic Force Microscopy*, Langmuir **13**, 6349 (1997).

[244] D. Raghavan, X. Gu, T. Nguyen, M. VanLandingham, and A. Karim, *Mapping Polymer Heterogeneity Using Atomic Force Microscopy Phase Imaging and Nanoscale Indentation*, Macromolecules **33**, 2573 (2000).

[245] M. H. Whangbo, G. Bar, and R. Brandsch, *Qualitative Relationships Describing Height and Phase Images of Tapping Mode Atomic Force Microscopy. An Application to Micro-Contact-Printed Patterned Self-Assembled Monolayers*, Applied Physics A: Materials Science and Processing **66**, S1267 (1998).

[246] D. J. Graham, D. D. Price, and B. D. Ratner, *Solution Assembled and Microcontact Printed Monolayers of Dodecanethiol on Gold: A Multivariate Exploration of Chemistry and Contamination*, Langmuir **18**, 1518 (2002).

[247] D. J. Fuchs, *Probing Nanoparticle Assemblies and Substrate Effects on Self-Assembled Monolayers*, Ph.D. Thesis, The Pennsylvania State University, 2004.

[248] C. D. Bain, J. Evall, and G. M. Whitesides, *Formation of Monolayers by the Coadsorption of Thiols on Gold: Variation in the Head Group, Tail Group, and Solvent*, Journal of the American Chemical Society **111**, 7155 (1989).

[249] F. Bensebaa, R. Voicu, L. Huron, T. H. Ellis, and E. Kruus, *Kinetics of Formation of Long-Chain n-Alkanethiolate Monolayers on Polycrystalline Gold*, Langmuir **13**, 5335 (1997).

[250] J. Lu, E. Delamarche, L. Eng, R. Bennewitz, E. Meyer, and H. J. Guntherodt, *Kelvin Probe Force Microscopy on Surfaces: Investigation of the Surface Potential of Self-Assembled Monolayers on Gold*, Langmuir **15**, 8184 (1999).

[251] J. Lu, L. Eng, R. Bennewitz, E. Meyer, H. J. Guntherodt, E. Delamarche, and L. Scandella, *Surface Potential Studies of Self-Assembling Monolayers Using Kelvin Probe Force Microscopy*, Surface and Interface Analysis **27**, 368 (1999).

[252] M. Jaschke and H. J. Butt, *Deposition of Organic Material by the Tip of a Scanning Force Microscope*, Langmuir **11**, 1061 (1995).

[253] H. Zhang, S. W. Chung, and C. A. Mirkin, *Fabrication of Sub-50-nm Solid-State Nanostructures on the Basis of Dip-Pen Nanolithography*, Nano Letters **3**, 43 (2003).

[254] C. L. Cheung, J. A. Camarero, B. W. Woods, T. W. Lin, J. E. Johnson, and J. J. De Yoreo, *Fabrication of Assembled Virus Nanostructures on Templates of Chemoselective Linkers Formed by Scanning Probe Nanolithography*, Journal of the American Chemical Society **125**, 6848 (2003).

[255] E. J. Peterson, B. L. Weeks, J. J. De Yoreo, and P. V. Schwartz, *Effect of Environmental Conditions on Dip Pen Nanolithography of Mercaptohexadecanoic Acid*, Journal of Physical Chemistry B **108**, 15206 (2004).

[256] S. Rozhok, P. Sun, R. Piner, M. Lieberman, and C. A. Mirkin, *AFM Study of Water Meniscus Formation between an AFM Tip and NaCl Substrate*, Journal of Physical Chemistry B **108**, 7814 (2004).

[257] P. V. Schwartz, *Molecular Transport from an Atomic Force Microscope Tip: A Comparative Study of Dip-Pen Nanolithography*, Langmuir **18**, 4041 (2002).

[258] P. E. Sheehan and L. J. Whitman, *Thiol Diffusion and the Role of Humidity in "Dip Pen Nanolithography"*, Physical Review Letters **88**, 156104 (2002).

[259] B. L. Weeks, A. Noy, A. E. Miller, and J. J. De Yoreo, *Effect of Dissolution Kinetics on Feature Size in Dip-Pen Nanolithography*, Physical Review Letters **88**, 255505 (2002).

[260] J. Y. Jang, S. H. Hong, G. C. Schatz, and M. A. Ratner, *Self-Assembly of Ink Molecules in Dip-Pen Nanolithography: A Diffusion Model*, Journal of Chemical Physics **115**, 2721 (2001).

[261] P. Manandhar, J. Jang, G. C. Schatz, M. A. Ratner, and S. Hong, *Anomalous Surface Diffusion in Nanoscale Direct Deposition Processes*, Physical Review Letters **90**, 115505 (2003).

[262] S. Rozhok, R. Piner, and C. A. Mirkin, *Dip-Pen Nanolithography: What Controls Ink Transport?*, Journal of Physical Chemistry B **107**, 751 (2003).

[263] NanoInk, Personal communication, 2004.

[264] C. D. Bain and G. M. Whitesides, *A Study by Contact Angle of the Acid-Base Behavior of Monolayers Containing W-Mercaptocarboxylic Acids Adsorbed on Gold: An Example of Reactive Spreading*, Langmuir **5**, 1370 (1989).

[265] The role of the water meniscus in ink transport during dpn, particularly when patterning at low relative humidity, is controversial. However, at the relative humidity of our experiments, (21%), there is no dispute that a meniscus forms.

[266] J. Y. Jang, G. C. Schatz, and M. A. Ratner, *How Narrow Can a Meniscus Be?*, Physical Review Letters **92**, 085504 (2004).

[267] *Handbook of Physical Properties of Organic Chemicals*, edited by P. H. Howard and W. M. Meylan (CRC Press, Boca Raton, FL, 1997).

[268] W. M. Meylan, P. H. Howard, and R. S. Boethling, *Improved Method for Estimating Water Solubility from Octanol Water Partition Coefficient*, Environmental Toxicology and Chemistry **15**, 100 (1996).

[269] N. T. Southall, K. A. Dill, and A. D. J. Haymet, *A View of the Hydrophobic Effect*, Journal of Physical Chemistry B **106**, 521 (2002).

[270] C. Tanford, *Theory of Micelle Formation in Aqueous Solutions*, Journal of Physical Chemistry **78**, 2469 (1974).

[271] C. Tanford, *The Hydrophobic Effect: Formation of Micelles and Biological Membranes*, second edition ed. (John Wiley and Sons, New York, NY, 1980).

[272] K. Salaita, A. Amarnath, D. Maspoch, T. B. Higgins, and C. A. Mirkin, *Spontaneous "Phase Separation" of Patterned Binary Alkanethiol Mixtures*, Journal of the American Chemical Society **127**, 11283 (2005).

[273] P. A. Derosa and J. M. Seminario, *Electron Transport through Single Molecules: Scattering Treatment Using Density Functional and Green Function Theories*, Journal of Physical Chemistry B **105**, 471 (2001).

[274] J. A. Larsson, M. Nolan, and J. C. Greer, *Interactions between Thiol Molecular Linkers and the Au13 Nanoparticle*, Journal of Physical Chemistry B **106**, 5931 (2002).

[275] C. A. Mirkin, S.-H. Hong, and L. M. Demers, *Dip-Pen Nanolithography: Controlling Surface Architecture on the Sub-100 Nanometer Length Scale*, ChemPhysChem **2**, 37 (2001).

Vita

Education

Ph.D., The Pennsylvania State University, Chemistry   May 2006

    Thesis Title: Controlling Molecular Assemblies
    Advisor: Prof. Paul S. Weiss

B.S., University of California at Santa Barbara, Creative Studies (Honors)   June 2001

Professional Experience

Graduate Research Assistant, PSU; Advisor: Prof. Paul S. Weiss   2001 – present

Teaching Assistant, physical chemistry laboratory, PSU; Professor: Dr. Daniel Sykes   2001

Undergraduate Research Assistant, UCSB; Advisor: Prof. Jacob Israelachvili   1999 – 2001

Undergraduate Research Assistant, UCSB; Advisors: Dr. Leroy E. Laverman and Prof. Geoffrey F. Strouse   2001

Summer Undergrad Research Experience (SURE) Fellow, Max-Plank Institute for Polymer Science, Mainz, Germany; Advisor: Prof. Dr. Wolfgang Knoll   2000

Honors and Awards

Rustum and Della Roy Innovation in Materials Research Award   2006
Weyenberg Fellowship   2005
AVS Dorothy M. and Earl S. Hoffman Travel Grant   2004
The Pennsylvania State University Travel Grant   2004, 2005
Roberts Graduate Fellowship   2001 – 2002
Creative Studies Honors   2001
Center for Polymer Interfaces and Macromolecular Assemblies (CPIMA) Undergraduate
Fellowship at the Max Plank Institute for Polymer Science, Mainz, Germany   2000
National Nanofabrication Users Network Undergraduate Fellowship at the University
of California at Santa Barbara   1999

Professional Memberships

American Chemical Society
American Vacuum Society
Materials Research Society
Semiconductor Research Corporation